# Computational Modelling of the HyperVapotron Cooling Technique for Nuclear Fusion Applications

Joseph Milnes

Submitted for the degree of Ph.D.

Department of Aerospace Sciences
Cranfield University
Cranfield, UK

2010

CRANFIELD UNIVERSITY

SCHOOL OF ENGINEERING

PhD THESIS

Academic Years: 2004 – 2010

Joseph Milnes

# Computational Modelling of the HyperVapotron Cooling Technique for Nuclear Fusion Applications

Supervisor: Prof D Drikakis

October 2010

This thesis is submitted in (100%) fulfilment of the requirements for the PhD.

# Abstract

Efficient heat transfer technologies are essential for magnetically confined fusion reactors; this applies to both the current generation of experimental reactors as well as future power plants. A number of High Heat Flux devices have therefore been developed specifically for this application. One of the most promising candidates is the HyperVapotron, a water cooled device which relies on internal fins and boiling heat transfer to maximise the heat transfer capability.

Over the past 30 years, numerous variations of the HyperVapotron have been built and tested at fusion research centres around the globe resulting in devices that can now sustain heat fluxes in the region of 20 – 30MW/m$^2$ in steady state. Unfortunately, there have been few attempts to model or understand the internal heat transfer mechanisms responsible for this exceptional performance with the result that design improvements are traditionally sought experimentally which is both inefficient and costly.

This thesis seeks to develop an engineering model of the HyperVapotron device using commercial Computational Fluid Dynamics software. To establish the most appropriate modelling choices, in-depth studies were performed examining the turbulence models (within the Reynolds Averaged Navier Stokes framework), near wall methods, grid resolution and boiling submodels.

Validation of the models is accomplished via comparison with experimental results as well as high order Implicit Large Eddy Simulation methods. It is shown that single phase cavity flows and their related heat transfer characteristics (time-averaged) can be accurately captured if the SST k-omega turbulence model is employed using a fine near-wall grid throughout the cavity (e.g. $y^+ < 1$ throughout). Separately, multiphase solutions with tuned wall boiling models also showed reasonable agreement with experimental data for vertical boiling tubes.

As more complex multiphase HyperVapotron models were constructed, it became clear that there is an intrinsic incompatibility between the fine grids required for the single phase heat transfer predictions and the coarser grids plus wall functions required by the boiling model. Ultimately, the full 3D solution was based on the coarser grids as the fall off in accuracy in single phase heat transfer only becomes significant for HyperVapotron designs with deeper cavities. Since it is also shown here that deeper cavities are generally less efficient, these grid induced errors become less relevant if the primary objective is to find optimised performance.

Comparing the CFD solutions with HyperVapotron experimental data suggests that a RANS-based, multiphase model is indeed capable of predicting performance over a wide range of geometries and boundary conditions. Whilst a definitive set of design improvements is not defined here, it is expected that the methodologies and tools developed will enable designers of future High Heat Flux devices to perform significant virtual prototyping before embarking on the more costly build and test programmes.

# Acknowledgements

First and foremost I would like to thank my colleagues at the United Kingdom Atomic Energy Authority for giving me the opportunity to undertake this research. In particular, David Martin and Chris Waldon have been exceptionally supportive, ensuring that I have had the time and resources required to complete this study whilst still a full time employee of the Authority.

On the academic front, I would like to thank my supervisor Dimitris Drikakis for his guidance throughout the years. In addition, my thanks must also go to Philip Rubini (my supervisor for the first 18 months of the PhD) for helping me get the research off to a good start and Evgeniy Shapiro for his advice during our regular technical discussions.

I am also indebted to the technical support team at ANSYS who showed considerable patience when dealing with my frequent queries. Worthy of special mention is Alan Burns on the ANSYS CFX development team whose expertise and guidance in the field of boiling heat transfer was invaluable in completing this research.

Finally, I'd like to thank my family for their love and support which has been invaluable in completing this work.

Joseph Milnes

*This work was partly funded by the United Kingdom Engineering and Physical Sciences Research Council under grant EP/G003955 and the European Communities under the contract of Association between EURATOM and CCFE. The views and opinions expressed herein do not necessarily reflect those of the European Commission.*

# Contents

# List of Figures

# List of Tables

# Nomenclature

## Acronyms

| | |
|---|---|
| AR | Aspect Ratio |
| BC | Boundary Condition |
| BSL | Baseline turbulence model (referring to ANSYS CFX k-omega and Re Stress turbulence models) |
| CCFE | Culham Centre for Fusion Energy (formally UKAEA) |
| CEA | Commissariat a L'Energie Atomique |
| CFD | Computational Fluid Dynamics |
| CHF | Critical Heat Flux |
| CHT | Conjugate Heat Transfer |
| FE | Finite Element |
| HHF | High Heat Flux |
| HIRECOM | High Resolution Computing methods |
| HTC | Heat Transfer Coefficient |
| HV | HyperVapotron |
| ILES | Implicit Large Eddy Simulation |
| IR | Infra-Red |
| ITER | International Thermonuclear Experimental Reactor |
| JET | Joint European Torus |
| LES | Large Eddy Simulation |
| MAST | Mega Amp Spherical Tokamak |
| NBH | Neutral Beam Heating |
| NS | Navier Stokes |
| PD | Power Density |

| | |
|---|---|
| RANS | Reynolds Averaged Navier Stokes |
| RPI | Rensselaer Polytechnic Institute |
| SFD | Saw-toothed Fin Duct |
| SST | Shear Stress Transport |
| STE | Swirl Tube Element |
| TC | ThermoCouple |
| TVD | Total Variation Diminishing |
| URANS | Unsteady Reynolds Averaged Navier Stokes |

## Greek Symbols

| | |
|---|---|
| $\alpha$ | Constant used in k-omega turbulence model |
| $\beta$ | Advection scheme blend factor |
| $\beta'$ | Constant used in k-omega turbulence model |
| $\beta''$ | Constant used in k-omega turbulence model |
| $x$ | Quality (mass fraction of vapour) |
| $\Gamma_{\alpha\beta}$ | Mass transferred per unit volume from vapour phase β to liquid phase α |
| $\Delta n$ | Distance between first and second grid point from the wall |
| $\Delta p$ | Pressure rise / drop |
| $\Delta \vec{r}$ | Vector from upwind node |
| $\Delta T$ | Temperature rise / drop |
| $\Delta T_{sub}$ | Near wall liquid subcooling |
| $\Delta T_{sup}$ | Wall superheating |
| $\delta$ | Identity matrix or Kronecker Delta function |
| $\varepsilon$ | Turbulence eddy dissipation |
| $\phi$ | Bubble contact angle |
| $\phi_i$ | Variable value at node i |
| $\phi_{ip}$ | Variable value at integration point |
| $\phi_{up}$ | Variable value at upwind node |

| | |
|---|---|
| $\Phi_{ij}$ | Pressure-strain tensor |
| $\lambda$ | Viscosity relating stresses to volumetric deformation |
| $\mu$ | Dynamic Viscosity |
| $\mu_t$ | Turbulent Viscosity |
| $\mu_{td}$ | Turbulent Viscosity of dispersed phase |
| $\nu$ | Kinematic Viscosity |
| $\rho$ | Density |
| $\rho_g$ | Gas density |
| $\sigma$ | Surface tension |
| $\sigma_k$ | Constant used in k-epsilon and k-omega turbulence models |
| $\sigma_\varepsilon$ | Constant used in k-epsilon and k-omega turbulence models |
| $\tau$ | Viscous stress tensor |
| $\tau_{ij}$ | Viscous stress component |
| $\tau_w$ | Shear stress at the wall |
| $\omega$ | Turbulent eddy frequency |

## Latin Symbols

| | |
|---|---|
| $a_l$ | Liquid Thermal Diffusivity |
| $A_c$ | Area of wall subject to convective heat transfer |
| $A_{\alpha\beta}$ | Interphase Area Density ($=\frac{6r_\beta}{d_\beta}$) |
| $c_p$ | Specific heat |
| $C_D$ | Drag coefficient |
| $C_{\varepsilon 1}$ | Constant used in k-epsilon turbulence model |
| $C_{\varepsilon 2}$ | Constant used in k-epsilon turbulence model |
| $C_\mu$ | Constant used in the two-equation eddy viscosity models |
| $d$ | Diameter |
| $d_\beta$ | Bubble diameter of dispersed vapour phase $\beta$ |
| $d_w$ | Bubble departure diameter |

| | |
|---|---|
| $D_c$ | Critical nucleation cavity diameter |
| $f$ | Bubble departure frequency |
| $h$ | Enthalpy |
| $h_o$ | Total Enthalpy $= h + \frac{1}{2}\left(u^2 + v^2 + w^2\right)$ |
| $h_{fg}$ | Latent heat of evaporation |
| $h_{mix}$ | Mixture static enthalpy |
| $h_{sat}$ | Saturation enthalpy |
| $h_c$ | Convective heat transfer coefficient |
| $h_q$ | Quenching heat transfer coefficient |
| $k$ | Turbulent Kinetic Energy per unit mass |
| $k_c$ | Thermal Conductivity |
| $k_g$ | Thermal Conductivity of Gas |
| $k_l$ | Thermal Conductivity of Liquid |
| $m_{\alpha\beta}$ | Mass flux from phase α to phase β |
| $\vec{M}_{\alpha}$ | Tensor describing interfacial forces acting on phase α due to the presence of other phases. |
| $n$ | Nucleation site density |
| $N_i$ | Element shape function |
| $Nu$ | Nusselt number |
| $p$ | Pressure |
| $p_{in}$ | Inlet pressure |
| $P_{ij,b}$ | Production term due to buoyancy in BSL Re Stress turbulence model |
| $P_k$ | Turbulence production term in k-epsilon turbulence model |
| $P_{kb}$ | Buoyancy term in k-epsilon turbulence model |
| $P_{\varepsilon b}$ | Buoyancy term in k-epsilon turbulence model |
| $Pr$ | Prandtl number |
| $q_{\alpha\beta}$ | Heat flux from phase α to phase β |
| $Q_w$ | Heat flux applied at the wall |
| $Q_c$ | Heat flux removed by convection to the liquid |
| $Q_q$ | Heat flux removed by quenching |
| $Q_e$ | Heat flux removed by evaporation |

| | |
|---|---|
| $Q_{cg}$ | Heat flux removed by convection to the gas |
| $r_\alpha$ | Volume fraction of liquid phase $\alpha$ |
| $r_\beta$ | Volume fraction of vapour phase $\beta$ |
| $r_{min}$ | Minimum volume fraction of vapour phase $\beta$ |
| $Re$ | Reynolds number |
| $Re_{TP}$ | Two phase Reynolds number |
| $S_h$ | Source of Enthalpy |
| $\vec{S}_M$ | Momentum Source Vector $\left[S_{Mx}, S_{My}, S_{Mz}\right]^T$ |
| $S_{Mx}$ | Momentum Source component in x direction |
| $S_{My}$ | Momentum Source component in y direction |
| $S_{Mz}$ | Momentum Source component in z direction |
| $St$ | Stanton number |
| $t$ | Time |
| $t_w$ | Waiting time between bubble departures |
| $T$ | Temperature |
| $T_{bulk}$ | Bulk temperature |
| $T_i$ | Incipient boiling temperature |
| $T_{in}$ | Inlet temperature |
| $T_{nw}$ | Near wall temperature |
| $T_{sat}$ | Saturation temperature |
| $T_w$ | Wall temperature |
| $\vec{U}$ | Velocity Vector $[u, v, w]^T$ |
| $\overline{\vec{U}}$ | Time averaged Velocity Vector |
| $\vec{u}$ | Time varying Velocity Vector |
| $u^+$ | Non dimensional velocity scale |
| $u*$ | Alternative velocity scale |
| $U_t$ | Velocity tangential to the wall |
| $u$ | Velocity component in x direction |
| $v$ | Velocity component in y direction |

| | |
|---|---|
| $V$ | Velocity magnitude |
| $w$ | Velocity component in z direction |
| $y^*$ | Alternative non dimensional distance to the wall |
| $y^+$ | Non dimensional distance to the wall $\left( = \frac{\sqrt{\tau_w / \rho} \cdot \Delta n}{\nu} \right)$ |

## Subscript Symbols

| | |
|---|---|
| $\alpha$ | Denotes continuous liquid phase |
| $\beta$ | Denotes dispersed vapour phase |
| l | Denotes liquid |
| g | Denotes gas |
| w | Denotes wall |

## Operator Symbols

| | |
|---|---|
| $\nabla \phi$ | Gradient operator $\left( = \frac{\partial \phi}{\partial x}\vec{i} + \frac{\partial \phi}{\partial y}\vec{j} + \frac{\partial \phi}{\partial x}\vec{k} \right)$ |
| $\nabla \cdot \vec{U}$ | Divergence operator $\left( = \frac{\partial U_x}{\partial x} + \frac{\partial U_y}{\partial y} + \frac{\partial U_z}{\partial x} \right)$ |
| $\vec{U} \otimes \vec{V}$ | Dyadic operator $\left( = \begin{bmatrix} U_x V_x & U_x V_y & U_x V_z \\ U_y V_x & U_y V_y & U_y V_z \\ U_z V_x & U_z V_y & U_z V_z \end{bmatrix} \right)$ |

# 1

# 1 Introduction

This thesis is concerned with the computational modelling of a HyperVapotron, a heat transfer device developed to cope with the extreme heat fluxes present within a Nuclear Fusion reactor.

Chapter 1 begins with a brief introduction into the principles behind magnetically confined fusion before proceeding with an in-depth history of the HyperVapotron itself. From its initial development as a cooling method for cylindrical electron tubes through to its modification to a rectangular geometry for Fusion applications, a great many empirical studies have been performed over the past 30 years. Since little was understood of its internal heat transfer mechanisms, several variations of the HyperVapotron concept have been built and tested and many of the key empirical results are included here. Detailed examination of these results was critical in guiding the research as well as providing valuable validation data against which prospective models could be tested.

## 1.1 Nuclear Fusion and associated High Heat Flux technologies

Nuclear Fusion is the process whereby two light nuclei are forced together producing a larger nucleus, releasing a significant amount energy (this is the process that powers the stars). On earth, this process can be reproduced in a device known as a Tokamak. A Tokamak uses a toroidal vessel and powerful magnetic fields to confine a hot plasma, allowing it to be heated to the conditions required to achieve fusion of the fuels (in most cases Deuterium and Tritium, the two isotopes of Hydrogen).

JET [1], the Joint European Torus, is currently the largest Tokamak in existence and is based at Culham in Oxfordshire (see Figure 1). The Culham Centre for Fusion Energy (CCFE) is responsible for maintaining and upgrading this device. JET, and its successor

ITER [2], are key steps on the road to developing a Fusion Power Plant, foreseen within the next 30 to 50 years (based on current funding levels).

Tokamak plasmas, without the benefit of the huge pressures generated by the gravitational forces in stars, require exceedingly high temperatures to achieve the necessary conditions (typically 100 to 200 million $^{o}$C). These conditions, combined with the output fusion power, necessitate the dissipation of heat fluxes of up to 10 to 20 MW/m$^2$ in both the tokamak itself and the auxiliary heating systems (such as the Neutral Beam Heating (NBH) system [3], see Figure 2 and Figure 3). More specifically, the most heavily loaded components in a fusion reactor are the tokamak's divertor (the channel at the bottom of the vessel shown in Figure 1) and the ion dumps, calorimeters and beam scrapers installed on the NBH systems (see Figure 3). To put these heat fluxes into context, these are typically an order of magnitude greater than those experienced in fission reactors (as illustrated by Chang [4], see Figure 4).

As tokamaks and their ancillary systems have developed into larger, more powerful machines, the fusion community has sought to develop High Heat Flux (HHF) technologies that can cope with the increasing power densities and pulse lengths required by these machines. Chang shows some typical examples of HHF devices (Figure 5), most of which have been subjected to a large amount of testing by many of the fusion research associations around the globe. One of the most promising devices is the HyperVapotron. It is the heat transfer mechanism and performance of this specific HHF device which is the subject of this study.

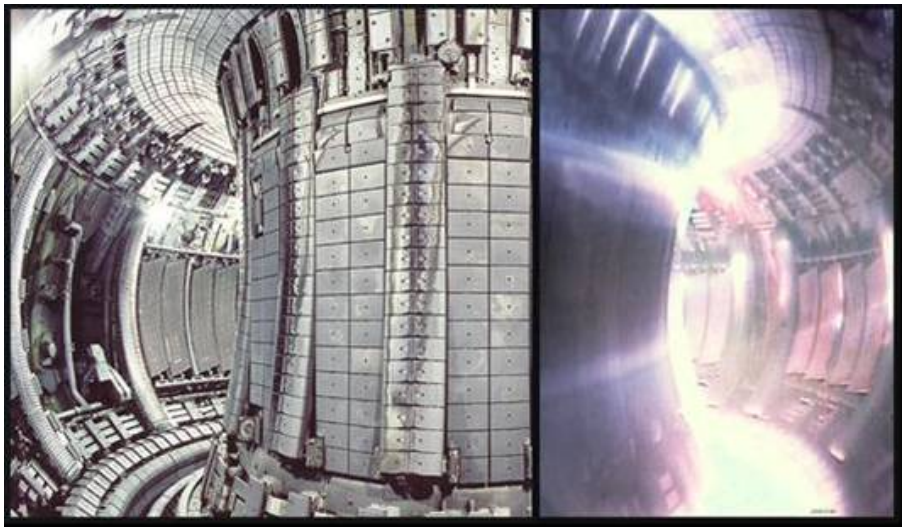

**Figure 1: View inside the JET Tokamak**

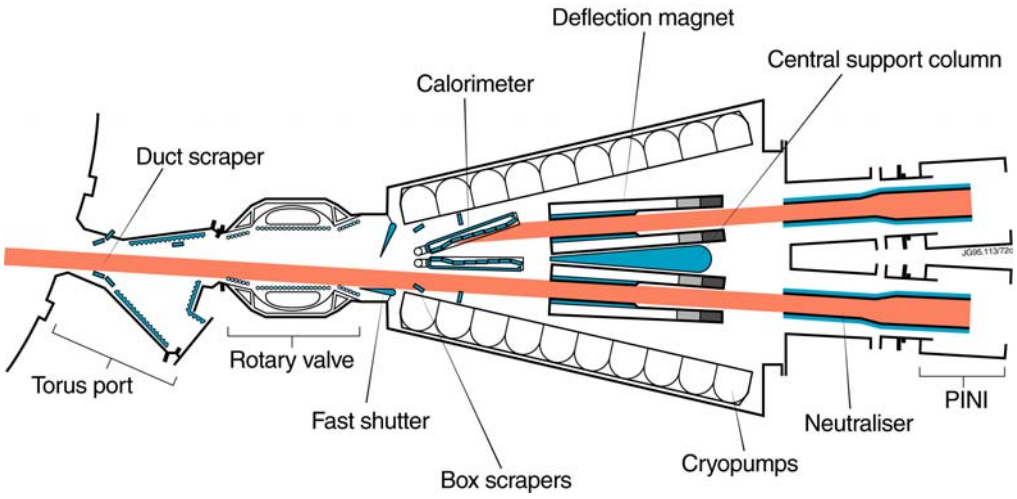


**Figure 2: JET Neutral Beam Heating systems – Plan View**

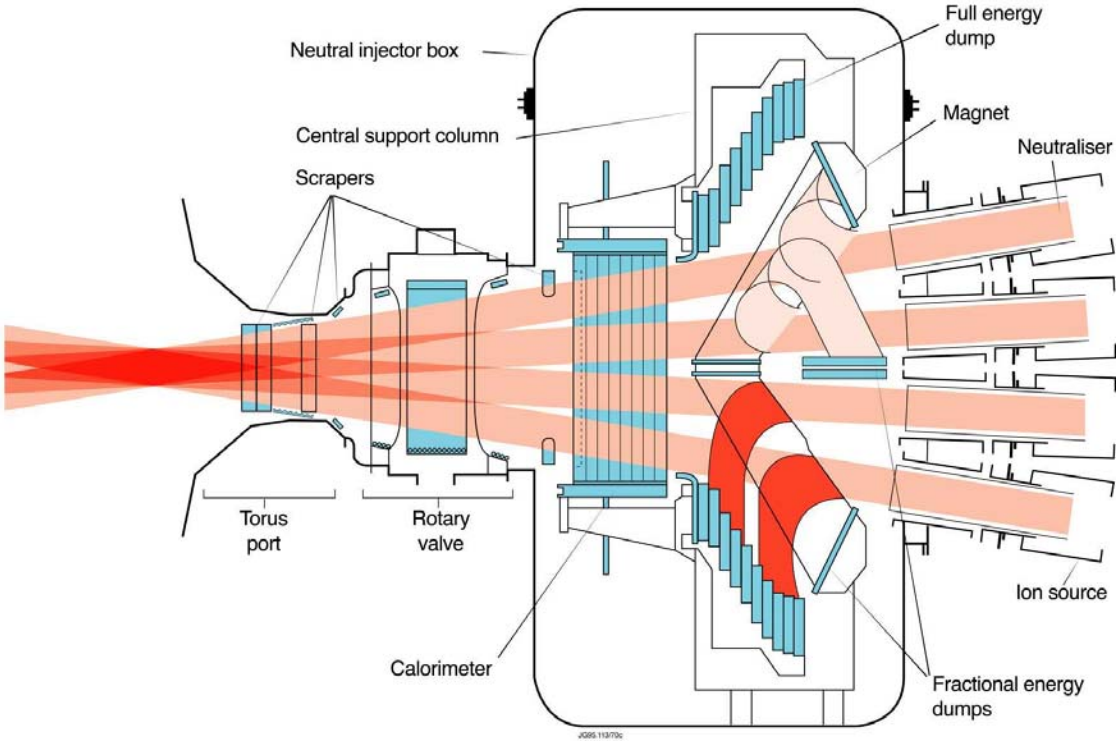


**Figure 3: JET Neutral Beam Heating systems – Elevation View**

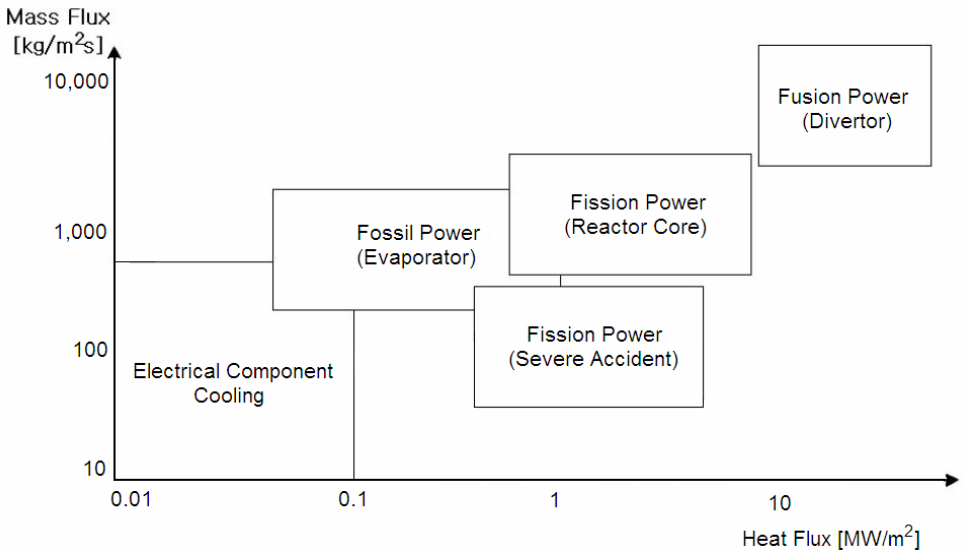


**Figure 4: The Application Areas of Critical Heat Flux (Chang [4])**

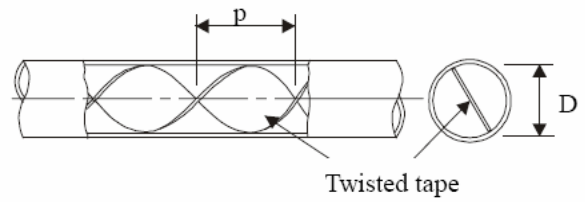


(a) Round tube with a twisted tape insert

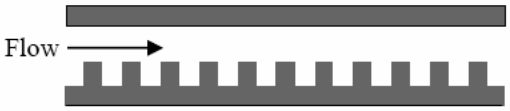


(b) Rectangular channel with a hypervapotron

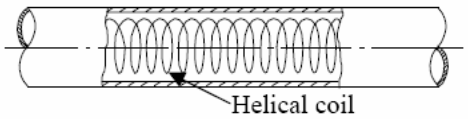


(c) Round tube with a helical coil insert

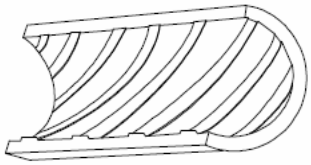

(d) Ribbed tube

**Figure 5: Chang's examples of some High Heat Flux technology [4]**

Information on HyperVapotrons is available through a number of different sources. As well as conference proceedings and journal papers, a wide range of results and analysis has also been reported in the form of JET Departmental Notes (not available in the public domain although key results have been summarised here). Many of these sources have given a useful insight into the development of these devices to the point where they have become key building blocks for many of the HHF systems present on current and future Nuclear Fusion devices.

## 1.2 HyperVapotrons – A history

### 1.2.1 Initial Vapotron development

In the first instance, it is important to understand where the term "HyperVapotron" originated and how this is differentiated from the Vapotron technology which has been industrially exploited since the 1950s.

In one of the earliest papers available (1970), Beutheret [5] examines the liquid/vapour structure in a finned heat exchanger. Beutheret suggests that, while the transition region between the critical boiling temperature[1] and the Leidenfrost temperature[2] is generally unstable under a constant heat flux boundary condition (zone ML in Figure 7), experience has shown that all types of vaporisation (from nucleate through to film boiling) can be stabilised along a non-isothermal wall. This is possible if the cold end of the wall is maintained at or below the incipient boiling temperature $T_i$, with stability being assured by conduction effects within the solid. It is this stabilisation of the boiling process along a non-isothermal wall that the author describes as the "Vapotron Effect".

Beutheret [5] proposes a number of potentially beneficial mechanisms that can result when the different types of vaporisation are juxtaposed on the same surface. For instance, he suggests that turbulence can cause the liquid front that separates the film and coalescing boiling regions to tear away from the wall, allowing vapour in the film to fill the bubbles in the coalescing region (see Figure 6) creating much larger bubbles in this region. This leads to a cyclic process as the large bubbles move away from the wall, liquid wets the area previously occupied by the film, a film is created and the whole process repeats itself. Forming the large bubbles takes work which ultimately increases the heat transfer from the surface. It should be noted that while experimental data is referenced in previous papers[3], none could be presented here to back up these proposals as this was not available in the public domain.

[1] Temperature at which departure from nucleate boiling occurs.

[2] Temperature at which film boiling becomes unstable.

[3] These were unavailable for this research.

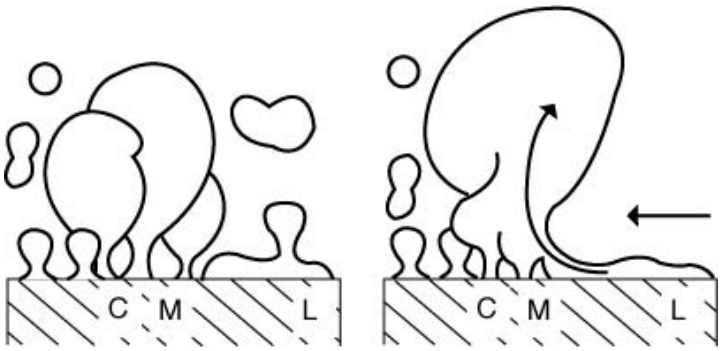


**Figure 6: Proposed interaction between film and coalescing boiling regions [5]**

Having established a definition of the Vapotron process, Beutheret goes on to examine potential improvements [5,6]. In particular, he describes a Super-Vapotron structure in which "adequate means are applied to the tips of each fin in order to establish there a cold point. Then, the bottom can operate safely on any point of the strongly stabilized zone ML […] and it becomes possible to increase by 100% the power applied to such a structure". The difference between a Super-Vapotron and Vapotron is therefore relatively subtle. It would appear from Beutheret's interpretation of the Nukiyama [7] curve (see Figure 7) that a Vapotron operates with the wall temperature safely below the Leidenfrost temperature (2) and the fin tip below incipient boiling (1) while the Super-Vapotron pushes the root of the fin up to the Leidenfrost limit (4) and allows the tip to exceed incipient boiling temperature (3). To achieve the level of heat removal required at the fin tips, "adequate means" could presumably be forced flow along the top of the fins, parallel to the fin direction (although this is not specified in any detail).

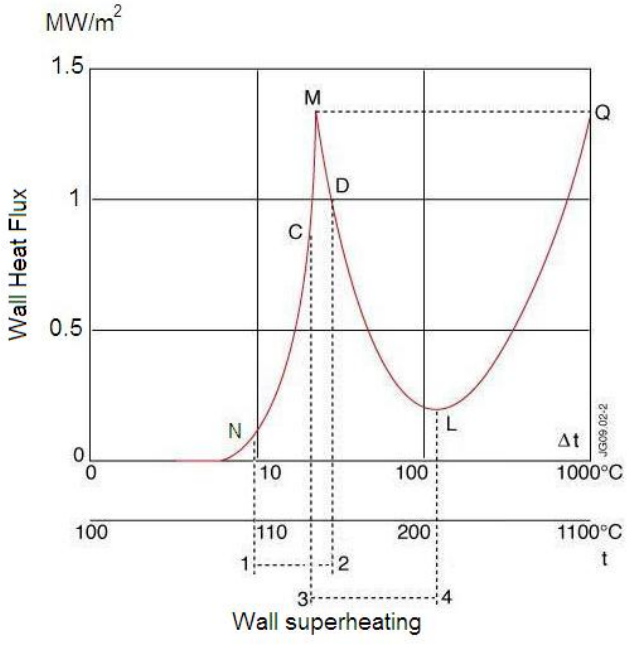


**Figure 7: Nukiyama Curve, 1-2 = Basic Vapotron, 3-4 = Super-Vapotron [6]**

In an attempt to increase performance still further, Beutheret suggests the process can be enhanced by narrowing the slots. Under certain conditions, this allows the vapour films on either side to join together (effectively filling the cavity with steam). The rapid heating and expansion of this volume of vapour results in large steam jets being ejected into the main channel. This periodic process (as the steam jet condenses and draws new, cold fluid into the cavity) apparently improves the heat transfer process still further (see Figure 9). To quantify this improvement, the paper quotes power handling figures of up to 5 MW/m$^2$ for the Super-Vapotron with narrow channels, compared to 3 MW/m$^2$ for Super-Vapotrons and 1.5 MW/m$^2$ for simple Vapotrons. A caveat to this conclusion is that the steam ejection enhancement has only been observed at relatively low flow rates. In fact, it has since been concluded by other researchers that this effect is not relevant at the high flow rates and high power densities required for a fusion application. Indeed, when Cattadori et al [8] attempted to visualise this effect using high speed photography (see Figure 8), it was concluded that this effect is neither observed nor critical to the removal of high (fusion relevant) heat fluxes (e.g. > 10MW/m$^2$).

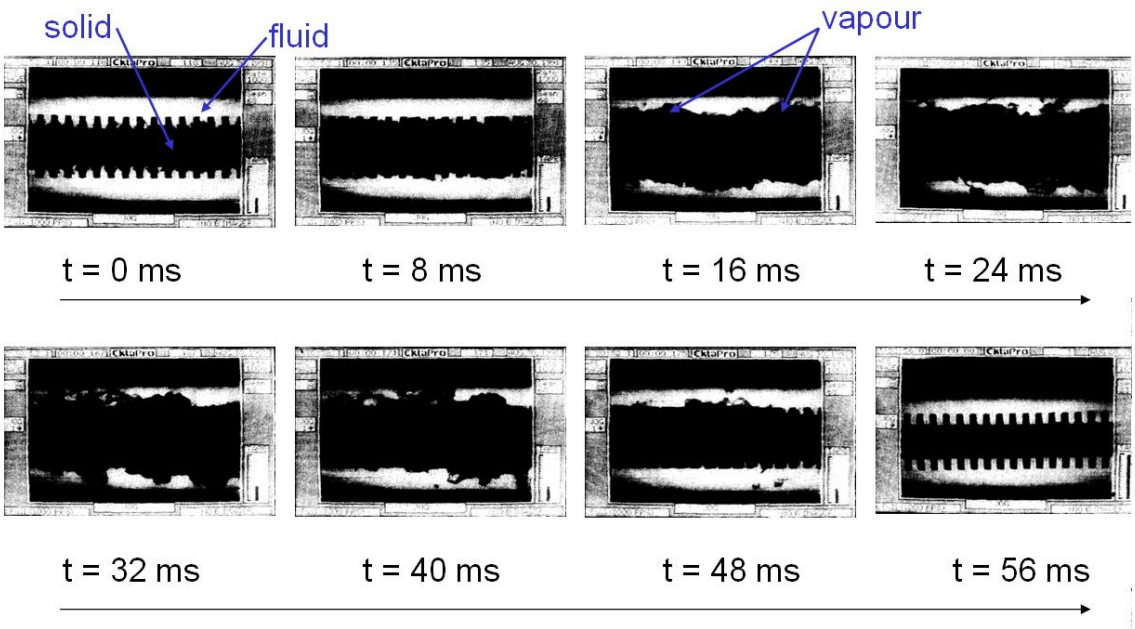


**Figure 8: Cattadori's visualisation of the cyclic steam ejection process within a HyperVapotron [8]**

As before, it is still not clear from Beutheret's paper where the coolant flows for a Super-Vapotron with narrow slots. It has been assumed here that the flow is parallel to the fins but generally does not enter the cavities (i.e. forced convection applied to the fin tips only). Indeed, it is shown experimentally that "the maximum heat transfer capability is not increased but reduced by forcing a flow of cold water along the narrow slots of the structure." For this reason, to minimise disturbance of this process, Beutheret proposed orientating the fins perpendicular to the flow. It is this crucial modification that turns a Super-Vapotron into a Hyper-Vapotron (see Figure 10).

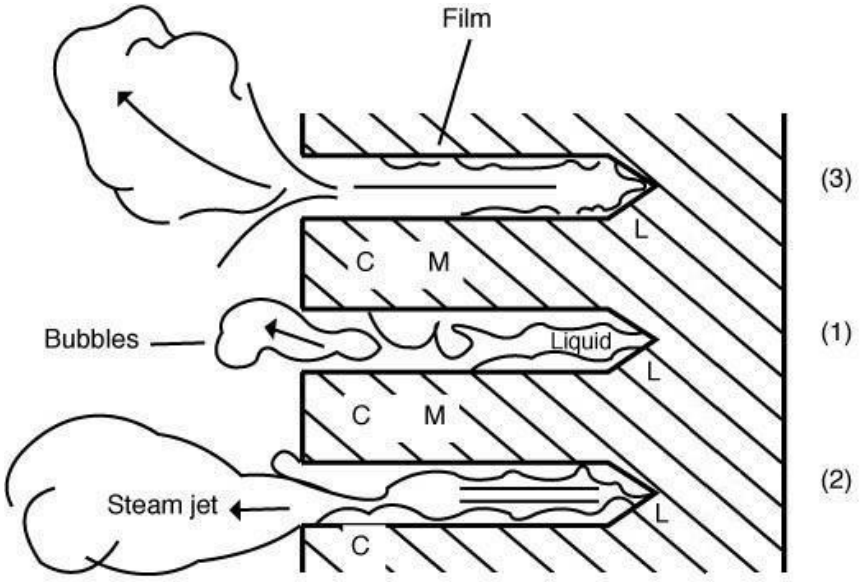


**Figure 9: Super-Vapotron with Narrow Slot Effect [6]**

| **Vapotron** | **Super-Vapotron** | **Super-Vapotron with narrow slot effect** | **HyperVapotron** |
|---|---|---|---|
| < 1.5 MW/m$^2$ | < 3 MW/m$^2$ | < 5 MW/m$^2$ | < 20 MW/m$^2$ |
| Means for cooling fins not specified. | Assumed forced flow <u>parallel</u> to fins | As for the Super-Vapotron but also benefits from steam jet ejection due to narrow slots. | Forced flow <u>perpendicular</u> to fins to avoid upsetting the vapour producing processes in the slots. |
| 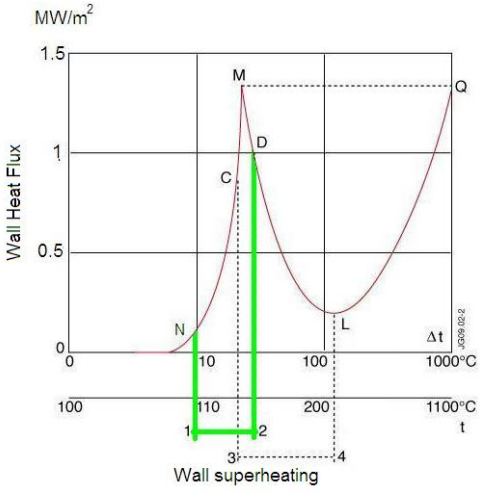 | | | 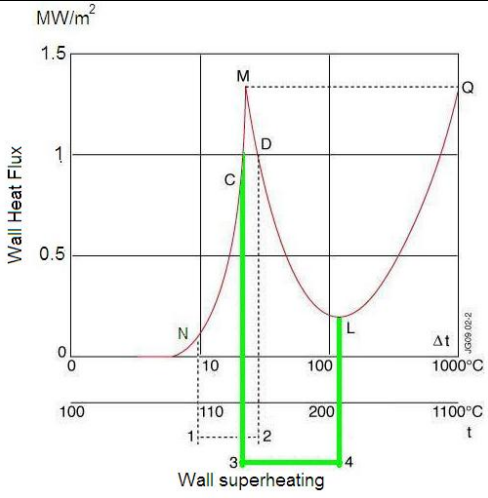 |



**Figure 10: Vapotron to HyperVapotron, Key differences**

The paper quotes power handling for the HyperVapotron of up to 20 MW/m$^2$ and highlights the benefit of minimal pumping requirements (most likely due to the majority of the flow passing straight over the cavities, with minimal resistance). It also prophetically suggests that limitations on heat flux may well be due to the solid performance rather than the cooling efficiency[4]. It is claimed, however, that this exceptional performance in part relies on "very high velocity of steam-jets (a few tens of m/s)". It will be argued here, however, that at the elevated flow velocities and heat fluxes relevant to a fusion device, this steam-jet mechanism is unlikely to occur but that comparable or even improved power handling can still be achieved (see Cattadori [8], Falter and Thompson [9]).

The term HyperVapotron therefore has a fairly strict definition. Specifically, it is a water cooled device with internal fins orientated perpendicular to the flow with a fin temperature profile bounded by the Leidenfrost temperature at the root and allowed to exceed incipient boiling temperature at the fin tip. For the purposes of this study, however, any device which relies on boiling heat transfer and uses rectangular shaped fins perpendicular to the driving flow will be defined as a HyperVapotron. In particular, it is not necessary that it uses narrow slots to promote high velocity steam jets (to enhance the heat transfer capability) nor relies on parts of the wetted surface operating at the Leidenfrost temperature.

In addition, it is worth highlighting that in all HyperVapotrons studied thus far, the fins have been manufactured with sharp corners. Whilst no definitive reason for this feature can be found in the HyperVapotron literature, it is likely that sharp corners are better from a heat transfer standpoint (e.g. compared to rounded fins) as these result in more acute boundary layer separation, increased turbulence and mixing in the cavity with associated improvement in transport of mass, momentum and heat. This process is illustrated in Figure 11.

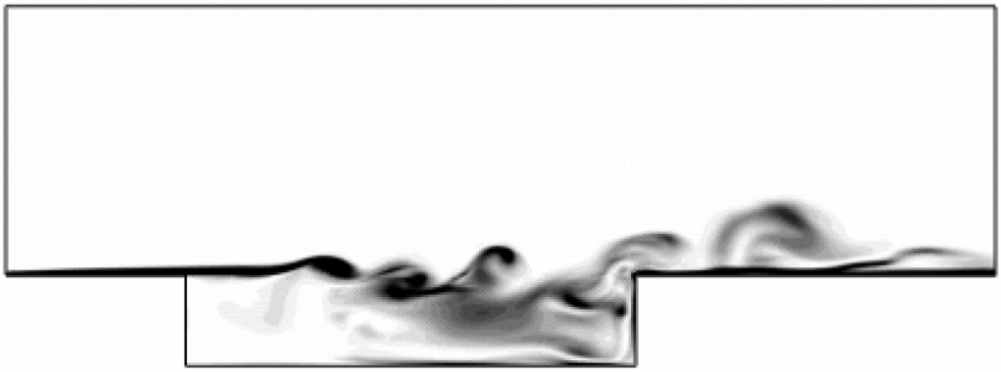

**Figure 11: Illustration of mixing caused by boundary layer separation over a cavity with sharp corners (image courtesy of Aybay et al [10])**

[4] It has been shown more recently that the extreme thermal gradients induced in the solid result in high stress concentrations and potentially short fatigue lives.

### 1.2.2 HyperVapotron use in Fusion Research

From a fusion perspective, the first relevant report was originated by the French company Thompson CSF in 1980 [11]. This report, commissioned by the JET Joint Undertaking, examined the viability of adapting the original cylindrical HyperVapotron design (developed by Thompson for cooling klystron electronic tubes) to a rectangular design, for use on the JET fusion experiment (see Figure 12). This was followed by a "JET Internal Communication" by Falter et al in 1983 [12] which apparently described the first test results of a rectangular HV design destined for a fusion application (typical dimensions 1000×100×30mm). Unfortunately, the contents of both these reports were not available but they are a useful indication of when HyperVapotron technology was first conceived as a solution to fusion's high heat flux requirements.

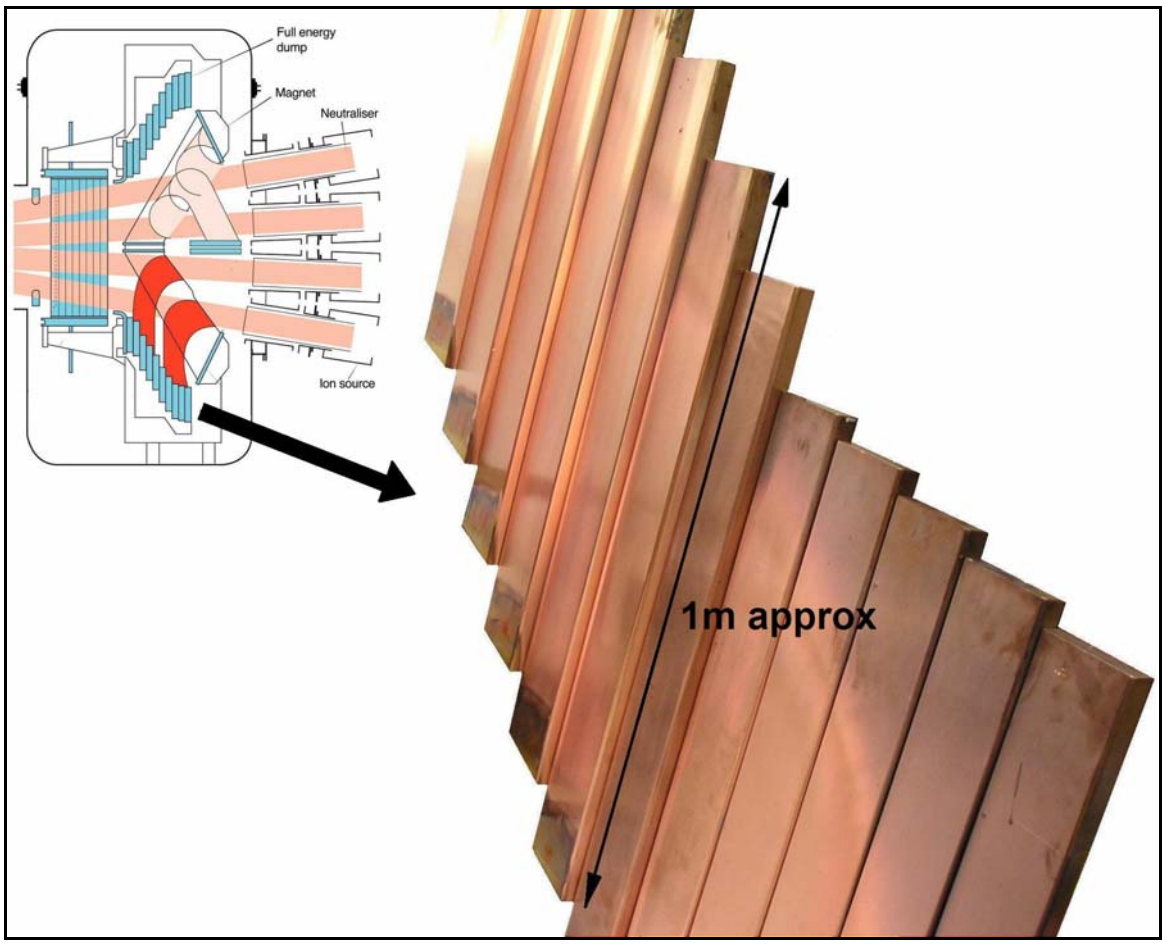


**Figure 12: Typical HyperVapotron array used on the JET machine**

The earliest available fusion reference was a paper from 1987 by Tivey et al [13] which reports the test results of the JET HyperVapotron design to be installed on key Neutral Beam sub-systems such as the Full Energy Ion Dumps and the Test Bed Beam Dump (see Figure 3 and Figure 13 respectively) . This twin-channel element, referred to here as the

Mk1 HyperVapotron, is shown in Figure 14. It should be noted that this had a side slot between the fin and outer wall but no slot between the fin and the central web.

Tivey showed a number of interesting results that might be of use when attempting to develop a CFD model of the HyperVapotron. Of particular interest was that the surface temperature above the central web was found to be considerably higher than above the fins (>100$^{o}$C difference at 10MW/m$^{2}$, see Figure 15). Recent Finite Element models [14], where a uniform Heat Transfer Coefficient (HTC) was applied across the internal surface, suggest a smaller difference (<50% of the measured difference). This suggests that for 8mm fins and no central slot, the heat transfer coefficient within this HyperVapotron may be considerably lower at the side walls compared to the centre of the fins.

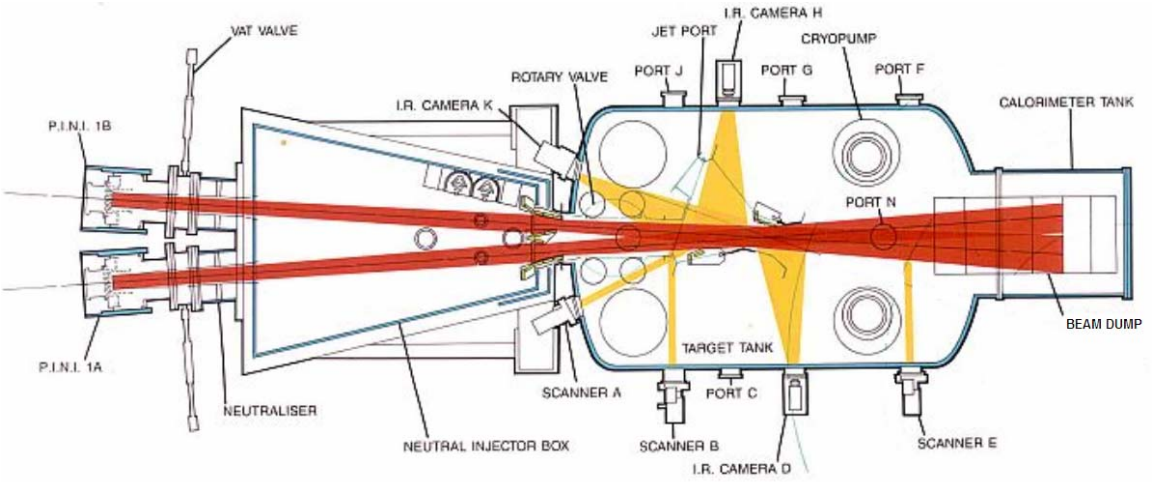


**Figure 13: Neutral Beam Test Bed - Beam Dump (plan view)**

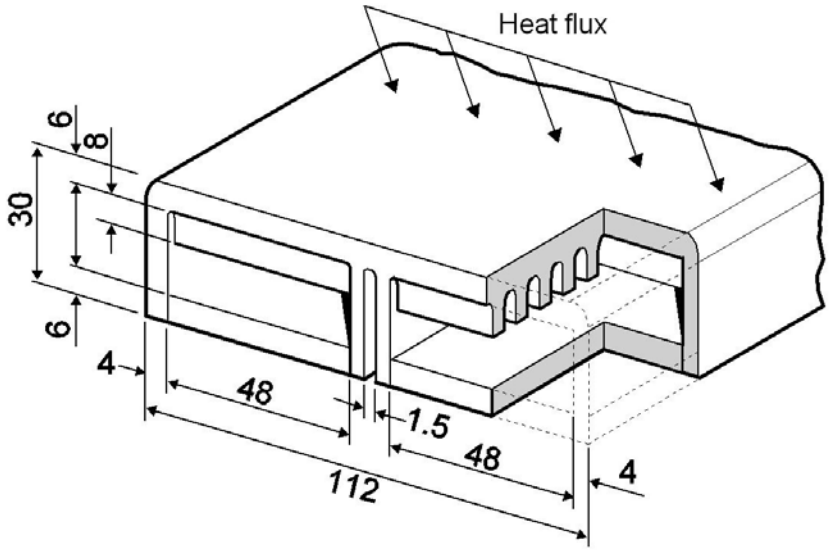


**Figure 14: Section through the JET MkI HyperVapotron**

Tivey's results also suggest that HyperVapotron performance improves with increasing pressure p (with surface temperature a function of 1/pV where V = flow velocity). In the paper, it is suggested that this pressure dependence is due to power handling being limited by the amount of vapour present "in the water channel behind the finned structure". It is assumed that the author was implying that higher pressures result in increased saturation temperatures and therefore less vapour in the main water channel (with improved performance). Care must be taken here as this dependence is not explicitly demonstrated and subsequent papers either report no noticeable effect or the opposite effect on performance [15,16,18]. In fact, the CFD solutions developed here indicate that vapour production and condensation is localised to the cavities and that more vapour actually improves performance when measured by temperature rise in the solid (see chapter 5).

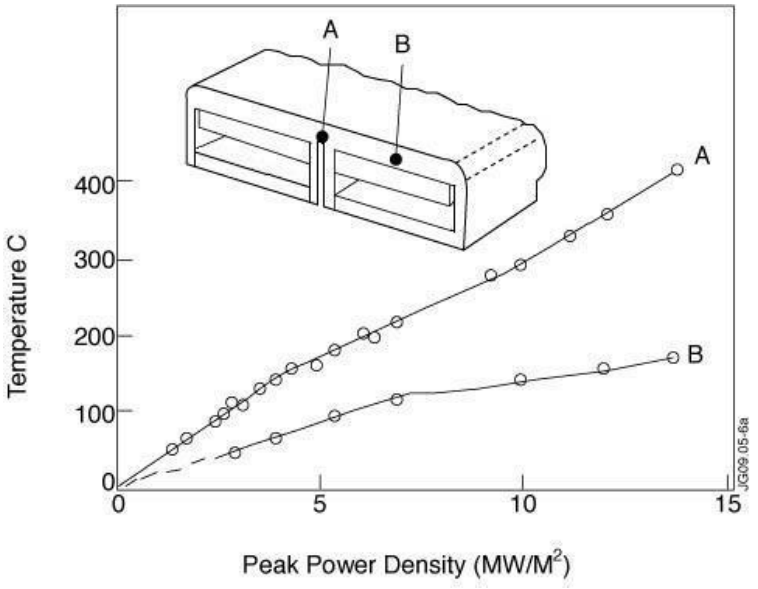


**Figure 15: MkI HyperVapotron – Performance difference between the fins and central web (points A and B are 3mm and 4.7mm below front surface respectively) [13]**

The next set of JET HyperVapotron tests are reported by Altmann et al [15] in 1989. Again the Mk1 HyperVapotron design is examined but the focus here is on the improvement in performance achieved when a slot is added between the fins and central web (see Figure 16).

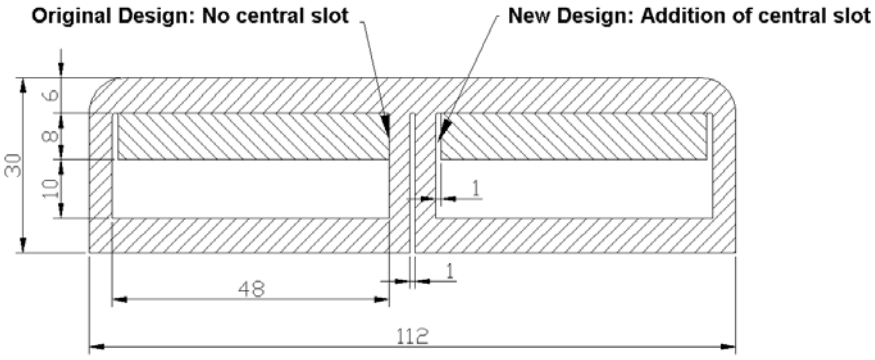


**Figure 16: Modified MkI HyperVapotron showing 1mm slot at the central web**

The impact of this modification is considerable with tests indicating a reduction in temperature above the web of up to ~100°C at 10MW/m$^2$ meaning the hottest part of the HyperVapotron is now above the centre of the fins (see Figure 17 and Figure 18). The performance curves for this design are shown in Figure 19. Unfortunately the paper doesn't specify whether this is absolute temperature or temperature rise or even where this temperature is measured. As a result, it is difficult to draw definitive conclusions about how its performance compares with other designs and it is of limited value when it comes to validating CFD models (see section 5.3.4 for methods adopted to use this data).

It should be noted that the beneficial effect of the slot is more pronounced the deeper the fins (65-100°C for 8mm fins compared to 15°C for 4mm fins [17]); however, it is not entirely clear why this is so. The reduction in the temperature of the solid in this region might be due to a local flow effect such as flow impingement on fin edge, better bubble transport / condensation effects in this region etc.

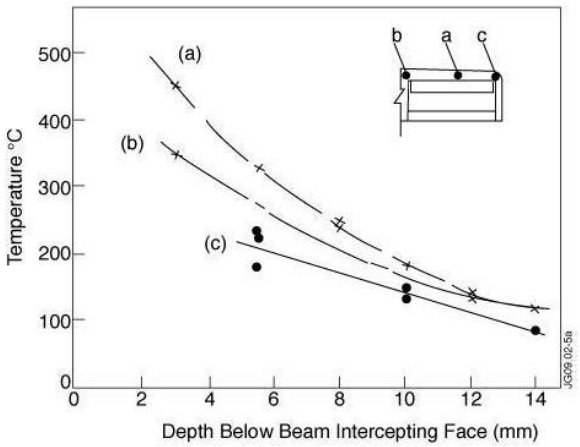


**Figure 17: Temperature gradient through the (a) Fin (b) central web and (c) sidewall for a coolant flow rate of 14.4m$^3$/hr and a total power of 0.9MW [15]**

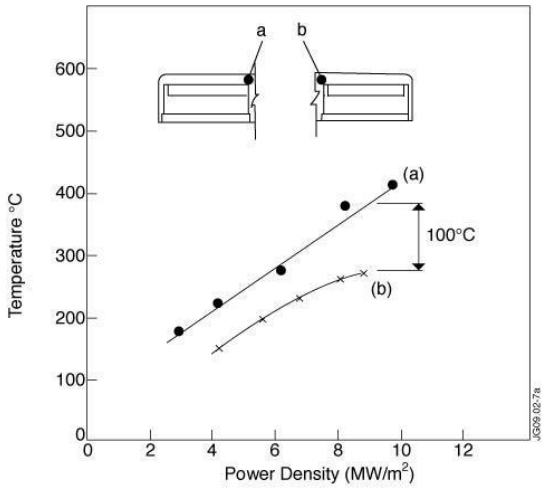


**Figure 18: A comparison of the temperature profile along the central web for (a) the single slotted HyperVapotron and (b) the double slotted HyperVapotron for identical total powers of 0.6MW [15]**

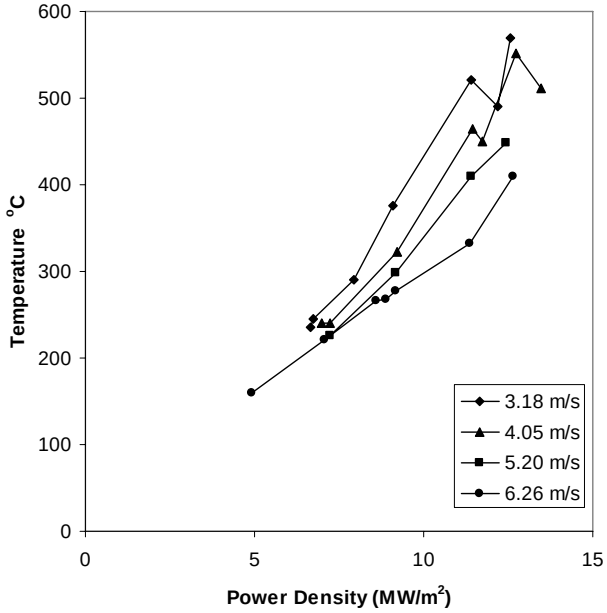


**Figure 19: Performance curves for the slotted MkI HyperVapotron (position of temperature measurement is uncertain)**

Two JET Divisional Notes were subsequently compiled in 1991 by Falter and Massmann et al [16,18]. Both examined new HyperVapotron designs, specifically aimed at the potential application of the JET Divertor (the exhaust region of the tokamak where power densities can frequently enter the 10 – 20MW/m$^2$ range).

Using an IR camera and thermocouple data to measure surface temperatures, Falter [16] tested 5 different HyperVapotron designs (although strictly speaking only 3 qualify as HyperVapotrons using the definition outlined at the end of section 1.2.1). These are illustrated in sketches a) and b) of Figure 20. Although it is not specified, it would appear from the figure that these are square bottom cavities rather than the circular bottom cavities tested by Altmann and Tivey.

For all three designs (which are differentiated in both the channel height and fin height) tests are performed over a wide range of power densities, covering all potential heat transfer regions from single phase flow up to Critical Heat Flux (CHF).

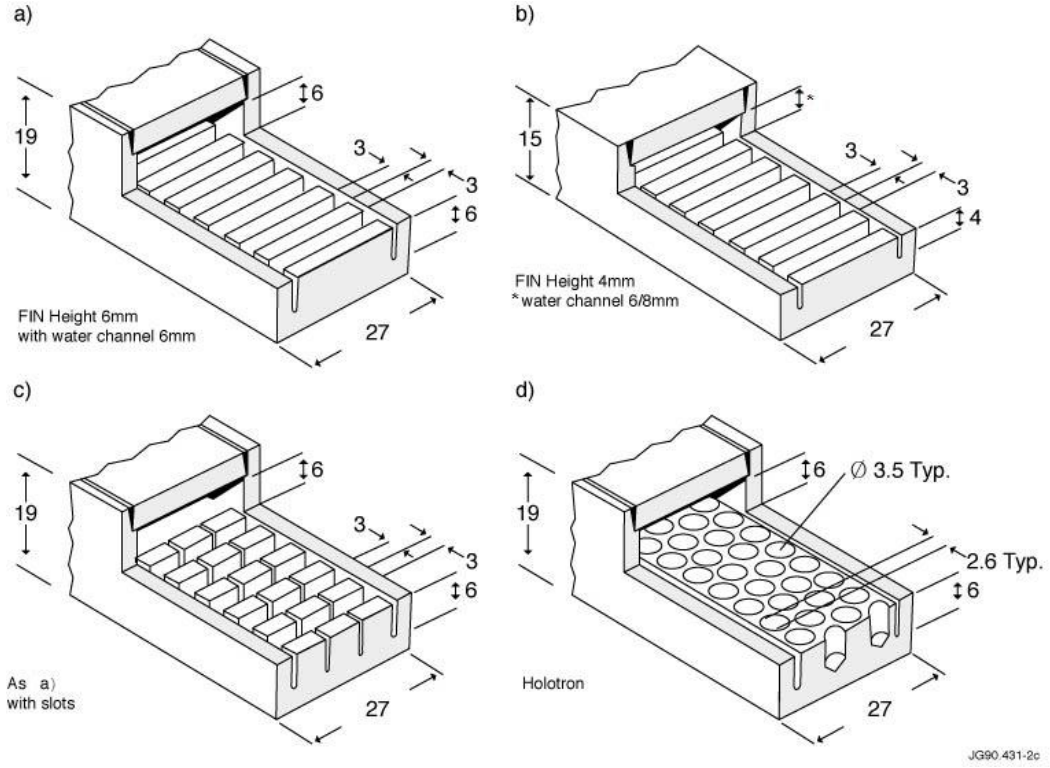


**Figure 20: HyperVapotron designs tested by Falter et al in 1991 [16]**

Falter agrees with Altmann that the power handling capacity of the side regions is greater than the centre. This is not quantified but evident via the observation that overheating occurs at the centre of the element (confirmed by IR camera and melting observed in this region in other tests). Falter suggests this may be due to increased thermal inertia of side wall. Whether it is due to this reason or Blatchford's [14] proposal that the cooling efficiency might be better in these side regions, this certainly suggests that care must be taken when specifying the total width of these elements and making assumptions about uniformity of the internal cooling mechanisms.

As with some of the previous papers, Falter's results clearly show 3 distinct operating regimes on the thermal performance plots (which illustrate single phase, nucleate boiling and transition to film boiling regimes). Unlike previous papers, however, Falter ran a significant number of tests with variations in input parameters allowing him to draw some additional conclusions. Amongst other things, he shows that, in the nucleate boiling regime, surface temperature rise appears to increase (and therefore performance decreases) with increasing water pressure (unlike so-called hard boiling[5], where the reverse is true). This is contrary to Tivey's findings, at least in the nucleate boiling regime, but no attempt is made to explain this phenomenon.

[5] Hard boiling refers to the violent, noisy boiling that occurs at high heat fluxes, often corresponding to a drop in heat transfer efficiency. Generally the proximity to burn-out and excessive vibrations mean HyperVapotrons are rarely operated in this regime when installed on a fusion sub-system.

Like Cattadori, Falter also exposes a different operating regime at low flow rates. By reducing the flow velocity from 4m/s to 0.75m/s, he notes a very different type of noise on the pressure signals (see Figure 21). Later Falter and Thompson [9] propose that the frequency of ~10-20Hz observed on the pressure trace is evidence of the steam-jet effect (predicted by Beutheret and observed by Cattadori) as this is the approximate frequency range predicted by comparing the number of Joules required to vaporise all the water in the cavity with the incident heat flux. Whilst indirect, this does seem to suggest that the steam jet effect is present under certain conditions. As previously mentioned, however, the fact that this seems to occur only at low flow velocities and surface heat fluxes means it may not be particularly relevant to fusion applications.

From these tests, coolant subcooling appears to have little influence on surface temperatures below 300°C. Since it has been shown that fully developed boiling is independent of subcooling [19] and that all types of boiling can be sustained along a HyperVapotron cavity wall [5], this result might indicate that it is these fully developed zones that dominate the overall performance of the device below this temperature limit (i.e. any areas of transition or film boiling are small in comparison to the nucleate boiling regions). In the hard boiling regime, however, increased subcooling does improve performance. If this regime corresponds to the extension of the vapour film at the root of the cavity and more violent boiling phenomena (hence the reduction in heat transfer efficiency and increase in vibration / noise), it could be conceived that increased subcooling would require more energy to vaporise the boundary layer and extend the vapour film, hence improving performance.

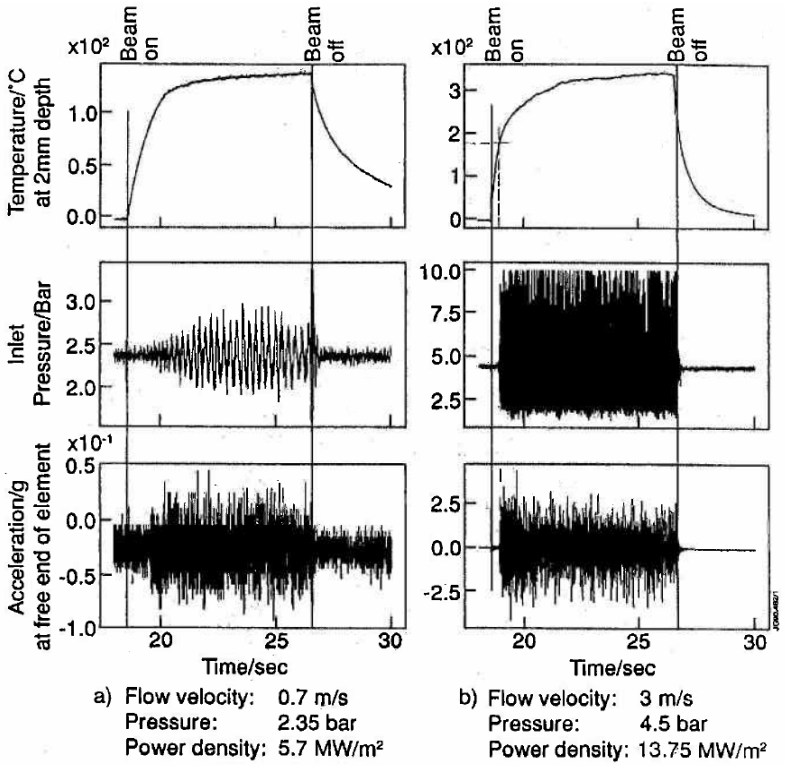


**Figure 21: Noise in the water and accelerometer signal [16]**

Massmann [18] subsequently performed a similar set of tests but these were restricted to a single geometry, specifically based on a 4mm fin and 3mm channel. This geometry was selected based on evidence that high flow velocities (induced by narrow, 3mm channels) and a 4mm deep fin resulted in exceptional thermal performance. In this case, the three operating regions are less distinguishable than in Falter's tests (the reasons for this are unclear). One of the more interesting findings is that similar performance can be observed at quite different thermal-hydraulic conditions. More specifically, it can be seen from Figure 22 that a significant increase in flow velocity does not necessarily improve performance in the single phase and nucleate boiling regimes if this is accompanied by a drop in pressure and an increase in inlet subcooling (of 27% and 15% respectively). Above ~15MW/m$^2$, however, performance does improve where it appears the conditions associated with the increased inlet velocity might be delaying the transition to hard boiling (where heat transfer efficiency is reduced).

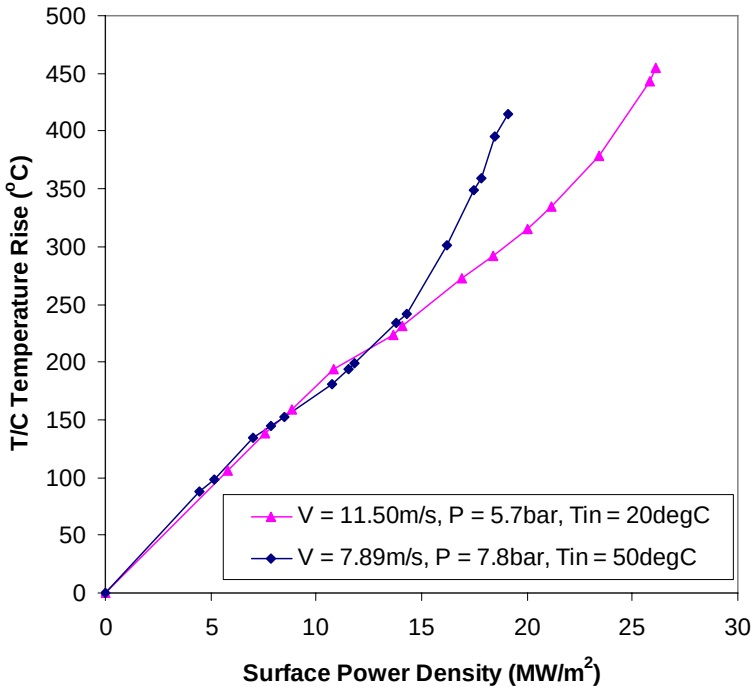


**Figure 22: Massmann's HV performance results at different thermal-hydraulic conditions**

One of Massmann's other proposals is the existence of a "universal" parameter that could be used to predict burnout (frequently thought to be difficult to predict by most researchers). Specifically, he suggests that the temperature difference "across the thermal boundary layer, $T_w - T_{bulk}$" should be limited to 400°C to avoid burnout "regardless of […] outlet temperature, subcooling or heat transfer coefficient". It is not clear whether this proposal was examined theoretically or tested against a wide range of geometries and test conditions (the author feels this is unlikely) but, if such a simple upper limit could be applied, this would certainly be of interest in practical applications.

In 1992, Baxi et al [20] appear to be the first to attempt model the heat transfer coefficient in a HyperVapotron structure. The technique, which has been used by other researchers [21], involved deriving a heat transfer coefficient as a function of wall temperature (see Figure 23[6]). A number of empirical correlations were used or modified (such as Dittus Boelter, Thom, Macbeth [19]) to calculate heat transfer coefficients in the different regimes (i.e. single phase convection, nucleate boiling, critical heat flux).

This variable heat transfer coefficient was then programmed into a finite element code to calculate the temperature response of the HyperVapotron. It reports good agreement over a range of flow parameters and two different geometries (although these differed only in channel height, 3 to 6mm, see Figure 24 to Figure 26). While the paper recommended further work to see if this model could be successfully applied to a wide range of geometries, it is not clear this was ever carried out and exploratory studies have suggested this method may not be widely applicable to a wide range of cases. Also, it must be acknowledged that the forced convection contribution[7] was modified to suit the experimental data in question (with the inclusion of a factor ff = 1.35 into the Dittus Boelter correlation). It is therefore hardly surprising that the results agree relatively well. Finally, no real understanding of the internal mechanisms is gained by this method giving it limited use in practice.

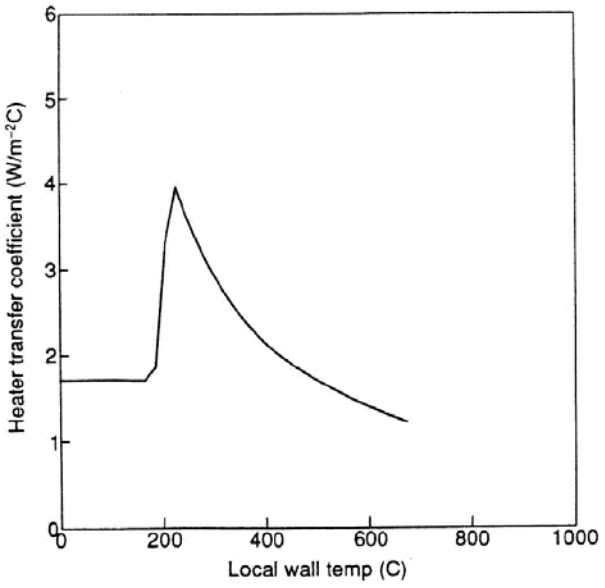


**Figure 23: Heat transfer coefficient for 6mm channel, V = 4.0m/s, p = 6.4bar [20]**

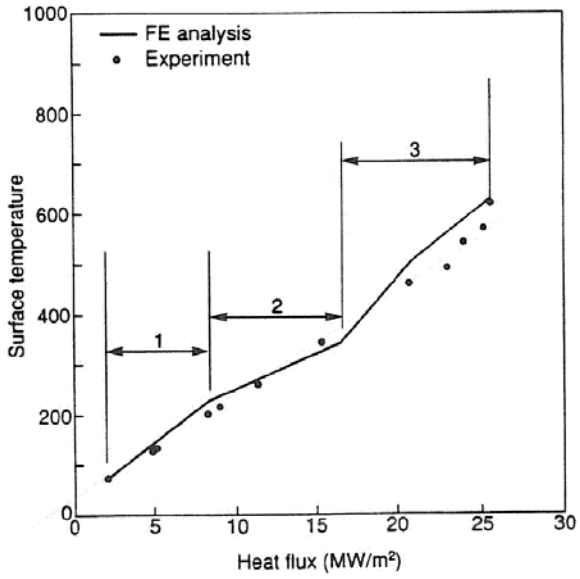


**Figure 24: Comparison of analysis and experiment for 3mm channel, V = 8.4m/s, p = 6.8bar [20]**

[6] It is assumed there is a typo in the values shown in this figure. At the Reynolds number of these devices, the heat transfer coefficients are typically in the order of $10^4$. As a result, it is thought the peak HTC in this figure should be ~40,000 W/m$^2$.C and not 4 as indicated.

[7] This contribution affects the total heat transfer in the nucleate boiling regime as well as the single phase heat transfer regime.

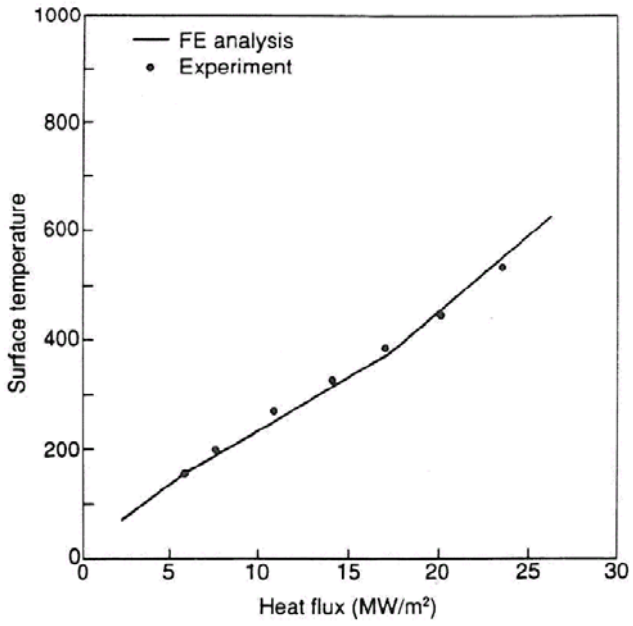


**Figure 25: Comparison of analysis and experiment for 3mm channel, V = 11.5m/s, p = 5.7bar [20]**

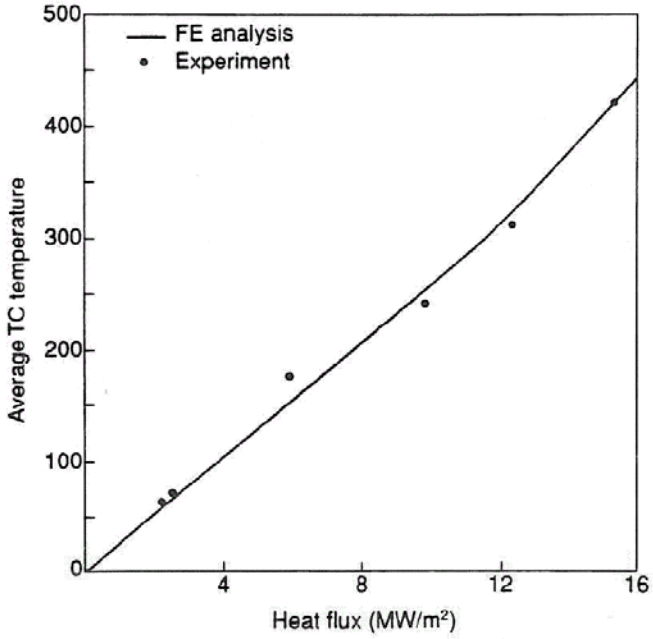


**Figure 26: Comparison of analysis and experiment for 6mm channel, V = 4.0m/s, p = 6.4bar [20]**

A significant number of papers from 1995 - 2006 then concentrated on evaluating HyperVapotrons in relation to other potential "high heat flux" elements [22,23,24,25,26,27]. These include swirl tubes, screw tubes, annular flow tubes and others. In particular, Escourbiac, Schlosser and colleagues at CEA (France) have built, tested and analysed the performance of a great number of such devices. It is proposed that these be used in key sub-systems of ITER. In particular, a section of the inner wall of ITER, known as the Divertor, requires the dissipation of heat loads up to 20MW/m$^2$. The inlet pressures and temperatures on this system are considerably higher than on JET allowing a comparison of performance over a wide range of flow parameters. The goal of most of these papers was to evaluate the best performing design rather than understand the heat transfer mechanism. They do, however, provide a large amount of experimental data which may prove useful when validating future CFD models.

In parallel, HyperVapotron development continued at JET with Ciric et al [17] reporting in 1996 the testing of a twinned-channel prototype element for the JET Boxscraper, having a 4mm front face, 4mm fins and 8mm channel depth. It was suggested that 4mm fins would exhibit improved thermal performance (based on the work by Falter and Massmann) and this proved to be the case at elevated heat fluxes (see Figure 27). This data is particularly useful from a validation standpoint as it covers a wide operating regime for a range of inlet flow velocities.

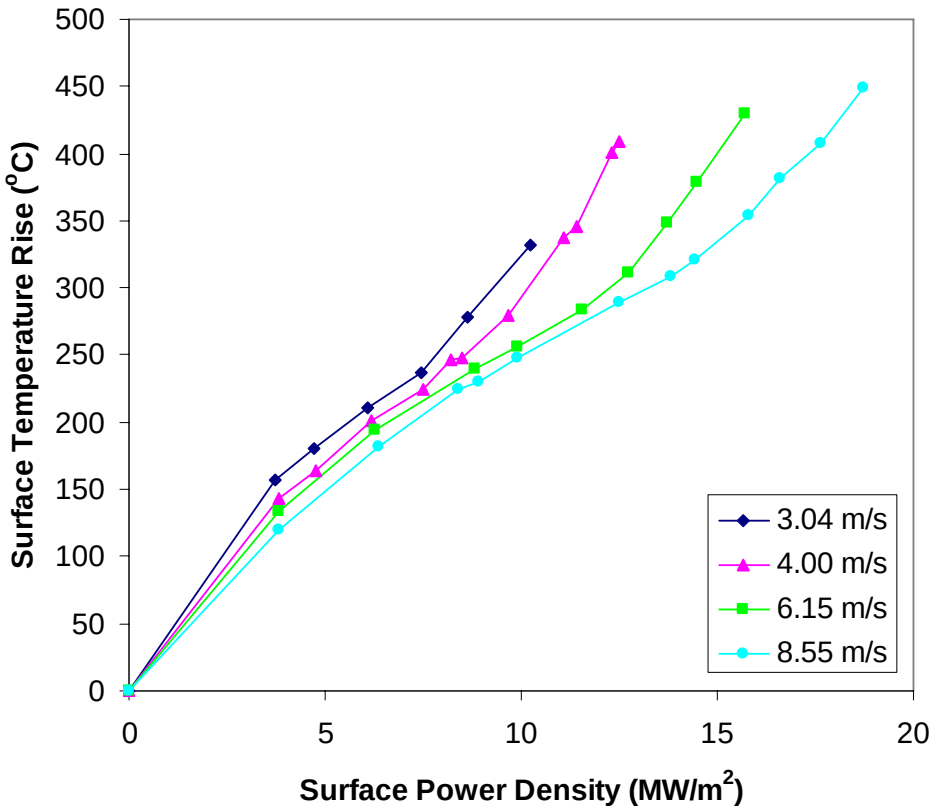


**Figure 27: Boxscraper HV performance**

In 2001, Baxi [28] summarised the steps required to perform a thermal analysis of a water cooled, HHF element (in this case a Swirl Tube Element or STE). Whilst this paper is concerned with a "rival" device, it is worth noting that Baxi makes a similar argument to Beutheret [5,6] on how certain HHF elements can sustain heat fluxes greater than the Critical Heat Flux. He states that "heat sinks made from high conductivity material, with one sided heating can survive beyond a local condition of CHF because the heat sink is still capable of removing the incident heat flux by heat conduction to surfaces which have not yet reached the CHF condition". He states this in general terms, suggesting this phenomenon can be present in other HHF designs; in other words, use of fins is not a pre-requisite to achieve stable operation beyond CHF.

In addition, Baxi warns that while these methods increase the CHF limit by up to a factor of 2 compared to smooth tubes, the penalty is increased pressure drop which can increase by a factor of 4. Other studies [29], however, have indicated this may be overly pessimisitic for HyperVapotrons.

The same year, Ezato et al [25] performed power handling tests on a triangular fin device, which they referred to as a Saw-toothed Fin Duct (SFD), see Figure 28 and Figure 29. Comparing performance curves for SFD-1 and HV3-1 (which both have fins orientated perpendicular to the flow) seems to show that triangular fins delay the transition to CHF, as the two performance curves only diverge at power densities greater than 10MW/m$^2$.

What is also striking is the significant improvement gained if the fins are no longer set completely perpendicular to the flow, with temperatures reduced by up to 20%, albeit at a penalty of increased pressure drop due to the swirl component introduced into the flow. Given that this latter effect is likely to be true for rectangular fins as well, both these effects may prove useful when optimisation studies are performed using the CFD models developed as part of this study.

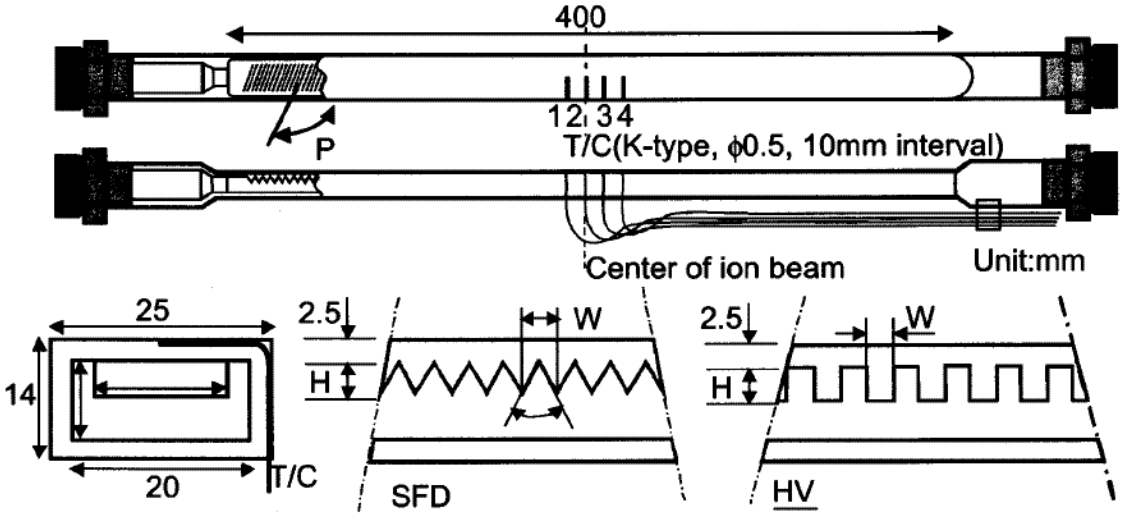


**Figure 28: SFD design compared to standard HyperVapotron (Ezato [25])**

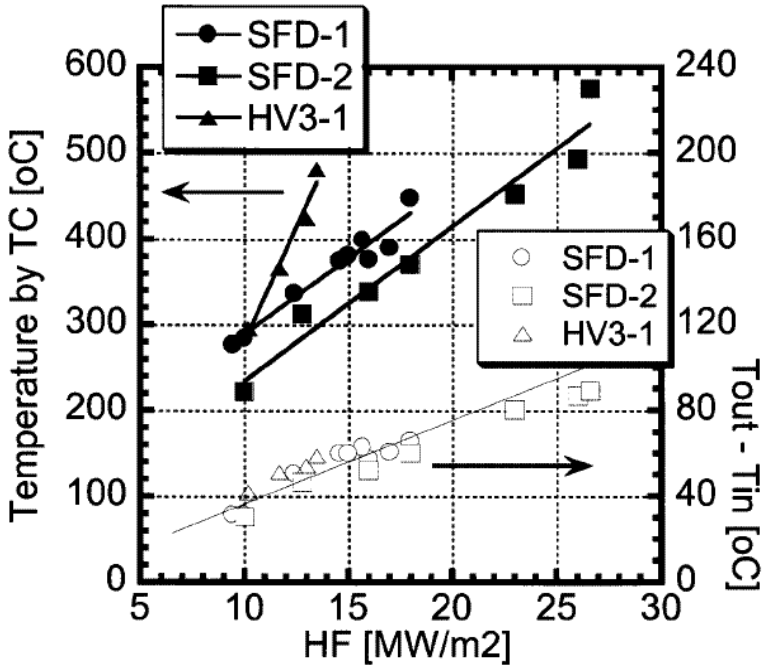


**Figure 29: Comparison of the surface temperatures of saw-toothed fin duct and HyperVapotron at the axial velocity of 2 m/s, local pressure of 1 MPa and inlet water temperature of 25 °C (Ezato [25])**

| No. of sample | Fin base, W, mm | Fin height, H, mm | Angle of fin to flow, P, deg |
|---|---|---|---|
| SFD-1 | 4.0 | 3.46 | 90 |
| SFD-2 | 4.0 | 3.46 | 70 |
| HV3-1 | 3.0 | 4.0 | 90 |

**Table 1: Detailed parameters of fin base, fin height and installation angle of fin to water flow (Ezato)**

In 2003, Milnes et al [30] tested a new HyperVapotron design, destined for the MAST Neutral Beam Heating systems (the design is therefore referred to as the MAST HyperVapotron). The key result worth reporting here was that this design appeared to exhibit the best thermal performance of all Culham HyperVapotrons tested to this point. The raw thermocouple data from the tests performed at a flow velocity of 6.96m/s are shown in Figure 30 (this shows temperature/time traces recorded during a 3 second pulse).

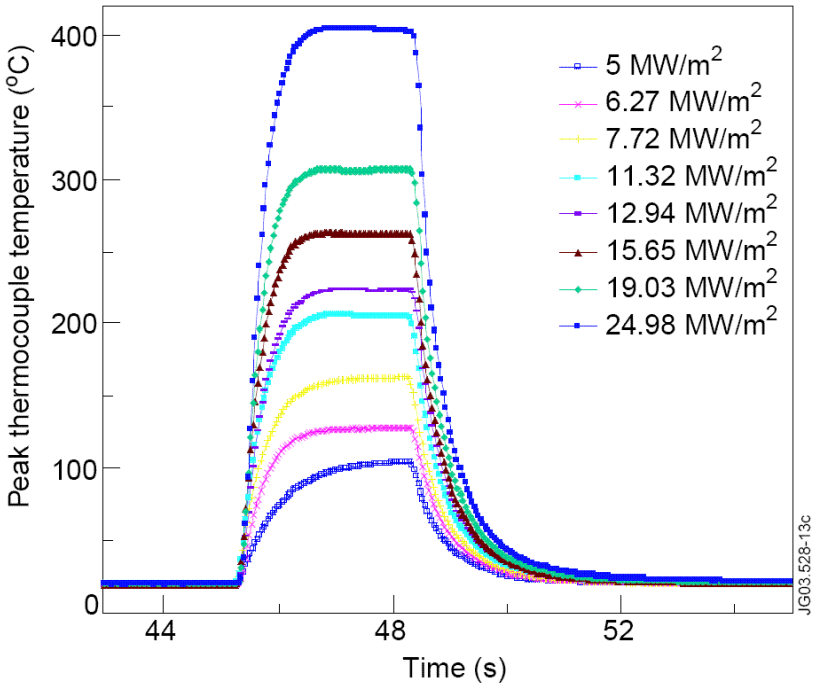


**Figure 30: Thermocouple results for the MAST HV (V = 6.96m/s, $p_{in}$ = 5.5bar, $T_{in}$ = 20°C) [30]**

To make a valid like-for-like comparison between this and other HyperVapotron designs, all power handling data has been normalised to display an equivalent surface temperature rise assuming a fixed front face thickness of 3mm (typical for a HyperVapotron application). 1D heat conduction was therefore used to extrapolate surface temperature from thermocouple measurements[8]. Without this normalisation process, the HyperVapotrons with increased surface thickness would exhibit higher surface

[8] The extrapolation assumed a thermal conductivity of solid material of ~ 345 W/m.C (CuCrZr alloy)

temperatures and therefore appear to be less efficient than those with thinner front faces.[9] Once all data has been suitably adjusted, a typical power handling limit for each design can be calculated based on applying the JET ageing limit of 450°C for CuCrZr (if this temperature is routinely exceeded, the alloy loses its strength and can lead to premature failure).

| | **MkI HV [15]** | **Boxscraper HV [17]** | **Divertor HV (6×6) [16]** | **Divertor HV (4×3) [16]** | **MAST HV [30]** |
|---|---|---|---|---|---|
| Fin height (mm) | 8 | 4 | 6 | 4 | 4 |
| Channel height (mm) | 10 | 8 | 6 | 3 | 3.4 |
| $P_{in}$ (bar) | ~6 (assumed) | ~6 (assumed) | 2.3 – 9.2 (not specific) | 2.3 – 9.2 (not specific) | 5.5 |
| $T_{in}$ (°C) | ~20 (assumed) | ~20 (assumed) | ~20 (assumed) | ~20 (assumed) | 20 |
| V (m/s) | 6.36m/s | 6.15 | 6.00 | 7.80 | 6.96 |
| **PD limit* ($MW/m^2$)** | **13.2** | **17.3** | **14.8** | **17.5** | **23.5** |

**Table 2: Comparison of Culham HyperVapotron performance at ~6-8m/s**

**Note: PD limit = Surface Power Density extrapolated from experimental results assuming a surface temperature of 450°C and a normalised front face thickness of 3mm.*

One surprising result of this "normalisation" is the apparent exceptional performance of the MAST design (which shows a power handling capability of 23.5MW/m$^2$ at 6.96m/s). It appears from Table 2 that, as well as significantly outperforming all designs previously tested at Culham, it also outperforms a prototype Divertor HV design with almost identical cross-section (i.e. same fin and channel height). With only minimal differences between the two designs[10] it is not clear whether this apparent difference in performance is genuine or should be attributed to experimental error. Some attempts have recently made to answer this question via examination of the data extracted from the MAST Neutral Beam system where the MAST HV design was finally installed. Indications thus far suggest this may have been experimental error and the MAST HV design does not actually perform as well as these original figures suggest (surface temperatures are in some case actually up to 20% greater than first thought). Due to the uncertainty in the MAST HV performance data, it will therefore not be used for validation purposes in this research and is presented here for information only.

Finally, one of the most interesting and recent studies on the HyperVapotron application was performed by Chen et al [31,32]. This is quite different from much of the research

[9] For the MkI HyperVapotron, it was unclear from Altmann's paper whether it was the thermocouple or surface temperature that was being reported. Given the author's experience, it has been assumed that it was thermocouple temperature as this ties in better with results from other experiments.

[10] Channel widths are slightly different and the Divertor element has a rectangular cavity compared to a rounded cavity for the MAST design.

above as it does not focus on the testing of a HyperVapotron device at fusion relevant conditions. Instead, it reports on experiments that attempt to visualise (and to some extent model) the boiling processes that occur in a HyperVapotron-like cavity[11]. A rig is built where relatively low heat fluxes are applied to a cavity structure and boiling can be achieved via the use of the refrigerant R134A as the coolant, instead of water (see Figure 31). Some of Chen's key findings along with potential interpretations are listed below:

- Two zones are identified for HyperVapotron heat transfer (see Figure 32): the first is reasonably similar to that for flat channels and shows a relationship[12] $q = \left(T_w - T_{sat}\right)^n$ where n ~ 3; essentially the wall heat flux is controlled by the development of the boiling process. The second zone, however, has a longer, more stable transition region than for a flat plate. As postulated by a number of other researchers [5,6,8], Chen suggested that the thick, massive structure of the fins delays overall nucleation saturation compared to flat channels. What is encouraging here is the similarity of the relationship between wall heat flux and wall superheat between the flat plate and cavity cases. This makes a reasonable case for applying nucleate boiling models tuned for straight channels (albeit usually circular not rectangular) to fin geometries. It also strongly suggests that the significant performance increase in the nucleate boiling regimes reported in many of the HyperVapotron studies is more likely to be due to increased surface area and turbulence rather than fundamental differences in the boiling mechanisms.
- Using advanced image processing methods, nucleation site densities are measured for a range of surface finishes (and for a material and geometry relevant to this study). A correlation is then derived whereby nucleation density is plotted against critical nucleation cavity diameter $D_c$ as defined by Wang and Dhir (where $D_c = \frac{4\sigma T_{sat}}{\rho_g h_{fg}\left(T_w - T_{sat}\right)}$ ). Chen suggests the following relationship based on his experimental results: $n = 9.7 \times 10^{-18} \times D_c^{-3.07}$. It may be an instructive exercise to use this correlation in a HyperVapotron boiling model to investigate whether this improves the accuracy compared to the standard nucleation site correlations derived in less relevant conditions.
- Bubble growth times and departure radii have been measured in a number of locations around the cavity (see Figure 33). It is shown that the growth rate agrees well with Zuber's [33] correlation and that departure radius is relatively constant around the cavity (between 30 and 60 microns for the conditions examined).

[11] Other than Cattadori [8], Chen's work appears to be the only other attempt to visualise these processes.

[12] Care must be taken here as this relationship is not dimensionally consistent and therefore assumes a particular choice of unit system (e.g. SI units).

- Bubble interaction at higher heat fluxes actually reduces the effective bubble departure diameter (as two bubbles merging cause bigger bubbles which can then depart).
- At high heat flux, bubble waiting time is so short as to be un-measurable.

As stated above, a refrigerant was used for these experiments, not water. Extreme care must be taken, therefore, when applying any of these findings to a water-cooled HyperVapotron application.

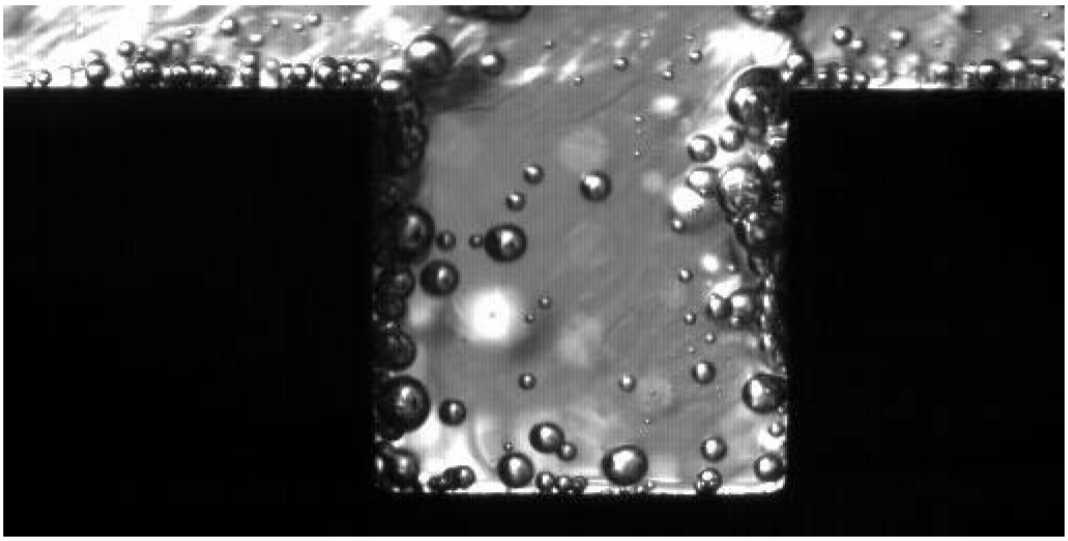

**Figure 31: Vapour production in HyperVapotron-like cavity (p=3.5MPa, V=0.2m/s, $T_w$-$T_{sat}$ = 4.3K) [32]**

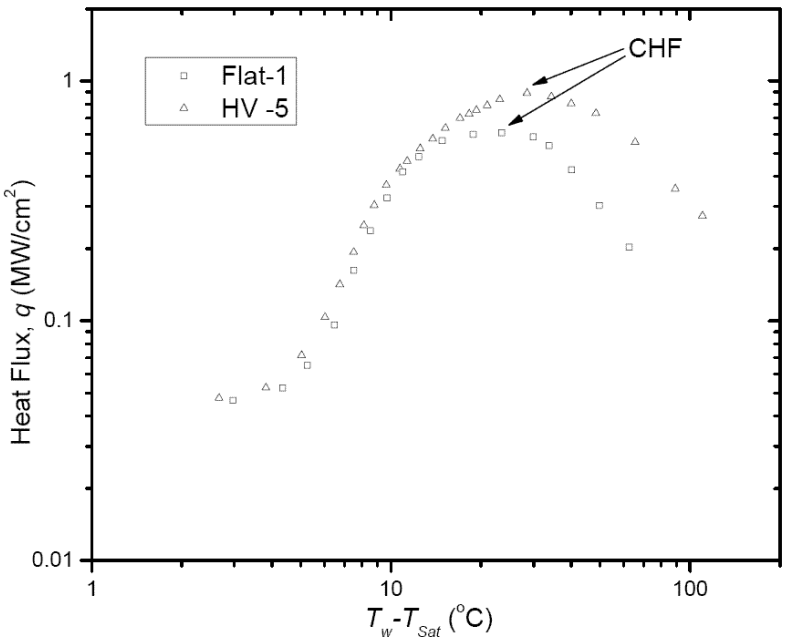


**Figure 32: Results showing comparison between flat plate and cavity case [32]**

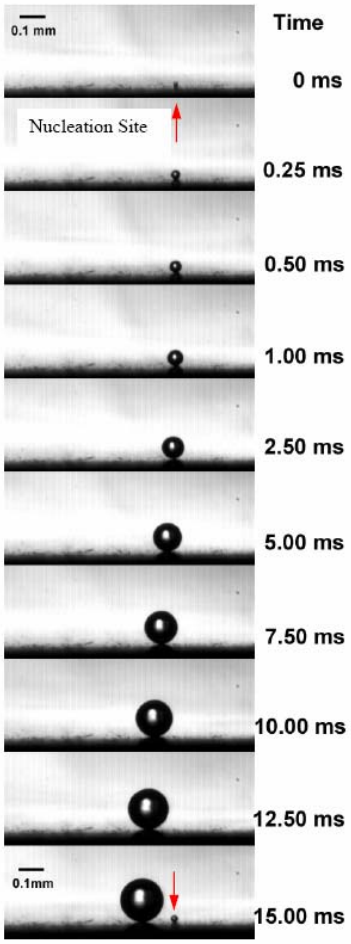


**Figure 33: Images of bubble growth at a pressure of 0.35MPa and a bulk velocity of 0.2m/s [32]**

### 1.2.3 Summary of key results

The results of the section 1.2 provide invaluable information for this study. Specifically, the most useful information can be categorised into three main areas:

1) A history of the design developments and reasoning behind many of the design decisions that have been taken (such as fin height, fin orientation, fin profile, addition of side slots etc). An awareness of these issues can help to point the research in more appropriate directions and avoids repeating past mistakes when examining potential design improvements.
2) Research into the internal flow and heat transfer mechanisms suspected of contributing to the exceptional performance of these devices, both theoretical and experimental (e.g. types of boiling supported around the fin surface, conditions at which large scale steam ejection occurs, bubble departure diameter and frequency etc). This should aid the development and tuning of boiling models for incorporation into the CFD study.

3) Experimental data, generally in the form of thermocouple results in the solid part of the HyperVapotron, for a range of geometries, flow parameters and surface heat fluxes. This data allows direct and indirect validation of the CFD models that are developed, building confidence in their accuracy and range of applicability before attempting to use them for design optimisation.

To compare performance range achieved from the HyperVapotrons developed at JET, the power handling data has been consolidated into a single figure (Figure 34). As in section 1.2.2, the data has been normalised to plot surface temperature assuming a 3mm front face thickness as a function of surface power density (this normalisation assumed 1D heat conduction to calculate surface temperature as a function of thermocouple temperature).

It can be seen straight away that performance variation between geometries and flow velocities is significant, particularly at elevated heat fluxes[13]. For instance, if the standard 450°C ageing limit were used to set a power handling limit (corresponding to a surface temperature rise of ~430°C), this would result in range of ~10MW/m$^2$ minimum (MkI design at 3.18m/s) up to 20MW/m$^2$ maximum (Divertor design at 11.5m/s).

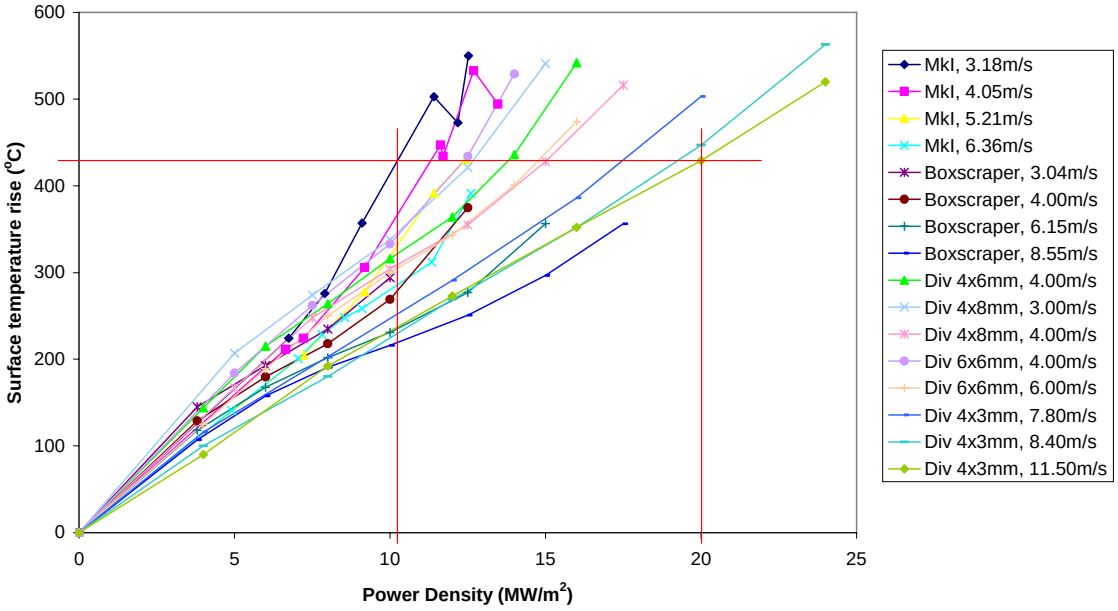


**Figure 34: HyperVapotron performance comparison (normalised to 3mm front surface thickness)**

[13] It should be acknowledged that experimental error bars are not included in this plot and that some of this variation must clearly be accounted for by uncertainties in measurement rather than genuine differences in performance. Also the MAST HyperVapotron data has been excluded from this plot due to the significant question marks over the accuracy of the data.

## 1.3 Objectives of this work

The key objectives of this study can therefore be summarised as follows:

1. Understand the origin, design philosophy and development of the HyperVapotron into one of the prime candidates for High Heat Flux applications within a fusion reactor and its ancillary systems[14].
2. Assess the suitability and accuracy of various RANS methods within a commercial CFD code for predicting HyperVapotron thermal performance in both the single phase and nucleate boiling regimes.
3. Contribute to the understanding of the physics of subcooled flow boiling in order to better understand the HyperVapotron's performance in nucleate boiling regime.
4. Develop and validate an engineering model of a HyperVapotron that captures the key features such as cavity flow, turbulence effects, recirculation and boiling heat transfer.
5. Use the above model to examine potential improvements to the HyperVapotron geometry.

To highlight the challenge of model development, the typical modelling choices involved in RANS simulation of a multiphase HyperVapotron case are listed in Appendix A. Whilst this list is not exhaustive, it does demonstrate the sheer number of settings and combinations thereof that could be used in this study, many of which could influence the model's performance predictions[15]. A significant part of this study is therefore focussed on a strategy to narrow down many of these modelling choices to a manageable subset, based on a review of the literature and consideration of the physics involved.

[14] It should be noted here that use of water-cooled HyperVapotrons within the tokamak itself on a power plant is unlikely due to the requirement of high thermodynamic efficiency and therefore high temperature operation. These temperatures are likely to require other cooling mediums and heat transfer enhancement techniques to sustain the high surface heat fluxes (e.g. high pressure Helium + jet impingement)

[15] In fact, trying to look at all possible combinations would result in well over $10^9$ simulations!

# 2

# 2 Description of numerical models

The models developed as part of this study are clearly dependent on the underlying equations for the transfer of mass, momentum and energy as well as the schemes used to discretise these differential equations. Whilst the methods used for single phase flows are relatively well established, there is still significant debate within the CFD community about how best to approach the modelling of multiphase flows (which are clearly relevant to the HyperVapotron application where boiling heat transfer plays an important role). The approach selected for this study along with justifications for the methodology and any key assumptions are outlined in this chapter.

After a brief description of the discretisation schemes, the strategies for key submodels are described, such as those used for modelling turbulence, flow near the wall and nucleate boiling. The favoured approach for incorporating boiling into the CFD model is reliant on expressions for key bubble parameters such as bubble departure diameter, frequency and nucleation site density. The literature revealed a wide range of methods for calculating these fundamental parameters, the most promising of which are included and discussed here.

Finally, to help guide the modelling strategy, the chapter concludes with a brief summary of the results derived by other researchers using various combinations of many of the models described below.

## 2.1 Governing equations

In a study such as this, it is important to understand the underlying equations that govern the transport of mass, momentum and heat both within the fluid and solid parts of the HyperVapotron. To accomplish this, Versteeg's "Introduction to Computational Fluid

Dynamics" [34], complemented by the ANSYS CFX help manuals [35] have proved most useful in this process

### 2.1.1 Single phase flows

Like most CFD solvers, ANSYS CFX solves the unsteady Navier-Stokes (NS). These are based on a set of partial differential equations that address conservation of mass, momentum and energy. To close this set of equations, additional relations are required for the shear stresses (Newtonian model) and equations of state. The basic equations are summarised below.

Conservation of Mass:

$$\frac{\partial \rho}{\partial t} + \nabla \cdot (\rho \vec{U}) = 0 \,(\text{compressible})$$

$$\nabla \cdot \vec{U} = 0 \,(\text{incompressible})$$

Conservation of Momentum:

$$\rho \frac{Du}{Dt} = \frac{\partial(-p + \tau_{xx})}{\partial x} + \frac{\partial \tau_{yx}}{\partial y} + \frac{\partial \tau_{zx}}{\partial z} + S_{Mx}$$

$$\rho \frac{Dv}{Dt} = \frac{\partial \tau_{xy}}{\partial x} + \frac{\partial(-p + \tau_{yy})}{\partial y} + \frac{\partial \tau_{zx}}{\partial z} + S_{My}$$

$$\rho \frac{Dw}{Dt} = \frac{\partial \tau_{xz}}{\partial x} + \frac{\partial \tau_{yz}}{\partial y} + \frac{\partial(-p + \tau_{zz})}{\partial z} + S_{Mz}$$

Alternatively, this can be written in vector notation as:

$$\frac{\partial(\rho \vec{U})}{\partial t} + \nabla \cdot (\rho \vec{U} \otimes \vec{U}) = -\nabla p + \nabla \cdot \tau + \vec{S}_M$$

where $S_M$ is the Momentum Source vector

Conservation of Energy:

$$\frac{\partial(\rho h_o)}{\partial t} + \nabla \cdot (\rho h_o \vec{U}) = \frac{\partial p}{\partial t} + [\frac{\partial(u\tau_{xx})}{\partial x} + \frac{\partial(u\tau_{yx})}{\partial x} + \frac{\partial(u\tau_{zx})}{\partial x} + \frac{\partial(u\tau_{xy})}{\partial y}$$

$$+ \frac{\partial(u\tau_{yy})}{\partial y} + \frac{\partial(u\tau_{zy})}{\partial y} + \frac{\partial(u\tau_{xz})}{\partial z} + \frac{\partial(u\tau_{yz})}{\partial z} + \frac{\partial(u\tau_{zz})}{\partial z}] + \nabla \cdot (k_c \nabla T) + S_h$$

where $S_h$ is the source of Enthalpy

Viscous Stresses:

$$\tau = \mu\left(\nabla \cdot \vec{U} + (\nabla \cdot \vec{U})^T - \frac{2}{3}\delta \nabla \cdot \vec{U}\right)$$

Equation of state:

$$\rho = \rho(p, T)$$

$$dh = \left.\frac{\partial h}{\partial T}\right|_p dT + \left.\frac{\partial h}{\partial p}\right|_T dp = c_p dT + \left.\frac{\partial h}{\partial p}\right|_T dp$$

$$c_p = c_p(p,T)$$

### 2.1.2 Multiphase flows

#### 2.1.2.1 Introduction

The field of multiphase flow modelling is immense and there is still significant debate on how best to represent the physics involved. Indeed, Kolev [36] states that "the creation of computer codes for modelling multi-phase flows in industrial facilities is very complicated, time-consuming and expensive. That is why the fundamentals on which such codes are based are subject to continuous review in order to incorporate the state of the art of knowledge into the current version of the code in question". It must be conceded, therefore, that the methods generally available within commercial CFD software will rely on a number of assumptions which are often incorrect.

In an attempt to understand the current state of the art of CFD modelling of multiphase flows, a number of review papers were initially considered [37,38,39,40,41]. These gave a useful introduction into the methods available for treating the continuous and dispersed phases present within a boiling problem such as this. In the end, however, given that one of the goals of this research was to tune or modify a commercial CFD code, the options available to the author were somewhat constrained to those available in the latest release of the code (in this case ANSYS CFX v.12).

Like most commercial codes, to maximise the breadth of applicability to industrial applications, ANSYS CFX has a number of different multiphase models to suit a variety of different topologies such as multiple fluid streams, bubbles, droplets, solid particles and free surface flows. It is critical therefore to select methodologies and submodels that are most applicable to the application in question as well as understanding the shortfalls and assumptions of the methods in question.

#### 2.1.2.2 Methods considered in this research

##### 2.1.2.2.1 Equilibrium Phase Change approach

One of the simplest methods for modelling water vapour within a liquid is to use the so-called equilibrium phase change model. Strictly speaking this is not a multiphase model as it solves a single set of transport equations for a homogeneous liquid-vapour mixture (i.e. the equations as laid out in section 2.1.2). As stated in the ANSYS CFX manual this model "assumes that the mixture of the two phases is in local thermodynamic equilibrium. This means that the two phases have the same temperature and that the phase change occurs very rapidly, such that the mass fractions may be determined directly from the phase diagram". Since heat and mass transfer are assumed to take place instantaneously, these models are most appropriate for very small, dispersed bubbles in a continuous liquid.

To determine the mass fraction of the vapour, or quality $x$, the flow solver uses the following method:

- If $h_{mix} < h_{sat,\alpha}(p)$ => $x = 0$. Here $h_{mix}$ is the mixture static enthalpy calculated by the flow solver (either directly or from total enthalpy) and $h_{sat,\alpha}(p)$ is the saturation enthalpy of the liquid.
- If $h_{mix} > h_{sat,\beta}(p)$ => $x = 1$ (where $h_{sat,\beta}(p)$ is the saturation enthalpy of the liquid and vapour).
- If $h_{sat,\alpha}(p) < h_{mix} < h_{sat,\beta}(p)$ => the lever rule is used to calculate vapour mass fraction: $x = \dfrac{h_{mix} - h_{sat,\alpha}(p)}{h_{sat,\beta}(p) - h_{sat,\alpha}(p)}$.

#### 2.1.2.2.2 Inhomogeneous Eulerian-Eulerian Multiphase approach

ANSYS CFX has two distinct methods for treating multiphase flows: Lagrangian Particle Tracking and Eulerian-Eulerian. The help manuals [35] lay out the pros and cons of each and, based on this and other recommendations from the literature, it was decided that the Eulerian-Eulerian method was most appropriate for modelling the boiling aspect of this problem, so the Lagrangian Particle Tracking method will not be addressed here.

In the inhomogeneous Eulerian-Eulerian treatment, each phase is resolved separately (i.e. 2 sets of transport equations) with interphase mass, momentum and heat transfer modelled using a number of correlations. In addition, for a nucleate boiling model, the Particle Model option is selected whereby the dispersed vapour phase β is assumed to be dispersed in the continuous liquid phase α[16]. In this case, the Interfacial Area Density, $A_{\alpha\beta}$ which is required to calculate the mass, momentum and heat transferred between the phases, can be equated to:

$A_{\alpha\beta} = \dfrac{6 r_\beta}{d_\beta}$, where $r_\beta$ is the local vapour volume fraction and $d_\beta$ is the bubble diameter.

The transport equations for each phase can then be written in the form below (note: only the equations for liquid phase $\alpha$ are shown, for the vapour phase equations simply reverse the subscripts $\alpha$ and $\beta$). It can be seen that one of the key assumptions here is that all phases share a common pressure field:

Conservation of Mass: $\dfrac{\partial}{\partial t}(r_\alpha \rho_\alpha) + \nabla \cdot (r_\alpha \rho_\alpha \vec{U}_\alpha) = \Gamma_{\alpha\beta}$

[16] As opposed to the Mixture Model which treats both phases symmetrically or the Free Surface Model which attempts to resolve the interface between the two phases

where $\Gamma_{\alpha\beta}$ is the mass transferred per unit volume from vapour phase β to liquid phase α (assuming no internal mass sources).

Volume conservation:

$$r_\alpha + r_\beta = 1$$

Pressure assumption:

$$p_\alpha = p_\beta = p$$

Conservation of Momentum:

$$\frac{\partial\left(r_\alpha \rho_\alpha \vec{U}_\alpha\right)}{\partial t} + \nabla\cdot\left(r_\alpha \rho_\alpha \vec{U}_\alpha \otimes \vec{U}_\alpha\right) = -r_\alpha \nabla p + \nabla\cdot\left(r_\alpha \mu_\alpha \left(\nabla\cdot\vec{U}_\alpha + \left(\nabla\cdot\vec{U}_\alpha\right)^T\right)\right)$$
$$+ \sum_{\beta=1}^{N_p}\left(\Gamma^+_{\alpha\beta}\vec{U}_\beta - \Gamma^+_{\beta\alpha}\vec{U}_\alpha\right) + \vec{S}_{M\alpha} + \vec{M}_\alpha$$

where $\left(\Gamma^+_{\alpha\beta}\vec{U}_\beta - \Gamma^+_{\beta\alpha}\vec{U}_\alpha\right)$ represents momentum transfer induced by interphase mass transfer. For details, see Interphase Mass Transfer

To close this set of equations, the term $\vec{M}_\alpha$, which describes the interfacial forces acting on phase $\alpha$ due to the presence of other phases, must be modelled in some manner. The literature reveals a wide variety of methods and correlations to accomplish this; indeed, this is often what distinguishes one from the next (as most take the Eulerian-Eulerian assumption as standard). Listing all available sub-models here would be far too lengthy and the reader is recommended to consult the literature [19,36,49]. Instead only the models that have been examined as part of this study are included and these can be found in section 2.4.2.4.2.

### 2.1.3 Heat transfer in the solid domain

Since Conjugate Heat Transfer (CHT) in the solid part will be important in this study (to assess the temperature distribution in the walls of the HyperVapotron), the equation for conservation of energy assuming zero internal heat generation and zero solid velocity can be written as follows:

$$\frac{\partial(\rho h)}{\partial t} = \nabla\cdot(k\nabla T) \tag{2.17}$$

## 2.2 Discretisation schemes

The details of the discretisation schemes can be found in [35]. Only the key methods and assumptions relevant to this study will be summarised here.

### 2.2.1 Element Shape Functions

Like many CFD solvers, ANSYS CFX is based on a finite volume method. More specifically, the CFX code stores variables at the nodes (i.e. vertices of the elements) and control volumes are created by joining the element centres (see Figure 35). Once the conservation equations have been integrated over these control volumes and Gauss' Divergence theorem has been applied, the volume and surface integrals can be discretised. In this case, volume integrals are discretised within each element sector and accumulated to the control volume to which the sector belongs while surface integrals are discretised to integration points and then distributed to the adjacent control volumes, see Figure 36.

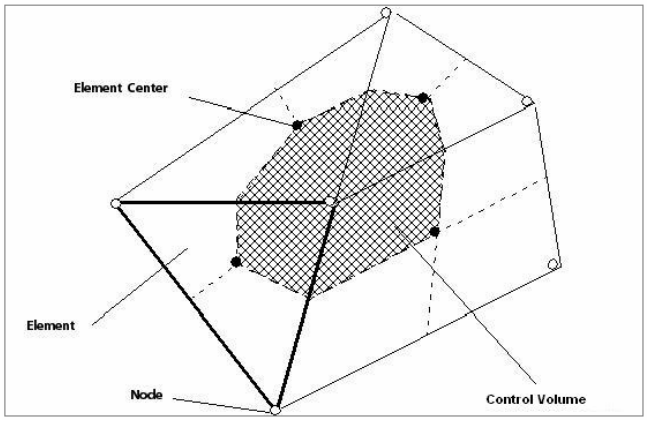


**Figure 35: ANSYS CFX control volume creation [35]**

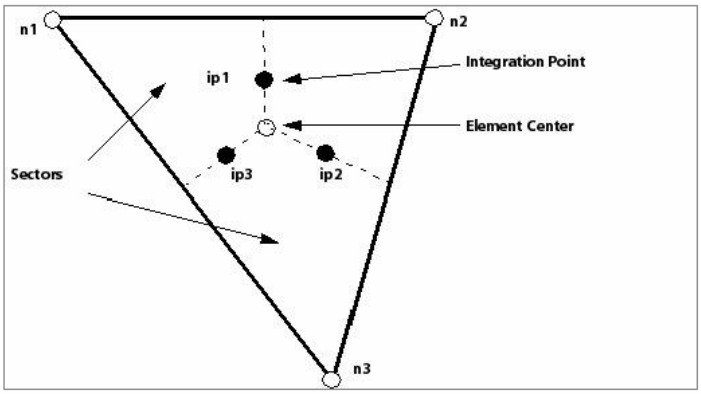


**Figure 36: ANSYS CFX element [35]**

For evaluating many of the terms, approximation of the solution fields (held at the nodes) must be made at the integration points. In order to do this, ANSYS CFX uses so-called Shape Functions. This Shape Function describes how a variable varies within an element based on the following equation:

$\phi = \sum_{i=1}^{N_{node}} N_i \phi_i$ where $N_i$ is the shape function for node $i$ and $\phi_i$ is the value of at node $i$.

Use of these shape functions allows a number of different elements types to be supported,

including hexahedral, tetrahedral, prisms (or wedges) and pyramids. As an example, a shape function for a tetrahedral element is shown below:

$$N_1(s,t,u) = 1 - s - t - u$$

$$N_2(s,t,u) = s$$

$$N_3(s,t,u) = t$$

$$N_4(s,t,u) = u$$

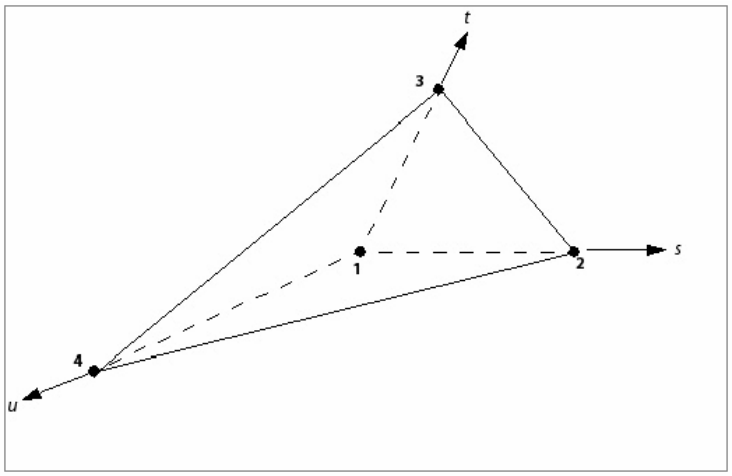


**Figure 37: ANSYS CFX tetrahedral element [35]**

### 2.2.2 Diffusion schemes

Diffusion is obtained by integrating gradients determined by shape functions over the control volume faces. It is essentially equivalent to central differencing on low order linear elements.

### 2.2.3 Advection Schemes

A key aspect of the discretisation of the advection term is the recipe used to determine integration point values of transported quantities from their nodal quantities. ANSYS CFX employs blended upwind schemes of the form:

$$\phi_{ip} = \phi_{up} + \beta \nabla \phi \cdot \Delta \vec{r}$$

where $\phi_{ip}$ and $\phi_{up}$ are variable values at the integration point and upwind node respectively, $\beta$ is a blend factor, $\nabla \phi$ is an average local nodal gradient (of element gradient) and $\Delta \vec{r}$ is the vector from the upwind node to the integration point. It is by varying the blend factor that the "average" order of accuracy can be tuned. For instance, if $\beta$ is set to 0, the scheme is first order accurate (in general this is robust but numerical diffusive, "smearing" areas of steep gradient). If $\beta$ is set to 1, the scheme is 2nd order accurate in space but is unbounded which "may cause non physical oscillations in areas

of rapid solution variation". The default setting in ANSYS CFX is therefore what is referred to as a High Resolution Scheme. This uses a "special non-linear recipe for $\beta$ at each node" which pushes the value of as close to 1 as possible (i.e. as close to a fully 2nd order accurate solution as possible). The method for achieving this is not included here but the reader is invited to refer to the relevant references [35,42].

It should be emphasised here that 1st order solutions were not considered as part of this study. Whilst these may benefit from potential improvements in computational time and robustness, the literature strongly suggested that for these types of flow, higher order solutions should be used. Given the large number of other modelling "variables" requiring examination as part of this study, it was decided to select High Resolution schemes in all cases.

## 2.3 Turbulence modelling and near-wall methods

### 2.3.1 Choice of approach: RANS vs LES

Whilst the governing equations as set out in section 2.1 can be used to describe all flows (laminar and turbulent), the grid sizes and timescales required to accurately capture the turbulence over all scales are unrealistic (in other works, Direct Numerical Simulation is not possible). As a result, some form of turbulence modelling is required to take account of how the turbulence affects the general flow field. Essentially, this comes down to a choice of two methods currently available within most CFD solvers:

1. Reynolds Averaging (RANS)
2. Large Eddy Simulation (LES)

The reader is referred to the large amount of literature available on the pros and cons of these approaches (see for instance references [34,35]). As stated in section 1.3, it has been decided here to adopt a RANS approach. This decision is based primarily on the following considerations:

1. The ultimate objective of this study is to use the CFD model(s) developed to optimise the HyperVapotron design. Optimisation often requires the modelling and comparison of a large number of designs. As a result, a relatively cheap method (computationally) is advisable.
2. LES methods are being used to examine the single phase flow as part of a complimentary study [43]. It was hoped that the results from these potentially more accurate solutions of the flow will be used to improve the accuracy of the RANS approach (see sections 3.1.2 and 4.1).

Having made this decision at an early stage in the research, the focus turned to evaluating the available RANS turbulence models. Obviously, given the choice of ANSYS CFX as the commercial software that would be used, focus was on the models available within this code.

### 2.3.2 A summary of the RANS methodology

In a turbulent flow, the variables in the NS equations can be decomposed into averaged and time-varying components:

e.g. $\vec{U} = \overline{\vec{U}} + \vec{u}$, where $\overline{\vec{U}} = \frac{1}{\Delta t}\int_t^{t+\Delta t} \vec{U} dt$

Inserting these decomposed variables back into the NS equations and with some algebraic manipulation, the Reynolds Averaged NS equations can be written as follows:

$$\frac{\partial\left(\rho\overline{\vec{U}}\right)}{\partial t} + \nabla\cdot\left(\rho\overline{\vec{U}}\otimes\overline{\vec{U}}\right) = -\nabla p + \nabla\cdot\left(\tau - \rho\vec{u}\otimes\vec{u}\right) + \vec{S}_M$$

Comparing this to the original transport equation reveals a new term, $-\rho\vec{u}\otimes\vec{u}$. The components of this tensor are known at the Reynolds Stresses and essentially describe how the presence of turbulence affects the mean flow quantities as shown. To evaluate this effect, a turbulence model is required to calculate the magnitude of these stresses.

One of the most popular RANS turbulence models is the so-called Eddy Viscosity model. These assume that the Reynolds Stresses are proportional to the mean velocity gradients:

$$-\rho\vec{u}\otimes\vec{u} = \mu_t\left(\nabla\cdot\overline{\vec{U}} + \left(\nabla\cdot\overline{\vec{U}}\right)^T\right) - \frac{2}{3}\delta_{ij}\left(\rho k + \mu_t\nabla\cdot\overline{\vec{U}}\right)$$

At this point, a model of the turbulent viscosity $\mu_t$ is required.

A popular subset of the Eddy Viscosity models are the Two-Equation models which "are very widely used, as they offer a good compromise between numerical effort and computational accuracy" [35]. The theory is that the turbulent viscosity can be calculated as the product of a turbulent velocity and length scale, each of which is solved by a separate transport equation. Of the Two-Equation models, the k-epsilon and SST k-omega variants are two of the most widely used; these are summarised in sections 2.3.2.1 and 2.3.2.2.

Alternatively, transport equations for all 6 components of the Re Stress tensor can be solved directly. One of the most popular Re Stress models in ANSYS CFX is the so-called Baseline (BSL) Re Stress model. Again, a brief description is provided in section 2.3.2.3.

It should be noted that there are many other turbulence models available within ANSYS CFX and throughout the community but focus here will be restricted to the 3 models listed above (as these are most relevant to the study, either because they are well known / well validated or have been shown to be relatively accurate for the types of flow anticipated). Furthermore, for a detailed explanation of these models and their associated near wall treatments, the reader is invited to consult the ANSYS CFX help manual or a number of validation reports available [44,45]; the sections below contain a brief summary only.

#### 2.3.2.1 The k-epsilon model

In this model $k$ is the turbulent kinetic energy and $\varepsilon$ is the turbulent eddy dissipation and the turbulent viscosity is calculated as follows:

$$\mu_t = C_\mu \rho \frac{k^2}{\varepsilon}$$

The values of $k$ and $\varepsilon$ come directly from the following transport equations:

$$\frac{\partial(\rho k)}{\partial t} + \nabla \cdot \left(\rho \vec{U} k\right) = \nabla \cdot \left[\left(\mu + \frac{\mu_t}{\sigma_k}\right)\nabla k\right] + P_k + P_{kb} - \rho\varepsilon$$

$$\frac{\partial(\rho \varepsilon)}{\partial t} + \nabla \cdot \left(\rho \vec{U} \varepsilon\right) = \nabla \cdot \left[\left(\mu + \frac{\mu_t}{\sigma_\varepsilon}\right)\nabla \varepsilon\right] + \frac{\varepsilon}{k}\left(C_{\varepsilon 1}\left(P_k + P_{\varepsilon b}\right) - C_{\varepsilon 2}\rho\varepsilon\right)$$

where $C_{\varepsilon 1}$, $C_{\varepsilon 2}$, $\sigma_k$ and $\sigma_\varepsilon$ are constants, $P_{kb}$ and $P_{\varepsilon b}$ represent the influence of buoyancy forces and $P_k$ is the turbulence production due to viscous forces, modelled as:

$$P_k = \mu_t \nabla \cdot \vec{U}\left(\nabla \cdot \vec{U} + \left(\nabla \cdot \vec{U}\right)^T\right) - \frac{2}{3}\nabla \cdot \vec{U}\left(3\mu_t \nabla \cdot \vec{U} + \rho k\right)$$

#### 2.3.2.2 The SST k-omega model

One of the issues with the k-epsilon model is that it requires complex non-linear damping near the wall to ensure a robust convergence in a wide range of cases. Even with these methods, very fine near wall grids are required to achieve a low-Reynolds treatment of the boundary layer ($y^+ < 0.2$).

The original k-omega model (as developed by Wilcox) assumes that the turbulent viscosity can be written as a function of turbulence kinetic energy and turbulent frequency as follows:

$$\mu_t = \rho \frac{k}{\omega}$$

The model then solves a transport equation for both k and ω as follows:

$$\frac{\partial(\rho k)}{\partial t} + \nabla \cdot \left(\rho \vec{U} k\right) = \nabla \cdot \left[\left(\mu + \frac{\mu_t}{\sigma_k}\right)\nabla k\right] + P_k - \beta' \rho k \omega$$

$$\frac{\partial(\rho \omega)}{\partial t} + \nabla \cdot \left(\rho \vec{U} \omega\right) = \nabla \cdot \left[\left(\mu + \frac{\mu_t}{\sigma_\omega}\right)\nabla \omega\right] + \alpha \frac{\omega}{k} P_k - \beta'' \rho \omega^2$$

where $\beta'$, $\alpha$, $\beta''$, $\sigma_k$ and $\sigma_\omega$ are all constants.

The key advantage of this method is that $\omega$ can be integrated all the way to the wall. It was found, however, that this model was highly sensitive to free stream conditions and does not account for the transport of turbulent shear stress. The SST version of the k-

omega model therefore makes a few modifications to the original model. First of all, it uses blend functions to blend between a k-omega formulation near the wall to a k-epsilon formulation away from it (again, these are not detailed here, the reader is advised to consult the help manuals [35]). Secondly, to avoid the over-prediction of eddy viscosity (due to the k-omega model's inability to account for transport of turbulent shear stress), it limits the eddy-viscosity as follows:

$$\nu_t = \frac{a_1 k}{\max(a_1 \omega, SF_2)}$$

*where*

$$\nu_t = \frac{\mu_t}{\rho}$$

$F_2$ is a blending function and S is an "invariant measure of strain rate".

It should be noted that this has been validated against a number of test cases and appears to be one of the most accurate two-equation models for examining cavity heat transfer [44].

#### 2.3.2.3 The Baseline Re Stress model

Whilst the majority of the work here is focussed on the k-epsilon and SST k-omega models, some exploratory studies are also performed using one of the Re Stress turbulence models available in the code. Re Stress models are based on the solving the transport equations for the 6 components of the turbulent stress tensor and the dissipation rate. Unlike the two-equation models above, it does not rely on the eddy viscosity hypothesis. The transport equation for the Re Stresses takes the following form:

$$\frac{\partial \rho \overline{u}_i \overline{u}_j}{\partial t} + \frac{\partial}{\partial x_k}\left(U_k \rho \overline{u}_i \overline{u}_j\right) = P_{ij} - \frac{2}{3}\beta' \rho \omega k \delta_{ij} + \Phi_{ij} + P_{ij.b} + \frac{\partial}{\partial x_k}\left(\left(\mu + \frac{\mu_t}{\sigma_k}\right)\frac{\partial \overline{u}_i \overline{u}_j}{\partial x_k}\right)$$

The reader is referred to the ANSYS CFX help manuals for details on the calculation of the shear and buoyancy turbulence production terms, $P_{ij}$ and $P_{ij,b}$, as well as the pressure-strain correlation $\Phi_{ij}$.

The BaseLine (or BSL) Re Stress model is an omega based turbulence model which, like the SST k-omega model above, switches from a wall function approach to a low Re near wall formulation if the grid is sufficiently refined (see help manuals for details of blending methods [35]). Given the success of the SST model at predicting separated and recirculating flows, it was thought that this was the most appropriate Re Stress turbulence model for this study.

#### 2.3.2.4 Multiphase turbulence models

For the k-epsilon turbulence model of a multiphase flow, the turbulent viscosity is modelled as:

$$\mu_{t\alpha} = c_\mu \rho_\alpha \left( \frac{k_\alpha^2}{\varepsilon_\alpha} \right)$$

The transport equations for k and epsilon then take the form:

$$\frac{\partial}{\partial t}\left(r_\alpha \rho_\alpha k_\alpha\right) + \nabla \cdot \left( r_\alpha \left( \rho_\alpha \vec{U}_\alpha k_\alpha - \left( \mu + \frac{\mu_{t\alpha}}{\sigma_k} \right) \nabla k_\alpha \right) \right) = r_\alpha \left( P_\alpha - \rho_\alpha \varepsilon_\alpha \right) + T_{\alpha\beta}^{(k)}$$

$$\frac{\partial}{\partial t}\left(r_\alpha \rho_\alpha \varepsilon_\alpha\right) + \nabla \cdot \left( r_\alpha \rho_\alpha \vec{U}_\alpha \varepsilon_\alpha - \left( \mu + \frac{\mu_{t\alpha}}{\sigma_\varepsilon} \right) \nabla \varepsilon_\alpha \right) = r_\alpha \frac{\varepsilon_\alpha}{k_\alpha} \left( C_{\varepsilon 1} P_\alpha - C_{\varepsilon 2} \rho_\alpha \varepsilon_\alpha \right) + T_{\alpha\beta}^{(\varepsilon)}$$

In this case, $T_{\alpha\beta}^{(k)}$ and $T_{\alpha\beta}^{(\varepsilon)}$ are interphase transfer terms for k and epsilon respectively. Similar methods are employed for the SST k-omega and BSL Re Stress turbulence models.

### 2.3.3 Near Wall Treatment

#### 2.3.3.1 Scalable Wall Functions

Traditionally, flow near the wall has been modelled using wall functions. These are derived empirically and show that the near wall tangential velocity has a log-law relationship with the wall shear stress. If the first near wall node is assumed to be in the fully turbulent portion of the boundary layer, the following non-dimensional expression is used to calculate the dependent variables at this location as a function of the wall condition:

$$u^+ = \frac{U_t}{u_\tau} = \frac{1}{\kappa} \ln\left(y^+\right) + C$$

*where*

$$u_\tau = \left( \frac{\tau_\omega}{\rho} \right)^{1/2}$$

$$y^+ = \frac{\rho \Delta y u_\tau}{\mu}$$

The first problem with this formulation is that is becomes singular as Ut approaches zero (e.g. at separation points). An alternative formulation is therefore proposed based on the following:

$$u^* = C_\mu^{1/4} k^{1/2}$$

$$u_\tau = \frac{U_t}{\frac{1}{k}\log(y^*) + C}$$

$$\tau_\omega = \rho u^* u_\tau$$

$$y^* = \frac{\rho u^* \Delta y}{\mu}$$

Even this alternative definition, however, relies on the distance of the nearest grid point to the wall and is therefore highly sensitive to near wall grid resolution. One way round this is to use Scalable Wall Functions.

Esch [44] describes the formulation of Scalable Wall Functions as a method of avoiding the problems created when the grid generates nodes within the viscous sublayer, where the log-law no longer applies. In summary, the code uses a new value of non-dimensional distance-to-the-wall, y*, is calculated using $y^* = \max(y^+, y^+_{lim})$. The limiting value $y^+_{lim} = 11$ corresponds to the intersection between the log and linear profiles within the boundary. For fine grids, "y* is therefore decoupled from the grid spacing". The physical interpretation is that "the wall is treated as if it would be the edge of the viscous sublayer". This allows wall functions to be used on arbitrarily fine meshes. The downside is the error generated by ignoring the displacement of the viscous sublayer; small for high device Reynolds number but increasing for flows at low device Re (where the size of the sublayer relative to the boundary layer increases).

The code uses Scalable Wall Functions as the default for the k-epsilon based turbulence models.

#### 2.3.3.2 Automatic Near Wall Treatment

Applied to the Omega-based turbulence models available with ANSYS CFX, this method switches from a low Re formulation where the grid is fine enough to resolve the viscous sublayer to a wall function approach where it is not. Validation work has shown this to be an accurate, cost-effective method of modelling flow near the wall on any unstructured mesh. That said, the code recommends that resolving the boundary layer into at least 10 elements to "take advantage of the reduction in errors offered by the automatic switch to a low-Re near wall formulation".

The subtleties of this approach are examined in more detail as the study progresses as it turns out that the choice of near wall treatment and mesh resolution are critical in the success of modelling flow / heat transfer within a cavity.

## 2.4 Boiling Sub-models

### 2.4.1 Identification of key sub-models

Both Rohsenow [19] and Kolev [36] provide excellent introductions to the topic of boiling heat transfer. Their summaries are particularly useful as they condense what is

undoubtedly a huge volume of work dedicated to this topic over the past half century. Indeed, Kolev remarks that nucleate boiling "is probably the most investigated phenomenon in the thermal sciences over [the last] 60 years".

Of particular interest are Kolev's chapters which examine in detail the physics, experimental data and modelling methods for the elementary boiling parameters. From these chapters and associated references, it appears that most researchers are focussed on a specific subset of boiling parameters selected due to their importance in determining the overall performance of a boiling system. In most cases, these include nucleation site density, bubble departure diameter, frequency and waiting time (between departing bubbles). Furthermore, most strategies for incorporating boiling heat transfer into a CFD solution are based on a mechanistic approach which relies on expressions or correlations for these parameters to calculate the mass source of vapour at the wall of the domain (see section 2.4.2.2). Clearly to achieve the most accurate CFD solution for a given application, choice of the most appropriate and accurate models for each parameter is critical.

### 2.4.2 Modelling Strategies

#### 2.4.2.1 Regimes of interest for the Hypervapotron

As suggested in section 1.2.1, a number of complex mechanisms and interactions are proposed for vapour formation within a HyperVapotron cavity. More specifically, under certain conditions, it is suggested that all types of boiling are present within the cavity (from onset to nucleate boiling right through to film boiling). Given the current state of the art for CFD methods and limitations on computing resource, it is highly unlikely a single model can be developed as part of this study that can accurately model all these regimes (from individual bubbles through to large vapour films). Even more challenging would be the modelling of large vapour jets being ejected from the cavities (as described in section 1.2.1). Fortunately, from work undertaken by researchers such as Beutheret, Cattadori and Falter, it would appear that this macroscopic effect is not particularly relevant to fusion-relevant conditions (where elevated power densities necessitate the use of high flow velocities and increased subcooling). As a result, it is unlikely that modelling this effect is essential to the success of this research.

As described in section 2.1.2, two different modelling approaches appear to be most appropriate for CFD modelling of the type of multiphase flow expected in a Hypervapotron application (i.e. small vapour bubbles dispersed in a continuous liquid):

1. The Equilibrium Phase Change approach
2. An Inhomogeneous, Eulerian-Eulerian Multiphase approach with an associated boiling model

Once one of these has been selected, a number of additional modelling decisions remain[17] which typically include:

[17] Some of these decisions are only relevant to one of the two modelling approaches listed.

1. How to model the vapour source (and associated liquid sink) at the wall (e.g. rely on near wall liquid superheating or calculate vapour mass source as a function of geometrical / fluid parameters)
2. Where relevant, which submodels should be used for the critical boiling parameters (e.g. bubble departure diameter, frequency, nucleation density, bubble diameter in the flow etc).
3. How to model the transfer of mass, momentum and heat between the two phases.

Some examples of how these issues might be addressed are included in the sections 2.4.2.2 to 2.4.2.4.

#### 2.4.2.2 Modelling the vapour source at the wall

A CFD model requiring nucleate boiling at the wall must incorporate some kind of vapour seeding at the wall; i.e. a mass source of vapour and an equivalent mass sink for the liquid (to maintain conservation of mass). This can be done in one of two ways:

1. Rely on superheating of the liquid in the first cell at the wall (i.e. bulk boiling) such that interphase heat and mass transfer is activated and vapour is created.
2. Impose a vapour source at the wall as a function of local quantities (such as wall superheating, near wall velocity, near wall subcooling etc).

In many cases, given that nucleate boiling at the wall can be initiated while the fluid is still substantially subcooled, the first method would be inadequate at predicting the onset of nucleate boiling if the near wall grid size was such that the average temperature was below saturation. As a result, one method of getting "sensible" results using this method is by artificially increasing the potential for significant vapour formation. One such method [35] is by specifying a minimum (and often arbitrary) vapour volume fraction or "seeding level" $r_{min}$ which is then used to calculate an initial interface area density at very low vapour fractions present when near wall liquid is still subcooled [18]:

$$A_{\alpha\beta} = \frac{6 r_\beta^*}{d_\beta}$$

*where*

$$r_\beta^* = \max(r_\beta, r_{\min})$$

The advantage of this method is that it is a robust method of vapour creation at the wall with no additional submodels required by the solution. The disadvantage is that the amount of vapour subsequently created is highly sensitive to the choice of $r_{min}$ and the near wall cell size (see section 3.2.1.3). This approach can essentially be considered as an overly-simplistic homogeneous nucleation model. It will be referred to from this point forward as the "non-equilibrium, bulk boiling model".

---

[18] This method relies on the user specifying a minimum vapour volume fraction throughout the domain, e.g. 1e-8. If this were initially set at 0, there would be no possibility of substantial vapour being created before the near wall cells reached saturation temperature.

The 2nd method, on the other hand, does have the potential to be grid independent (particularly if near wall quantities are taken at a fixed value of $y^+$) and, if tuned correctly, has been shown to be relatively accurate in a number of cases [47,48,52,53]. One of the key issues when setting up this type of model is deciding on the number of heat transfer mechanisms that are taking place (and therefore how the heat flux at the wall will be split in the model). The literature review has revealed various methodologies where the wall heat flux has been split into 2, 3 or even 4 parts. Early models were often based on a two-way split of the wall heat flux: i.e. convection to the liquid and boiling (e.g. Zeitoun and Shoukri [46] and Steiner et al [47]). Many of the more recent models, however, have included a third term to account for the heating of the cooler liquid that replaces departing bubbles (often referred to as quenching). Finally, some models have also added a 4th term to model convection to the vapour (where it is claimed that inclusion of this term allows the model to account for dryout).

Once a decision has been made on the number of mechanisms to model, a method must be formulated for calculating how the applied heat flux is split between the various mechanisms. One of the simplest methods is to use an empirical correlation to calculate the heat flux fractions as a function of wall superheating and/or local subcooling (Zeitoun and Shourkri [46]). Alternatively iterative methods can be used to calculate the split based on mechanistic models for bubble formation at the walls [48,49,50,51,52,53,54].

This type of method has been employed by a number of researchers [50,51,52,53,54] who used a method originally developed by Podowski et al [48,49] at the Centre for Multiphase Research (Rensselaer Polytechnic Institute (RPI), USA). The so-called RPI boiling model is based on a 3-way partition of the heat flux applied at the wall $Q_w = Q_c + Q_q + Q_e$, where $Q_c$ is the heat flux corresponding to convective heat transfer, $Q_q$ is the heat flux corresponding to quenching and $Q_e$ is the evaporation heat flux. In some cases, it has been shown that this can be relatively accurate when compared to experiment [48,52]. Indeed it is the RPI method which has recently been incorporated into ANSYS CFX (version 12) as its in-built wall boiling model. Once a decision has been made on wall heat flux partitioning, the next step is to derive models for the individual terms:

1. Evaporation: This is simply based on the mass of vapour leaving the wall divided by the enthalpy difference between the liquid and vapour phases, $Q_e = \dot{m} h_{\mathrm{lg}}$. The mass flow rate can then simply be calculated as the product of (bubble mass)×(number of bubbles)×(frequency of departure), i.e. $\dot{m} = \frac{\pi d_W^3}{6} \rho_G f n$. Submodels to calculate bubble frequency, departure diameter and nucleation site density are therefore essential to this method (see section 2.4.2.3).
2. Convection to the liquid: This can be calculated a number of ways:
    1) Correlations, e.g. for a pipe $Q_c = A_c St \rho_l c_{pl} U_l (T_w - T_l)$, where *St* is the Stanton number (=*Nu/RePr*).

2) 1D conduction (if the grid is fine enough, e.g. $y^+<1$), i.e. $Q_c = -k_l \frac{(T_w - T_{nw})}{\Delta y}$

3) Use of standard wall functions and a fixed value of $y^+$ to calculate the a "near wall" temperature difference and associated heat flux due to convection (this is the default method employed by the ANSYS CFX implementation of the RPI boiling model).

3. Quenching: Most models [52,53,55] where quenching is considered rely on an expression developed by Del Valle and Kenning [56] (typical flow velocities of 1 – 2 m/s and inlet subcooling of up to 100K) where the quenching heat transfer coefficient $h_q = 2k_l f \sqrt{\frac{t_w}{\pi a_l}}$ where $a_l = \frac{k_l}{c_{pl}\rho_l}$ is the liquid diffusivity and bubble waiting time is frequently taken as $t_W = \frac{0.8}{f}$. The quenching heat flux is then calculated using $Q_q = A_q h_q (T_w - T_l)$

4. Convection to the vapour: Finally, there are a few select examples where this component of the heat flux is taken into account. In particular, Pascal-Ribot et al. [53] argue that since they are attempting to model the boiling heat transfer in a HyperVapotron right through to film boiling, this component of the heat transfer can be important. In this case, the vapour flow is assumed to be laminar and 1D conduction is used to calculate this component of wall heat flux, i.e. $Q_{cg} = -k_g \frac{(T_w - T_{nw})}{\Delta y}$.

Whilst it's true that the in-built ANSYS boiling model is based on the RPI methodology, it is worth highlighting here the two key differences in implementation between the original method and the ANSYS CFX v12 implementation:

1. The ANSYS model uses wall functions to calculate near wall quantities as well as the percentage of heat flux going into single phase convection. The original RPI method, however, relied on a Stanton number correlation to calculate values at the centre of a circular tube.
2. The ANSYS model avoids mesh dependence by extrapolating all near wall quantities to a fixed value of $y^+$ (default value of $y^+ = 250$) whilst the original method was mesh dependent.

#### 2.4.2.3 Submodels for the critical boiling parameters

##### 2.4.2.3.1 Bubble departure diameter

The literature reveals many different correlations for bubble departure diameter, the choice of which can have significant effects on the results. Whilst a number of early attempts used relatively simple correlations (e.g. Tolubinski and Kostanchuk correlation where diameter is simply a function of local subcooling), it has been shown that more

sophisticated approaches based on force balance approaches or more complex correlations (which take into account many other parameters) can sometimes be more suitable and applied to a wider range of cases.

The models examined in this study are listed in Table 3.

| **Study** | **Model** |
|---|---|
| Tolubinski and Kostanchuk [57], 1970 | $d_w = \min\left( d_{ref} \cdot \exp\left( -\frac{\Delta T_{sub}}{\Delta T_{ref}} \right), d_{\max} \right)$ , $d_{\max} = 1.4\text{mm}$, $d_{\text{ref}} = 0.6\text{mm}$, $\Delta T_{\text{ref}} = 45\text{K}$ where $\Delta T_{\text{sub}} = T_{\text{sat}} - T_{\text{liq}}$ (local liquid subcooling) |
| Cole and Rohsenow [58], 1969 | $d_w = \sqrt{\frac{\sigma}{g(\rho_l - \rho_g)}} \left(1.5 \times 10^{-4}\right) \left( \frac{\rho_l c_{pl} T_{sat}}{\rho_g h_{\text{lg}}} \right)^{5/4}$ |
| Unal [59], 1976 | $d_w = 2.42 \times 10^{-5} p^{0.709} \left( \frac{a}{b\sqrt{\varphi}} \right)$ *where* $a = \frac{(Q_w - h_c \Delta T_{sub})^{1/3} k_l}{2c^{1/3} h_{\text{lg}} \rho_g \sqrt{\pi k_l / \rho_l c_{pl}}} \sqrt{\frac{k_w \rho_w c_{pw}}{k_l \rho_l c_{pl}}}$ $b = \frac{\Delta T_{sub}}{2\left(1 - \rho_l / \rho_g\right)}$ $c = \frac{h_{fg} \mu_l \left[ c_{pl} / (0.013 h_{\text{lg}} \text{Pr}^{1.7}) \right]^3}{\sqrt{\sigma / (\rho_l - \rho_g) g}}$ and $\varphi = \max\left( \frac{U_b}{U_0}, 1 \right)$ where $U_0 = 0.61 m/s$ |

| Study | Model |
|---|---|
| Pascal-Ribot et al [53], 2005 | $d_w = \min(D_{unal}, D_{turb}, D_{geo})$<br>*where*<br>$D_{unal} = 2.42\times10^{-5}\, p^{0.709}\, \frac{a}{\sqrt{b\phi}}$<br>*with*<br>$a = \frac{\Delta T_{\sup} k_w}{2\rho_g h_{lg}\sqrt{\pi k_w/\rho_w c_{pw}}}$,<br>$b = \frac{\Delta T_{sub}}{2\left(1-\rho_g/\rho_l\right)}$, *if* $St < 0.0065$<br>$b = \frac{Q_w}{2\left(1-\rho_v/\rho_l\right)\times 0.0065\times \rho_l c_{pl} U_l}$, *if* $St > 0.0065$<br>$D_{turb} = C_\mu^{3/4}\frac{k^{3/2}}{\varepsilon}$,<br>$D_{geo} = 0.1\times D_{system}$ |
| Kolev [60], 2004 | $\left(\frac{D_{1d}}{D_{1d,nc}}\right)^3 + \left(\frac{D_{1d}}{D_{1d,fc}}\right)^2 = 1$<br>*where*<br>$D_{1d} = \left\{\frac{6A}{[(\rho_2-\rho_1)g\sin(\varphi+\theta_o]}\right\}^{1/3}$,<br>$D_{1d,fc} = \left\{\frac{A}{\left[\rho_2 V_{2ld}^2\left(\frac{1}{2}c_{lift}\sin\theta_o + 0.3c_{wall}^2\cos\theta_o\right) + 0.3\rho_2\overline{\overline{V_2'^2}}\cos\theta_o\right]}\right\}^{1/3}$<br>*and*<br>$A = D_{1c}^{*}\sigma + 3\eta_2 c_{form} B^2\left[1+0.1\left(\frac{c_{form}B^2\rho_2}{\eta_2}\right)\right]^{3/4}\sin\theta_o$<br>*In this case:*<br>• $D_{1d}$ = *bubble departure diameter,* $d_w$,<br>• $D_{1d,nc}$ = *bubble departure diameter for pool boiling conditions,* |

| Study | Model |
|---|---|
| | • $D_{1d,fc}$ = *bubble departure diameter for forced convection boiling conditions.*<br>*Details of all other coefficients and variables can be found in Kolev's[60] original paper.* |

**Table 3: Example of models developed for bubble departure diameter**

The Tolubinski-Kostanchuk model is used by the ANSYS CFX RPI boiling model by default. This is one of the simplest of the models above but is empirically derived, depends only on near wall subcooling and uses dimensional constants. As a result, it may not be widely applicable to forced convection boiling cases.

Unlike Tolubinski, Cole and Rohsenow use a mechanistic approach which sets the bubble departure diameter to coincide with the point when the bubble is of sufficient size that the "upwards" buoyancy force just balances the surface tension force tying the bubble to the wall. Whilst mechanistic approaches are generally preferred to empirical methods, this approach unfortunately does not take into account key variables that will undoubtedly influence bubble diameter in most forced convection boiling cases (such as wall superheating, near wall subcooling and near wall velocity).

Unal's model is also mechanistic model but this, however, does take into account many of the relevant parameters (including pressure, wall superheating, local subcooling, near wall velocity and material properties). As a result, it was hoped this model should have a much wider range of applicability and a number of researchers have proposed this as the optimum submodel for this parameter [52,61]. It is worth noting that this correlation depends on the convective heat transfer coefficient which will need to be calculated in one of the 3 methods illustrated in section 2.4.2.2. It also goes to infinity as subcooling goes to zero and is invalid if $Q_w < h_c \Delta T_{sub}$. Additional constraints must therefore be imposed to ensure it is applicable in a wide variety of cases (not ideal).

Pascal-Ribot's method uses a modified Unal correlation (where coefficient *a* is based on the material properties of the wall rather than the liquid) and additional limits are placed on bubble diameter based on local turbulence and geometric constraints. This appears to be one of the only attempts to incorporate local turbulence and geometric constraints into the derivation of bubble diameter and may make this method more tuneable to a HyperVapotron application. Furthermore, to avoid the problem of bubble diameter going to infinity as near wall temperature approach $T_{sat}$, a new formulation for the coefficient *b* is derived if the Stanton number drops below a critical value.

Finally, Kolev's model stands out as by far the most complex and was formulated in response to the poor performance he observed with some of the models listed above (and others) [60]. The evidence he presents to back this up is illustrated in Figure 38 and Figure 39. Unfortunately, the equations he has derived require a non-linear solution and access to a very wide range of flow parameters; as a result, it was not possible to

incorporate such a complex submodel into an ANSYS CFX boiling solution within the timescales of this research[19]. That said, it can be seen in Figure 38 that most of the data shows a similar trend with wall superheating, even though this was measured over a relatively wide range of thermal-hydraulic conditions. Consequently, a much simpler alternative approach could be conceived whereby a relationship is derived between bubble departure diameter and wall superheating based on a best-fit curve applied to the experimental data shown below.

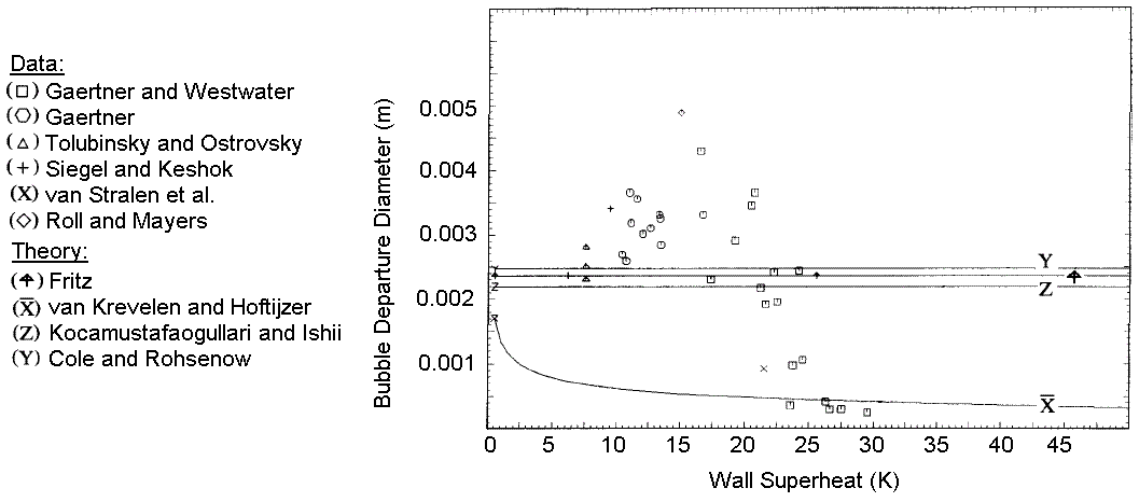


**Figure 38: Kolev's demonstration of inadequacy of many bubble departure diameter models [36]**

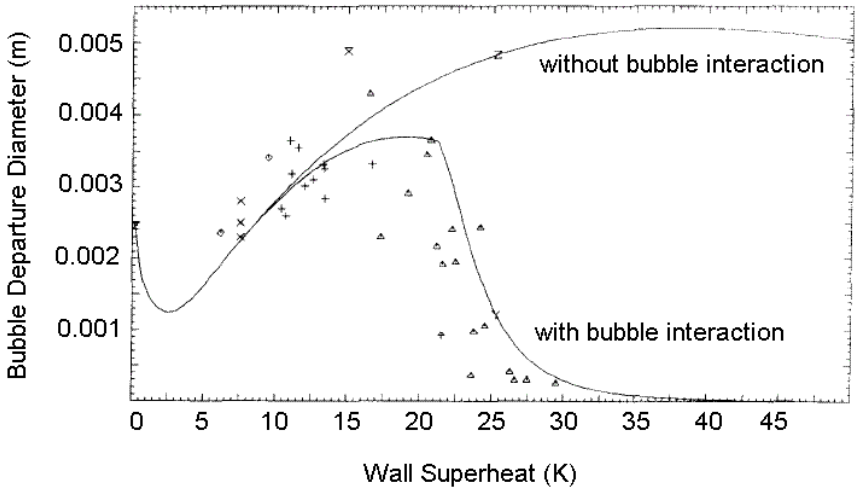


**Figure 39: Kolev's models compared to experiment [36]**

### 2.4.2.3.2 Bubble departure frequency

Clearly, as well as the size of departing bubbles, the frequency of departure has a large influence on the heat transfer efficiency of the system (more bubbles leaving per second

[19] Long term, it would certainly be of interest to attempt this given the methods used to derive it and its claimed improvement in accuracy compared to a wide range of experimental data.

results in more heat removed from the surface). The expressions for bubble departure frequency considered in this study are listed in Table 4.

| **Study** | **Model** |
|---|---|
| Cole [62], 1960 | $f = \sqrt{\frac{4g(\rho_L - \rho_G)}{3d_W \rho_L}}$ |
| Zuber [63], 1963 | $f = 0.5\frac{1.18\left[\sigma g(\rho_L - \rho_G)/\rho_L^2\right]^{1/4}}{d_W}$ |
| Situ [64], 2008 | $f = \frac{N_{fd} a_l}{d_w^{\,2}}$<br>*where*<br>$N_{fd} = 10.7 N_{qNB}^{0.634}$<br>$N_{qNB} = q_{NB} d_w / a_l \rho_g h_{fg}$<br>$q_{NB} = \left[ S(0.00122)\left[ \frac{k_l^{0.79} c_{pl}^{0.45} \rho_l^{0.49}}{\sigma^{0.5} \mu^{0.29} h_{fg}^{0.24} \rho_g^{0.24}} \right] \Delta T_{\text{sup}}^{0.24} \Delta p'^{0.75} \right] \Delta T_{\text{sup}}$<br>$S = 1/\left(1 + 2.53 \times 10^{-6}\, \text{Re}_{TP}^{1.17}\right)$<br>$\Delta p' = p(T_w) - p(T_{sat})$ |

**Table 4: Example of models developed for bubble departure frequency**

Many of the boiling models that require knowledge of bubble departure frequency rely on the expression derived by Cole where he assumed that the product of bubble departure diameter and frequency is equal to bubble rise velocity (which is derived from force balance of buoyancy force and drag force).

Zuber pursues a similar method but ends up with a slightly modified correlation as shown in the above table. Comparing the two correlations shows that Zuber's method predicts greater frequencies at smaller bubble diameters but low frequencies at increased bubble diameters (e.g. taking the liquid and vapour densities of water at atmospheric pressure, Zuber predicts a departure frequency of ~900Hz at a bubble diameter of 0.1mm, while Cole only predicts ~350Hz. At a bubble diameter of 2mm, this flips with Zuber predicting 50Hz compared to 80Hz predicted by Cole). Depending on the "average" bubble size for a given system, choice between these two correlations could make a significant difference to the heat transfer of the system.

One of the most recent and comprehensive studies on bubble departure frequency was performed by Situ et al in 2008. In particular, Situ examined a wide range of

experimental data and showed that many of the well-known correlations often struggled to predict the correct results over the entire data set. For instance, it was found that Cole's model could "over-predict [departure frequency] with water […] with an averaged error of ±52.2%". Zuber's model was found to be slightly better "with ±20.4% as an averaged uncertainty". A new expression was therefore developed based on new, more appropriate dimensionless groups which is shown to be more accurate against all experimental data compiled or generated by Situ.

It is worth noting at this point that Situ's expression relies on Chen's calculation of the nucleation boiling heat flux, $q_{NB}$. This poses two potential problems:

1. It is precisely the nucleation boiling heat flux that this study is trying to calculate so a CFD boiling model relying on this parameter poses a bit of paradox.
2. Chen's correlation is also reliant on knowledge or calculation of the two phase Reynolds number $Re_{TP}$. This is not always easy to extract as it requires knowledge of the local quality of the flow (which in the HyperVapotron problem is not available as it is one of the key outputs of the study).

Even with these drawbacks, however, this will still be considered given the improvement claimed by its originators.

#### 2.4.2.3.3 Nucleation site density

Once the size and frequency of bubbles emanating from a single nucleation site has been determined, the model must specify how many of theses "average" sites are likely to occur on the boiling surface. As a result, many studies have been undertaken investigating the nucleation site density.

The models considered are listed in Table 5.

| Study | Result |
|---|---|
| Lemmert and Chawla, 1977 [65] | $n = \left(210\Delta T_{\text{sup}}\right)^{1.805}$<br>where $\Delta T_{\text{sup}} = T_{\text{wall}} - T_{\text{sat}}$ (wall superheat). |
| Kocamustafaogullari and Ishii, 1983 [66] | $n = \dfrac{f\left(\rho^*\right)\left(R_c^*\right)^{-4.4}}{d_w{}^2}$<br>where $f\left(\rho^*\right) = 2.157\times10^{-7}\left(\rho^*\right)^{-3.2}\left(1+0.0049\rho^*\right)^{4.13}$,<br>$\rho^* = \left(\rho_l - \rho_g\right)/\rho_g$,<br>$R_c^* = \left(D_c / d_w\right)$ and<br>$D_c = \dfrac{4\sigma T_{sat}}{\rho_g h_{fg}\left(T_w - T_{sat}\right)}$ |
| Wang and Dhir, 1993 [67] | $n = 5\times10^{-27}(1-\cos\phi)/D_c^6$ where $\phi$ is the bubble contact angle. |
| Basu et al, 2002 [68] | $n = 0.34\times10^{4}(1-\cos\phi)\Delta T_{\text{sup}}^{2.0}$, $\Delta T_{ONB} < \Delta T_{\text{sup}} < 15^o C$<br>$n = 3.4\times10^{-1}(1-\cos\phi)\Delta T_{\text{sup}}^{5.3}$, $15^o C < \Delta T_{\text{sup}}$ |

**Table 5: Example of models developed for nucleation site density**

What is interesting to note here is that the key independent variable in nearly all the expressions above is wall superheating. Hardenberg [69] suggests, however, that nucleation site density is likely to be a function of more parameters than simply wall superheating and surface finish and, along with Del Valle [56], highlights the multiple phenomena which inhibit or promote nucleation sites. In short, predicting the number of active bubble nucleation sites on any given surface is highly complex.

That said, the boiling model envisaged as part of this study requires knowledge of the number of individual sites so some kind of expression or correlation is required. Furthermore, it should be noted that Krepper [52], acknowledging the shortcomings of the Lemmert and Chawla model used in his CFD solution, conducted a sensitivity study which showed (at least for his case) that halving or doubling the number of sites had a negligible influence on his predictions for void fraction or wall temperature (within the uncertainty of the experimental measurements). Similar studies could also be performed as part of this research.

The Lemmert / Chawla model is selected as the default in the ANSYS CFX RPI model (although non-dimensionalised in its implementation). It can be seen straight away that at a wall superheating of 10K, nucleation site densities in the order of $10^6$ $m^{-2}$ would be expected (or one every $mm^2$).

Kocamustafaogullari and Ishii's correlation was derived assuming that the site density was dependent on surface conditions and the thermophysical properties of the fluid (which, for a given fluid, can be described as a function of pressure only). This has been recommended by a number of researchers who claim it gives relatively accurate results over a wide range of cases.

Finally, it can be seen that the last two expressions, by Wang/Dhir and Basu, are fundamentally based on the contact angle, this can often be difficult to ascertain for a given surface / coolant combination. Comparing the two expressions, it can be seen that the Wang/Dhir correlation also relies on the critical bubble radius. This not only depends on wall superheat but also takes account of other variables which intuitively should influence the number of sites active on any boiling surface (such as surface tension, latent heat and gas density).

The exponents in the Wang/Dhir and Basu correlations mean these both result in a relatively small number of sites at wall superheats up to ~15K. After that, however, the number of sites grows exceedingly fast and quickly exceeds the predictions made by the Lemmert / Chawla model. Depending on the level of superheating found in the HyperVapotron application, choice between these 3 correlations will have a significant effect on number of sites and therefore the performance of the system.

#### 2.4.2.3.4 Bubble diameter in the bulk flow

A number of CFD boiling simulations model the bubble diameter in the flow using the Anglart and Nylund [70] approximation, i.e. bubble diameter is a linear function of local liquid subcooling over a particular range (e.g. subcooling temperatures of 13 to -5K): $d_B = \frac{d_1 - d_o}{T_1 - T_o} T_{sub} + \frac{d_o T_1 - d_1 T_o}{T_1 - T_o}$, where $T_{sub}$ is the local liquid subcooling, and $d_o$ and $d_1$ are the bubble diameters at reference liquid subcoolings, $T_o$ and $T_1$, respectively.

The resultant distribution (with diameter assumed constant outside the range and smoothing applied) is shown in Figure 40.

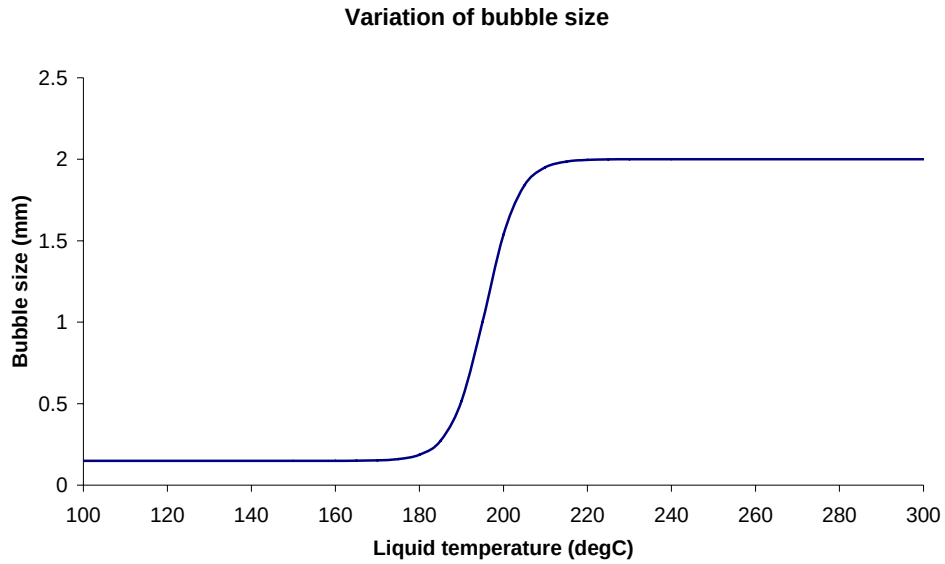


**Figure 40: Anglart and Nylund approximation for bubble size in the bulk fluid**

As stated by Krepper [52], "…a constant bubble diameter in the bulk doesn't exist since the process is transient" (bubbles grow in superheated liquid and shrink in subcooled liquid). As a result, some of the more recent approaches [71] have gone further and have started to take account of bubble coalescence and breakup phenomena. Multiple Size Groups have been modelled and empirical relations used to calculate mass transfer between the groups (i.e. coalescence or breakup). Although these are still in their early stages and often require unrealistic simplifications (e.g. the assumption that all sizes move at the same velocity), they have been shown, in some cases, to improve the accuracy of predicting void fraction distributions.

Alternatively, other correlations can be considered which take into account a larger number of parameters than simply the local liquid subcooling. For example, Zeitoun and Shoukri [46] proposed the following expression which has been shown to be an improvement in a number of cases [52,76]:

$$\frac{d_B}{\sqrt{\sigma / \left(g\left(\rho_l - \rho_g\right)\right)}} = \frac{0.0683\left(\rho_l / \rho_g\right)^{1.326}}{\mathrm{Re}^{0.324}\left(Ja + \dfrac{149.2\left(\rho_l / \rho_g\right)^{1.326}}{Bo^{0.487}\,\mathrm{Re}^{1.6}}\right)}$$

### 2.4.2.4 Modelling interphase mass, momentum and heat transfer

#### 2.4.2.4.1 Interphase mass transfer

For interphase mass transfer, ANSYS CFX has an in-built "Thermal phase change" model which calculates the mass transferred from one phase to the other based on

interphase heat fluxes and the difference in enthalpies (it can be shown that mass flux from phase α into phase β is $m_{\alpha\beta} = (q_{\alpha\beta}+q_{\beta\alpha}) / (h_\beta - h_\alpha)$)

#### 2.4.2.4.2 Interphase momentum transfer

Momentum transfer is dictated by the forces that come into play between the continuous liquid and dispersed vapour phases. These can be classified as follows:

##### 2.4.2.4.2.1 Drag Force

Three drag force correlations are considered suitable for the vapour bubbles in this boiling model:

1. Schiller Naumann, recommended for fluid particles that are small enough to be considered "spherical"
2. Ishii-Zuber, which takes into account bubbles in distorted ellipsoidal regime.
3. Grace model, which was originally developed using air-water data, (and therefore may not be as relevant for a water / vapour mixture).

Given the fluids in question and evidence that suggests the spherical bubble assumption is valid, the Schiller Naumann correlation is selected. For this model, the drag curve is derived using $C_D = \max\left(\frac{24}{\mathrm{Re}}\left(1 + 0.15\,\mathrm{Re}^{0.687}\right), 0.44\right)$.[20]

##### 2.4.2.4.2.2 Non Drag Forces

Non Drag Forces include:

1. Lift force (perpendicular to direction of relative motion of phases)
2. Virtual mass force (proportional to relative phasic accelerations)
3. Wall lubrication force (to model observation of near wall concentration of dispersed phase in vertical pipe flow)
4. Turbulent Dispersion force

Koncar et al have performed a useful examination of the relative influence of these forces [72]. For this study, however, most of these will be ignored as they are either not relevant to the HyperVapotron geometry (e.g. wall lubrication force) or are shown to have negligible effect compared to drag.

#### 2.4.2.4.3 Interphase heat transfer

Interphase heat transfer requires knowledge of the heat transfer coefficients as well as interphase surface area to be calculated. For this particular application, it is recommended that the primary resistance to heat transfer be set on the continuous, liquid "side" of the bubble. The heat transfer coefficient itself can be modelled using correlations such as the Ranz Marshall correlation [73]; $Nu = 2 + 0.6Re^{0.5} Pr^{0.3}$.

[20] This takes into account the fact that at sufficiently large particle Reynolds numbers, the drag coefficient becomes independent of Re (and is equal to 0.44).

#### 2.4.2.4.4 Interphase Area Density

As highlighted in section 2.1.2.2.2, knowledge of the interphase area density is critical to the calculation of transfer of mass, momentum and energy and, assuming the bubbles are spherical, this can be equated as $A_{\alpha\beta} = \frac{6r_\beta}{d_\beta}$.

There is clearly a flaw in this relationship, however, as this expression predicts a non-zero interphase area density as the vapour volume fraction tends to 1. As a result, a modified expression for this parameter is used:

$$A^*_{\alpha\beta} = \left(A_1^B + A_2^B\right)^{(1/B)}$$

*where*

$$A_1 = \frac{6 \times \max(MinVFforArea, r_\beta)}{d_\beta}$$

$$A_2 = A_{1\max} \frac{\max\left(\left(1 - r_\beta\right), MinVFforArea\right)}{\left(1 - MaxVFforArea\right)}$$

$$B = Blend\ Factor = -2$$

$$MinVFforArea = 1 \times 10^{-8}$$

$$MaxVFforArea = 0.8$$

$$A_{1\max} = \frac{6 \times MaxVFforArea}{d_\beta}$$

As an example, for a bubble diameter of 1mm, Figure 41 shows how this new expression modifies the relationship between vapour volume fraction and interphase area density.

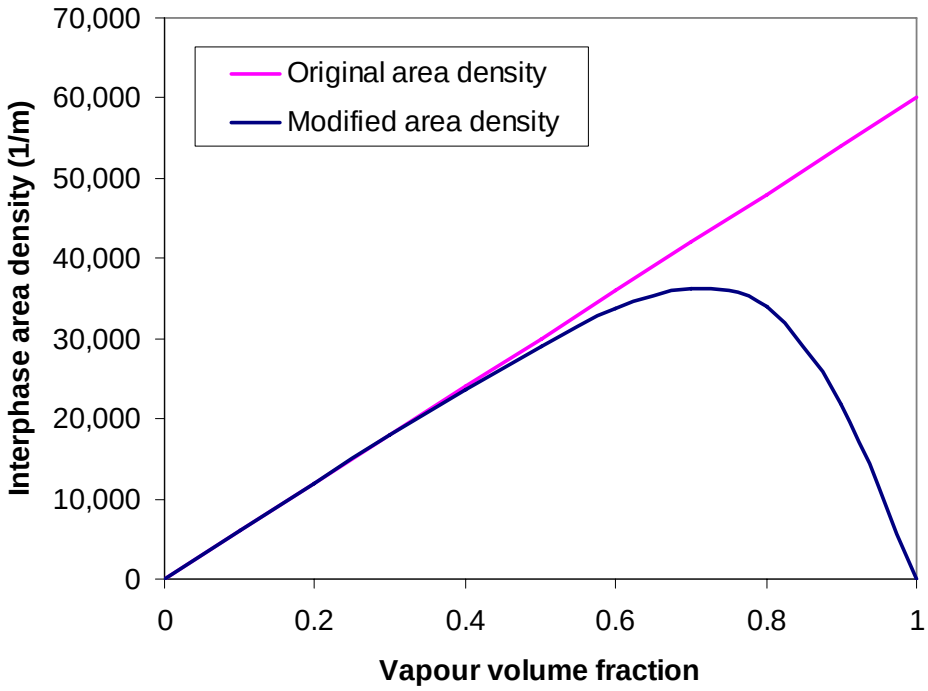


**Figure 41: Relationship between vapour volume fraction and interphase area density using modified expression for area density**

#### 2.4.2.5 Turbulence modelling in the vapour phase

For the vapour bubbles, the "Dispersed Phase Zero Equation" model is used. In this case the Eddy Viscosity hypothesis is maintained and the turbulent viscosity of the dispersed phase $\mu_{td}$ is related to that of the continuous phase as follows:

$\mu_{td} = \frac{\rho_d}{\rho_c}\frac{\mu_{tc}}{\sigma}$, where $\sigma$ is a turbulent Prandtl number.

According the ANSYS CFX literature [35], "in situations where the particle relaxation time is short compared to turbulence dissipation time scales, you may safely use the default value $\sigma = 1$". In addition, for liquid vapour combinations where $\rho_d << \rho_c$, the turbulence viscosity of the vapour phase tends to zero and the flow in the vapour phase can be assumed to be laminar.

#### 2.4.2.6 Summary of recent results using Eulerian-Eulerian approach

Various combinations of some of the submodels above have been attempted by a large number of researchers. Some of the more interesting and relevant findings are described below.

The first researchers to attempt to validate the RPI method were Kurul et al [49] and Anglart [50]. Initially, they both used the original RPI implementation based on a Stanton number correlation for convective heat flux. This had a number of drawbacks,

not least that it led to mesh dependent results. A number of improvements were subsequently implemented (some of which are outlined in section 2.4.2.2) as other researchers continued to validate this approach against a various experimental results. Krepper in particular has undertaken quite a lot of relevant research in this area using various versions of the CFX software [52,74]. In the first of these two papers, he validates his boiling models against Bartolemei's results [75] for water boiling in straight, vertical pipes (with a typical length and diameter of 2m and 15mm respectively). This is of particular interest here as many of the modelling techniques described in his paper are later adopted by ANSYS CFX as its "standard" boiling model (see section 3.2.1.4). Whilst he shows relatively good agreement for predictions of average void fractions along the pipe as well as vapour concentrations near the wall, the model over-predicts vapour production when compared with experiments using higher heat fluxes and mass flow rates (although trends are correct). He concludes that the model (and correlations it is based on) is most appropriate for pressures from 1.5 to 5MPa, heat fluxes in the order of ~1MW/m$^2$ and mass fluxes of about 1000kg/m$^2$.s, with the model showing significant inaccuracies at low pressure. He strongly recommends switching to mechanistic boiling submodels (e.g. force balance method for calculating bubble departure diameter). Since HyperVapotrons tend to operate at higher heat fluxes and lower pressures, these conclusions and recommendations will need to be taken seriously if an accurate HV solution is to be found.

These conclusions are echoed in a number of other papers (e.g. Zeitoun and Shoukri's [46] and Tu and Yeoh [76]) where it is also stated that empirical models developed for high pressure applications may not be valid at low pressures[21]. It is suggested that the substantially different vapour structures at low and high pressures mean the importance of the individual heat transfer mechanisms also varies significantly (Tu and Yeoh, for instance, show that heat transfer at the wall due to quenching, commonly not accounted for in high-pressure subcooled boiling models, is significant at low pressures because of the larger departing bubbles).

Tu and Yeoh, along with a number of other researchers [52,53, 72], also gives careful consideration to the submodel used for bubble departure diameter and its influence on overall results. By and large, of the correlations available at the time, Unal's correlation is shown to give the best agreement with experiment (see section 2.4.2.3.1).

One of the more surprising results is produced in 1993 by Lai and Farouk [77]. Before the wall partitioning method became one of the more popular methods for modelling wall boiling, these researchers built a boiling model which simply relied on inlet seeding and interfacial heat transfer to generate vapour in the flow[22]. Validation of their simplified model against results for vertical pipes and rectangular ducts seemed to show that this

---

[21] High pressure typically indicates in the region of 30bar and low pressure ~1bar.

[22] One of the reasons for this simplification is that the authors claim that no adequate models for the quenching heat flux component. Whilst this statement is neither confirmed nor denied here, it is certainly true that the Del Valle quenching correlation used in many of the other models "contains a large number of experimentally measured parameters".

model could be as accurate as the full wall partitioning model used by most of the other researchers quoted here [48,52,53,48,71,74,76,72]. Unfortunately, when this type of approach was attempted here, the accuracy compared to experiment was poor (see section 3.2.1.3). As a result, focus was primarily on the wall partitioning methods.

# 3

# 3 Model Validation

The first step in any study such as this is validation of the numerical models. Without it, it is very difficult to have any confidence in the results, conclusions or design recommendations [78]. Unfortunately, there is little experimental data available for the HyperVapotron that can be directly compared to the results of a CFD model. In fact, useful experimental data is limited to thermocouple measurements in the solid walls which provides only indirect validation of the heat transfer processes within the fluid.

If, however, the models are reduced to predicting only one of the two aspects of the HyperVapotron problem, namely single phase flow in a driven cavity or subcooled nucleate boiling, there is significant experimental data available in the literature that can be used to validate the modelling strategies. The first part of this chapter is therefore concerned with identifying the most appropriate grid resolution, near wall treatment and turbulence model for modelling single phase flow and heat transfer within a driven cavity [79]. The 2nd half of the chapter then focuses on validating the multiphase, boiling aspects of the model via comparison with experimental results for vertical tubes.

It is assumed that the combination of the choices dictated by these independent validation exercises will yield the most appropriate model for the HyperVapotron, where accurate predictions of the flow within the cavity and the quantity of vapour produced are both essential to the model's success.

## 3.1 Single phase cavity flows

### 3.1.1 Grid resolution and near wall treatment for a RANS solution

As with most numerical methods, it is advisable to carry out grid sensitivity studies at an early stage to establish what resolution is required to ensure the results are "grid

independent". To reduce the number of geometries and simulations required, a relevant configuration was selected and modelled as illustrated in Table 6.

These settings seemed a natural choice as the geometry[23] and Reynolds number are close to those found in the majority of HyperVapotrons installed on the JET machine and this particular turbulence model was recommended by ANSYS CFX for applications where flow separation and recirculation is expected.

| | |
|---|---|
| Geometry: | A single 8x3mm cavity |
| Reynolds number: | 12,000 (based on water at 20$^{o}$C, an inlet velocity of 4m/s and cavity width of 3mm) |
| Turbulence model: | SST k-omega |
| Near wall treatment: | Automatic (see section 2.3.3 for definition of this treatment) |
| Advection scheme: | High Resolution (see section 2.2.1 for definition of this scheme) |

**Table 6: Case chosen for grid sensitivity study**

The study involved systematically refining a uniform hexahedral grid from a cell size of 250μm down to 4μm (the 1$^{st}$ step in this process is illustrated in Figure 42). It was found that this had a dramatic affect on the steady flow pattern established in the cavity (see Figure 43 and Figure 44). Using total heat removed around the cavity as the integral quantity for assessing grid convergence, it was found that the grid must be refined such that the first cell near the wall is no larger than ~8μm (equivalent to a non dimensional near wall distance $y^+$ of less than ~2.5 throughout the cavity). The resulting flow pattern for the grid independent solution is shown in Figure 44.

This gives a strong indication that even with the automatic near wall treatment as described in section 2.3.3.2, the laminar sublayer of the boundary layer must still be resolved for the ANSYS CFX code to accurately capture the flow physics and heat transfer within the cavity.

[23] The choice of a relatively deep cavity (i.e. 8mm) is important as it will be shown that the flow pattern and subsequent thermal performance for this geometry is particularly sensitive to grid resolution and near wall treatment (due to multiple vortices anticipated in the cavity). For shallower cavities (e.g. 4mm deep) this becomes less critical as experiments suggest only a single large recirculation occurs.

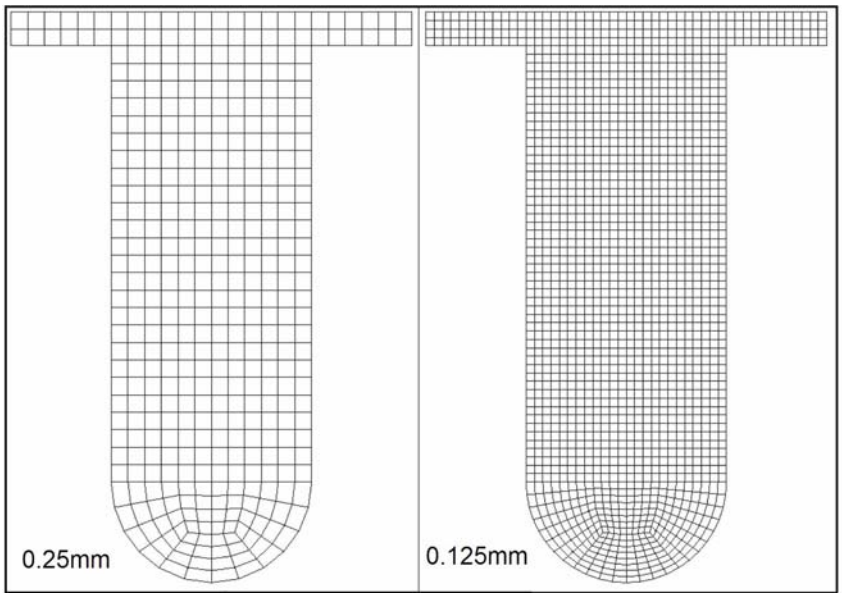


**Figure 42: Example of mesh refinement as part of grid sensitivity study**

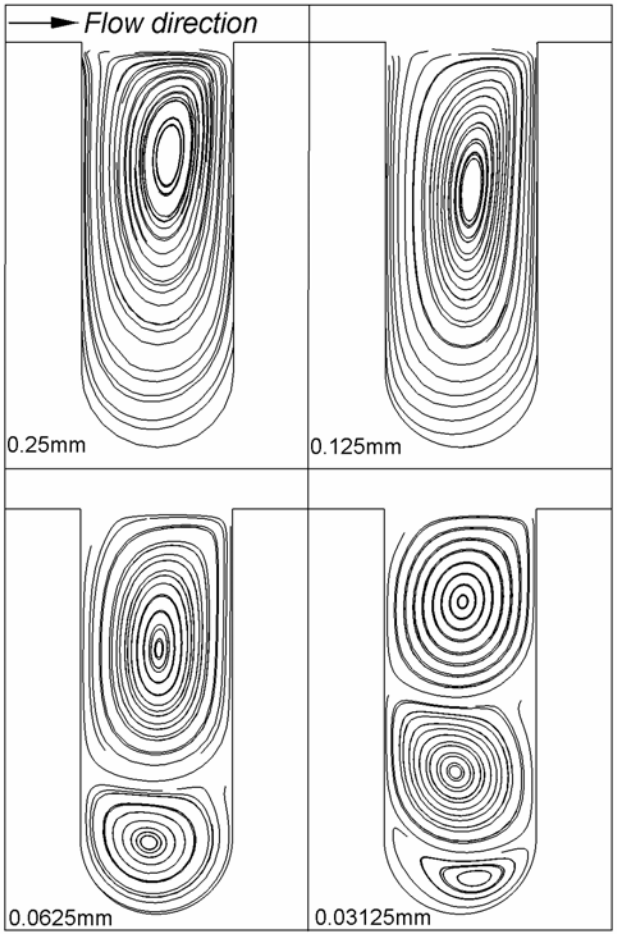


**Figure 43: Steady state flow pattern at each grid resolution**

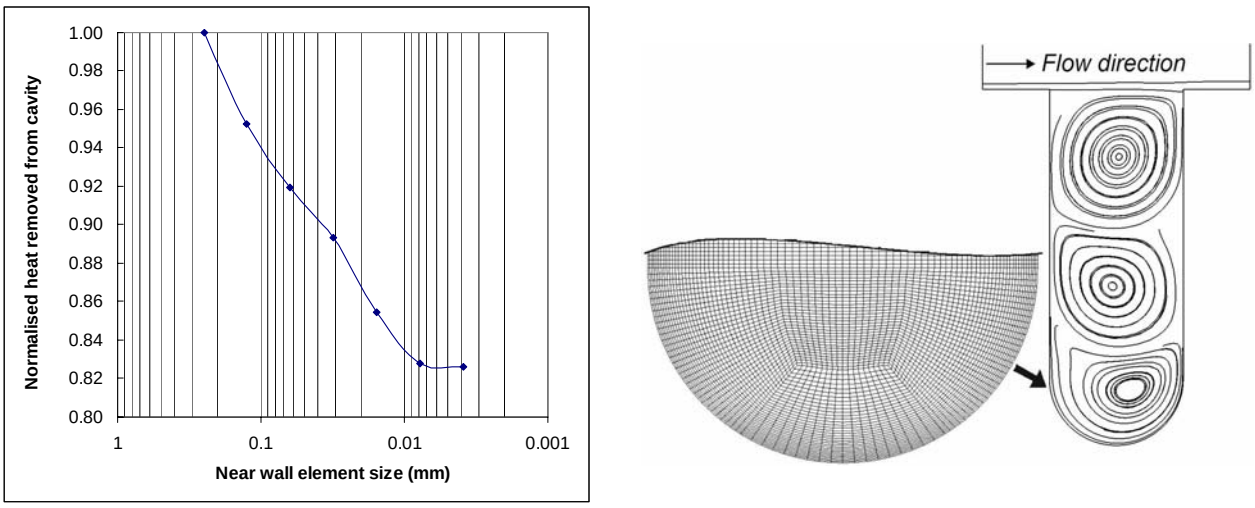


**Figure 44: Achievement of grid independence and resultant grid resolution and steady-state cavity flow pattern**

Having established the required boundary layer resolution required by ANSYS CFX for predicting the vortex patterns within cavities such as these, various turbulence models were examined and compared to experiment [80,81] to check the accuracy of the solutions. Unfortunately, flow visualisation or heat transfer data for cavities with identical aspect ratios was not available. However, the experiments selected have similar Reynolds numbers and do show a tendency for vortex separation and generation of secondary vortices which would appear to be a likely feature of the flow within deeper HyperVapotron cavities. The ability of a CFD model to predict these features gives a strong indication on their potential accuracy in predicting HyperVapotron flow (and heat transfer).

Yamamoto et al [80] performed flow visualisation and heat transfer measurements on air flowing over cavities with aspect ratios ranging from 0.04 up to 1 at Reynolds numbers between 4,000 and 50,000 (where aspect ratio is defined as depth D divided by width W). Some qualitative validation could therefore be attempted by applying the k-epsilon, SST k-omega and BSL Re-Stress turbulence models [35] on identical grids and comparing streamlines to the photographs of the smoke flow. It can be seen in Figure 45 that the SST and BSL models, both of which allow for a low-Re near wall formulation in areas of appropriate grid resolution, give relatively accurate representations of both the primary and secondary recirculation zones. The k-epsilon model, however, uses scalable wall functions to bridge the near wall laminar sublayer and fails to predict flow separation or reattachment at any point within the cavity with the result that it incorrectly predicts a single cavity vortex.

For a more quantitative comparison, Metzger et al [81] performed heat transfer measurements along the bottom of a cavity where the aspect ratio was varied from 0.1 to 0.5. Since flow patterns were not available, the predicted variation of Nusselt number (non-dimensional HTC) along the bottom of the cavity was compared with experiment (in this case Nu = C.h/k, where C = channel depth above the cavity (5.08mm), h = local

heat transfer coefficient and k = thermal conductivity of the fluid). The results for the D/W = 0.2 cavity are shown in Figure 46 and show that the SST model again gives best agreement, with disagreement only really evident for X/W < 0.3 (where X is the distance along the cavity bottom measured from the upstream corner). Again, both the SST and BSL turbulence models give best results, each picking up the peak HTC at the upstream edge of the cavity bottom due to reattachment of the separated flow at this position. It is interesting to note whilst both use the same near wall treatment, the SST model performs better in the central section of the cavity while the BSL model significantly under predicts the heat transfer in this region.

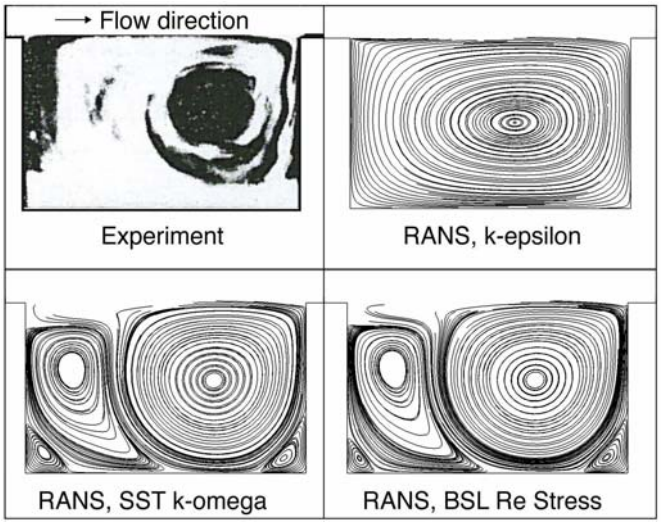


**Figure 45: Validation against Yamamoto experiment [80]**

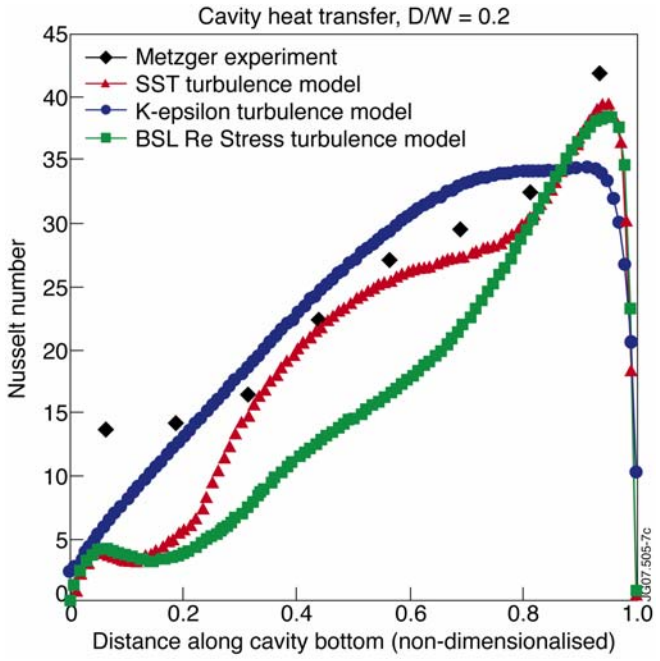


**Figure 46: Validation against Metzger experiment (D/W = 10.16/50.8mm)**

Although initial and inlet boundary conditions were not available in either case, it seems reasonable to make the qualitative conclusion that the ANSYS CFX k-epsilon model, with its associated scalable wall functions, is not appropriate for examining flow and heat transfer in a driven cavity (particularly where multiple vortices are expected). It would appear that the SST k-omega model most accurately calculates bulk flow patterns and boundary layer flows and therefore resultant heat transfer within the cavity. As a result, this model, used on a suitably refined grid, has been adopted as the standard approach for the majority of the solutions of HyperVapotron cavities presented here.

### 3.1.2 Lid driven cavity, RANS vs ILES

In parallel with this RANS approach, Z Malick [43] performed a study using an in-house code developed at Cranfield University, HIRECOM, where Implicit Large Eddy Simulation (ILES) methods were used to examine the single phase flow and heat transfer within driven cavities. HIRECOM, uses a finite volume artificial compressibility solver (or alternatively a pressure projection method in its more recent version), with inviscid fluxes approximated using the characteristics-based method [82,83,84,85] combined with the third order variables reconstruction [82,83]. Viscous fluxes were computed using the second order central approximation. The integration in pseudo-time for the artificial compressibility formulation was performed using the fourth-order Runge-Kutta method [82,83].

A good case against which to validate both RANS and ILES methods is the lid-driven cavity case. Here uncertainty of both initial and boundary conditions is minimised and detailed experimental data is available. In particular, Prasad et al [86] provided extensive data on such a case. The experimental set up is shown in Figure 47. Unfortunately, while experimental data was available for the turbulent fluctuations, this was insufficient to make a calculation of experimental turbulent kinetic energy and therefore allow a comparison with the RANS prediction of this quantity.

To enable a fair comparison, the grids used in both RANS and ILES solutions are identical, with grid resolution set at a level that was judged “acceptable” when comparing the higher order ILES solutions with the experimental results. This turned out to be a grid of 64×64×64 = 262,144 cells, with near wall resolution increased such that the first near wall cell is ~0.7mm wide (equivalent to a $y^+$ at the lid of ~2.5). The resultant grid is shown in Figure 48. Comparison of various RANS solutions as well as the high order ILES solution with experiment are shown in Figure 50 and Figure 51 (at cavity Reynolds numbers of 3,200 and 10,000 respectively).

In all RANS solutions, the following settings were maintained:

1. Domain type: 3D
2. Solution type: Steady State
3. Element type: Hexahedral
4. Near wall mesh size: 0.7mm

5. Moving Wall BC: Constant velocity
6. Stationary Wall BC: No slip
7. Reference pressure: 1bar
8. Heat transfer: Isothermal (25$^{o}$C)
9. Turbulence Numerics: First Order
10. Advection Scheme: High Resolution

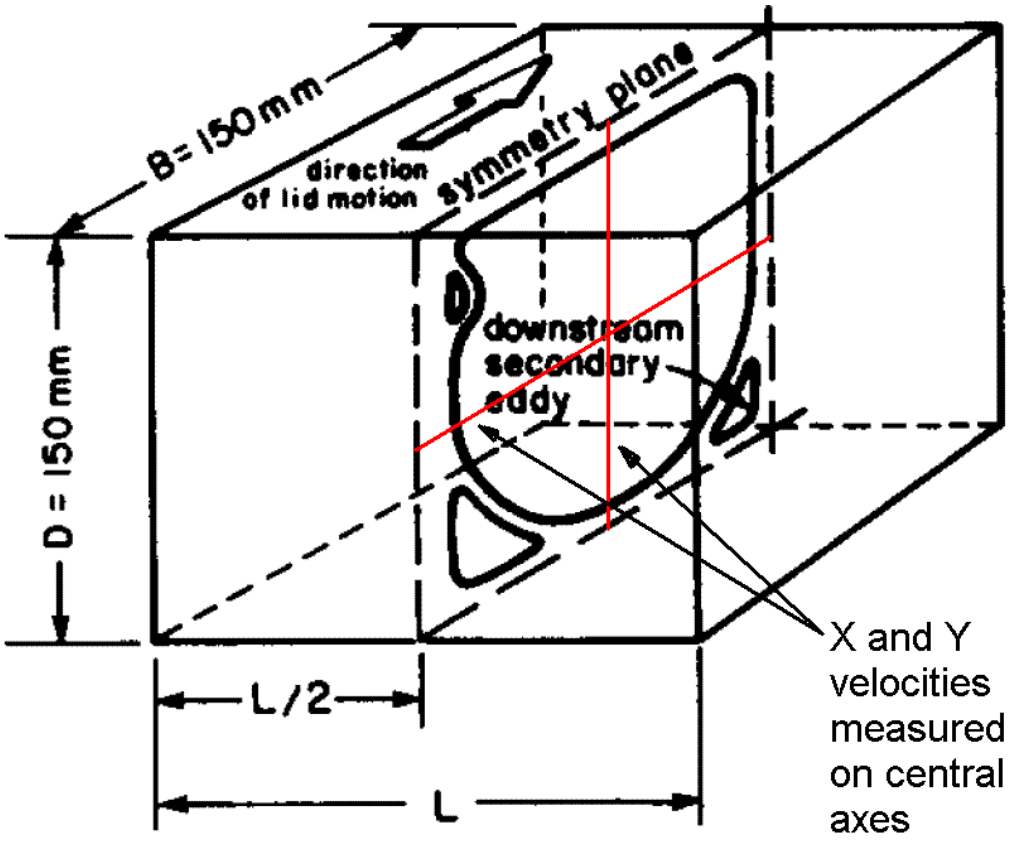


**Figure 47: Lid driven cavity examined by Prasad et al [86]**

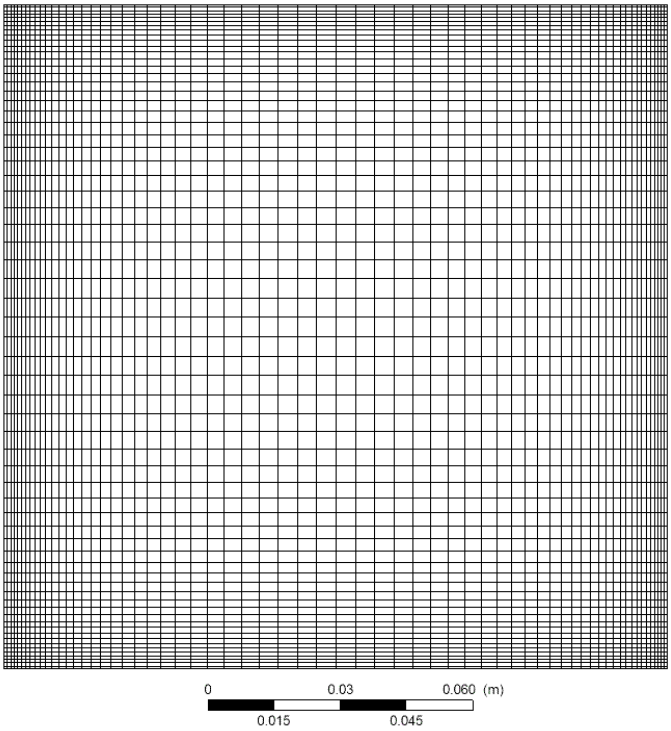


**Figure 48: 64x64x64 grid used in both RANS and ILES cases**

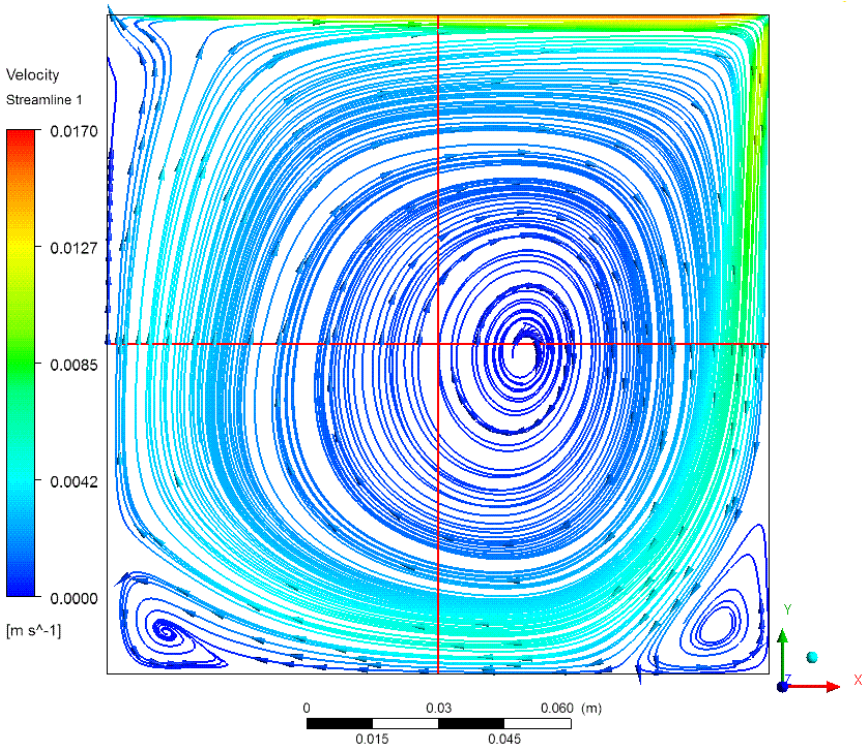


**Figure 49: Streamlines predicted by the RANS SST model for the Prasad Lid Driven Cavity**

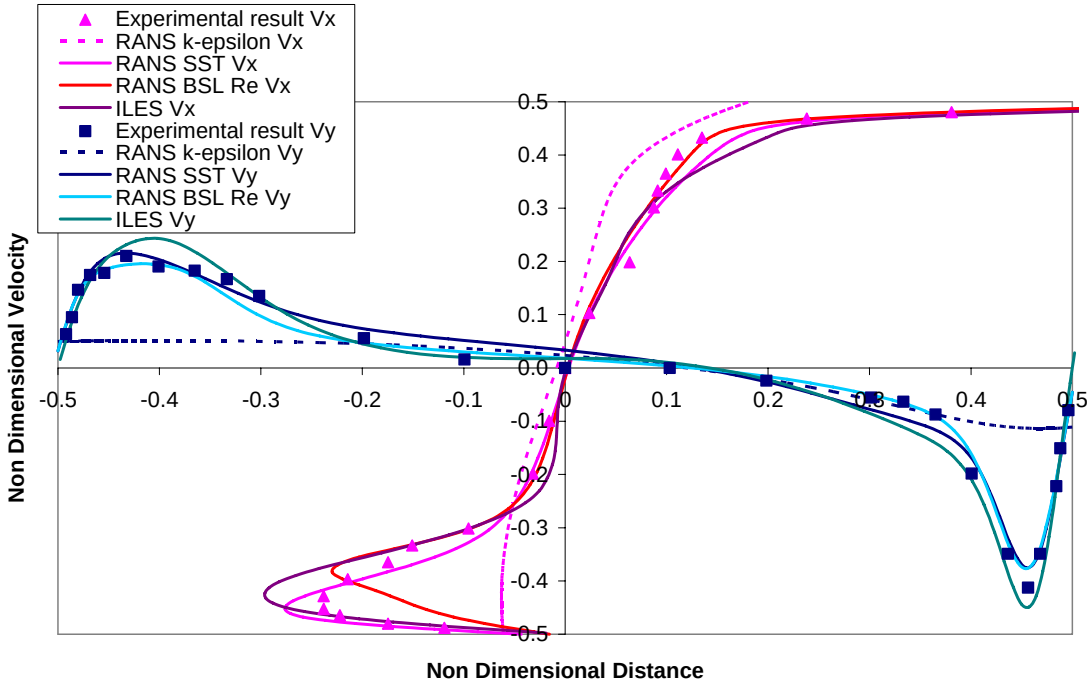


**Figure 50: Comparison of RANS and ILES methods with lid driven cavity data, Re = 3,200**

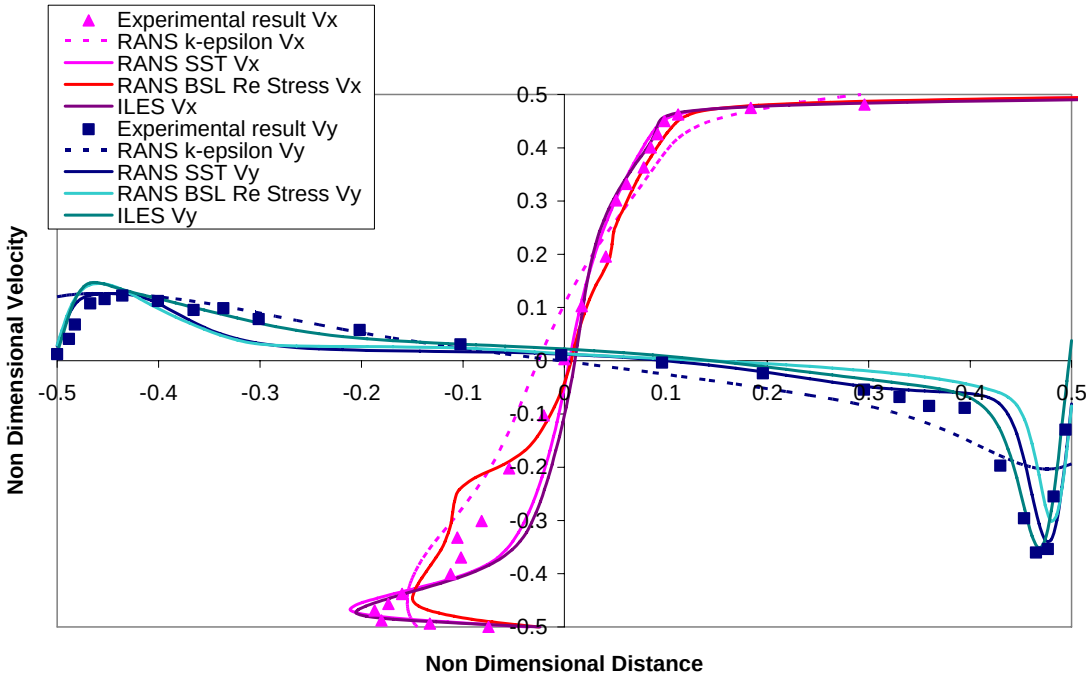


**Figure 51: Comparison of RANS and ILES methods with lid driven cavity data, Re = 10,000**

During this exercise, it was found that:

- Convergence of the RANS solutions becomes more difficult at higher Reynolds number and when using the BSL Re Stress turbulence model.
- Again, the k-epsilon model (with scalable wall functions) completely fails to accurately predict the velocity profiles; in particular it has a tendency to "flatten out" the large gradients near the wall (which is likely to have a strong effect on heat transfer predictions for these types of driven cavity).
- The SST and BSL Re Stress turbulence models do reasonably well in both cases, giving comparable accuracy to the ILES solution (at least for the averaged quantities shown here). It should be noted that the ILES solution also gave excellent agreement for the turbulence components which, for a CFD code, is considerably more challenging (as explained above, turbulence quantities could not be verified for the RANS solutions).
- Accuracy of the BSL Re Stress model falls off slightly at the higher Reynolds number and doesn't seem to be pick up the velocity gradients near the lower wall as well as the SST model.
- Unlike for the HyperVapotron like cavity, it appears that comparable accuracy for averaged velocity can be achieved between certain RANS solutions and ILES without the penalty of finer grid resolution.

This is further evidence that the SST k-omega turbulence model is most appropriate for this study. The most likely explanation for its superior performance is that it uses the more accurate k-omega model to capture near wall effects that lead to flow separation and secondary vortices in the cavities but then switches to a k-epsilon model away from the wall which is better at predicting the turbulent transport of mass, momentum and energy in the free flow.

## 3.2 Boiling Heat Transfer

### 3.2.1 Boiling in vertical tubes

In order to examine the performance of the various boiling models presented here, two sets of experimental data have been selected. As in many of the references listed in section 2.4.2.6, validation is performed against vertical tube experiments where either axial or radial measurements for vapour volume fraction have been measured. In this case, experimental results derived by Bartolemei et al [75] and Lee et al [87] have been used (see Figure 52 and Figure 53). Whilst some of the boiling models presented here have already been validated using this data [48,52,77], the author believed it necessary to include these cases for completeness and to ensure the up-to-date version of the software was still performing in the manner reported in the original analyses (particularly since the developers confirmed non-trivial changes in the algorithm between current and previous versions of the code).

The details of the geometry and material properties are shown in Table 7 and Table 8. In order to make a fair comparison between the wall boiling models, the settings in the bulk of the flow as well as the grid sizes should be maintained the same throughout. These are illustrated in Table 9 and Figure 54 respectively.

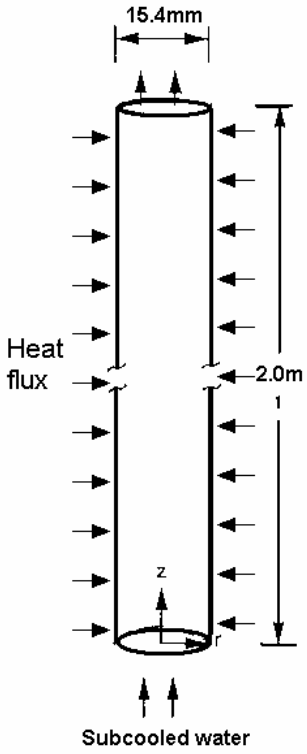


**Figure 52: Bartolemei et al experimental set up [75]**

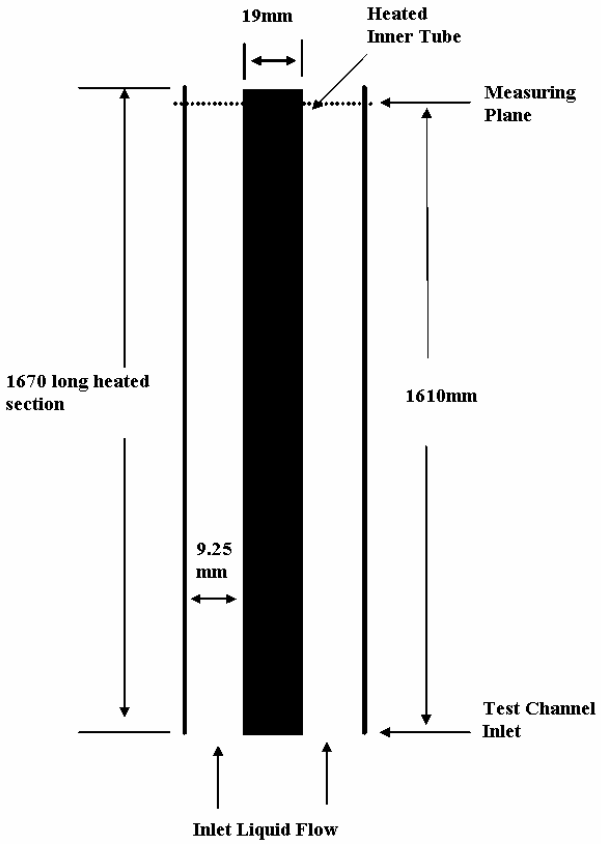


**Figure 53: Lee et al experimental set up [87]**

| **Geometry and boundary conditions** | | **Material Properties** | | |
|---|---|---|---|---|
| **Pipe height** | 2m | | **Vapour** | **Liquid** |
| **Pipe radius** | 0.0077m | **Density** | 7.35 kg/m$^3$ | 868 kg/m$^3$ |
| **Inlet Pressure** | 1.5 MPa | **Enthalpy** | 2.79E+06 J/kg | 8.38E+05 J/kg |
| **Saturation temperature** | 200$^o$C | **Specific Heat** | 2,790 J/kg.$^o$C | 4,480 J/kg.$^o$C |
| | | **Dynamic Viscosity** | 15.656 Pa.s | 135.54 Pa.s |
| | | **Thermal Conductivity** | 0.0363 W/m.$^o$C | 0.667 W/m.$^o$C |

**Table 7: Bartolemei case used to validate boiling models**

| Geometry and boundary conditions | | Material Properties | | |
|---|---|---|---|---|
| **Pipe height** | 1.61m | | **Vapour** | **Liquid** |
| **Annulus outer radius** | 0.01875m | **Density** | 0.8195 kg/m$^3$ | 958 kg/m$^3$ |
| **Annulus inner radius** | 0.0095m | **Enthalpy** | 2.69E+06 J/kg | 4.60E+05 J/kg |
| **Inlet Pressure** | 0.142 MPa | **Specific Heat** | 2.12E+03 J/kg.$^o$C | 4.23E+03 J/kg.$^o$C |
| **Saturation temperature** | 109.3$^o$C | **Dynamic Viscosity** | 12.6 Pa.s | 255 Pa.s |
| | | **Thermal Conductivity** | 0.0262 W/m.$^o$C | 0.682 W/m.$^o$C |

**Table 8: Lee case used to validate boiling models**

| Submodel | Setting |
|---|---|
| Liquid Turbulence model | SST |
| Vapour Turbulence model[24] | Dispersed phase zero equation |
| Vapour heat transfer model[24] | Thermal Energy |
| Inlet turbulence | Turbulent intensity = 5% |
| Inlet vapour volume fraction | 1e-15 |
| Wall influence on vapour flow | Free slip |
| Bubble Diameter in the bulk | Varies from 0.15 to 2mm, Anglart and Nylund model [88] |
| Buoyancy[24] | Included |
| Drag Force[24] | Included, Schiller Naumann model [35] |
| Lift Force[24] | Not included |
| Virtual Mass Force[24] | Not included |
| Wall lubrication Force[24] | Included, Antal model [35] |
| Turbulent Dispersion Force[24] | Included, Favre model [35] |
| Turbulence transfer model[24] | Included, Sato Enhanced Eddy Visc model [35] |
| Advection scheme | Upwind |
| General - Residual target | 1e-5 (RMS) |
| Vapour mass – Residual target | 1e-3 (RMS) |

**Table 9: Settings used throughout boiling model validation exercise**

[24] These settings are clearly not relevant to the equilibrium, single phase model

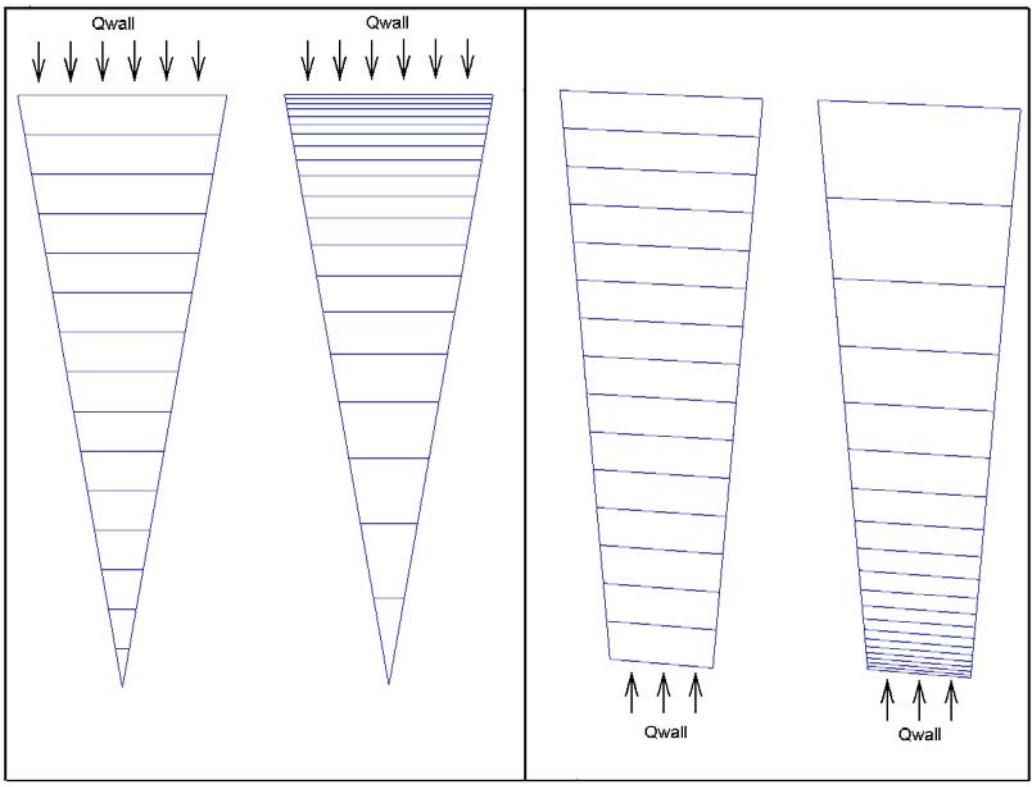


**Figure 54: Grids used to model Bartolemei and Lee cases**

#### 3.2.1.1 Results

A comparison of the 3 boiling models examined against the two sets of experiments are shown in the figures below[25]. Discussion on the relative merits of each approach can be found in sections 3.2.1.2 to 3.2.1.4.

[25] To facilitate a comparison of the vapour volume fraction contours, the domains have been stretched in the radial direction

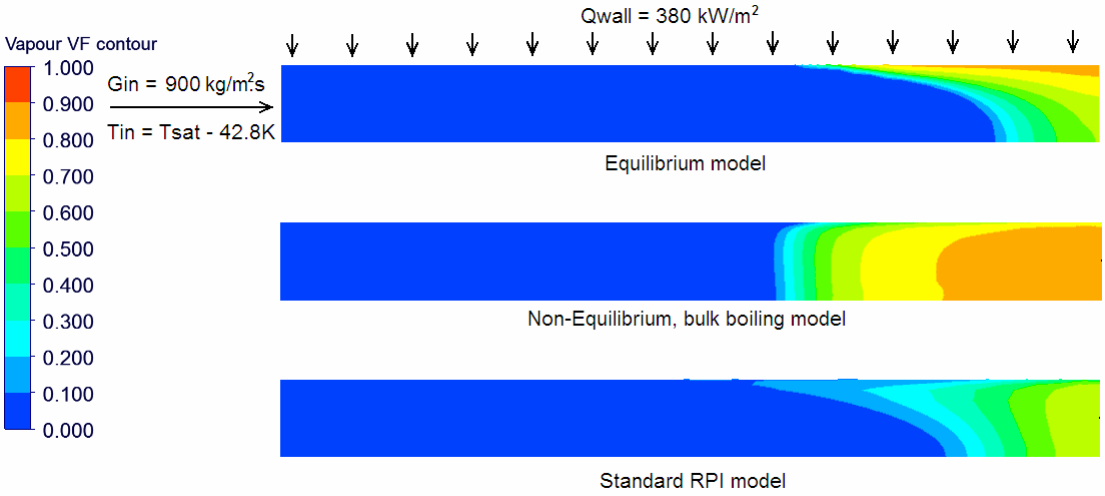


**Figure 55: Vapour volume fraction contour plots for 3 boiling models, Bartolemei experiment (coarse grid, typical $y^+$ ~ 100). Contours stretched in the cross-steam direction**

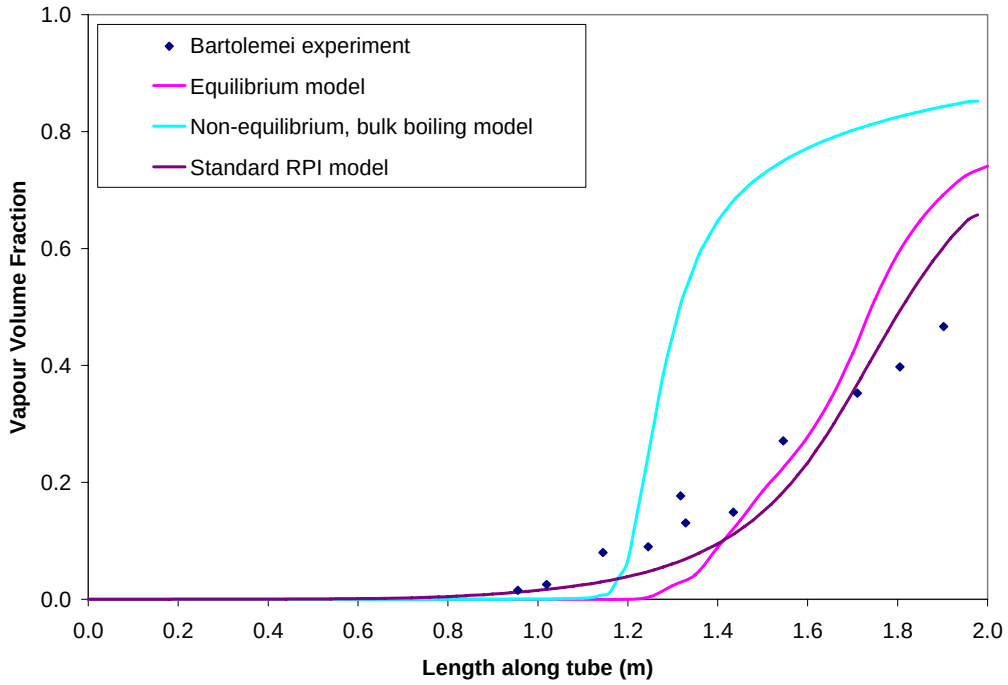


**Figure 56: Comparison of 3 boiling models with Bartolemei experiment (coarse grid, typical $y^+$ ~ 100)**

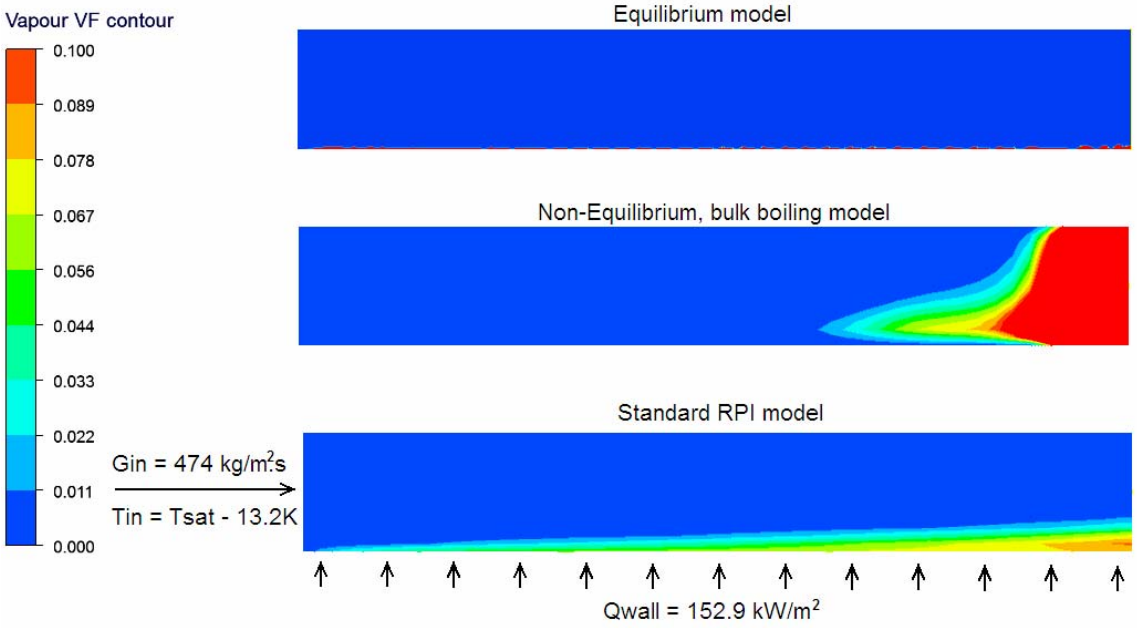


**Figure 57: Vapour volume fraction contour plots for 3 boiling models, Lee experiment (coarse grid, typical $y^+$ ~ 70). Contours stretched in the cross-steam direction**

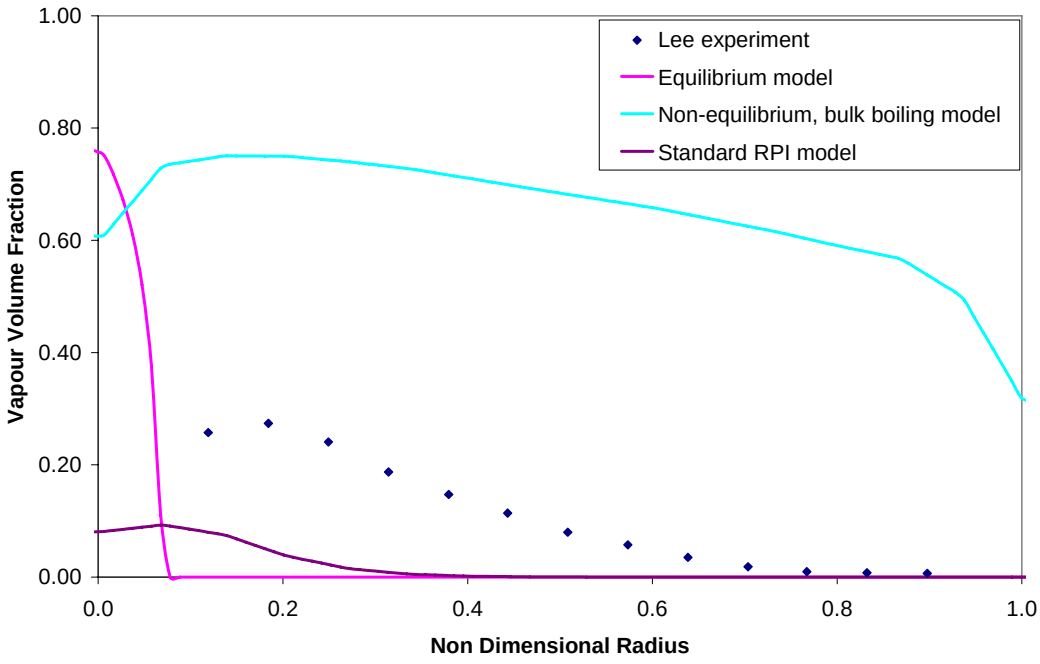


**Figure 58: Comparison of 3 boiling models with Lee experiment (coarse grids, typical $y^+$ ~ 70)**

### 3.2.1.2 Model 1: Equilibrium multi-component model

As stated in section 2.1.2.1, the fluid in these models is a single phase, homogeneous liquid-vapour binary mixture, where local enthalpy is used to determine the relative mass

fraction of each component (liquid or vapour). Since vapour and liquid must share the same velocity (only one set of momentum equations are solved) and heat and mass transfer are assumed to take place instantaneously, these models are most appropriate for very small, dispersed bubbles in a continuous liquid. Since the limitations were not quantified, a study was performed here to see how accurate this approach could be for the two experimental cases listed above.

What is somewhat surprising (given the model's simplicity) is that, in some cases, this approach provides a relatively accurate prediction of both the onset of vapour production and subsequent development of total vapour production within the tube (see Figure 56). It should be highlighted that these results are highly mesh dependent as the model relies on a calculation of local enthalpy to determine the mass fraction of vapour. This variable is "averaged" over a particular cell and will therefore depend on the size cell and position. This is evident as the finer mesh model[26] predicts vapour production at a slightly earlier stage in the tube (see Figure 59). That said, even the coarse mesh appears to capture with reasonable accuracy the development of vapour production along the tube.

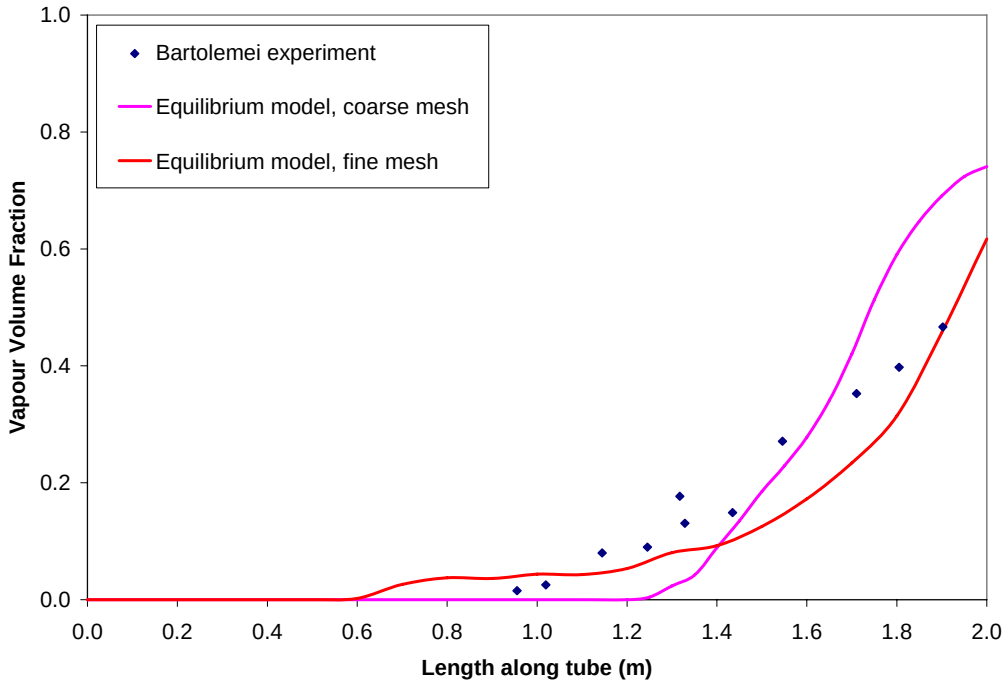


**Figure 59: Comparison of equilibrium model with coarse and fine grids**

Whilst it appears that the equilibrium model works relatively well at predicting cross-sectional average values of vapour along the tube, what is not clear is how accurately the radial variation of vapour is predicted (Bartolemei's experiments did not measure this).

[26] A fully converged solution for the fine grid was not achieved so this result serves as a qualitative comparison only.

This is important as radial variation can be considered a good test of the model's capability to account for interphase mass, momentum and heat transfer as the combination of the effects is ultimately what determines how the vapour at the wall is transported through the flow.

To examine these effects, the experiments performed by Lee et al [87] are used, where radial variation of void fraction is measured at the end of two concentric tubes with boiling occurring on the inner wall (see Figure 53).

It becomes quite obvious from Figure 57 and Figure 58 that the equilibrium model is unable to predict this variation. The vapour volume fraction is over-predicted at the wall while no vapour is predicted beyond a non-dimensional radius of ~ 0.14. It is suggested here that the size and number of bubbles in this case result in significant bubble-bubble interaction as well as other forces (besides drag) on the bubbles, often acting perpendicular to the relative bubble motion (e.g. lift). This model clearly cannot take into these effects and this is one of the reasons why it fails to predict the radial variation.

In addition, since the equilibrium model requires the heat flux at the wall to first pass to the liquid (to superheat it) before vapour can be created, this model cannot take account of the enhancement to wall heat transfer that occurs when boiling begins. This is critical in this study as it is precisely the enhancement in heat transfer due to boiling that the HyperVapotrons rely on to achieve their superior performance. Once these deficiencies were identified, this approach was no longer pursued in the modelling strategy.

#### 3.2.1.3 Model 2: Non-Equilibrium, bulk boiling model

Having abandoned the equilibrium approach, how does the simplest multiphase approach fair? As described in section 2.4.2.2, the principle behind this approach is to set a relatively high value for the quantity "Minimum Volume Fraction for Area"[27].

Unfortunately, it is clear from Figure 56 and Figure 58 that this model too simplistic and, because it is not based on any attempt to calculate a "realistic" quantity of vapour generated at the walls, fails to accurately predict the onset of boiling, the development of average vapour volume fraction along the tube or the radial variation measured in Lee's experiment (even the equilibrium model, with all its assumptions, gets considerably closer to Bartolemei's measurement of average vapour volume fraction along the tube).

This main problem with this approach is that the amount of vapour created is highly dependent on the choice of the seeding value MinVFforArea. The choice here of 1e-3 is arbitrary and has been chosen such that significant vapour production begins somewhere close to the correct position along the tube. However, had half this value been chosen (i.e. 5e-4), this curve would simply be shifted downstream by ~20% (see Figure 60).

In both cases, vapour production only occurs at wall superheats in excess of 60 or 70K. It is widely known that in reality, incipient boiling occurs when the wall exceeds the saturation temperature by only a few degrees. Theoretically, this could be improved: if the near wall grid size was refined sufficiently, the near wall cell temperature would

[27] In this case a value of 1e-3 was selected by trial and error.

approach the solid wall temperature and incipient boiling would occur much closer to the point where Twall > Tsat. However, additional convergence difficulties combined with the flaws identified mean this approach was also abandoned.

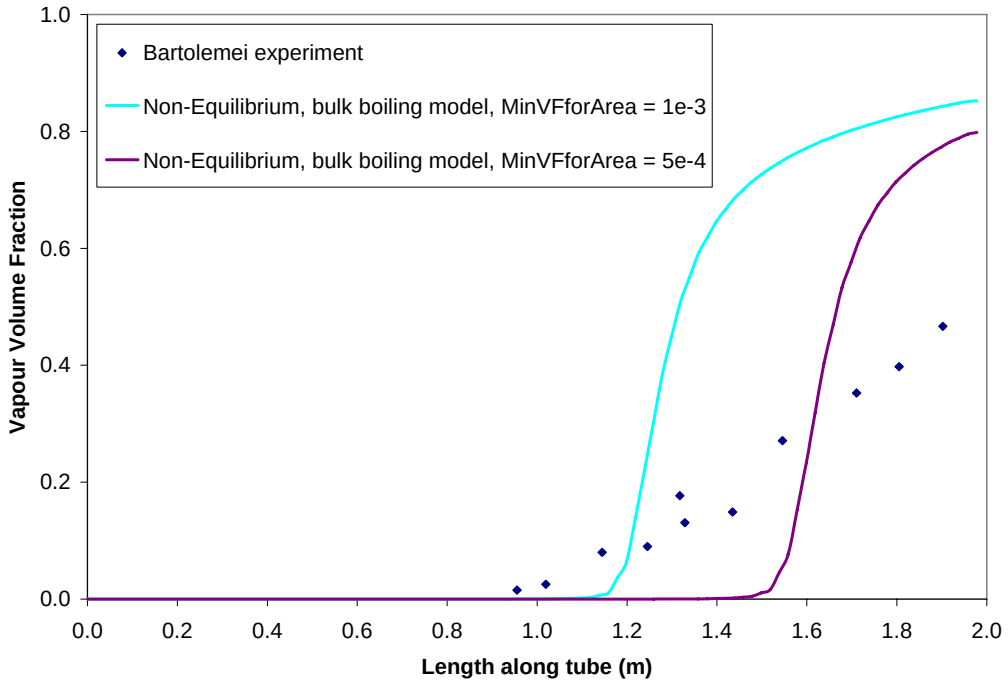


**Figure 60: Effect of MinVFforArea on Non-Equilibrium, bulk boiling model**

### 3.2.1.4 Model 3: Standard RPI model

The RPI approach is described in section 2.4.2.2. As indicated in section 2.4.2.3, there are a great number of boiling submodels that can be used in conjunction with this approach. In this instance, the choice of submodels as illustrated in Table 10 will be hence forth referred to as the "Standard" RPI model[28].

[28] In actuality, these are the submodels built into the ANSYS CFX v12 boiling model and therefore used as the defaults in this codes application of the RPI methodology.

| Submodel / Parameter | Option / Value | Comments |
|---|---|---|
| Bubble Diameter Influence Factor | 2.0 | Same philosophy as Kurul and Podowski [49] where the diameter of influence of a nucleating bubble is assumed to be twice the bubble departure diameter. |
| Max Area Fraction of Bubble Influence | 0.95 | The default value for this parameter is actually 0.5 but consultation with the ANSYS CFX developers found this to be an error (indeed, for high levels of nucleation, values closer to 100% are much more reasonable) |
| Fixed $y^+$ for Liquid Subcooling | 250 | The single phase convective heat transfer to the liquid phase is modelled using the turbulent wall function and this fixed value of $y^+$. |
| Bubble Departure Diameter | Tolubinski Kostanchuk | See section 2.4.2.3.1. |
| Wall Nucleation Site Density | Lemmert Chawla | See section 2.4.2.3.3. |
| Bubble Detachment Frequency, f | Cole | See section 2.4.2.3.2. |
| Bubble Waiting Time | 0.8 / f | Same philosophy as Kurul and Podowski [49] where the bubble waiting time is assumed to be 80% of the bubble detachment period. |
| Liquid Quenching Heat Transfer Coefficient | Del Valle Kenning | See section 2.4.2.2. |

**Table 10: Boiling submodels for the Standard RPI model**

As before, the suitability of this approach is assessed via comparison with the Bartolemei and Lee results as illustrated in Figure 55 and Figure 58. It can be seen that like the Equilibrium Model, the Standard RPI model is capable of accurately predicting the onset of nucleate boiling and the subsequent increase of the average void fraction along the tube. Unlike the Equilibrium and bulk boiling models, however, it also gives relatively sensible results for the radial variation as measured by Lee. In particular it shows a peak void fraction away from the wall and a smooth drop off in void fraction away from this point. Unfortunately, even this most sophisticated approach under-predicts the peak void fraction by >60%, suggesting some improvements can still be made[29]. Specifically it appears that for a given wall heat flux; the boiling model should be producing more vapour at the wall and that this vapour must then be allowed to extend further across the

[29] This significant inaccuracy was surprising given that virtually all the default settings in the ANSYS CFX v12 RPI boiling model were identical to those used by researchers such as Krepper, Yeoh and Lee who reported much better agreement in cases such as these. Indeed, the beta version of the RPI model available in ANSYS CFX v11 did give excellent agreement with the Lee experiments. This difference in performance between v11 and v12 was highlighted to the ANSYS developers but, in these limited timescales, they were unable to find the discrepancy in the code to explain this. The strategy therefore has been to ignore the interim successes of the v11 beta model and focus on customising and improving the model available in ANSYS CFX v12.

tube before condensing back into liquid. The customisation process employed to incorporate both these effects is illustrated in section 3.2.1.5.

### 3.2.1.5 Model 4: Customised RPI model

Customisation in this case primarily involves tuning of the submodels on which the RPI approach is based. Section 2.4.1 described a number of alternatives for the 3 key submodels, namely Bubble Departure Diameter, Bubble Departure Frequency and Nucleation Site Density. Focussing on the Lee results, the initial approach involved systematic substitution of each alternative into the Standard Model to examine its influence on the solution. The results are shown in Figure 61 to Figure 63. Unfortunately, very few have a positive influence on the peak amount of vapour produced. In fact only the simplified Kolev expression for bubble departure diameter (where diameter is set as a function of wall superheat based on Kolev's collated experimental results) actually results in an increase in vapour production, and even this is somewhat short of the experimental value.

In addition to the alternative models, scaling of the default models was also attempted to gauge the importance of each parameter in the overall production of vapour. Specifically, the default models for bubble departure diameter, bubble departure frequency and nucleation site density were each multiplied by a factor of 2 to see how much additional vapour would be produced (see Tolubinski x 2, Cole x2 and Lemmert x2 in the relevant figures). This simple exercise seemed to indicate that the most effective way of increasing the quantity of vapour produced was to increase the bubble departure diameter.

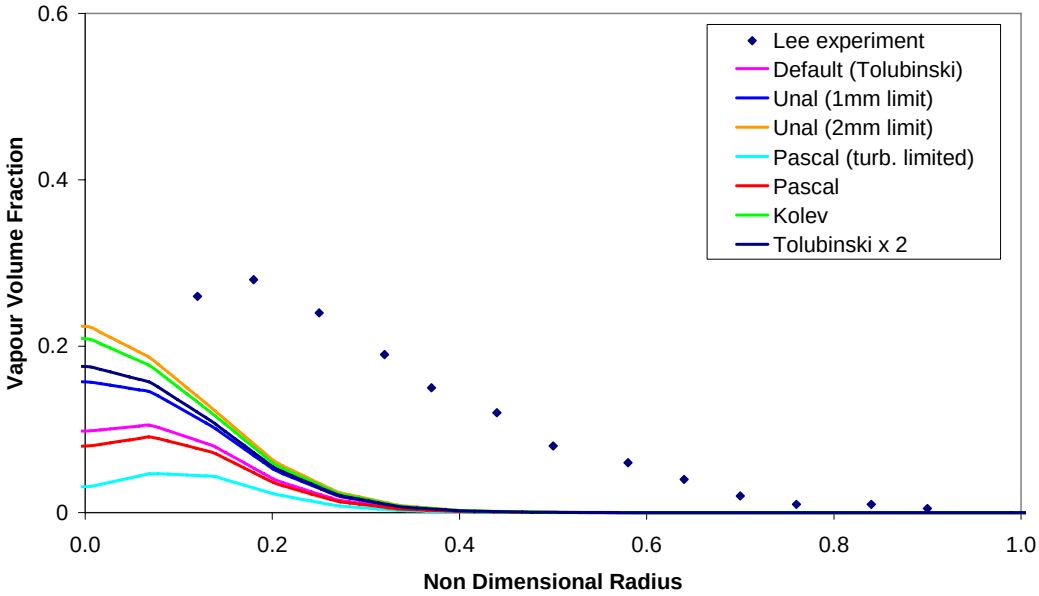


**Figure 61: Effect of alternative models for bubble departure diameter**

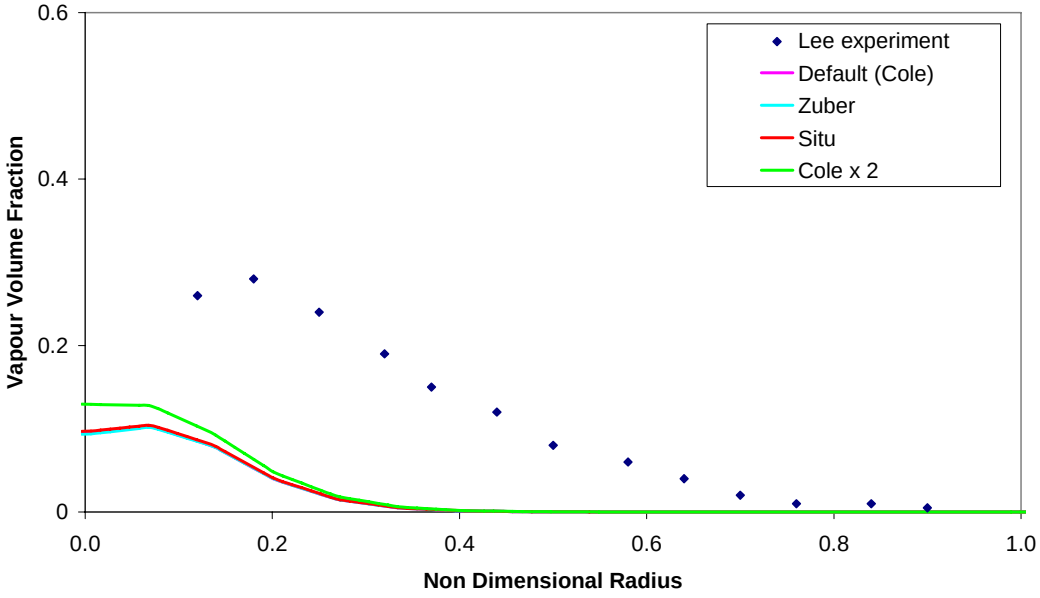


**Figure 62: Effect of alternative models for bubble departure frequency**

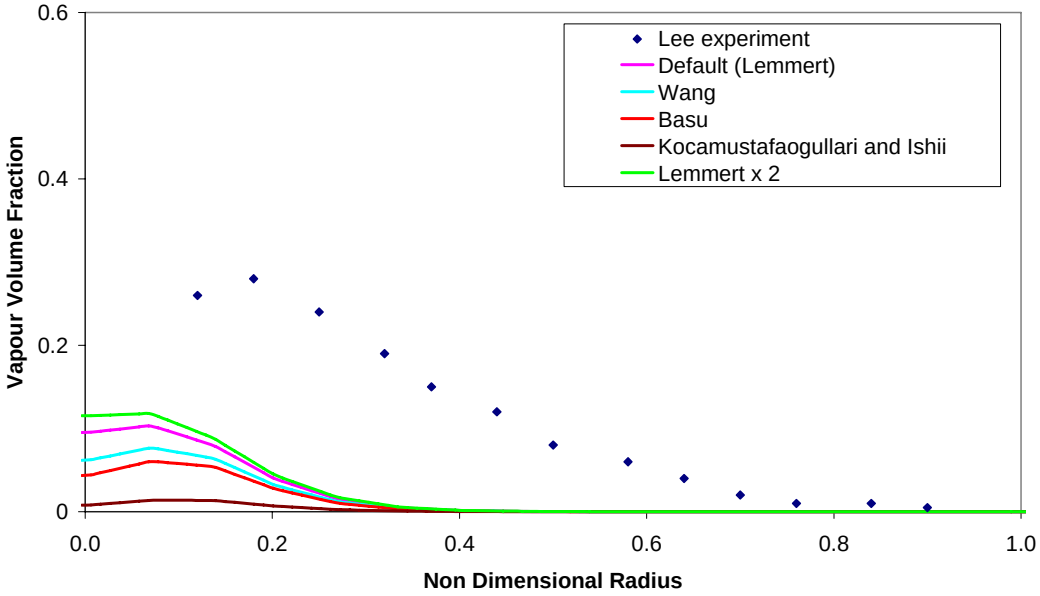


**Figure 63: Effect of alternative models for nucleation site density**

At this stage, it was decided to modify multiple settings (in a logical manner) in an attempt to get closer to the experimental data. Based on the findings above, the first conclusion was that the vapour was condensing too fast away from the wall. Even with

the Kolev correlation for bubble departure diameter, where a significant peak near the wall was predicted, this still falls to zero a lot quicker than experimental values. One way to reduce this effect is to reduce the amount of heat (and therefore mass) transferred from the vapour back to the liquid phase. This can be done in a number of ways but here it was decided to reduce the interphase heat transfer by fixing the interphase Nusselt number at a value of 2. This was found to significantly improve agreement with experiment but the peak vapour volume fraction was still not in the correct location. In this case, trials showed that the wall lubrication force was critical. A number of alternative correlations are available within ANSYS CFX for calculating this force [35] but, in the end, it was found that the derivation offered by Frank et al [89] gave best agreement (as shown in Figure 64). This model is not described in detail here and the reader is invited to consult the ANSYS Help Manuals [35] and the references therein for more details.

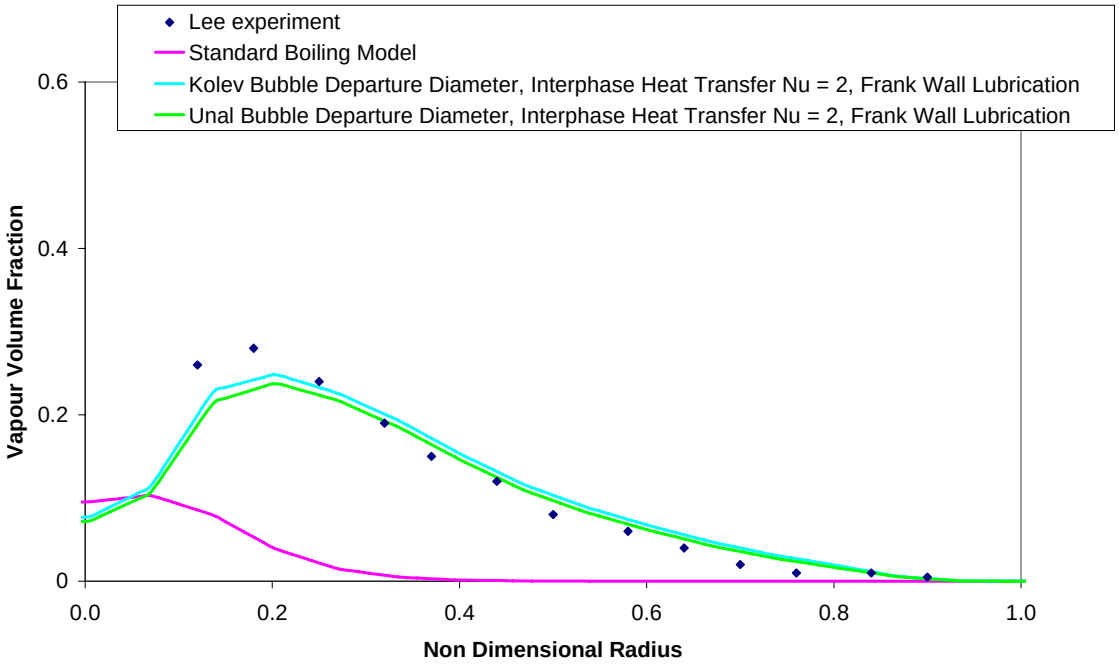


**Figure 64: Improvement in boiling model modifying bubble departure diameter, interphase heat transfer correlation and wall lubrication correlation**

To examine whether these settings gave good agreement at a range of boundary conditions, a second data set generated by Lee was also examined. The key differences between the two experiments are highlighted in Table 11. It can be seen from Figure 65 that although the customised model does predict an increase of vapour at for the 2$^{nd}$ data set, this is now well short of the experiment. This is improved by reducing the interphase heat transfer still further to a value of 1 but at a compromise to accuracy for the first experiment (see Figure 66). Whilst this problem has not been completely resolved here, it is still reasonable to suggest that interphase heat transfer coefficients predicted by the Ranz Marshall correlation seem high and that in reality interphase Nusselt numbers are

likely to be in the range 1 to 2. It should be noted that this uncertainty may not be critical to the success of this study if it makes little difference to wall temperature predictions and overall performance of the device.

| | Experiment 1 | Experiment 2 |
|---|---|---|
| Inlet Subcooling (K) | 13.2 | 21.3 |
| Inlet Mass Flux (kg/m$^2$.s) | 474 | 718.8 |
| Inlet Velocity (m/s) | 0.495 | 0.75 |
| Wall Heat Flux (kW/m$^2$) | 152.9 | 320.4 |

**Table 11: Differences between two Lee experimental data sets**

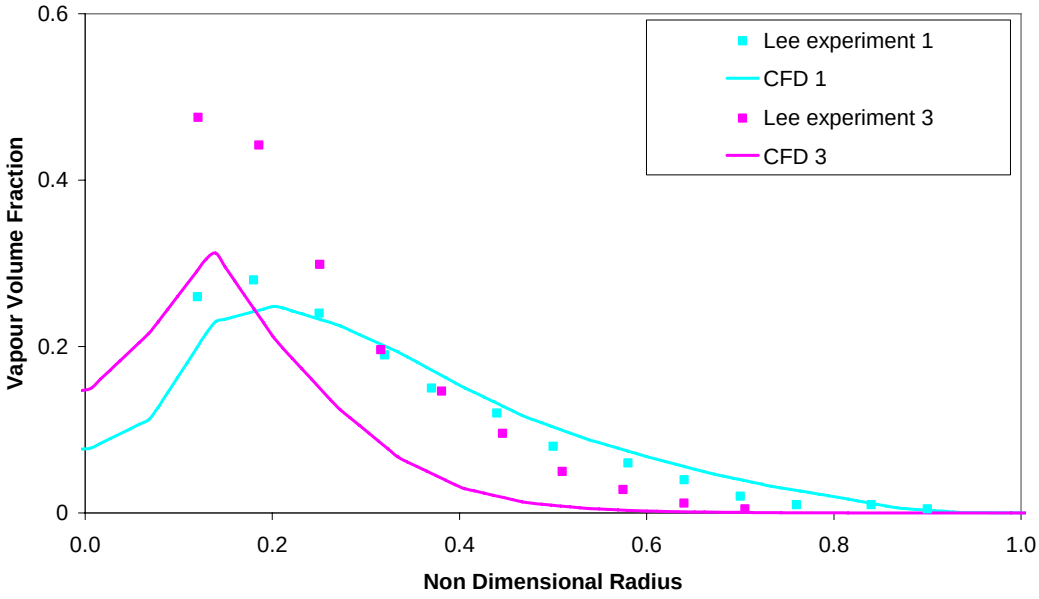


**Figure 65: Comparison of customised model with two sets of experimental data (Nu = 2.0)**

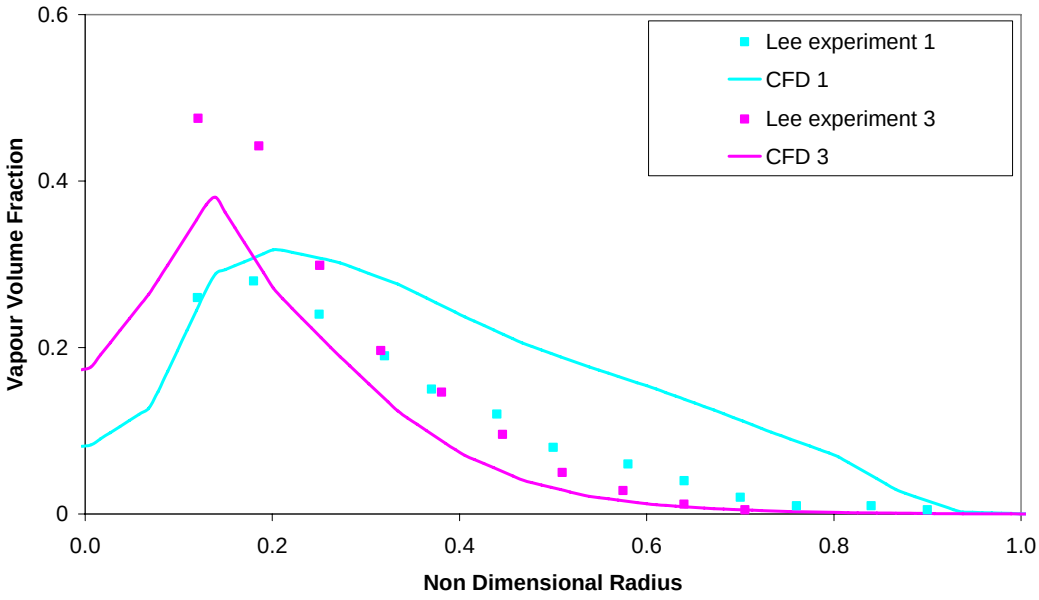


**Figure 66: Comparison of customised model with two sets of experimental data (Nu = 1.0)**

### 3.2.2 Model selection for Hypervapotron application

Section 3.2 has examined the accuracy of various approaches for incorporating boiling heat transfer into a CFD model. Whilst the geometry is not particularly relevant to the study of HyperVapotrons, it has been possible to use the results from vertical tube experiments to focus down on a subset of boiling models by eliminating those which are unable to capture the basic physics involved or the subsequent overall performance. In particular:

1. Preliminary validation of the models against Bartolemei's experiments showed that the Non-Equilibrium, bulk boiling model is too simplistic and should not be considered for this study.
2. Validation against Lee's experiments showed the inadequacy of single phase equilibrium approach.
3. Lee experiments also demonstrated that the RPI multiphase boiling model is most appropriate but that this needs some level of tuning to get a level of accuracy acceptable for this engineering study.

One of the surprising results during the customisation exercise was that few of the alternative correlations for the boiling submodels had a noticeable effect on the overall model's output. There are three good reasons, however, why these should not be abandoned at this point:

1. Looking in more detail at the boundary conditions selected by Lee, it was found that these just happened to induce similar outputs for some of the alternative correlations as those generated by the default set up. In other cases where boundary conditions can be quite different (e.g. the HyperVapotron application where wall superheating can be significantly higher), choice of alternative models may indeed impact the overall performance (in fact this is shown to be the case in section 5.3).
2. Even though alternative correlations show little influence on vapour distribution in the bulk domain, the corresponding total heat flux at the wall may actually be quite different. Given that the only experimental variable measured was vapour volume fraction, this effect could not be verified here.
3. Some of the default correlations in the ANSYS CFX RPI model are empirical and outdated. Even if substitution by more recent, more appropriate mechanistic models show little influence in these experiments, these should still be considered as they may well yield a wider range of applicability.

Finally, it is worth noting that it is not trivial to derive and implement "grid-independent" versions of some of the alternative expressions for the boiling sub-models. As a result, care must be taken not to draw any incorrect conclusions that may simply be down to the grid-dependence of a particular sub-model.

Therefore, the key conclusions gained in this section that will be of use in an engineering model of the HyperVapotron device (see chapter 5) are as follows:

- The general approach will be based on use and customisation of the Standard RPI boiling model.
- Initially, customisation should consider incorporating Kolev's correlation for bubble departure diameter and reduced interphase heat transfer as these modifications have been shown to improve the accuracy of the model in the vertical tube experiments.
- Alternative expressions for boiling submodels should also be considered if accuracy is still not acceptable. In particular these should try to single out models based on mechanistic approaches (e.g Unal's expression for bubble departure diameter) or those which have been shown to be an improvement to the RPI defaults (e.g. Situ's correlation for bubble departure frequency).
- Grid-dependent submodels should be avoided if possible. If not possible, studies should be carried out to ensure this does not incorrectly affect any conclusions.

# 4

# 4 Numerical modelling aspects of single phase HyperVapotron flows

With the lessons learnt in Chapter 3, the next step is to assess the accuracy of the RANS approach for geometry and boundary conditions specific to the HyperVapotron (single phase only at this stage). The strategy here is to use the results produced by high order ILES solutions as a virtual experiment. The ILES set-up has been extensively validated [43] and can give highly detailed information at any point in the flow to compare with the RANS equivalent (unlike experimental data which is often limited to only a few locations and can contain significant uncertainty). Comparisons are therefore made between the RANS and ILES solutions for velocity and turbulence distribution along axes within the flow as well as transient thermal performance in the solid. The results in most cases are surprisingly good, particularly in light of the significant differences in complexity between the two approaches.

To help guide the geometrical study in Chapter 5, the 2$^{nd}$ part of the chapter then explores the influence of cavity aspect ratio on overall performance (assessed using total heat flux removed at the wall as the indicator). This reveals a number of useful conclusions and likely trends carried forward to the full scale engineering model of the HyperVapotron.

## 4.1 RANS vs ILES

In Section 3.1, the optimum modelling choices were described for a RANS approach to single phase cavity flow (including grid resolution, near wall treatment, turbulence models etc). This was based on validation against results derived both experimentally and using high resolution, implicit LES methods. Having established best practice methods for this type of problem, attention could now be turned to modelling of the single phase fluid flow through the internal channels of a HyperVapotron device. In this

case, given the lack of useable experimental data, validation of the RANS solutions can only be performed against equivalent ILES results.

Before describing the results of this study, it is worth examining the "typical" HyperVapotorn cavity geometry. It can be seen in section 1.2.2 that these are generally "closed" cavities with aspect ratios that will tend to inhibit the flow in the main channel from penetrating a large proportion of the cavity. The interaction between cavity and channel is generally confined to the turbulent shear layer caused by the separation of the boundary layer at the upstream corner of the cavity. For these types of system, Rossiter [90] developed the following semi-empirical relation for predicting the instability frequencies associated with the boundary layer separation (as illustrated in Figure 11):

$$Str = \frac{fL}{U} = \frac{n - \gamma}{M + 1/k},$$

where $f$ is the frequency, $L$ is the cavity length, $U$ is the channel velocity, $n$ is the mode number and $k$ and $\gamma$ are constants of 0.57 and 0.25 respectively.

For a HyperVapotron cavity with a typical flow velocity of 4m/s and cavity length of 3mm, this would suggest a frequency for the first mode of this instability of ~570Hz[30]. It would clearly be interesting to note whether URANS methods are capable of predicting this unsteadiness.

With this in mind, a 2D URANS method was initially compared to the full 3D ILES solution. In both cases, 3 cavities were modelled with periodic boundary conditions in the streamwise direction to represent the hundred or so cavities typically present within a HyperVapotron device. In the ILES case, periodicity was also added in the out-of-plane direction to enable the 3D turbulent structures to be captured. A qualitative comparison of the flow structures is shown in Figure 67. It can be seen that, although multiple vortices are predicted by both models, the RANS solution fails to capture fails to capture the Rossiter instability described above. In fact, it was found that, for all timesteps and grid resolutions examined, transient, periodic 2D RANS solutions always settle down to a stabilised flow virtually identical to that achieved from a steady-state solution for a single cavity without periodic boundaries (this is evident when comparing the transient snap shot shown in Figure 67 with the steady state results shown in Figure 44).

The 2D URANS model was subsequently extruded in the third dimension to create an identical 3D model as used in the ILES solution. Again, identical grids and boundary conditions were applied but the turbulence structures predicted by the ILES[31] solution were still not captured by the RANS model. It would appear therefore that, if side walls are ignored, the averaging intrinsic to the SST turbulence model means a steady state, 2D RANS model of a single cavity with inlet / outlet boundary conditions is just as accurate

[30] This assumes a value of 1,482m/s for the speed of sound in water

[31] Unfortunately, insufficient data was supplied to enable an accurate comparison of the frequency of the ILES instability with that predicted by Rossiter's correlation.

as a transient, 3D model of multiple cavities with periodic boundary conditions. This is a useful result for subsequent investigations as solution times for the former will clearly be very much shorter than for the latter (enabling conclusions to be reliably extracted much more efficiently, see section 4.2).

It should be acknowledged here that the periodic 3D models do not actually represent the real HyperVapotron geometry. What these represent is a HyperVapotron channel with quasi-infinite width, ignoring the effects of the channel side walls. The use of periodic boundary conditions in the third dimension was primarily used as a simple method to construct a 3D ILES model to verify that it could pick up 3D turbulent structures. It will be shown in chapter 5 that modelling the side walls is actually of particular importance to this problem, particularly given nearly all HyperVapotrons in existence have longitudinal slots near the side walls which clearly induce a highly 3-dimensional aspect to the flow (see section 1.2.2). It is the necessity of capturing these effects that ultimately drive the requirement of a 3-dimensional model of this device, not the attempt to capture additional turbulence effects (which the RANS model fails to do in this case).

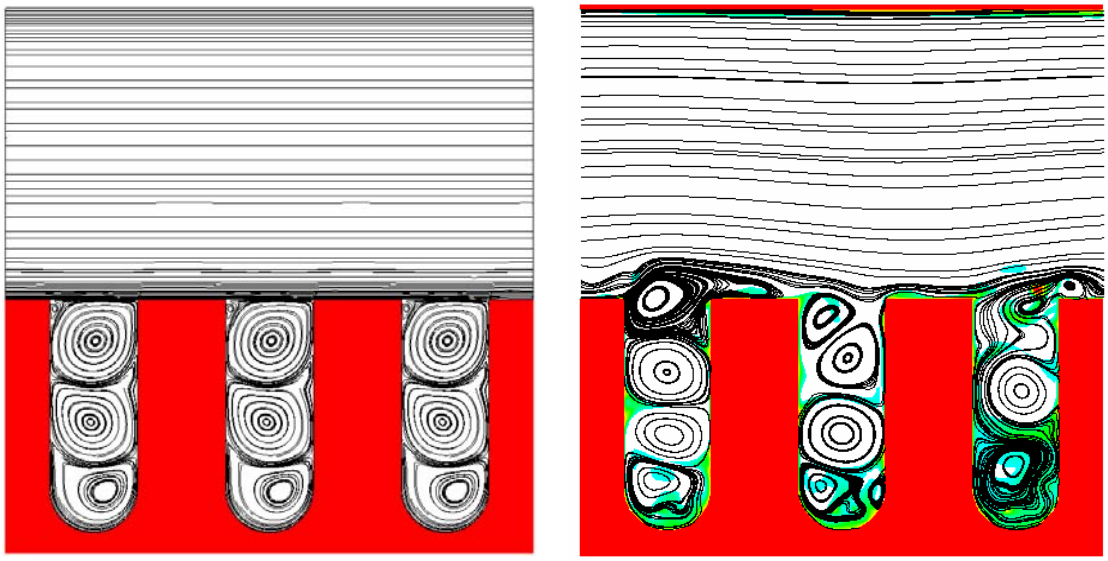

**Figure 67: Periodic HyperVapotron cavities, RANS (stabilized) vs ILES (snapshot) [43]**

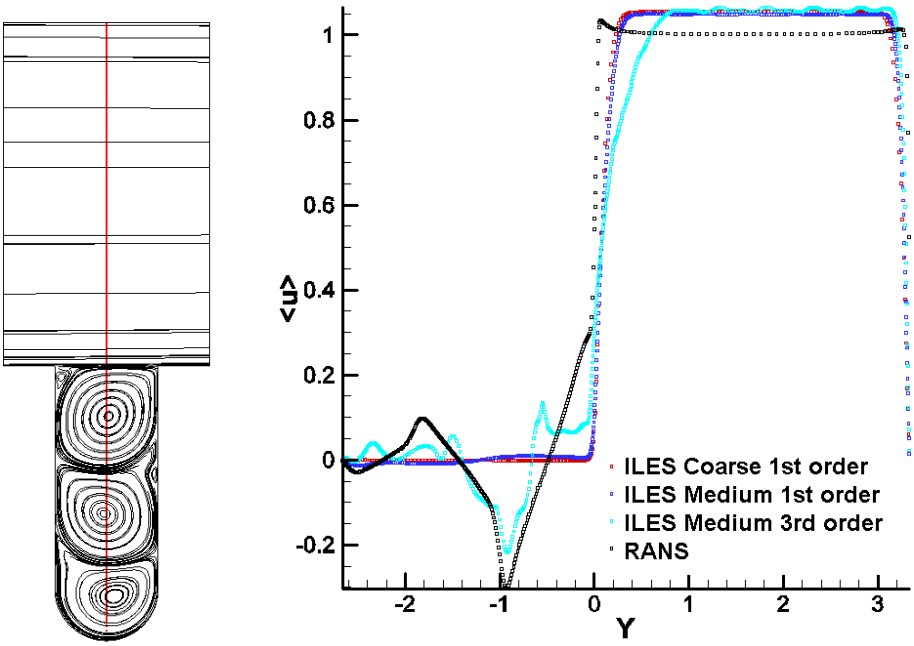


**Figure 68: Comparison of Velocity U along vertical axis [43]**

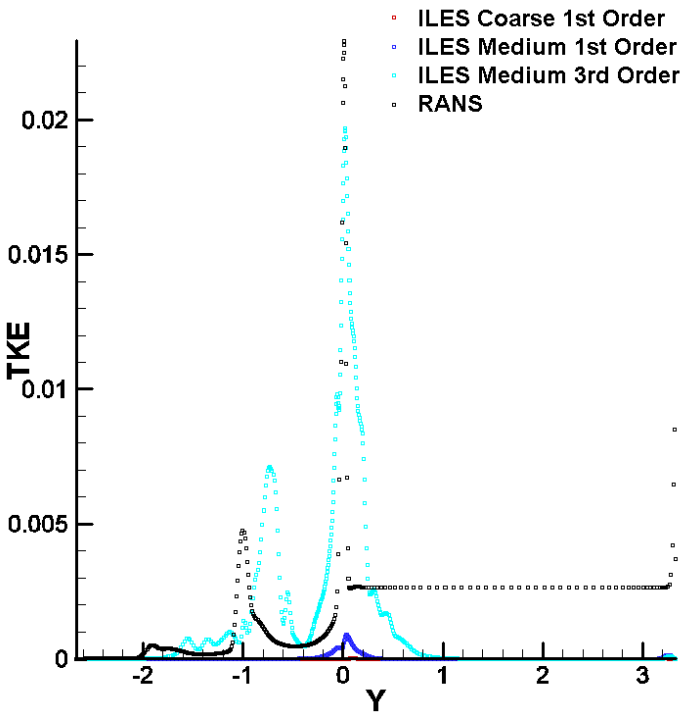


**Figure 69: Comparison of kinetic energy along vertical axis [43]**

The key question here is whether the RANS model's failure to predict the detailed fluctuations shown by the ILES solution is critical to its heat transfer predictions. In other words, are RANS turbulence models capable of capturing with sufficient accuracy the transfer of heat from the cavity (as ultimately it is heat transfer performance of the HyperVapotron device that is of interest in this study)?

To assess this, thermal solutions for the RANS and ILES solutions must be compared. To do this, a CHT model is constructed in both cases. The solid domain is then set at some elevated reference temperature at t = 0s, then allowed to cool due to the convective cooling at the fluid/solid interface[32]. The temperature contours in the solid domain at various times are shown Figure 70. A number of turbulence models are tested in this manner, namely no turbulence model, the k-epsilon and SST turbulence models; Figure 71 shows the flow patterns predicted. Ultimately, for a quantitative comparison of performance, the cooldown curves are plotted in Figure 72 (for the RANS and ILES solutions).

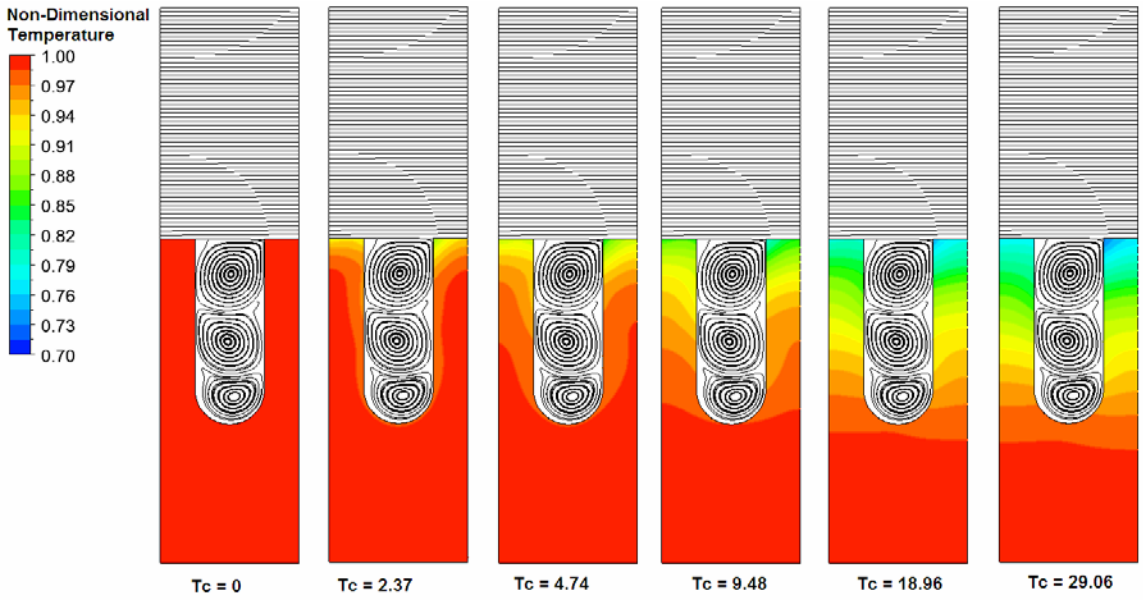


**Figure 70: Temperature development in the solid domain of a single cavity vs time (non-dimensionalised)**

[32] Whilst this appears to be an indirect method for calculating heat transfer efficiency, this was the only way that the RANS and ILES solutions could be compared.

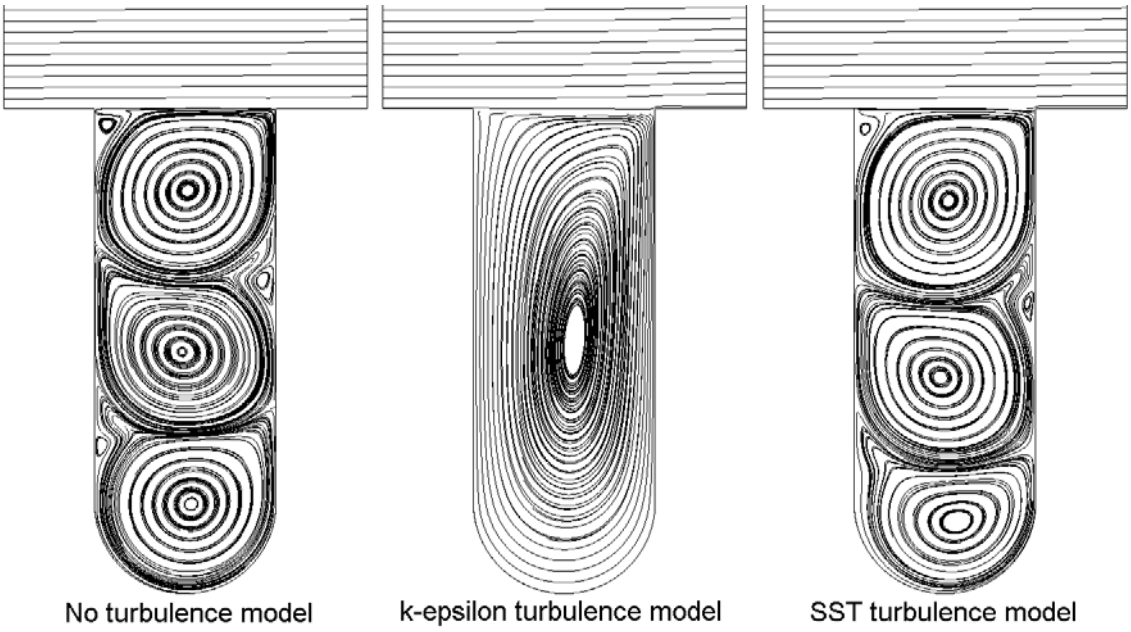


**Figure 71: Flow patterns predicted by the various RANS turbulence models**

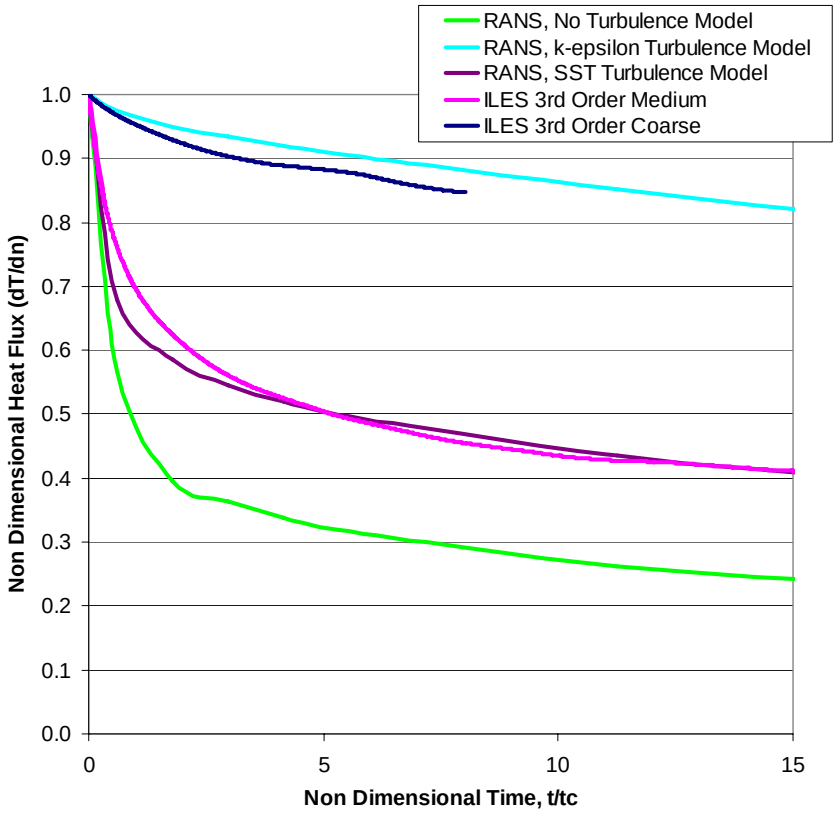


**Figure 72: Total Heat Flux extracted from the 8×3mm HyperVapotron cavities, Re = 18,000**

A number of conclusions can be drawn from this comparison:

- Given the grossly incorrect flow pattern predicted by the k-epsilon turbulence model (with its use of a scalable wall function), it is hardly surprising that it doesn't get close to predicting the "correct" thermal profile (i.e. the ILES 3rd Order Medium solution). What is noteworthy is how similar it is to the lower order ILES prediction.
- The RANS solution without additional turbulence modelling is capable of predicting the multiple vortices in the deeper cavities. This would seem to indicate the ANSYS CFX methods for discretising and solving the NS equations contains some intrinsic viscosity enhancement (it is this effect that the turbulence models are actually trying to capture). Alternatively, it's possible that the Reynolds numbers reduce to such an extent in the base of the cavity that the flow becomes laminar.
- Whilst the simulation without turbulence model is capable of predicting the multiple vortices in these deeper cavities (see Figure 71), it fails to adequately predict the transfer of heat from the wall and through the fluid. This suggests that modification to the fluid's transport properties (e.g. viscosity) via inclusion of a turbulence model is indeed critical to examining heat transfer in HyperVapotron cavities.
- The most striking result from this comparison is how well the SST turbulence model agrees with the higher order ILES solution. In some sense, this level of agreement is very surprising given the apparent large differences between the two methods. In particular, the ILES solution is a 3D, transient solution (based on very small timesteps), with periodicity in both the streamwise and cross-streamwise directions; while the SST RANS solution is a 2D, steady state solution with simple inlet / outlet boundary conditions. It is suggested here that the reason for such good agreement is the combination of the following conclusions.
    - The 2D simplification in the RANS solution is acceptable as the cross-stream fluctuations are negligible given the periodic boundary conditions in the ILES solution.
    - The simplifications included in the RANS turbulence model are offset by the finer grid resolution used compared to the ILES solution.
    - Finally, the SST turbulence model has been tuned for these types of recirculating flows and therefore does a good job of approximating the turbulent transfer of heat through the cavity.

While it was shown in section 3.1 that the SST turbulence model (with suitably refined grid) could adequately predict flow patterns in cavities where large scale flow separation occurs, these additional results confirm that the resultant thermal predictions are relatively accurate as well. This suggests that the failure to capture the larger scale eddy structures predicted by the ILES is compensated by the turbulence model's ability to

enhance the transfer of heat from the cavity to the main channel due across the highly turbulent shear layer in this region.

## 4.2 Influence of cavity aspect ratio

With the confidence gained in section 4.1, an optimisation study can now be performed to examine the influence of cavity aspect ratio on the heat removal capacity of the cavity. This can be performed relatively efficiently using the small 2D grids developed in the previous section[33]. Essentially, this optimisation is an attempt to quantify the benefit of the additional surface area and turbulent effects induced by the cavity on single phase heat transfer (with respect to a simple smooth channel).

Initially, a solution was extracted for an isothermal, smooth channel (i.e. no cavities) with periodic boundary conditions to establish quasi-developed velocity and turbulence profiles (see Figure 73). These profiles were then used as inlet conditions to the smooth channel case with a fixed temperature applied to the wall to calculate a nominal total heat flux removed from the hot wall. The results serve as a datum against which the cavity results can be compared and normalised (with the smooth channel assumed to remove a non-dimensional total amount of heat of 1). A cavity is then incorporated into the model and progressively extended with total heat flux extracted from the hot wall calculated at each cavity depth (this exercise is performed for both square and rounded cavities).

To make the results as relevant as possible to the HyperVapotron case, the channel height and cavity width are fixed at 10mm and 3mm respectively and the inlet Reynolds number is fixed at ~12,000[34] (equivalent an inlet velocity of 4m/s). These figures are typical for the MkI JET HyperVapotron design.

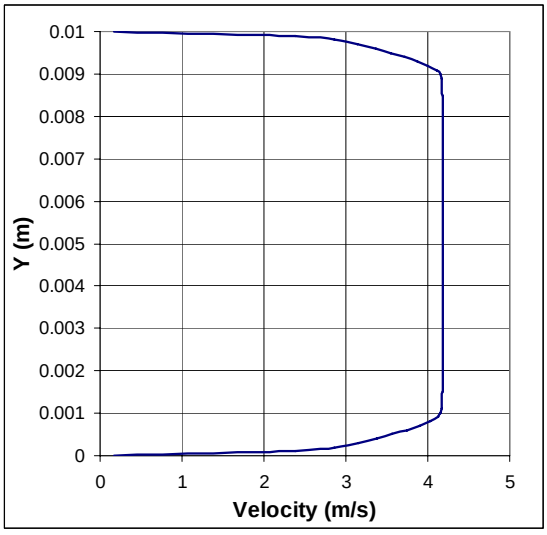


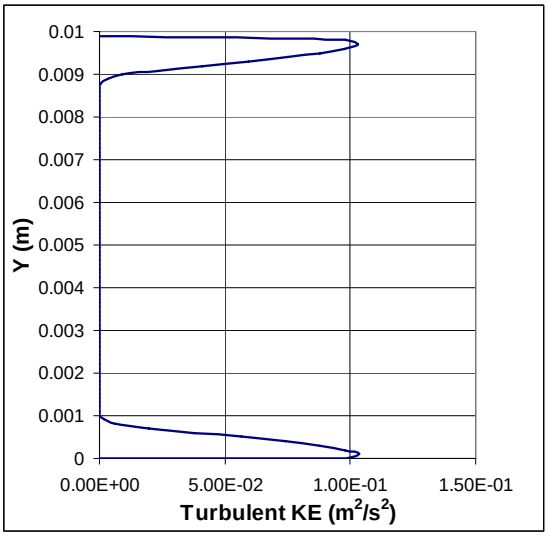


[33] It is likely this would have taken orders of magnitude more time to perform this type of study using the ILES methods against which these RANS methods have been validated.

[34] Here the Reynolds number is based on inlet velocity and cavity width.

**Figure 73: Profiles used at the inlet of the thermal solutions for the smooth channel and cavities**

The flow patterns and temperature distributions for a range of cavity aspect ratios is plotted in Figure 74 and Figure 75 (square and rounded cavities). The normalised heat flux removed from the hot wall in each case is then plotted as a function of aspect ratio, see Figure 76.

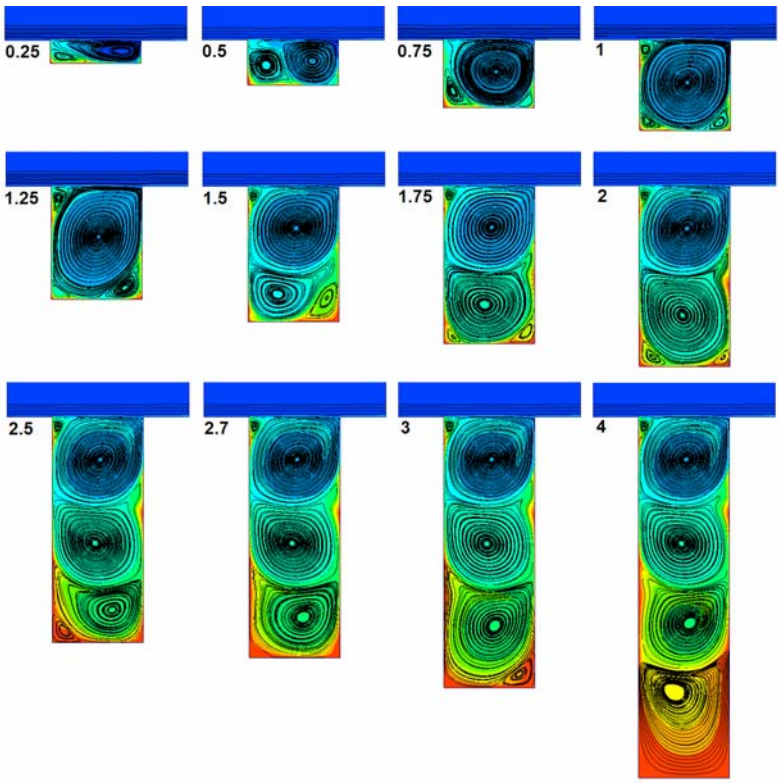


**Figure 74: Flow patterns and fluid temperature distributions for square cavities up to an AR of 4**

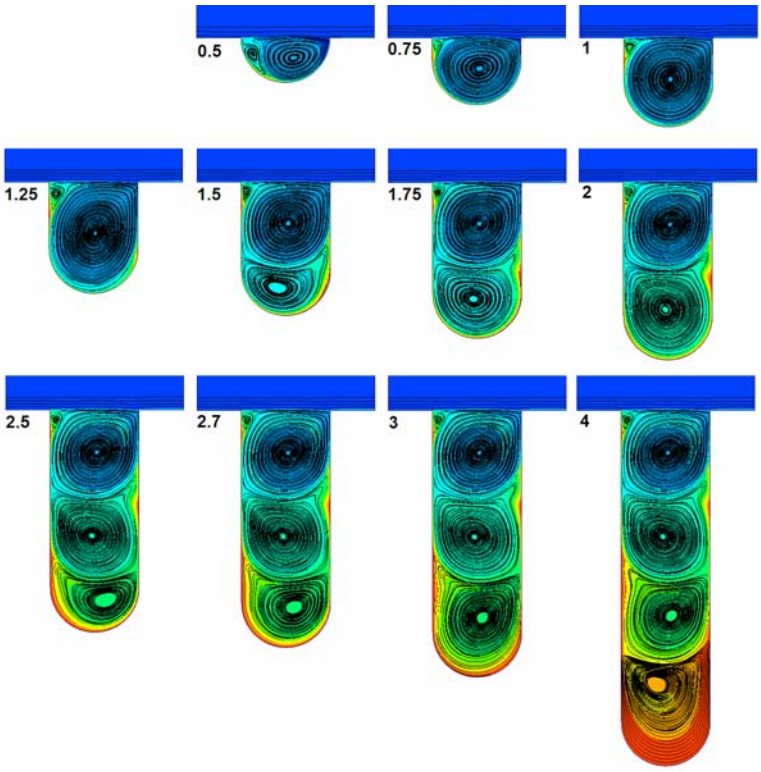


**Figure 75: Flow patterns and fluid temperature distributions for rounded cavities up to an AR of 4**

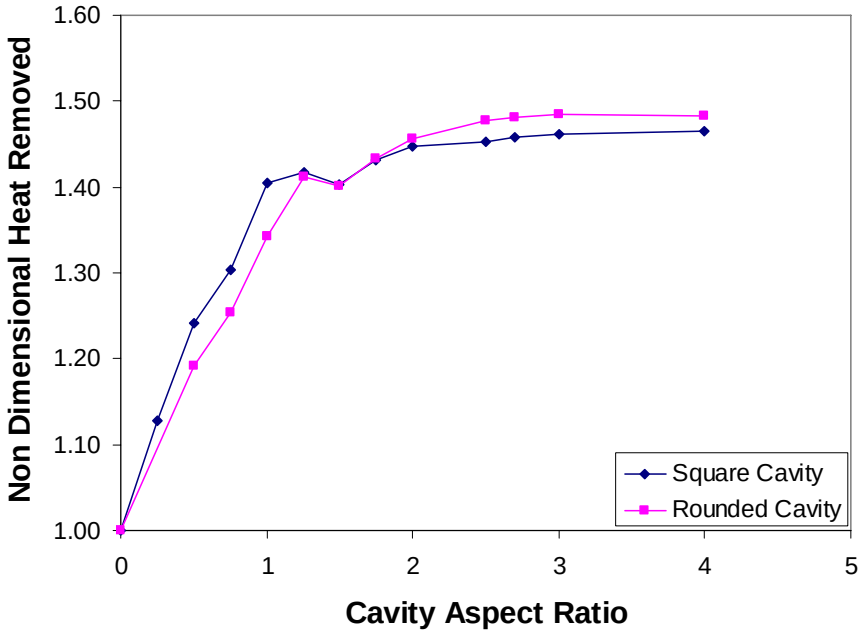


**Figure 76: Heat removed from cavity as a function of cavity aspect ratio**

It can be seen from Figure 76 that the profiles for both square and rounded cavities have a similar shape: a relatively linear dependence of heat removal with respect to aspect ratio

up to an AR of ~1.25 then, as the cavity depth increases beyond this value, the total heat removed drops slightly before rising slowly again, almost asymptotically towards a maximum value of almost 1.5 times the power extracted from a flat plate.

The similarity in the two curves allows the provisional conclusion that, for single phase heat transfer at least, the choice of whether to machine a square or rounded bottom into the cavity makes little difference to the performance of the device. Care must be taken, however, when examining the boiling case where the presence of sharp corners (and associated small areas of separation) might result in significant difference in vapour production and therefore performance (see chapter 5).

Examining the flow patterns sheds some light on why a local maximum appears at an aspect ratio of ~1.25: it appears that up until this cavity depth, the large, single vortex tends to stretch to fill most of the cavity and is the dominant factor in determining how much heat is removed from the cavity. Beyond this value, however, it appears the near wall flow can no longer overcome the adverse pressure gradients and the flow separates from the wall, inducing a secondary vortex, much weaker than the primary. In fact, it can be seen in Figure 77 and Figure 78 that the maximum velocity in each vortex decreases almost linearly so, by the time the 4$^{th}$ vortex has been induced in the deepest cavity, the vortex velocity is very low indeed.

What also becomes apparent from this study is that 80% of the performance improvement is achieved once an aspect ratio of 1.25 has been reached. This suggests that a cavity of aspect ratio 1.25 benefits from a near optimum compromise between large surface area and high heat transfer coefficients at the walls. Any increase in cavity depth from this point on and the heat transfer from the lowest parts of the wetted wall become progressively weaker resulting in negligible gains in total performance.

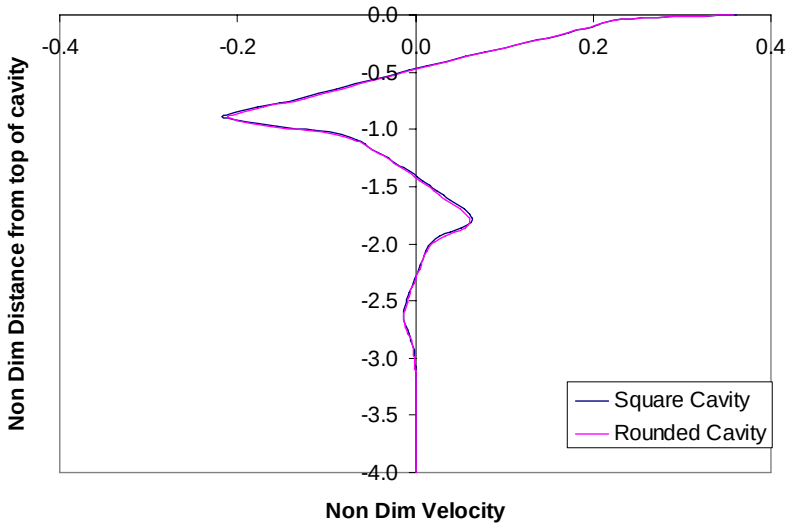


**Figure 77: Velocity profiles along cavity vertical centreline**

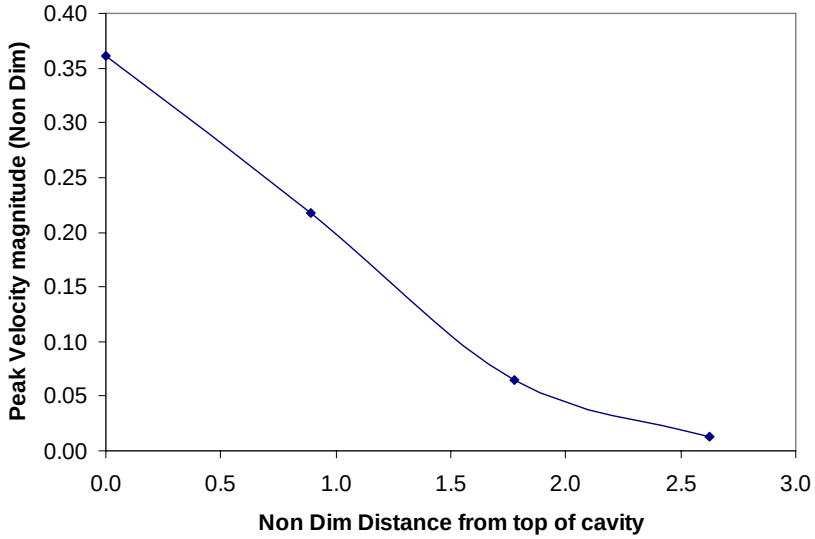


**Figure 78: Variation of peak vortex velocity with distance from top of cavity**

At this stage, it is worth highlighting how misleading these results could have been had a grid sensitivity study not been undertaken (see section 3.1.1). If coarser grids had been used (with identical turbulence models and near wall treatments), much larger vortices would have been predicted (elongated in the vertical direction as shown in Figure 43) which would have delayed the point at which the performance curves reached a maximum (induced by the presence of secondary and tertiary vortices). This is illustrated in Figure 79. Results using coarser grids would suggest that significant improvement in the heat transfer performance of a single phase driven cavity could still be gained all the way up to a cavity aspect ratio of 2 with 180% times the heat removal of a flat plate. Whereas the grid-independent, fine grid solution suggests that beyond an aspect ratio of 1.25 the gain in performance is negligible and that the maximum heat that can be removed will be less than 150% of the flat plate total (ignoring boiling).

These conclusions give valuable information before proceeding with the full engineering model of a HyperVapotron.

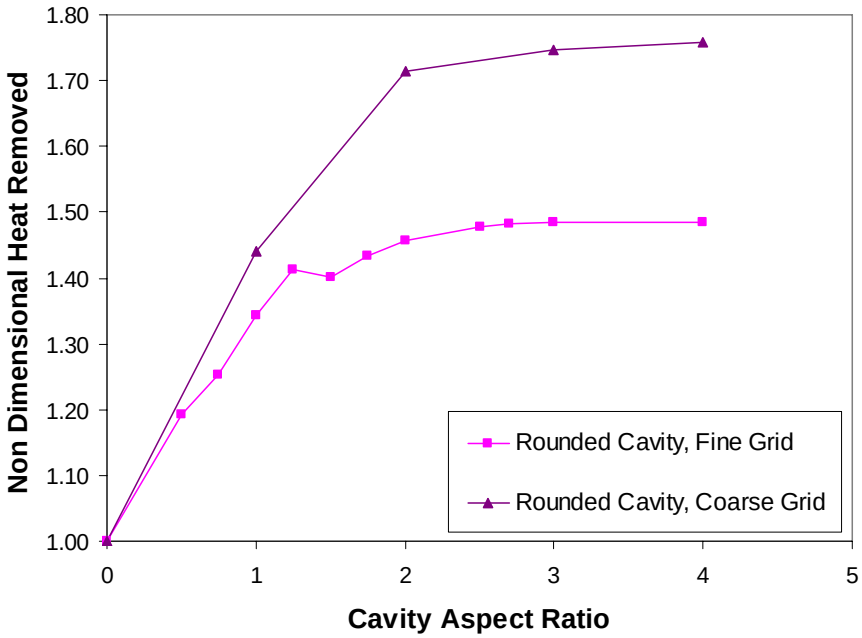


**Figure 79: Comparison of heat removed from cavity as a function of cavity aspect ratio for fine and coarse grids**

# 5

# 5 Engineering model of a HyperVapotron device

The objective of this final chapter is to develop a complete engineering model of the HyperVapotron that can accurately predict the performance of the device. Restricting the model to the single phase and nucleate boiling regimes, this is primarily achieved by comparing the model's output with results from four experimental cases chosen both for their quality of the data and the variation in boundary conditions and geometry (to properly test the applicability of the model).

Strategies are described to minimise the number of grid points to a manageable level, make the most appropriate choices for the non-critical input parameters and to achieve efficient convergence for a wide number of cases. The results from the CFD models are then compared with experiment, generally in the form of performance curves which plot surface temperature of the solid as a function of power density. This comparison, along with detailed examination of the temperature, velocity and vapour distributions, allows some useful conclusions to be drawn before examining modifications / improvements to the HyperVapotron geometry.

This study, whilst not using formal optimisation methods, gives some useful insights into which modifications might improve performance and which make little or negative impact. Those that make little difference to thermal performance may still be relevant to the HHF community as the modifications examined may be beneficial from a structural standpoint (e.g. offering longer fatigue life for the component at no cost to thermal performance).

## 5.1 Operating regime of interest

Having concluded in section 1.2.3 that the HyperVapotron goes through a number of operating regimes as the surface heat flux increases, it can be argued that for applications

in a nuclear reactor, where safety and structural integrity are of paramount importance, designers should attempt to limit the working range of these devices to the edge of the nucleate boiling regime. In other words, operation in the noisy boiling regime, where it is postulated that areas of the fins are now operating at CHF, is not recommended[35].

For this study, this assumption is advantageous as the range of interest (i.e. single phase through to nucleate boiling) also coincides with a range that can realistically be modelled via a single engineering model. Although transition to CHF is interesting experimentally, the complexity of deriving a single model that can account for the transition from discrete nucleation sites to a thin vapour film at the wall means few (if any) researchers have successfully formulated such a model.

It is worth highlighting here that Pascal-Ribot et al [53,54] do actually attempt to account for dryout in their boiling model applied to a HyperVapotron application. As noted in section 2.4.2.2, this is done by including a 4$^{th}$ term in the portioning of wall heat flux which calculates the heat conducted to the laminar vapour layer created in these conditions. Comparison with experiment is shown in Figure 80 where it can be seen that the model over-predicts surface temperature (or underpredicts the heat transfer capability). Unfortunately, it is not clear from these results how important the dryout term is in the calculation of the total heat removed from the surface. It certainly doesn't show the drop in heat transfer at elevated heat fluxes that is sometimes evident in these performance curves (although the error bars on the experimental results mean these aren't observed experimentally either).

That said, the uncertainty in how this approach handles the change in morphology (i.e. going from discrete bubbles to a distinct vapour layer) and as well as how relevant this is to the regime of interest means this will not be pursued here.

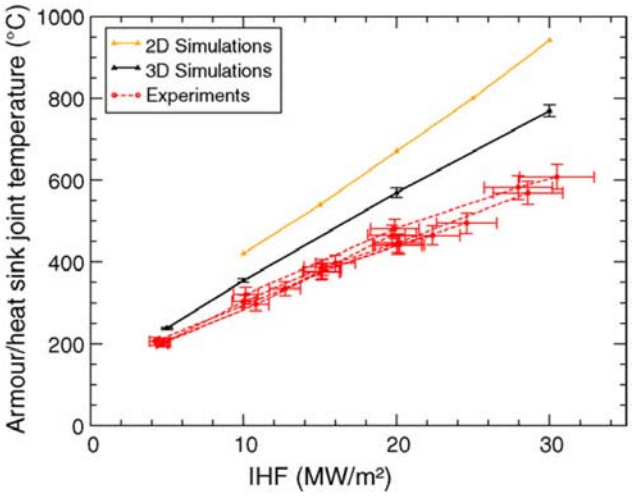


**Figure 80: Comparison of Pascal-Ribot HyperVapotron model with experimental results [54]**

[35] Whilst Chen and others have demonstrated that the presence of fins gives some warning of impending CHF, the catastrophic failure that can occur were CHF to be attained mean the routine operation in this regime is likely to be unacceptable from a regulatory standpoint.

## 5.2 Methodology

### 5.2.1 Validation cases

Given the lack of detailed experimental results for boiling in water-cooled cavities, acceptance of any engineering model of a HyperVapotron device will largely be based on its ability to predict results (or trends) observed over a wide range of HV geometries and flow conditions. In particular, the most useful data is available in the form of performance curves where surface temperature is plotted against applied surface heat flux for a particular geometry (see Figure 34).

When selecting experimental data against which the model can be validated, a number of selection criteria were considered. These included:

1. The data should ideally cover the full range of operating regimes (from single phase through to "noisy" boiling). At fusion relevant operating conditions, this typically corresponds to a power density range from 2-3MW/$m^2$ up to and beyond 15MW/$m^2$.
2. To check the model is valid over a wide range of Reynolds numbers, it is desirable that the experimental data should also be plotted for a number of different inlet flow velocities.
3. Data where experimental error is minimised is obviously preferable. This is often difficult to assess given the lack of error bars in almost all the data; as a result, accuracy of the experimental results can instead be measured by the clear distinction of different heat transfer regimes in the performance data. More specifically, transition from the single phase regime through to burnout is generally characterised by 3 different gradients in the plots of surface temperature vs power density. Ideally, validation cases will be restricted to experimental data where this is clearly visible.

Based on selection criteria above, the following experimental data has therefore been selected as validation cases for the CFD models (see section 1.2.2), with the four geometries illustrated in Figure 81:

| | Validation case 1 | Validation case 2 | Validation case 3 | Validation case 4* |
|---|---|---|---|---|
| **Hypervapotron design** | Boxscraper | Div 4×3mm | Div 6×6mm | MkI JET |
| **Channel height** | 8mm | 3mm | 6mm | 10mm |
| **Channel width (z direction)** | 48mm | 21mm | 21mm | 48mm |
| **Cavity depth** | 4mm | 4mm | 6mm | 8mm |
| **Cavity width (x direction)** | 3mm | 3mm | 3mm | 3mm |
| **Front wall thickness** | 4mm | 3mm | 3mm | 6mm |
| **Cavity profile** | Rounded | Square | Square | Rounded |
| **Thermocouple position** | Between twin channels, 3mm below from front surface | In the side wall, 2mm from the front surface | In the side wall, 2mm from the front surface | Between twin channels, 3mm below from front surface |

**Table 12: Summary of HyperVapotron validation cases**

**Note: The data for this particular configuration is not ideal (in that it doesn't meet a number of the criteria set above). That said, it is the only data available for 8mm deep fins and is therefore of certain value in checking the engineering model for this more challenging configuration.*

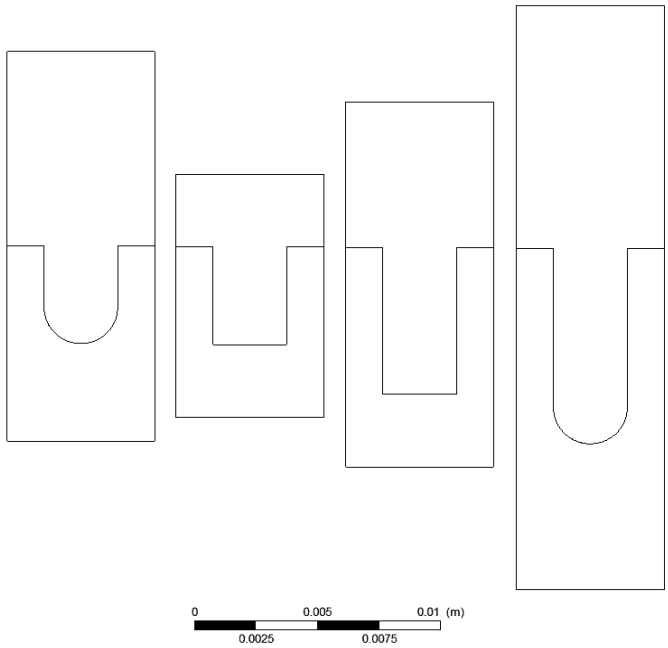


**Figure 81: 2D geometries for HyperVapotron validation cases**

### 5.2.2 Strategy for modelling 3D domains

Initially there was some concern that extending the exceptionally fine 2D grids (required to accurately predict the single phase flow distribution) in the third dimension would result in an unacceptably large number of cells. Add to this the necessity of solving 2 sets of equations (one for each phase) and the requirement to include a solid domain[36] and there is strong motivation to keep the number of cells as small as possible.

Attempts were therefore made to reduce the overall number of cells while maintaining good near wall resolution and accurate flow distributions (e.g. use of large expansion ratios away from the wall). It was quickly found, however, that even if adequate reductions could be made in the total number of cells, the fine near wall resolution essential to get good single phase results caused significant problems for the RPI boiling model. Specifically, convergence became very difficult and results become nonsensical (for instance, vapour was produced but, for a fixed wall heat flux, the temperature of the wall increased instead of decreasing). The most likely explanation for this is that the boiling model uses logarithmic wall functions to extrapolate near wall values (such as temperature) to a fixed value of $y^+$ (the default value used is $y^+ = 250$). For this extrapolation to be valid, the nearest point to the wall needs to be in the logarithmic part of the boundary layer; for fine grids used here, this isn't the case. The grid requirements for accurate single phase flow distribution and sensible boiling results are therefore in fundamental opposition.

For shallower cavities where only one primary vortex is expected this is less of a problem as coarser grids and wall functions can yield acceptable accuracy (see section 5.3.1). For deeper cavities (such as the 8×3mm cavity examined in section 4.1), this is more of an issue. The methods adopted to account for this are described in sections 5.3.3 and 5.3.4.

One simplification that can be consistently made is the use of symmetry. If the flow can be shown to be symmetrical about the centre of the cavity, a half-model of the cavity would be acceptable, halving the number of cells in one step (see Figure 82). Verification was performed by examining the flow patterns for full width cavities (see Figure 83). This is also confirmed by the temperature predicted at the thermocouple position (see point highlighted in Figure 83) which agrees to within 0.01% for the full and symmetrical cases.

[36] Without the solid domain, it is very difficult to assess the accuracy of the engineering model given that nearly all experimental data is derived from thermocouple readings in the solid body of the device.

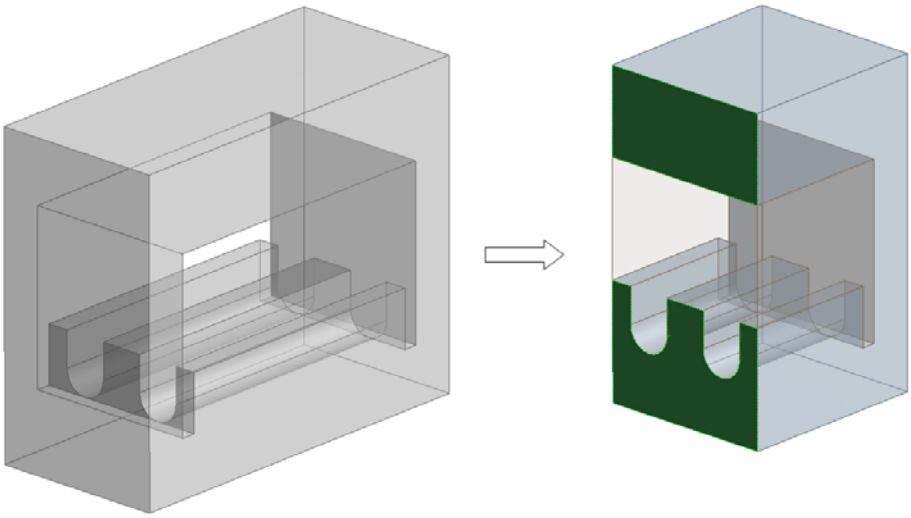

**Figure 82: Potential symmetry plane to reduce number of cells by a factor 2**

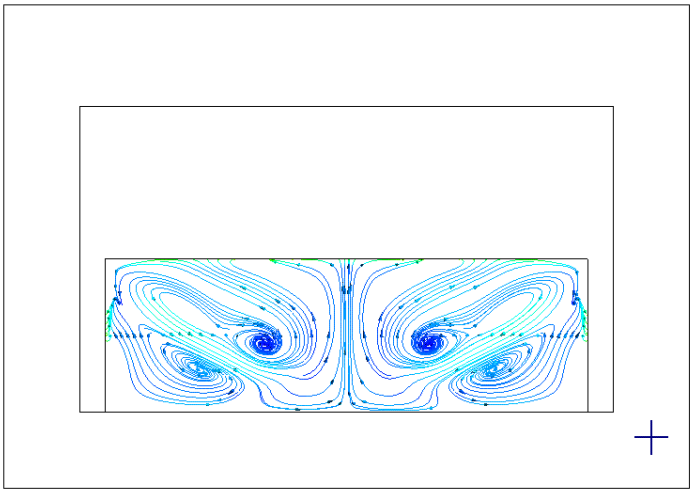

**Figure 83: Illustration of symmetrical flow observed in the 3D cavity (Div 6x6mm case chosen)**

### 5.2.3 Model set up

The following table lists the standard settings used for all the models in this section:

| Setting | Modelling choice | Comments |
|---|---|---|
| **Element type** | Hexahedral | This is the most efficient element type for this type of geometry. |
| **Inlet velocity profile** | Uniform | No experimental data on inlet profile available, use of uniform profile has been shown to make negligible difference to overall performance (compared to fully developed profile) |
| **Inlet temperature profile** | Uniform | |
| **Inlet turbulence profile** | Uniform, 5% intensity | Again no experimental data available. Results shown to be relatively insensitive to choice of inlet setting. |
| **Inlet vapour volume fraction** | Uniform, VF = 1e-8 | Non zero value reduces convergence issues |
| **Outlet type** | Outlet | As opposed to opening, although this makes little or no difference to results. |
| **Liquid RANS turbulence model** | SST k-omega | In sections 3.1 and 4.1 , it was established that this was the most appropriate choice for this problem |
| **Buoyancy model** | Density Difference | |
| **Bubble diameter in the flow** | Anglart and Nylund [70] | This sets the bubble diameter as a function of subcooling, varying from 0.15 to 2mm. |
| **Heat transfer in the vapour** | Thermal Energy | As opposed to isothermal at Tsat (on the advice of the developers at ANSYS CFX) |
| **Vapour RANS turbulence model** | Dispersed Phase Zero Equation | No other choices available within ANSYS CFX. |
| **Liquid wall slip condition** | No slip | Default. |
| **Liquid wall slip condition** | Free slip | Trials show choice of no slip vs free slip for vapour makes little difference to the results. Free slip is popular choice amongst other researchers. |
| **Lift Force** | Included, Lift Coefficient = 0.5 | Default. |
| **Drag Force** | Included, Schiller Naumann | Default. |
| **Virtual Mass Force** | Not included | Trials show that inclusion of this force makes virtually no difference to the results. |
| **Wall lubrication Force** | Not included | Trials show that inclusion of this force makes virtually no difference to the results |
| **Turbulent Dispersion Force** | Favre Averaged Drag Force | Default. |
| **Turbulence transfer model** | Sato Enhanced Eddy Viscosity | Default. |
| **Bubble Diam Influence Factor (in boiling model)** | 2 | Default. Assumes a departing bubble affects an area of diameter 2d. |
| **Max. Area Fract of Bubble Influence (in boiling model)** | 0.95 | Default is 0.5. Given likely presence of significant amount of vapour within the cavity, a choice of 95% seemed reasonable. |
| **Fixed y+ for Liq. Subcooling (in boiling model)** | 250 | Default. Value most likely fixed to match correct location in vertical tube experiments for which the RPI methodology was originally derived. |
| **Advection scheme** | High Resolution | Default. Good compromise between accuracy and robustness. |
| **Turbulence numerics** | 1st Order | Default. |

| Setting | Modelling choice | Comments |
|---|---|---|
| **General – Re. target** | 1e-5 (RMS) | Required for acceptable accuracy of an "engineering" solution. |
| **Vapour mass – Res. target** | 1e-4 (RMS) | Target reduced relative to global target as this is more easily achieved and has been shown to be acceptable when examining the overall performance of the device. |
| **Vapour heat transfer – Res. target** | 1e-4 (RMS) | Target reduced relative to global target as this is more easily achieved and has been shown to be acceptable when examining the overall performance of the device. |

**Table 13: General settings applied to engineering models of the various HyperVapotron geometries**

### 5.2.4 Convergence strategy

Ideally, a strategy should be derived that is both robust and fast. In this case, simply using the full multiphase, boiling model and starting from uniform initial conditions requires long solution times to get to a converged result. This is because a relatively small timestep is required for the multiphase fluid solution compared to the overall time constant for the system to achieve a steady solution.

Through trial and error, the following strategy was therefore adopted:

1. An isothermal model is solved using liquid only in the fluid domain to quickly establish a steady state flow pattern within the fluid domain.
2. Heat transfer is then permitted and with an appropriate heat flux applied to the front wall of the solid. The solution then automatically terminated when the wetted wall superheating reaches 5K (typical superheating at which incipient boiling occurs).
3. The full multiphase, boiling is then solved using the above as initial conditions. This ensures a gradual increase in vapour creation which can tolerate larger timesteps than if large parts of the near wall fluid were allowed to become superheated prior to turning the boiling model on.

## 5.3 Validation results

### 5.3.1 Validation case 1: Boxscraper HyperVapotron

#### 5.3.1.1 Experimental Data

Of the 4 validation cases chosen, the data for this HV design is probably the most useful. In particular, the scan over surface heat flux and inlet velocity is comprehensive and covers the 3 regimes of interest. The characteristic shape of the performance curves also gives confidence that the error bars in the measurements are small.

The only drawbacks are the lack of information on inlet conditions, specifically inlet temperature (subcooling) and pressure. In this case, a best-guess had to be made based on typical conditions used on the test bed where the data was collected. As a result, it was assumed that the inlet temperature was between 20 and 30$^{o}$C and the operating

pressure was approximately 6bar. Given that the CFD model only represented a small section of the total length, it must also be assumed that the performance measurements were taken at the centre of the element where surface heat fluxes are generally highest. Assuming the total power on the element resulted in a bulk temperature rise in the water of 50°C, the inlet temperature at the CFD model will be set at 25 + 50/2 = 50°C.

To reduce the number of runs to a reasonable level, it was decided to select only 2 of the 4 curves, specifically those corresponding to inlet flow velocities of 4 and 8.55m/s respectively. This validation data set is shown in Figure 84.

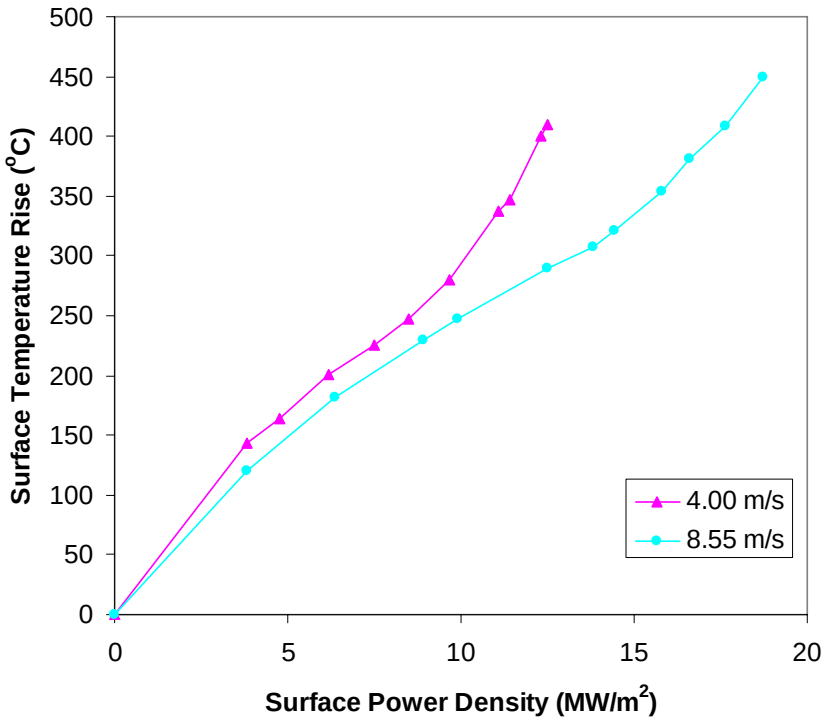


**Figure 84: Boxscraper experimental data to be used in the CFD validation exercise**

### 5.3.1.2 CFD grid

As suggested in section 5.2.2, the relatively shallow cavities of this geometry means only a single, primary vortex is likely to exist within the cavity volume. 2D analysis can therefore be used to confirm that much coarser grids (with associated use of wall functions) are sufficient to get a relatively accurate prediction of the single phase flow pattern. In particular, the near wall cell size can be increased from 0.008mm to 0.1mm with very little impact on accuracy. Using expansion ratios of ~1.2 to increase the cell size away from the wall results in a typical grid resolution as illustrated in Figure 85.

It should be noted here that, to reduce the total number of cells as much as possible, a reduced back wall thickness of 6mm was used compared to the 14mm found on the actual geometry. Given that this part of the geometry plays little role in performance (other than negligible heat distribution around the fluid domain), this simplification was judged acceptable.

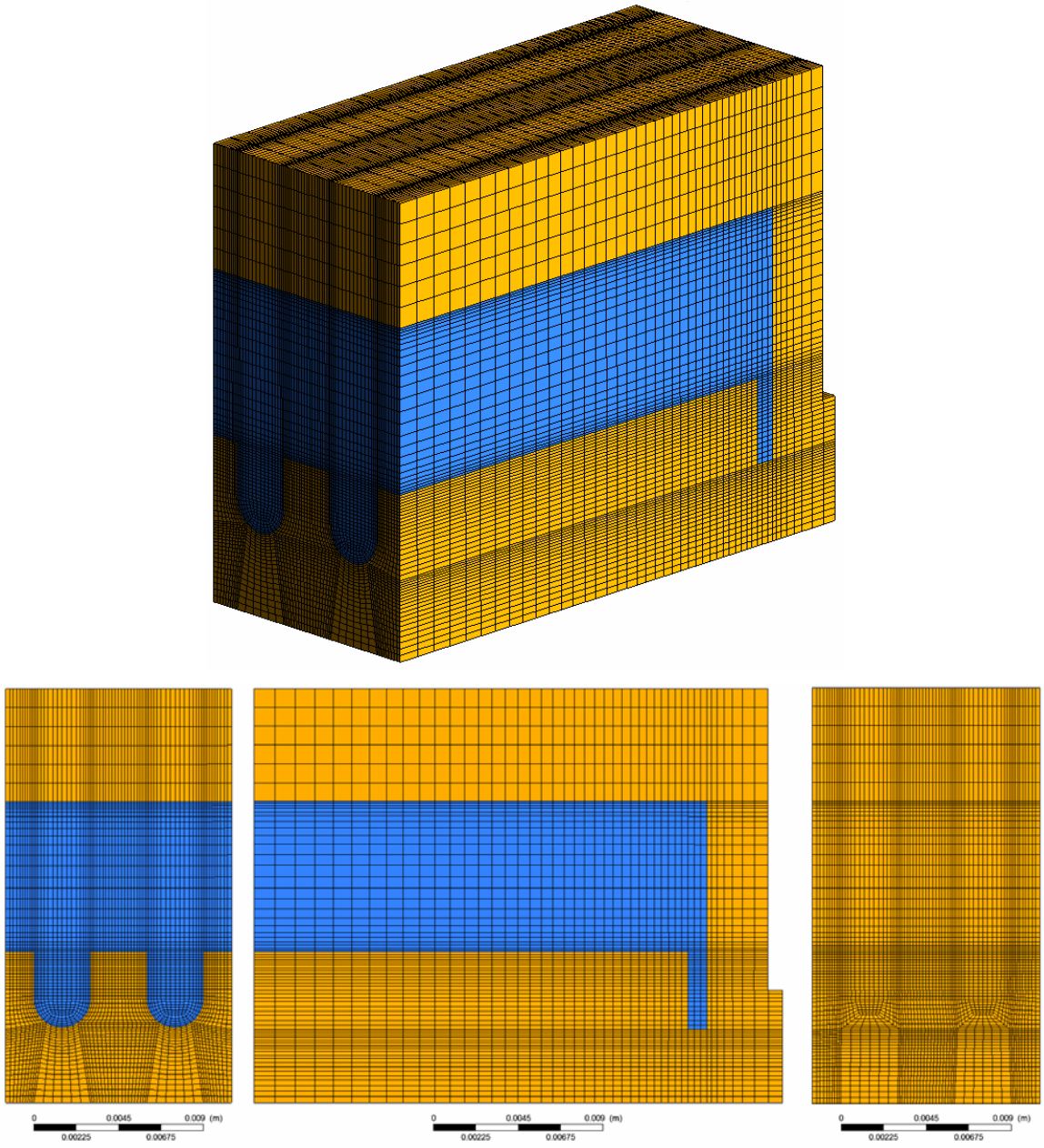


**Figure 85: Boxscraper HyperVapotron CFD grid**

### 5.3.1.3 Standard boiling model

Initially, the so-called Standard boiling model was incorporated into the model to assess its performance in this application. As well as the general settings listed in section 5.2.3, the settings listed in Table 14 were applied. Selected results from this model are shown in Figure 86 to Figure 88.

| Setting | Modelling choice | Comments |
|---|---|---|
| **Inlet velocity** | Uniform, Vin = 4 and 8.55m/s | These are the two extremes for inlet velocity and correspond to Re of ~12,000 and 25,600 respectively |
| **Inlet temperature** | Uniform, Tin = 50$^{o}$C | Whilst not explicitly stated in Ciric's paper, the typical inlet temperature on the test bed is 20-30$^{o}$C. This was increased to 50$^{o}$C in the analysis to account for the ~20-30$^{o}$C bulk heating that typically occurs half way along the HyperVapotron element, where performance measurements are generally taken. |
| **Outlet pressure** | Uniform, Pref = 6bar | This is not stated in the experimental paper but it is known that this is the typical operating pressure of the system. |
| **Saturation temperature** | Constant, Tsat = 158.8$^{o}$C | Water saturation temperature at a pressure of 6bar. |
| **Bubble Departure Diameter** | Tolubinski Kostanchuk | Default correlation chosen for the Standard approach. |
| **Wall Nucleation Site Density** | Lemmert Chawla | Default correlation chosen for the Standard approach. |
| **Bubble Detachment Frequency** | Cole | Default correlation chosen for the Standard approach. |
| **Bubble Waiting Time** | = 0.8×Detachement Period | Default correlation chosen for the Standard approach. |
| **Liquid Quenching Heat Transfer Coefficient** | Del Valle Kenning | Default correlation chosen for the Standard approach. |
| **Interphase Heat Transfer** | Ranz Marshall | Default correlation chosen for the Standard approach. |
| **Bulk Bubble Diameter** | Anglart and Nylund | Default correlation chosen for the Standard approach. |

**Table 14: CFD settings used in the Standard boiling model of the Boxscraper HyperVapotron**

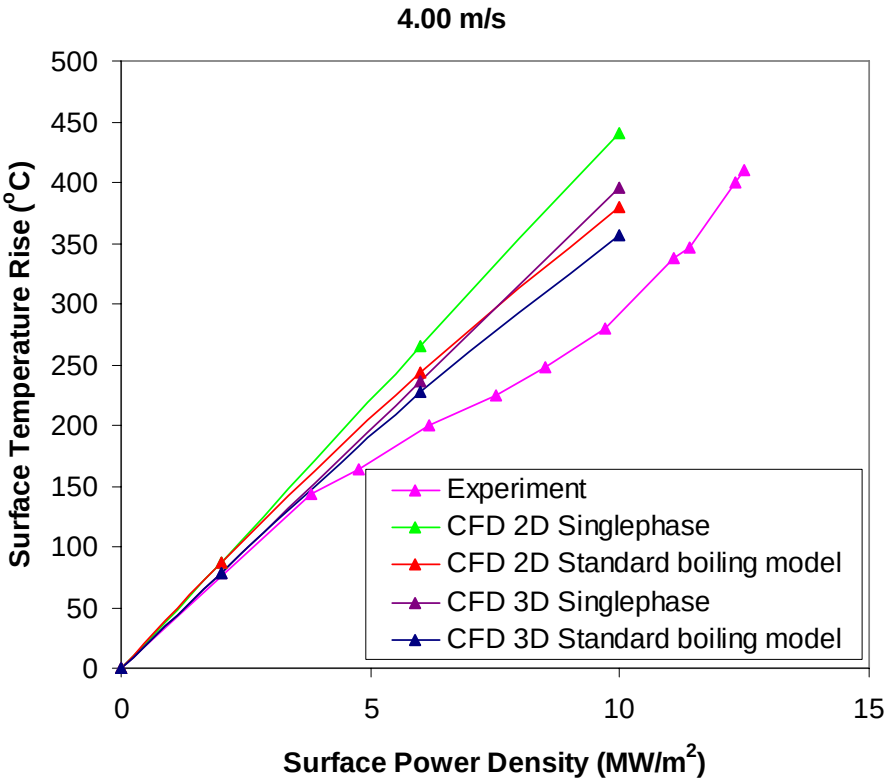


**Figure 86: Performance of single phase and standard boiling models against Boxscraper HV (Vin = 4m/s)**

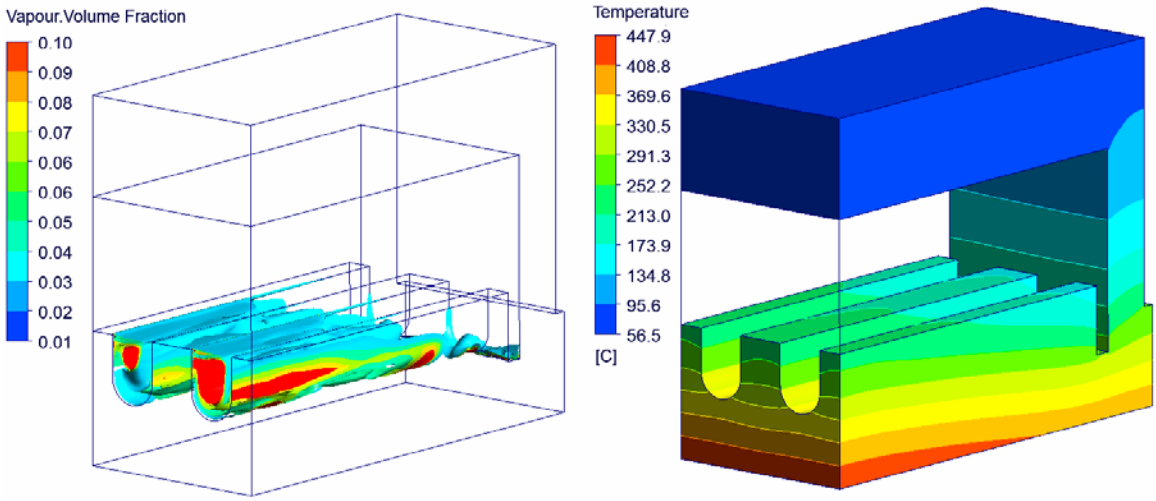


**Figure 87: Vapour volume fraction and Temperature distribution for the 3D multiphase solution of the Boxscraper HyperVapotron (Vin = 4m/s, Tin = 50°C, Qwall = 10MW/m$^2$)**

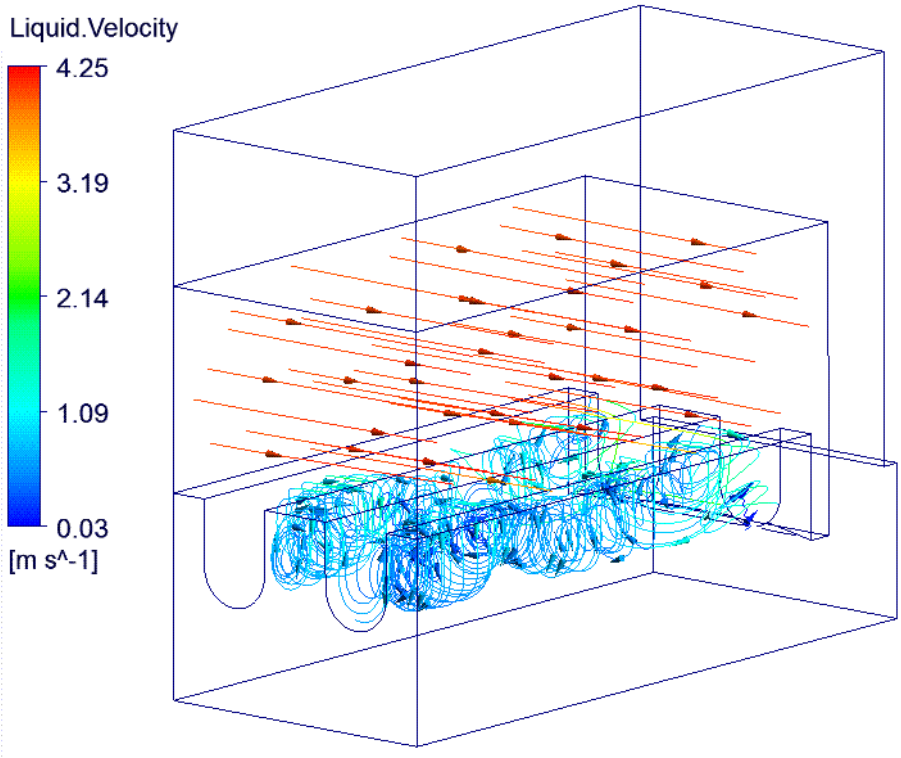


**Figure 88: Liquid streamlines for the 3D multiphase solution of the Boxscraper HyperVapotron ((Vin = 4m/s, Tin = 50°C, Qwall = 10MW/m$^2$)**

Examining Figure 86, it is clear that inclusion of the boiling model improves heat transfer performance and takes the CFD results closer to the experimental curve (in both 2D and 3D cases). This confirms the importance of including boiling in the CFD simulation of these devices. What is also apparent is that a 2D model is not capable of accurately predicting the devices real performance. This is most likely due to a combination of its intrinsic inability to capture the 3 dimensional aspects of the flow but also that the surface temperature rise predicted by the 2D solution corresponds to the middle of an infinitely wide cavity, not the position where the temperature is actually measured which is located in the side wall (in fact, the thermocouple is inserted in a slot between the two channels of this particular design, see Figure 89). The latter therefore requires a 3D model of the solid domain to account for the thermal profile in the solid and give make a prediction of the temperature in the correct position.

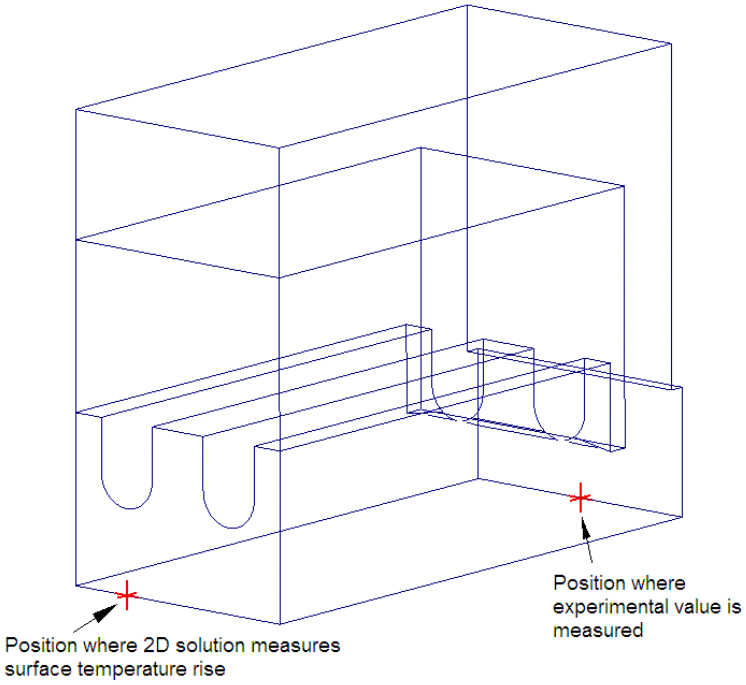


**Figure 89: Comparison of the 2D solution temperature measurement with the position as measured in the experiment**

Examining the 3D solutions, it was found that whilst the Standard multiphase solution (see Table 14) was an improvement on single phase solution, it still over predicts surface temperature rise by as much as 27%. Some efforts were therefore made to try and tweak the model, based on sound reasoning, to see if this discrepancy could be reduced. This is detailed in section 5.3.1.4.

Whilst the 2D models are not suitable for experimental predictions, they are useful for examining the relative effect of some key settings. In particular, it was not initially clear how important the presence of buoyancy was in the performance of the device. By turning buoyancy on and off and comparing the results, it was found that the presence of this body force makes negligible difference to both quantity of vapour produced as well as the temperatures calculated in the solid. In fact, if the HV were orientated such that buoyancy acted to push the vapour out of the cavity, the CFD predicts only a 0.5% reduction in surface temperature compared to the non-buoyant solution which is well within the margin of error of both the experimental and CFD data.

A 2$^{nd}$ investigation was also undertaken into the importance of inlet subcooling. Given the uncertainty of this variable for this particular experiment, a sensitivity study was performed to examine how this affected the performance of the CFD model. It was found that whilst absolute temperature in the solid is reduced by lowering inlet water

temperature, the surface temperature rise in the solid is actually increased[37]. This indicates that reducing the inlet subcooling actually results in better heat transfer performance (most likely due to more vapour created). In reality, however, excessive reduction in inlet subcooling would be limited by other factors such as safety margin to CHF and mechanical issues in the solid at high temperature.

#### 5.3.1.4 Customised boiling model

The tuning of the Standard RPI model against Lee's experimental results gave good indications about where improvements could be made. Initially, 2D solutions were used to gain a qualitative indication of whether alternative submodels improved performance and were therefore worthy of incorporating into the full 3D solutions.

Starting with bubble departure diameter, the two expressions of interest were the simplified Kolev and Unal models (see section 3.2.1.5). Unfortunately, neither was particularly successful. The Kolev model was found to induce significant instabilities in the solution and a converged result could not be achieved. The Unal model was found to give very large bubbles for HyperVapotron flow parameters and boundary conditions. This is illustrated in Figure 90 where it can be seen that for the realistic subcooling range, bubble are predicted to be greater than 5mm in diameter, i.e. larger than the width of the cavity. Given the extreme likelihood that bubble formation and condensation is a local effect within the cavity itself, these bubble sizes are clearly not compatible with this particular application.

Next the Zeitoun correlation for bulk bubble diameter was incorporated into the standard model (based on recommendations in [46]). In this case, convergence was still robust but unfortunately this didn't actually improve performance and resulted in slightly less, not more vapour being produced. Furthermore, it was found that when this was combined with other alternative submodels (e.g. for bubble departure diameter), convergence was exceptionally difficult to achieve. Again, for these reasons this was not pursued any further.

[37] At an inlet temperature of 20°C (equivalent to subcooling of ~140°C), the peak surface temperature at 10MW/m$^2$ is 414°C, or a rise of 394°C. If the inlet temperature was then increased to 50°C (i.e. subcooling reduced to ~110°C), the peak surface temperature rise actually reduced to 381°C.

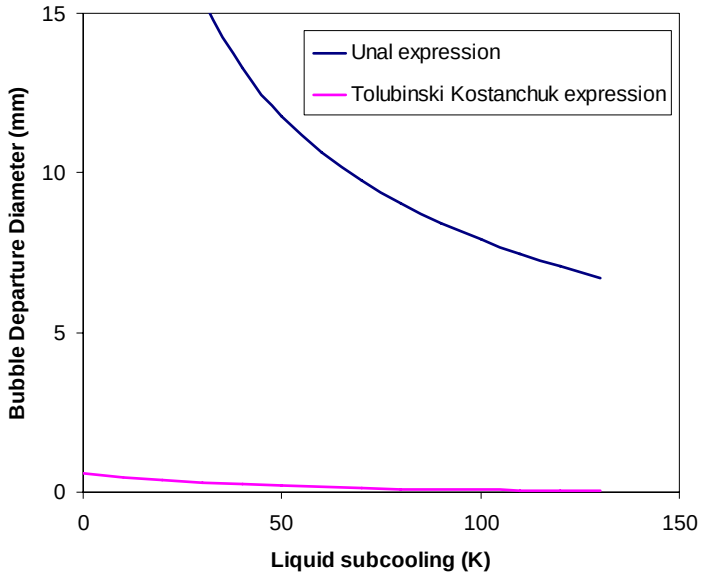


**Figure 90: Bubble departure diameters predicted by Unal correlation at typical HyperVapotron conditions**

Validation against Lee's experiments also seemed to indicate that interphase heat transfer in the Standard model may be overestimated. The next modification made was therefore to reduce the interphase heat transfer coefficient to a constant Nusselt number of 2 (instead of using the Ranz Marshall correlation which predicts Nusselt numbers greater than 2 for non-zero interphase Reynolds numbers). It was found that this had two consequences:

1. It seemed to improve the robustness of the model, with a converged solution achieved in less time.
2. More vapour was created and the surface temperature was very slightly reduced, although not by much (less < 1%, see Figure 91).

These two findings, particularly the point 1, meant this modification was maintained for boiling models used from this point forward.

As was highlighted previously, whilst validation against Lee's experiments seemed to show negligible influence on performance, it was noted that these just happened to agree with each other at this particular operating point. In other words, for the HyperVapotron application where heat fluxes and wall superheats can be an order of magnitude greater, choice of alternative, more appropriate correlations for the boiling submodels may indeed help to bring the CFD results closer to experiment.

The next modification therefore involved selecting a more up-to-date and accurate correlation for bubble departure frequency. Examining Situ's correlation for this variable seemed to suggest this would be a more appropriate choice than the Cole expression used by default which appears to have been developed based on pool boiling experiments (see section 2.4.2.3.2). In particular, at high levels of wall superheat (as is the case in a

HyperVapotron application) this correlation predicts significantly greater departure frequencies which should ultimately result in more vapour and more heat removed from the wetted surface. The only modification that had to be made to this correlation was that the parameter S, which relies on the two phase Reynolds number $Re_{TP}$, was replaced by the single phase Reynolds number (itself based on the cavity width). This simplification was made because there was insufficient information available to calculate $Re_{TP}$ and a sensitivity study showed that the final calculation of departure frequency had a relatively weak dependence on this variable.

Unfortunately, with this correlation substituted into the RPI model, it was found that the solution often crashed, particularly when the heat flux was increased to high values (e.g. >10MW/m$^2$). On closer inspection, it was found that departure frequencies of up to 5,000Hz were calculated on the hottest parts of the HV wetted wall (compared to the ~150Hz predicted by Cole at the same conditions). Situ states that his correlation is valid for wall Ja numbers up to 60 whereas values of up to 100 are typical for the HyperVapotron. Extrapolation of this level would therefore seem to be ill-advised.

To get the solution to converge and to limit the departure frequency to a "sensible" value, the correlation was subsequently modified to incorporate an upper limit. This limit was based on a similar argument used by Pascal-Ribot et al [53]. In their boiling model, the frequency was set equal to $1/T_r$ where $T_r$ is the "rotation time of liquid in the groove". Like Pascal-Ribot, this was approximated here using the inlet velocity and the wetted length of the cavity, 4m/s[38] and 9.7mm respectively:

$T_r = 9.7\times10^{-3} / 4 = 2.4\text{ms}$

=> Bubble departure frequency limit = $1/1.8\times10^{-3} = 412\text{Hz}$

It can be seen that this modification allowed the solution to converge and showed a marked improvement compared to the standard boiling model (see Figure 91), with the error reduced from 24 to 13% at a heat flux of ~10MW/m$^2$.

What is interesting to note is how different the distributions of bubble departure frequency around the cavity are for this new approach compared to the original RPI model (which used Cole's correlation for frequency).

[38] It could be argued that this approach would be more valid is the average near wall velocity in the cavity was used instead which, in this case, would be approximately 1.5m/s. This is not pursued here, however, for no other reason than this would result in a considerably reduced upper limit of ~150Hz, less vapour and a reduction in accuracy when compared to experiment

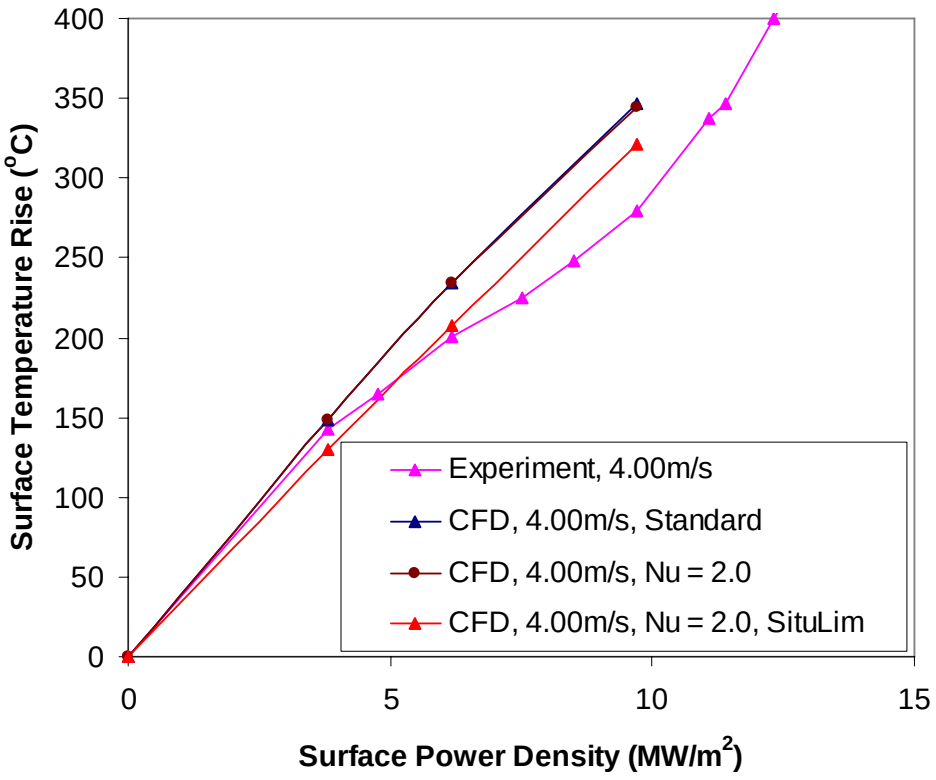


**Figure 91: Effect of modifying interphase heat transfer and incorporating Situ correlation (with upper limit) for bubble departure frequency**

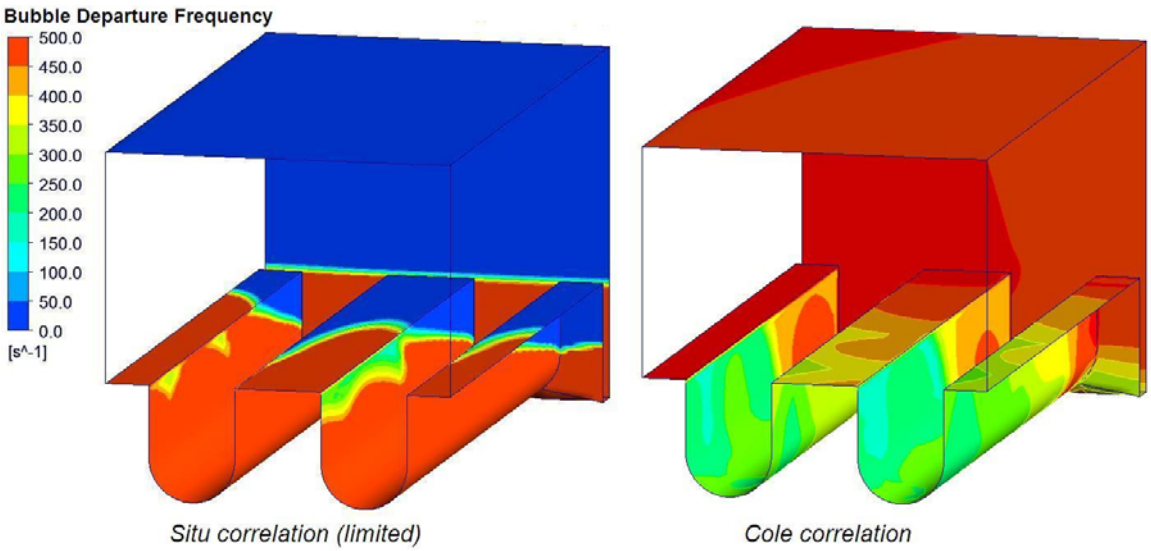


**Figure 92: Comparison of bubble departure frequency distribution between Situ and Cole correlations**

As highlighted in section 5.3.1.1, the Boxscraper HV experimental data is particularly useful as it gives performance curves at a range of inlet flow velocities. So, does this new boiling model improve performance when the inlet flow velocity (and therefore Reynolds number) is more than doubled? It can be seen in Figure 93 that the customised boiling model is certainly capable of predicting the significant performance improvement when flow velocity is increased in this manner. Quantitatively speaking, however, the curve does not turn over as much as expected at elevated heat fluxes and consequently the model over-predicts the surface temperature rise by 26%. It would appear therefore that the model is still not quite capturing all the heat transfer mechanisms occurring within the internal channels of the HyperVapotron.

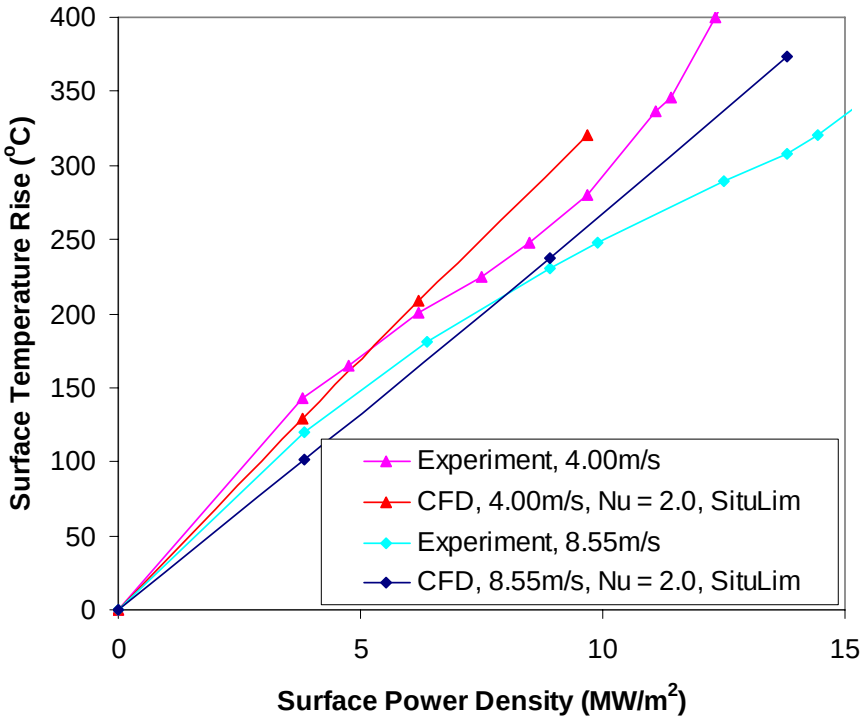


**Figure 93: Performance of modified boiling model against Boxscraper experiments at increased flow velocity**

Whilst the accuracy of the boiling model has been enhanced with some carefully selected modifications, there is still room for improvement. It was decided therefore to examine the last submodel not yet studied, namely nucleation site density. Given the inclusion of critical bubble radius in the expression, Wang and Dhir's correlation was chosen over Basu's expression (see section 2.4.2.3.3). The contact angle was fixed at 45° as values for this experimental set up were unknown for this configuration and, for a typical range of values, choice of contact angle doesn't have a significant influence on total number of nucleation sites predicted. Unsurprisingly, given the form of the expression involved, use of this correlation resulted in a huge increase in the number of sites in the hottest parts of the cavity (an unrealistic peak of $10^{15}$ sites in some places compared to just $10^{7}$ for the

default Lemmert Chawla expression). What was surprising, however, is that this resulted in only a small increase in the amount of vapour produced and virtually no change in performance. It was postulated that this may have been due to internal limits set within the code (to ensure robust convergence for the boiling model) but initial indications from the ANSYS developers suggest this is not the case. Whatever the reason, given that it didn't improve the performance of the model, this modification to the boiling model was abandoned.

The conclusions from this first validation exercise are as follows:

1. Accuracy of the RPI boiling model can be improved for the HyperVapotron application by modification of specific submodels (although this drops off slightly at increased Reynolds numbers).
2. Interphase heat transfer should be reduced by fixing the interphase Nusselt number at a value of 2 (this aids accuracy and convergence). This will be maintained for the remaining validation cases.
3. Alternative correlations for bubble departure diameter and nucleation site density were either inappropriate for the application (e.g. predictions clearly unrealistic for the HyperVapotron geometry or flow) or failed to improve accuracy when compared to experimental results.
4. Incorporating the Situ correlation for bubble departure frequency with slight modifications did results in a significant improvement in accuracy. This is therefore maintained for subsequent validation cases.

### 5.3.2 Validation case 2: Div 4x3mm HyperVapotron

#### 5.3.2.1 Experimental Data

The JET divisional note in which this data is presented not only gives performance curves but actually gives tables of data extracted from the test bed archives. Of the 4 validation cases, it is the only one to give all the main inlet parameters required to accurately define the boundary conditions in a CFD simulation (including inlet temperature, pressure and velocity as well as raw thermocouple data). The two cases that will be used in this validation exercise are shown in Figure 94.

As highlighted in section 1.2.2, performance up to a power density of 15MW/m$^2$ is very similar despite the two cases having quite different thermal hydraulic inputs. The potential reasons for this are discussed further in section 5.4 but here it is simply worth noting that replicating this surprising result would be a strong endorsement of the selected CFD approach.

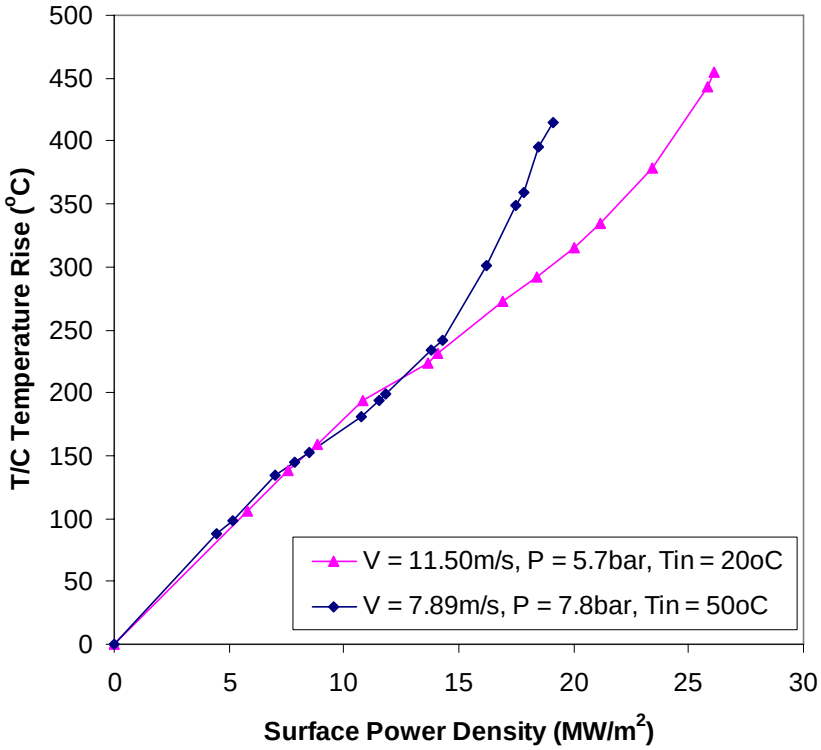


**Figure 94: Div 4x3mm experimental data to be used in the CFD validation exercise**

### 5.3.2.2 CFD Grid

A similar grid sizing as used in the validation case above was employed here, resulting in the grid as shown in Figure 95.

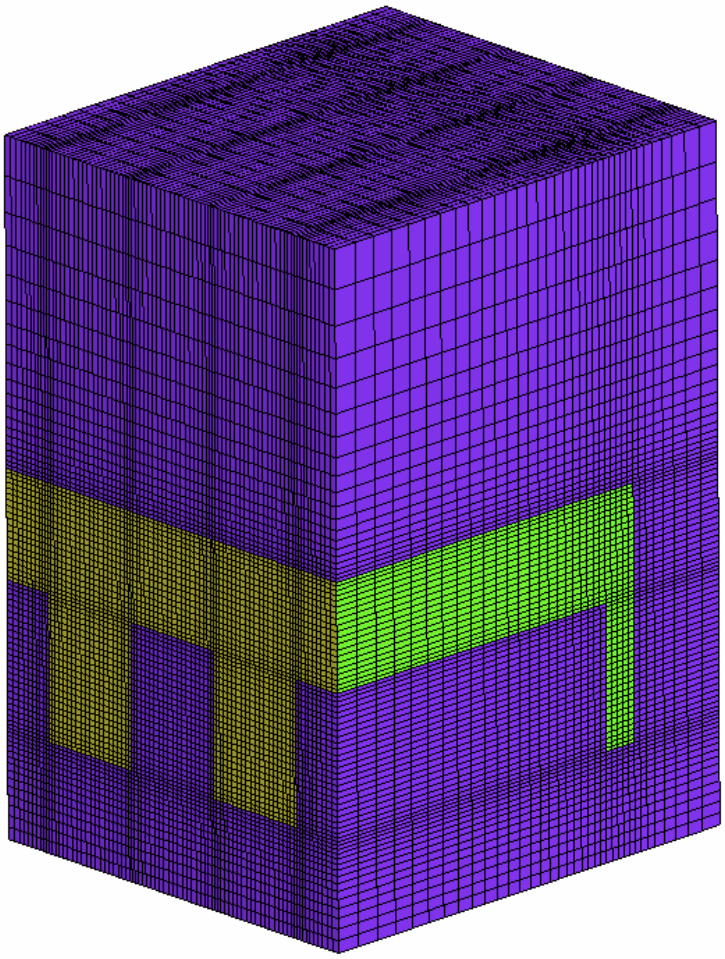

**Figure 95: Div 4x3mm HyperVapotron CFD grid**

#### 5.3.2.3 Customised boiling model

Given the relatively successful validation against the Boxscraper configuration, an identical customisation of the boiling model was applied here; i.e. interphase heat transfer set at Nu = 2 and the Situ correlation incorporated for calculating bubble departure frequency (for the flow velocities of 7.89m/s and 11.5m/s the upper limits on departure frequency because 717 and 1045Hz respectively). The results are shown in Figure 96. Again, it can be seen that the customised boiling model performs relatively well against experimental data. In particular, the CFD is capable of reproducing similar performance curves observed at quite different experimental conditions, with a maximum error in all cases of < 13% (had the standard boiling model been used, this would have been closer to 20%).

It should be noted that the model is still limited to the single phase and nucleate boiling regimes only and is not able to predict the third heat transfer zone clearly visible in the experimental data at 7.89m/s (increase in slope at ~15MW/m$^2$). As stated in section 2.4.2.1, however, it is unlikely that operators of a Fusion device would want HyperVapotrons operating in this third regime so exact performance predictions here are

not essential. What is essential is simply that this third zone exists and is sufficiently wide so that a gradual transition to CHF is observed allowing safe diagnosis and shutdown in case of excessive heat loads or reduced cooling capacity associated with off-normal events. The presence of any fins with reasonable thermal capacity and conductivity should allow for this.

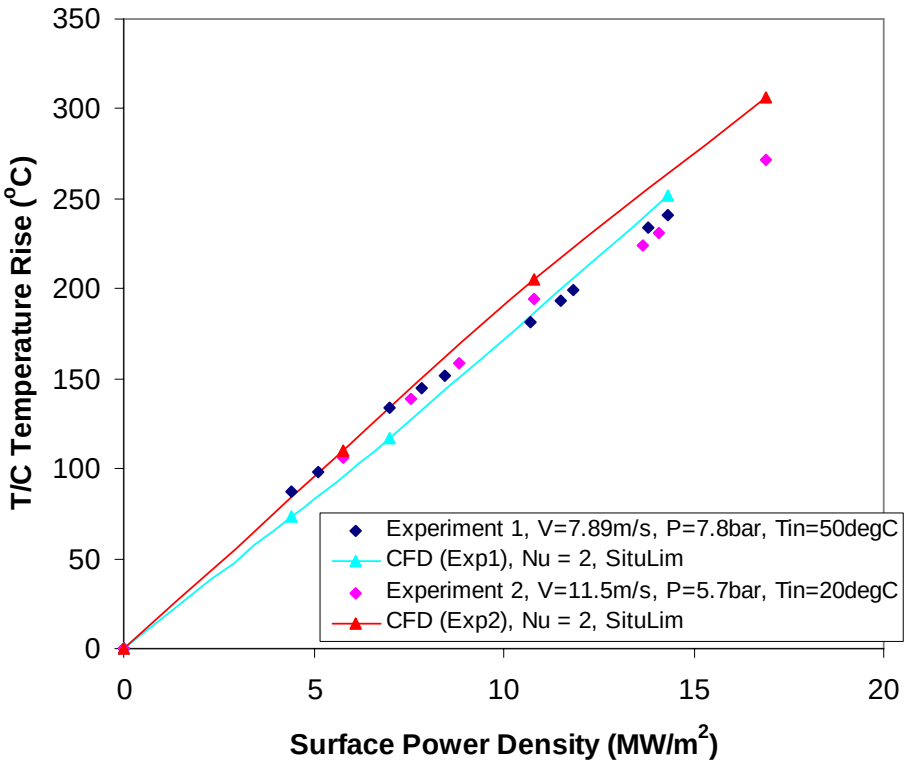


**Figure 96: Performance of customised boiling model against Div 4x3mm HV**

### 5.3.3 Validation case 3: Div 6x6mm HyperVapotron

#### 5.3.3.1 Experimental Data

Like the Boxscraper case, the performance curves for this design exhibit the characteristic HyperVapotron profile suggesting reasonable measurement accuracy. One of the drawbacks of this data, however, is that it lacks information on the operating pressure and inlet temperature at which it was derived. With respect to pressure, given that the tests were performed on the JET Neutral Beam Test Bed, it will be assumed that the inlet pressure was approximately 6 bar (see section 5.3.1.1).

In terms of inlet temperature, it is interesting to note from the curves in Figure 97 that choice of this parameter seems to make little difference to the performance of the device in the single phase and nucleate boiling regimes. This can be concluded as the inlet temperature for the "downstream" element is taken as the outlet temperature from the

"upstream" element and is therefore significantly higher (in the order 10's of degrees K). Since the upstream and downstream performance curves are virtually coincident (up to a heat flux of ~12MW/m$^2$), it can be concluded that inlet subcooling has little effect on the temperature rise in the solid[39]. As a result, it was considered acceptable to fix the inlet temperature for all CFD models at a typical value for the system, i.e. 50$^o$C.

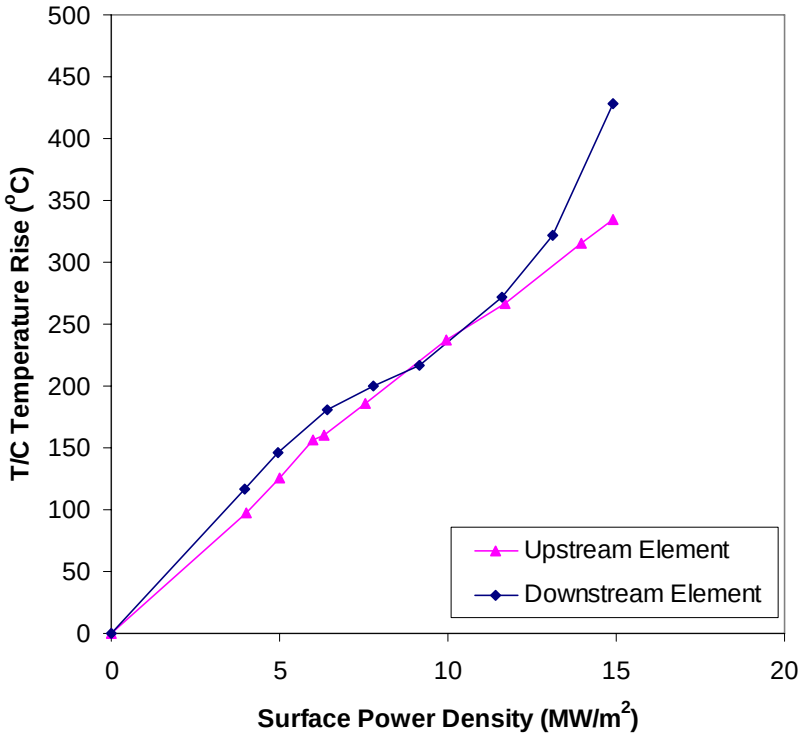


**Figure 97: Div 6x6mm experimental data to be used in the CFD validation exercise (Vin = 6m/s)**

### 5.3.3.2 CFD Grid

A similar grid sizing as used in the validation case above was employed here, resulting in the grid as shown in Figure 98.

[39] Increased inlet subcooling does have an effect at very high power densities in that it tends to delay the transition to CHF. Whilst this doesn't affect the CFD modelling choices at this stage, this should be a consideration when optimising the flow parameters for a particular application.

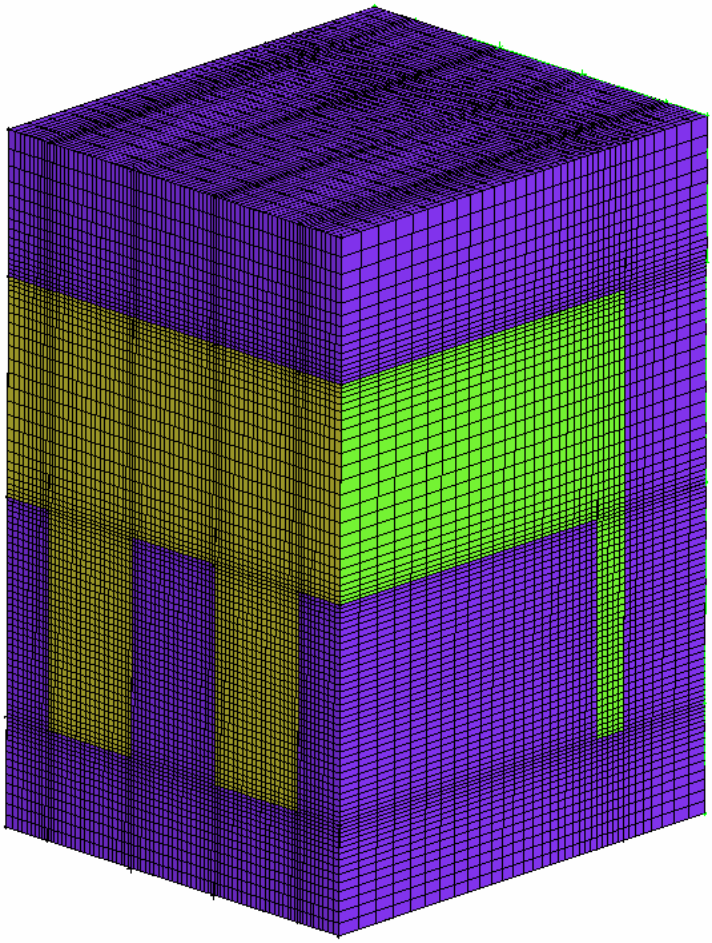

**Figure 98: Div 6x6mm HyperVapotron CFD grid**

#### 5.3.3.3 Customised boiling model

As before, the same customisation is applied to the CFD model of this configuration. The big difference between this and the previous case is that the cavity depth has increased from 4 to 6mm (i.e. a cavity aspect ratio of 2). It was shown in section 4.2 that a grid-independent solution for this type of cavity (at a Reynolds number in the order $10^4$) would exhibit two large vortices occupying most of the cavity (see Figure 74). As part of the same analysis, it was also shown that coarser grids would incorrectly predict a single vortex and therefore over-predict the single phase heat transfer coefficients. Given that coarse grids are required for the engineering model, care must be taken here.

With this mind, the flow patterns for the 3D boiling model of the Div 6x6mm HV are shown in Figure 99 and Figure 100. Whilst the 2D flow pattern does show a second recirculation zone at the bottom of the cavity, this is quite different to the grid-independent 2D solution and is induced by 3D effects due to the presence of the side slots (see Figure 100). It should be acknowledged therefore that the single phase heat transfer coefficients calculated by this model are likely to be too high and that the predicted performance curves may be optimistic. It is important to try and take this effect into

account as neglecting it in subsequent optimisation work may lead to the conclusion that deeper cavities perform better than they do in reality. One simple method of accounting for this is to use a scaling factor based on comparison of single phase 2D solutions using fine and coarse grids. These curves are included in Figure 102 and show that the coarse grid solutions predict temperature rises 15% lower than their fine grid equivalents. Crudely, this factor can be applied to the coarse grid 3D boiling solutions resulting in the curve entitled "CFD, 3D, Nu = 2, SituLim, Scaled". This scaling brings the predicted performance somewhere between the upstream and downstream results suggesting a good level of accuracy for the model. The success of the scaling method could be used to justify inclusion of a so-called "deep cavity" factor for any CFD modelling of a HyperVapotron cavity with aspect ratio greater than 1.25 (based on Figure 74 and Figure 75).

The other slight complication with modelling deeper cavities is the use of $1/T_r$ (= Cavity Length / Inlet Velocity) to limit bubble departure frequency. This parameter becomes less representative of the characteristic circulation frequency within the cavity when multiple vortices are present. That said, the excellent agreement with experiment obtained using this method along the lack of anything better means this will continue to be the method used for engineering models of HyperVapotron devices.

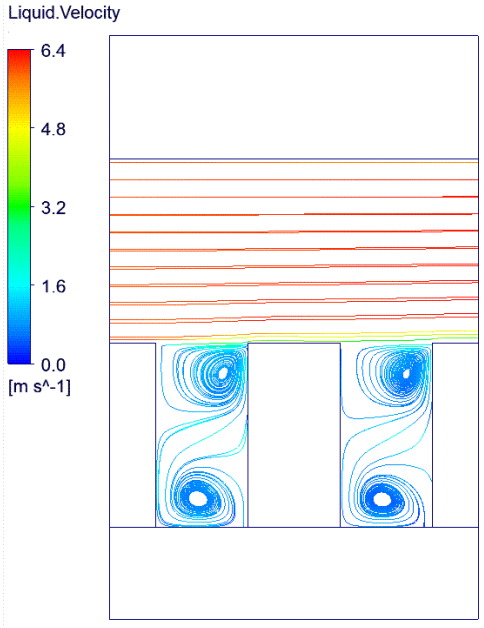


**Figure 99: 2D streamlines at quarter width across Div 6x6mm design**

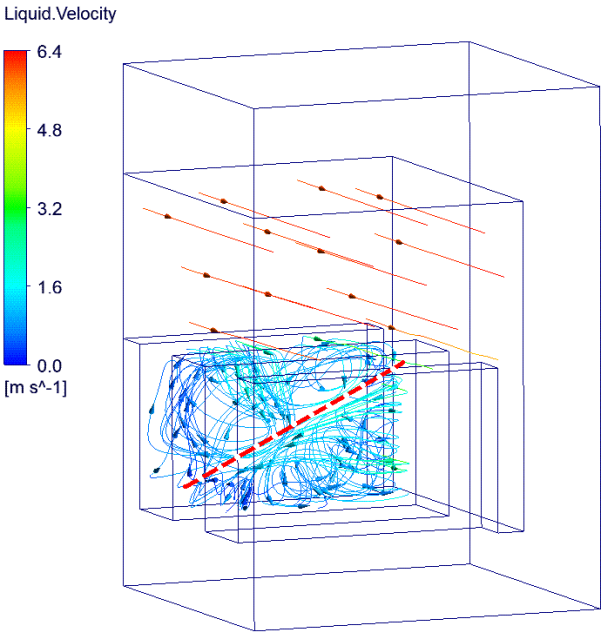


**Figure 100: 3D streamlines within a cavity of the Div 6x6mm design (red line indicating two distinct regions)**

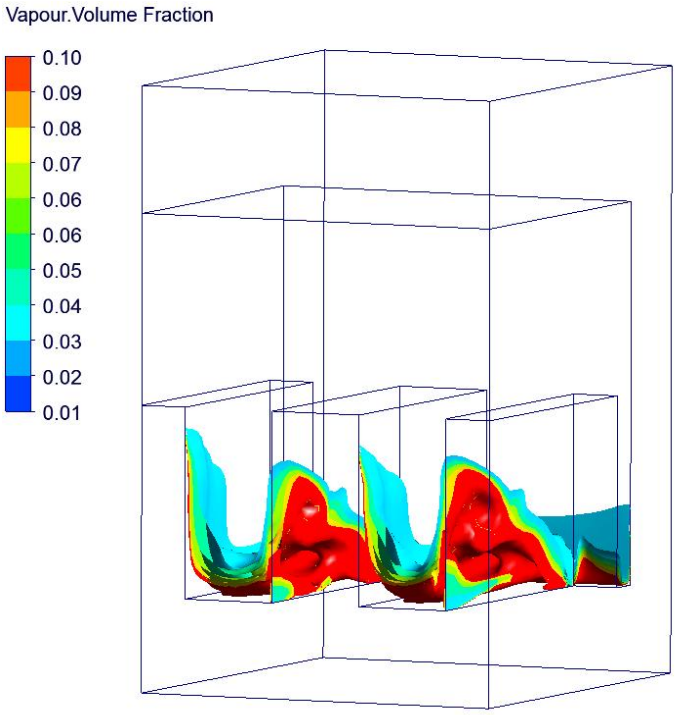


**Figure 101: Vapour volume fraction predicted in Div 6x6mm design at 15MW/m$^2$**

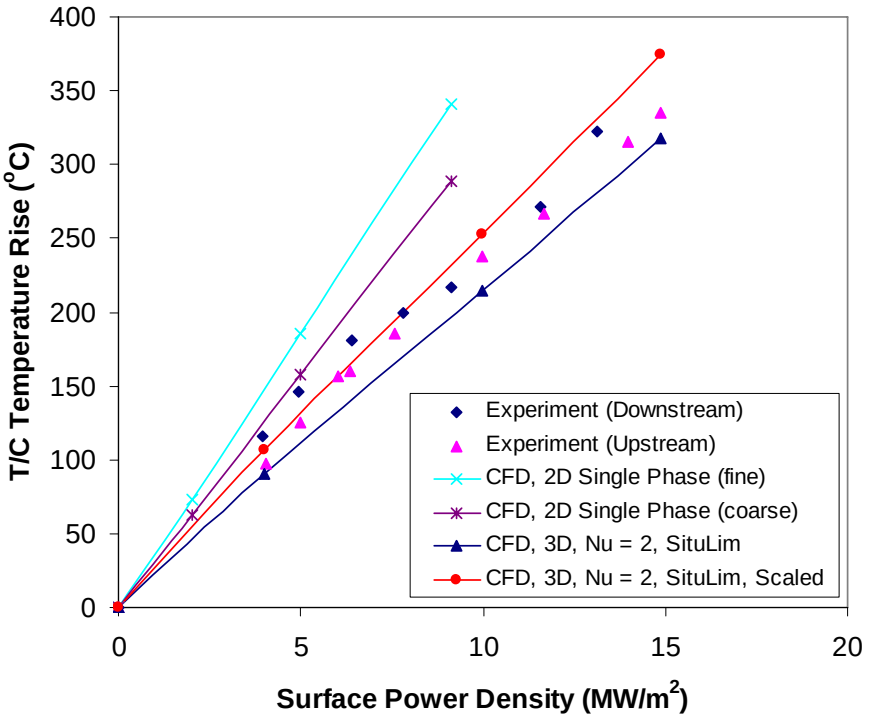


**Figure 102: Performance of customised boiling model against Div 6x6mm HV**

### 5.3.4 Validation case 4: Mk I JET HyperVapotron

#### 5.3.4.1 Experimental data

The experimental data for this design is not ideal. First of all, whilst error bars are not given in the original paper, the spread of data points indicates potentially significant errors in the measurement of surface power densities and / or temperatures. In addition, as well as not specifying the inlet temperature, the paper doesn't clarify whether the temperature plotted is the thermocouple temperature (rise or absolute) or surface temperature (rise or absolute). However, these are the only performance curves available for deep, 8×3mm cavities which present the greatest test of the CFD model's capabilities.

To make it useful from a validation standpoint, the data was therefore interpreted in a number of different ways and then transformed into what the thermocouple temperature rise would have indicated (based on the different assumptions). The resultant data with error bars is shown in Figure 103. For instance, if the original data was in fact absolute surface temperature with an inlet temperature of ~50°C, this would yield the data at the lower bound of the error bars (once it was transformed to give the equivalent thermocouple temperature rise). If, however, the original data was indeed a direct measure of the thermocouple temperature rise, this would yield the values at the upper bound of the error bars.

The minimum acceptance criteria for any CFD model of this geometry will therefore be its ability to predict performance curves that lie in the ranges indicated.

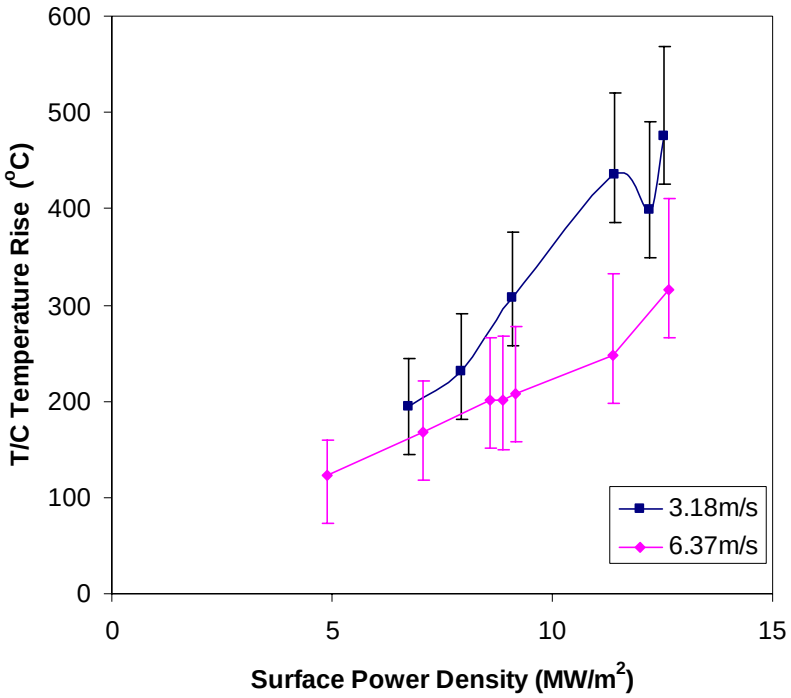


**Figure 103: MkI JET HV experimental data to be used in the CFD validation exercise**

#### 5.3.4.2 CFD Grid

A similar grid sizing as used in the validation case above was employed here, resulting the grid as shown in Figure 104.

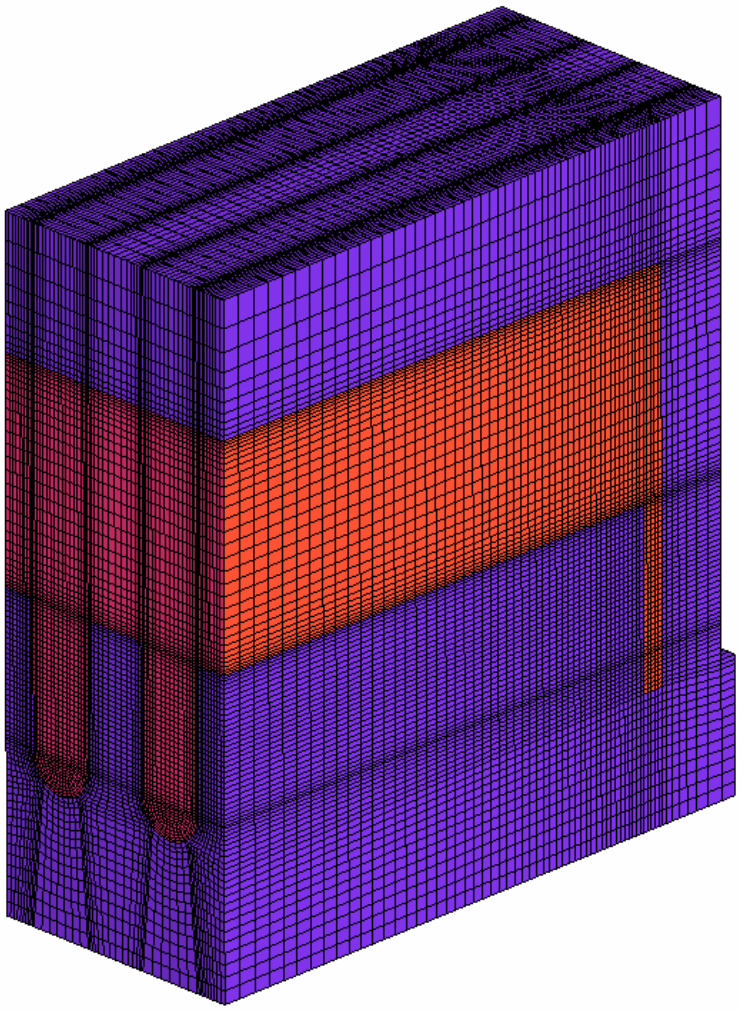

**Figure 104: MkI JET Hypervapotron CFD grid**

#### 5.3.4.3 Customised boiling model

This design exhibits the deepest cavities of the four validation cases. Again, the analysis performed in section 4.2 can be used to predict that several quasi-stable vortices would be expected in a cavity with this aspect ratio. As a result, like the Div 6x6mm case, the 3D engineering model of this configuration will suffer from inaccuracies due to the requirement of a coarser mesh to work with the boiling model. In addition, convergence at the high heat fluxes (>10MW/m$^2$) was not always achieved. Any solutions where the r.m.s. of mass and heat transfer residuals was not <= 1e-4 were not included in the performance curves.

It can be seen from Figure 105 that, for an inlet velocity of 6.37m/s, scaled 3D boiling solutions[40] just enter the upper range of the experimental data. If the original data corresponded to "Thermocouple Temperature Rise", this would suggest that the customised boiling model was relatively accurate (if not, errors could be as much as 90%).

To assess whether the model could pick up the typical change in performance exhibited by this design when the flow velocity is reduced by a factor of 2, the solutions were also run at an inlet velocity of 3.18m/s. Experimentally, this resulted in a reduction in performance of approximately 50% at 10MW/m$^2$. Unfortunately, at the reduced flow velocity, convergence of the CFD model could not be achieved. It is postulated that vapour growth becomes unstable in lower corners of the cavity where flow velocities are low, reducing the heat transfer capability below a threshold where more and more vapour is produced within the cavity, eventually filling the cavity and causing the solution to fail. Clearly in reality, a stable operating regime is achievable at these conditions but this may correspond to the macroscopic vapour jets described in section 1.2.1 which are not within the modelling capabilities of this approach.

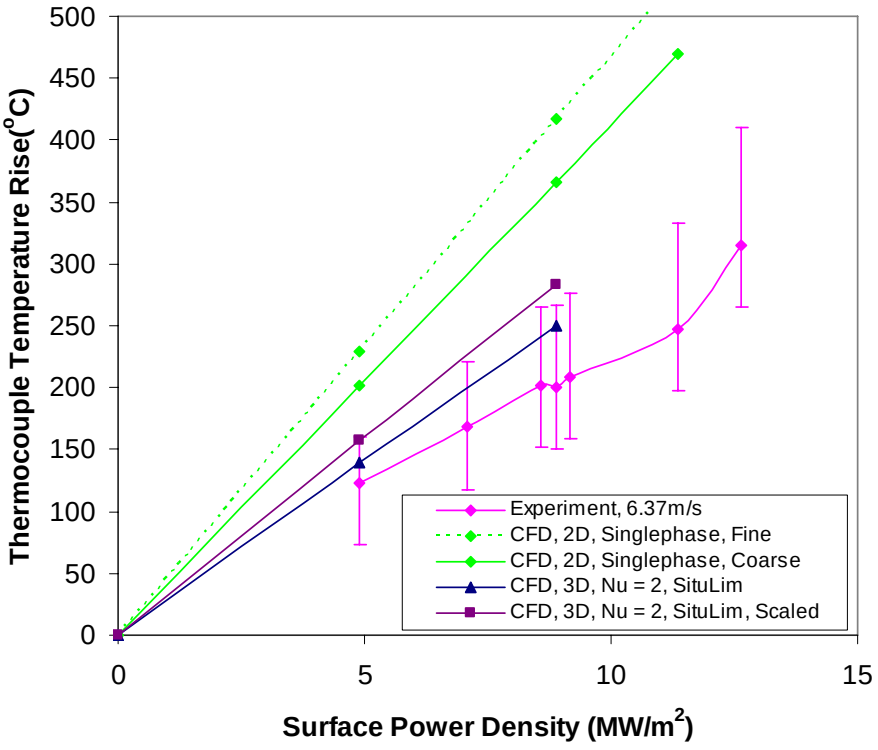


**Figure 105: Performance of customised boiling model against MkI JET HV (Vin = 6.37m/s)**

[40] In this case, the scaling factor was found to be 14%, very similar to the 15% applied to the Div 6x6mm case

## 5.4 Discussion of validation results

Validation of the CFD model against the 4 cases above reveals a number of interesting conclusions. These include:

- For relatively shallow 4mm cavities, the CFD model is relatively accurate in both single phase and nucleate boiling regimes (rms errors for Boxscraper and Div 4x3mm cases are 13.1% and 10.2% respectively)
- For these cases, the model can successfully take account of variations in inlet velocity, subcooling and pressure when predicting the thermal performance of the device.
- What is particularly interesting to note is that while the inclusion of boiling heat flux significantly improves agreement with experiment (see Figure 86), vapour production only contributes in the order of 1% of the total heat removed from the solid.
- Examining how the wall heat flux is split between convection to liquid and vapour production also offers a potential explanation of why performance is similar for the high velocity / high subcooling and low velocity / low subcooling cases (one might expect the former to significantly outperform the latter). It is suggested here that the first case benefits from increased single phase heat transfer coefficients (due to the high velocities) but the increased subcooling means less vapour is produced and therefore the heat transfer coefficient due to boiling is reduced (see Figure 106). Examining the CFD results confirms that the percentage of wall heat flux going into vapour production is almost 70% lower for the high velocity / high subcooling case (0.36% of total compared to 1.1% for low velocity / low subcooling case). Whilst both these values are small, it has been shown above that even small increases in the amount of heat flux going into vapour production can have a significant impact on overall performance, offering a potential explanation of why overall heat transfer coefficients are similar for both cases[41].
- Unfortunately, as the cavity depth is increased beyond 4mm, the model's accuracy reduces due to the necessity of using wall functions to get sensible solutions from the boiling model. This is primarily because the use of wall functions compromise the accuracy of single phase flow distribution and heat transfer predictions.
- In fact, for deeper cavities, the use of wall functions tends to overpredict the device's performance. This magnitude of this overprediction appears to be relatively constant for both 6 and 8mm cavities and over a range of flow rates (in

[41] Since performance is plotted using thermocouple temperature rise, the fact that the absolute temperature of the fluid and solid might be higher for low subcooling case is not taken into account in the performance curves.

the order of 12 to 15% based on 2D single phase analysis). This suggests that the use of a scaling factor when using this model for deeper cavities may be a valid method for compensating for this effect.

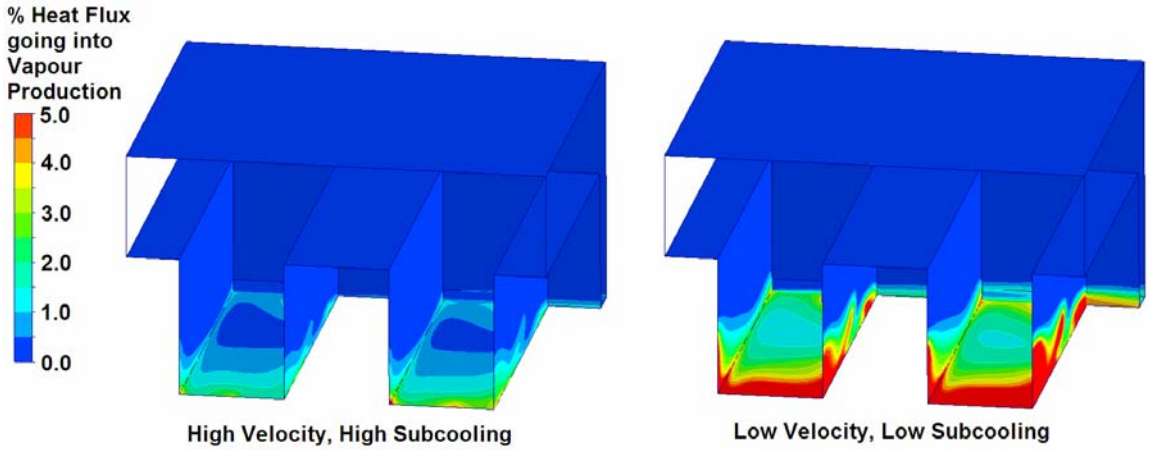


**Figure 106: Influence of inlet velocity and subcooling on percentage of heat flux going into evaporation**

- If such a scaling method is used for the 6mm fins, the rms error for the CFD model is 9.5% (comparable to the shallow cavity results). Surprisingly, had this effect not been taken into account, the model would actually have given better agreement of 7.4%. This is misleading and is the result of the underprediction of boiling heat transfer being compensated for by an overprediction in single phase heat transfer. It is suggested that scaled results should be used in any optimisation studies as this is at least likely to capture the single phase (dominant) heat transfer mechanism to a reasonable degree of accuracy.
- Unfortunately, for the deepest cavities modelled, the experimental data was not of a sufficient quality to draw definitive conclusions on the model's accuracy. All that can be concluded is that the CFD model predicts performance within the error band of the experimental results.
- At flow velocities and levels of liquid subcooling typical of fusion applications, the CFD model confirms that vapour production and condensation is localised to the cavity and doesn't result in vapour spilling out into the main channel. This agrees with Pascal-Ribot et all findings [53,54] and confirms what had been suspected for a number of years.
- As stated previously, it would appear that the Cole model for bubble departure frequency is not appropriate for this application. It was derived using pool boiling experiments, relies on buoyancy effects (shown here to be negligible) and ultimately fails to give accurate results in the full engineering model of the device (exhibiting an odd distribution of departure frequency over the wetted surface). In particular, it predicts lower frequencies in the hotter areas of the cavity which is

counter intuitive (see Figure 92). All of this seems to suggest that use of an alternative correlation for this parameter is a valid improvement to the model.

- Finally, whilst not explicitly modelled in this study, examination of the experimental results does indicate some qualitative conclusions about how certain parameters can delay the transition to CHF (which is almost always a key factor in the design of the design of a HHF device). Specifically it appears that increasing inlet subcooling and velocity, while not necessarily offering benefits in performance in the "normal" operating range, can in fact delay the transition to the third, hazardous operating regime by several $MW/m^2$.

Whilst many of the conclusions above give interesting insights into the applicability of the model and details of the heat transfer mechanisms, it should be acknowledged that the experimental data on which the validation is based is not ideal. Specifically, the following deficiencies must be taken into account:

- In a number of cases, inlet temperature and pressure are not specified for the experiment and "typical" values have therefore been specified in the CFD model (having said that, both experimental results and the CFD results suggest these have a relatively small effect on performance in the single phase and nucleate boiling regimes).
- Even in cases where the inlet temperature and pressure are specified, the position along the HyperVapotron where thermocouple measurements are taken is not stated. Given the fluid will undergo bulk heating and pressure losses all the way through the device means there will always be uncertainties in the exact fluid conditions at the point of measurement.
- Manufacturing tolerances will also affect the temperatures recorded. In particular, wall thicknesses and exact thermocouple positions are known to vary by several 100 microns which will affect the temperature measured.
- The exact material properties of the Cu alloy used for the HyperVapotron are also subject to some uncertainty. These are temperature dependent and also depend on the content and heat treatment of the alloy which have been subject to small variations in the history of HyperVapotron development at CCFE. To minimise the errors attributed to these effects, temperature dependent material properties have been applied in the CFD model and ITER-grade material properties have been assumed which are very close to those used for the JET material [91].
- Finally, for experiments where surface temperature is given, this is either calculated by extrapolating the thermocouple temperature using the 1D heat conduction equation or a calibrated IR camera, both of which introduce additional errors into the results.

For clarity, the validated model developed here is based on the modelling choices summarised in Table 15

.

| Feature | Description | Ref |
|---|---|---|
| **Geometry** | 3D | N/A |
| **Grid** | Structured (Hexahedral) | N/A |
| **Boundary Conditions** | Inlet, Uniform Velocity | N/A |
| | Outlet | N/A |
| | Symmetry at midplane | N/A |
| **Turbulence modelling** | Multiphase, RANS, SST k-omega | See sections 2.3.2.2 and 2.3.2.4 |
| **Near wall method** | Automatic near wall treatment | See section 2.3.3.2 |
| **Wall Boiling Model** | RPI method | See section 2.4.2.2 |
| **Bubble Departure Diameter** | Tolubinski Kostanchuk model | See section 2.4.2.3.1 |
| **Bubble Departure Frequency** | Situ model, capped using liquid rotation time in cavity. | See sections 2.4.2.3.2 and 5.3.1.4 |
| **Bubble Waiting Time** | T = 0.8 × Detachment Period | See section 2.4.2.2 |
| **Liquid Quenching Heat Transfer Coefficient** | Del Valle Kenning | See section 2.4.2.2 |
| **Nucleation Site Density** | Lemmert and Chawla model | See section 2.4.2.3.3 |
| **Bubble diameter in the bulk flow** | Anglart and Nylund model | See section 2.4.2.3.4 |
| **Interphase mass transfer** | Thermal Phase Change model | See section 2.4.2.4.1 |
| **Interphase momentum transfer** | Drag force included (Schiller Naumann correlation)<br>All non-drag forces ignored | See section 2.4.2.4.2 |
| **Interphase heat transfer** | Interphase Nusselt number fixed, Nu = 2.0 | See section 5.3.1.4 |

**Table 15: Summary of validated HyperVapotron model**

The recommended convergence strategy for this model is as follows:

1. An isothermal model should be solved using liquid only in the fluid domain to quickly establish a steady state flow pattern within the fluid domain.
2. Heat transfer should then be activated with an appropriate heat flux applied to the front wall of the solid. The solution should be terminated when the wetted wall superheating reaches 5K (typical superheating at which incipient boiling occurs). This can be done manually or automatically.
3. The full multiphase, boiling can then solved using the above as initial conditions. This ensures a gradual increase in vapour creation which can tolerate larger timesteps than if large parts of the near wall fluid were allowed to become superheated prior to turning the boiling model on.

## 5.5 Exploration of potential improvements to the geometry

The final step in this study is to examine whether geometrical changes could be found that could improve the HyperVapotron's performance (using the validated model above). A problem such as this, where the geometry can be defined by a finite and relatively small number of parameters (such as fin depth, fin width, channel depth, fin angle etc), would appear to lend itself to formal optimisation methods that have been well established for many years (the Taguchi method [92] for instance). Some initial attempts were made at this but it was quickly found that the sensitivity of convergence to the combination of geometry and boundary conditions made this extremely difficult. Alternative methods were therefore sought that could at least begin to examine potential improvements in the HyperVapotron's geometry.

The method selected was to begin with an initial geometry based on the lessons learnt from Chapter 4 then incorporate progressive changes, discarding those which had negative or no effect and keeping those which improved the thermal performance of the device. Clearly this is not ideal (e.g. it doesn't account for how the various combination of individual changes affect the performance) but it does illustrate how significant virtual prototyping could be used to improve the geometry before building a real prototype for full power handling tests.

To establish the starting point, it was decided to take the 4 different cavity sizes examined in chapter 4 then standardise on all boundary conditions and the remaining geometrical parameters (such as front wall thickness, cross-stream width, channel height, see Figure 107). A performance comparison could then be made to establish the optimum cavity dimensions to use as a starting point. The model set up is illustrated in Table 16.

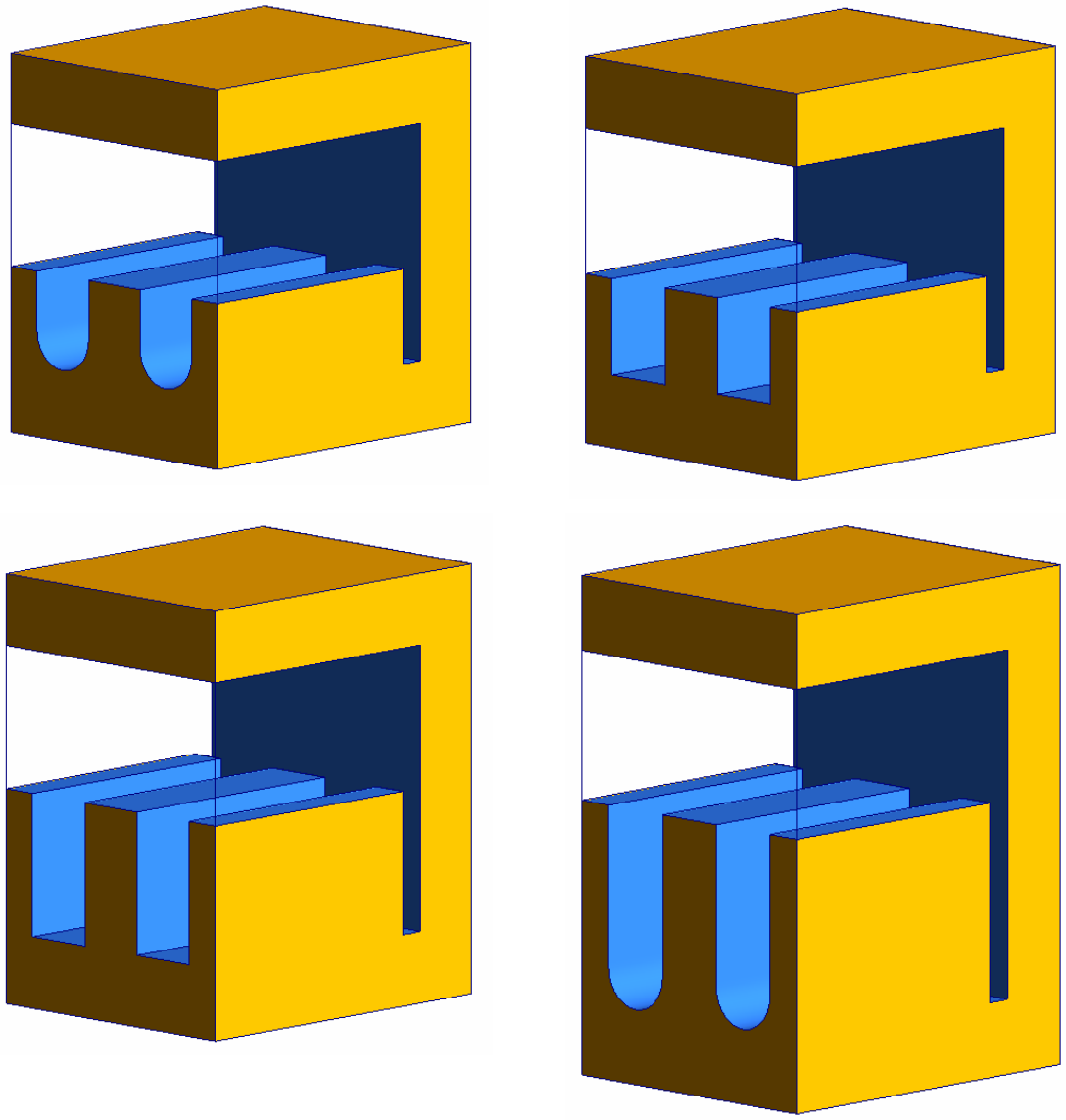

**Figure 107: Existing HyperVapotron cavity geometries (standardised)**

| Setting | Modelling choice | Comments |
|---|---|---|
| **Channel height** | 6mm | This allows sufficient flow rates (at reasonable pressure drops) to ensure coolant remains well subcooled for the typical powers seen by these devices in fusion applications (studies have also shown that this has little influence on performance at a given flow velocity). |
| **Wall thicknesses** | 3mm | Good compromise for optimal thermal performance and pressure handling capability. |
| **Side slot width** | 1mm | Value used in most HyperVapotron tests |
| **Channel width (cross-stream)** | 12mm | Approximate average of values tested |
| **Inlet velocity** | Uniform, Vin = 6m/s | Typical value for a JET-relevant HyperVapotron. |
| **Inlet subcooling** | Uniform, Tsat - Tin = 110K | Typical value for a JET-relevant HyperVapotron. |
| **Inlet pressure** | Uniform, Pref = 6bar | Typical value for a JET-relevant HyperVapotron (Note: For ITER and future reactors, if water is used as the coolant the inlet pressure tends to be significantly higher, e.g. ~20bar for ITER) |
| **Surface heat flux** | Q = 10MW/m$^2$ | Typical value for a fusion-relevant HyperVapotron. |

**Table 16: Standard geometry and boundary conditions used in the assessment of existing HyperVapotron cavities**

The performance of the existing cavity sizes illustrated above is compared by examining the surface temperature profile across the width of the device, just below the central fin (see Figure 108). The results are shown in Figure 109 (normalised relative to peak temperature rise found in 4×3mm square cavity case and shown as if the whole cavity width had been modelled). It can be seen that, even without the scaling factors that should be applied to the deeper cavities, the square, 4mm cavity is clearly best from a thermal standpoint (yielding lowest temperatures in the solid). Comparing square and rounded versions of the 4mm cavity shows that the square bottom, with its additional surface area, is slightly better relative to the rounded equivalent. What was slightly surprising is that convergence also seemed slightly better for this configuration. As a result, the square 4×3mm case is a good starting point when examining changes to the geometry that could potentially improve the HyperVapotron's performance.

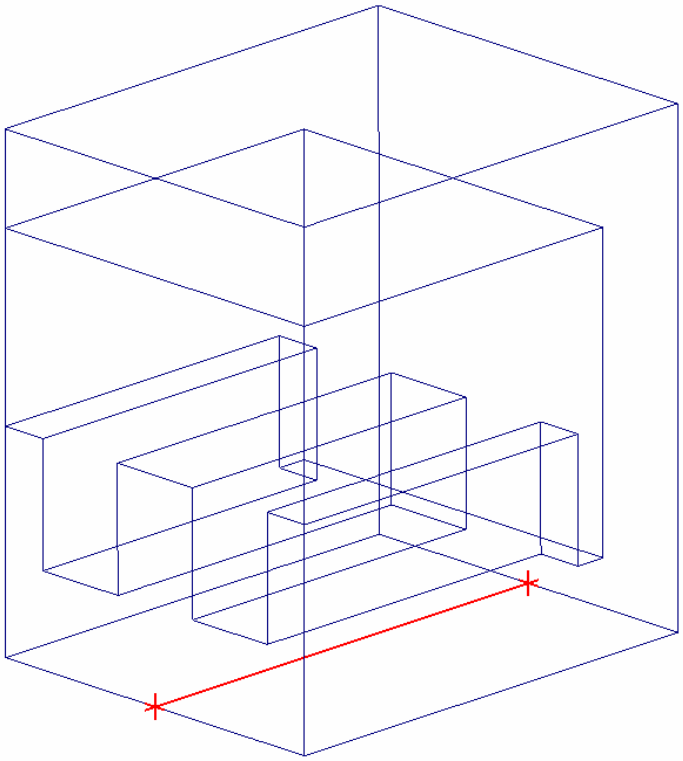

**Figure 108: Axis along which the temperature in the solid is measured**

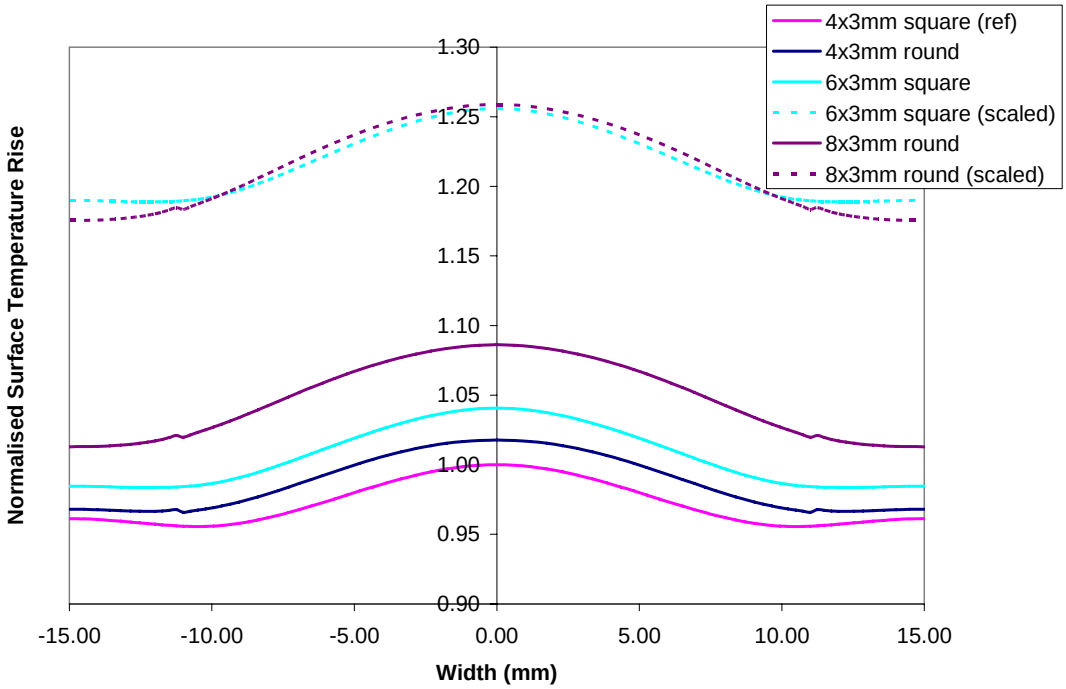


**Figure 109: Comparison of existing HyperVapotron cavity designs (normalised to peak temperature rise in 4x3mm square case)**

Before examining potential improvements to the geometry, a short investigation into the effect of inlet pressure was undertaken. There have been contradictory statements in various publications over the effect of this parameter on the performance of the device [13,15]. To evaluate its effect, the 4×3mm reference geometry was rerun with inlet pressure reduced from 6 to 2bar. For a fair comparison, the inlet temperature was also reduced to 10°C, maintaining the same level of inlet subcooling at ~110K. Even so, the CFD solutions showed that the reduced inlet pressure case actually resulted in a small reduction in the amount of heat removed from the solid and an increased peak temperature rise of 305K (compared to 280K for the 6bar solution). It is thought this is most likely due to small changes in fluid properties (such as a decrease in liquid thermal conductivity for example). This reduction in heat transfer performance, however, is more than compensated for by the cooler bulk temperature of the fluid (10°C compared to 50°C for the 6bar case). As a result, absolute temperature in the low pressure case is actually 15°C lower than in the 6bar case (315°C compared to 330°C).

It can therefore be concluded that for a fixed value of inlet subcooling, a reduction in inlet pressure results in a small reduction in the amount of heat that can be removed from the solid but that this may well be acceptable if lower absolute temperatures and pressure stresses in the wall of the device were desirable.

Having examined the effect of inlet pressure on performance, a number of potential improvements to HyperVapotron geometry can now be considered. These are evaluated at the fixed inlet conditions described in Table 16. Some of the proposed modifications are based on experimental findings whilst others are based on a better understanding of the contributions to performance of the various heat transfer mechanisms gained in chapters 3 and 4. The modifications are listed in Table 17 and illustrated in Figure 110.

| No's | Modification | Comments |
|---|---|---|
| 1 | No fin | It is worth confirming that the conclusions about the benefits of including a fin made for single phase flows still applies when boiling is included. |
| 2 | 2mm deep fin | Likewise, whilst a 4mm is known to better than a 6 or 8mm fin, a reduced 2mm fin was also examined to ensure that 4mm is indeed near the optimum |
| 3,4 | Side slot width increased to 2 and 3mm | As shown by Altmann (and others) the incorporation of a side slot of 1mm width greatly improves performance at the side wall. Could enlargement of this slot increase performance any further? |
| 5 | Fin profile angled both sides | Would this facilitate mass and heat exchange between the cavities and the main channel increasing thermal performance? |
| 6 | Fin top cut away* | Would this increase the flow impingement on a larger part of the fins increasing overall performance? |
| 7 | Fin orientation relative to flow* | Ezato showed that angling the fins to the flow could also improve thermal performance (although in that case it was for triangular fins). There doesn't appear to be a strong reason why this wouldn't be the case for rectangular fins. |

**Table 17: Description of modifications examined as part of this study**

**Note: For these geometries, the simple 2 fin, symmetric model could not be used so new geometries had to be developed. For these, a square 4×3mm cavity equivalent was also constructed (not shown here) to get a fair assessment of any changes in performance induced by the modifications.*

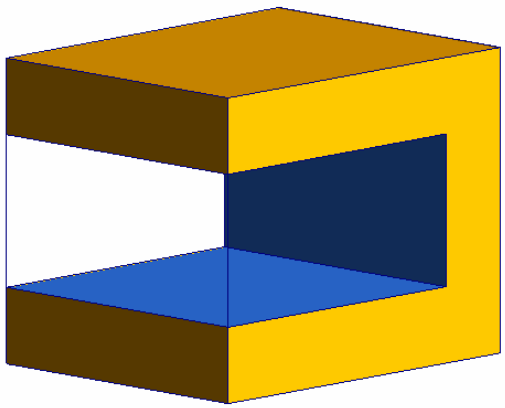

**1**

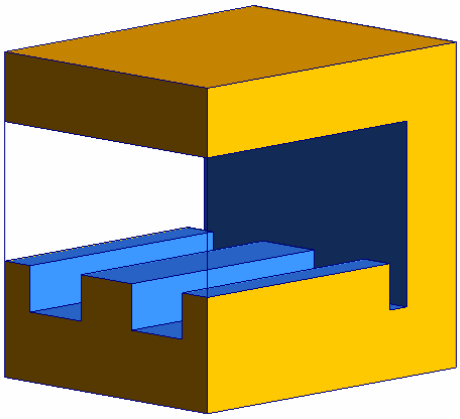

**2**

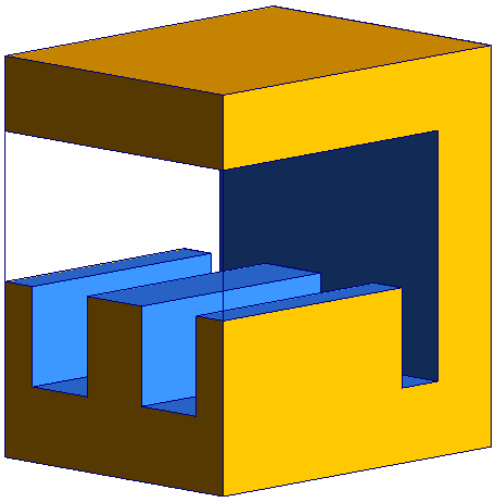

**3**

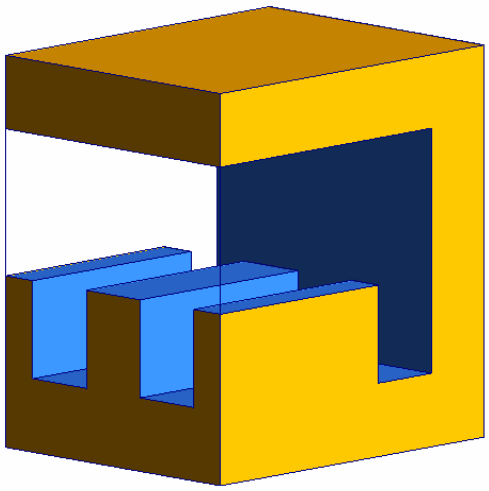

**4**

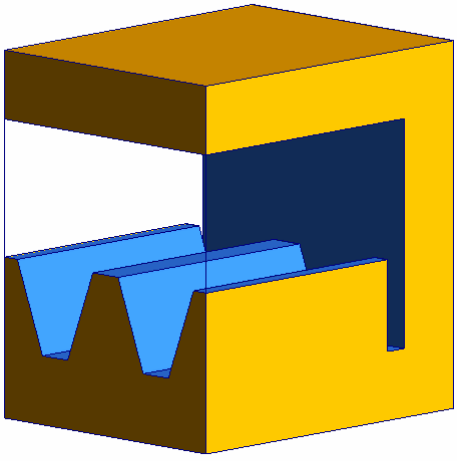

**5**

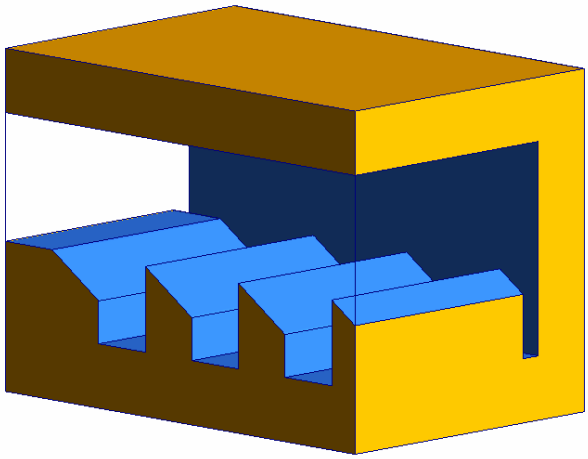

**6**

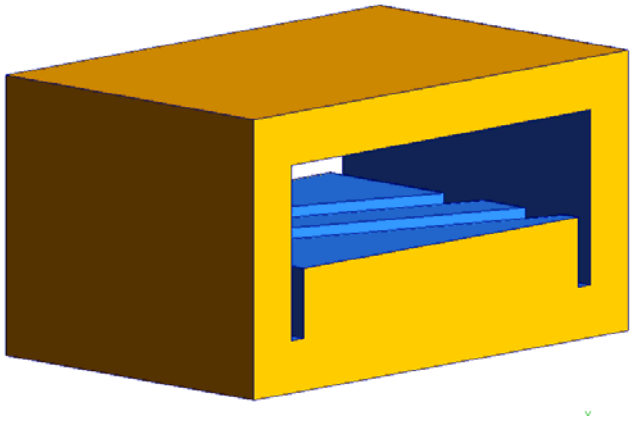

7

**Figure 110: Illustration of modifications examined as part of this study**

The results of these modifications are shown in Figure 112 to Figure 115 (in all cases, performance is again normalised against the 4×3mm square reference case). Examining Figure 112 reveals definitively that a 4×3mm cavity is close to optimum when compared to the no fin, 2mm, 6mm and 8mm fin cases (the latter two examined in Figure 109). It also demonstrates that incorporation of fins into a High Heat Flux device can improve the thermal performance by ~20%, all other things being equal (e.g. inlet velocity, subcooling, power density etc).

The remaining curves suggest small reductions in surface temperature rise are possible albeit in localised spots. Unfortunately, none of the modifications attempted here have resulted in a significant improvement in performance over the entire width of the device. Some points of interest, however, are noted below:

- Increasing the width of the side slot reduces the heat transfer capability at the side walls but provides a small improvement in the centre of the device (neither is significant, see Figure 113). Recent studies have suggested that increasing the side slot width can be beneficial from a thermo-mechanical standpoint as it reduces the peak stress in this location (extending the fatigue life). Results from a Finite Element structural analysis performed by the author are shown in Figure 111; these show a reduction in the peak stress at the root of the slot of up to 20%. So while there appears to be little thermal benefit in this modification, this result might allow HyperVapotron designers to improve the structural performance of the device with no penalty in terms of thermal performance.
- Unsurprisingly, with the fin angled relative to the flow, the thermal distribution across the width of the device is no longer symmetrical (see Figure 114). Overall, there appears to be little improvement in performance, with only small temperature reductions resulting at one of the side walls. What is certainly not apparent is the 25% reduction in surface temperature reported by Ezato (see Figure 29). It is suggested that this is less to do with the difference fin profile between this geometry and Ezato's (rectangular relative to triangular fins) and

more likely due to the modelling approach. In particular, care must be taken here as only a single fin has been modelled using inlet / outlet boundary conditions. Whilst this may have been acceptable for the perpendicular fins (as shown in section 4.1), it is likely that larger models, with periodic boundary conditions are required to set up the swirling aspect of the flow that Ezato suggests may be responsible for the improved performance. This could not be done within the scope of the study but it is suggested that the modelling approach developed here should still be suitable and could therefore be used to try and reproduce and optimise this effect as part of future work (see section 6.2).

- Finally, introducing a slope to the tops of the fins (to encourage more flow impingement and better heat transfer) reduces surface temperature rise by ~1% at the side walls but results in no change in the peak (see Figure 115).

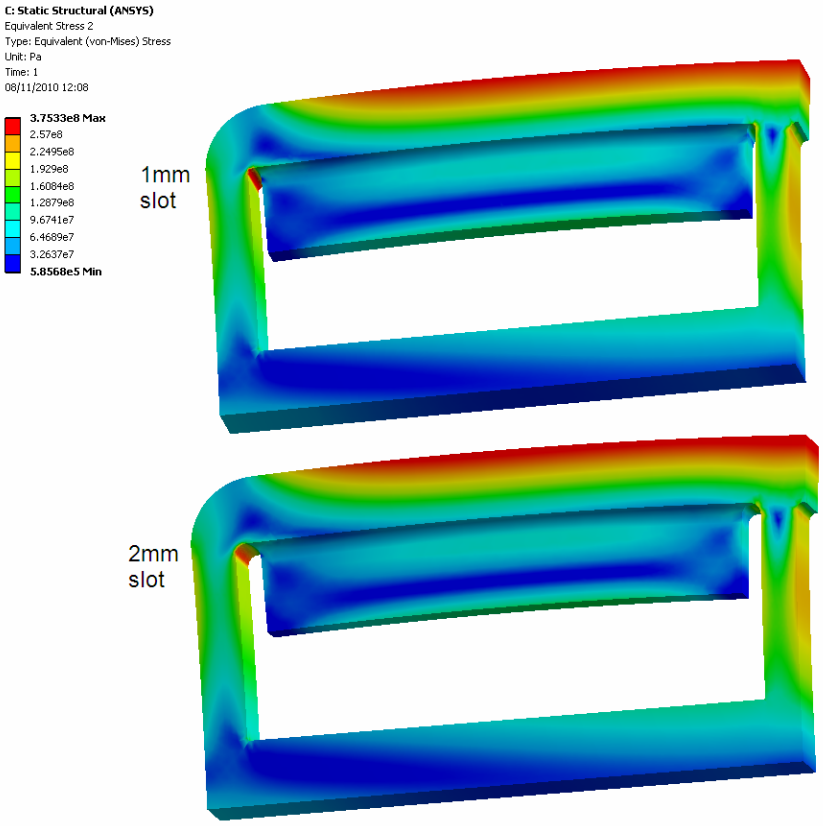


**Figure 111: Finite Element Analysis demonstrating reduction in stress concentration that can be achieved by widening the side slots.**

Whilst no significant improvement on the square 4×3mm fin has been derived here, it is clear that only a limited number of cases have been examined within the time constraints of this research. With more time and computing resources dedicated to this problem, the author strongly believes that the methodology and submodels developed here will allow designers of future high heat flux components to indeed extend the operating range of these devices to meet the demanding requirements foreseen in a fusion reactor.

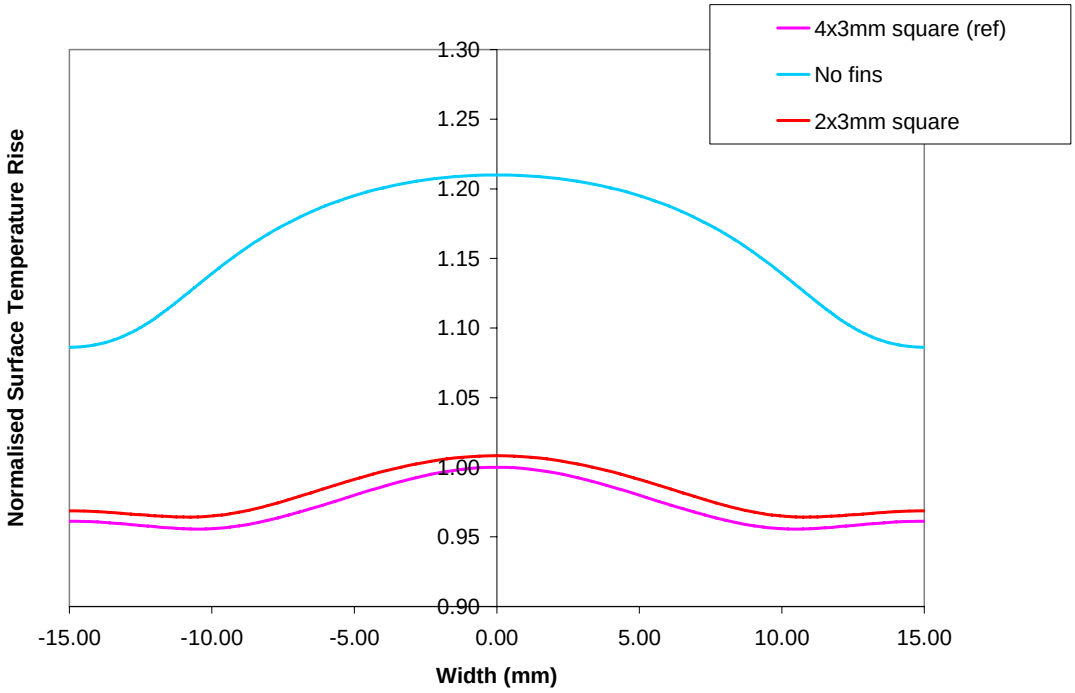


**Figure 112: Impact of reducing fin depth or eliminating fin altogether**

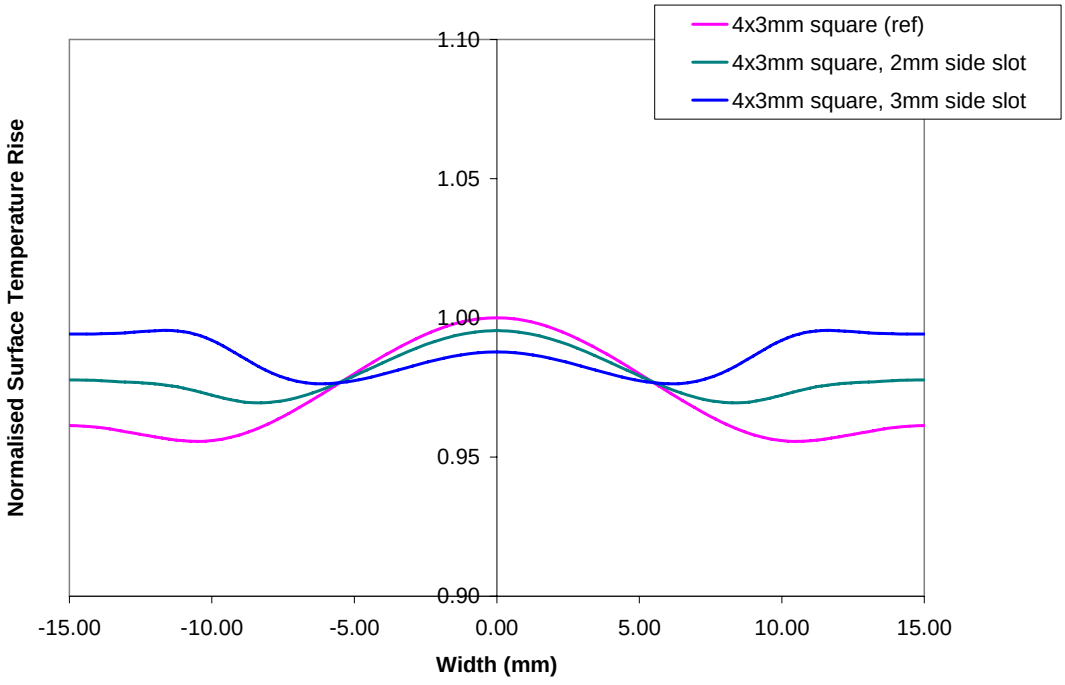


**Figure 113: Impact of increasing side slot width**

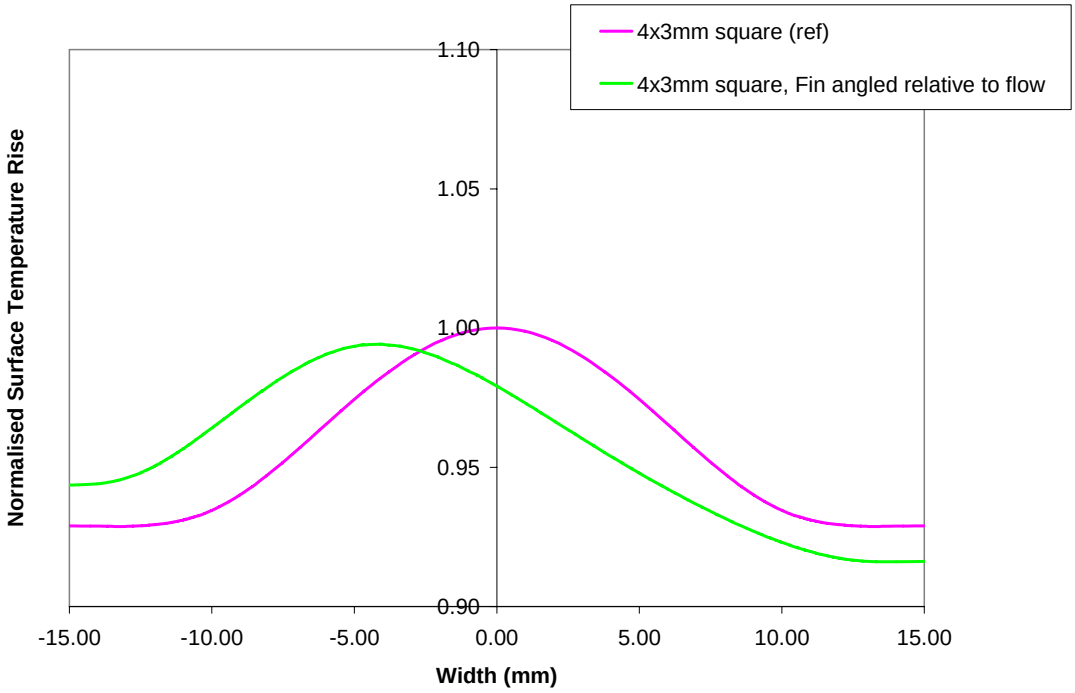


**Figure 114: Impact of angling fins relative to flow**

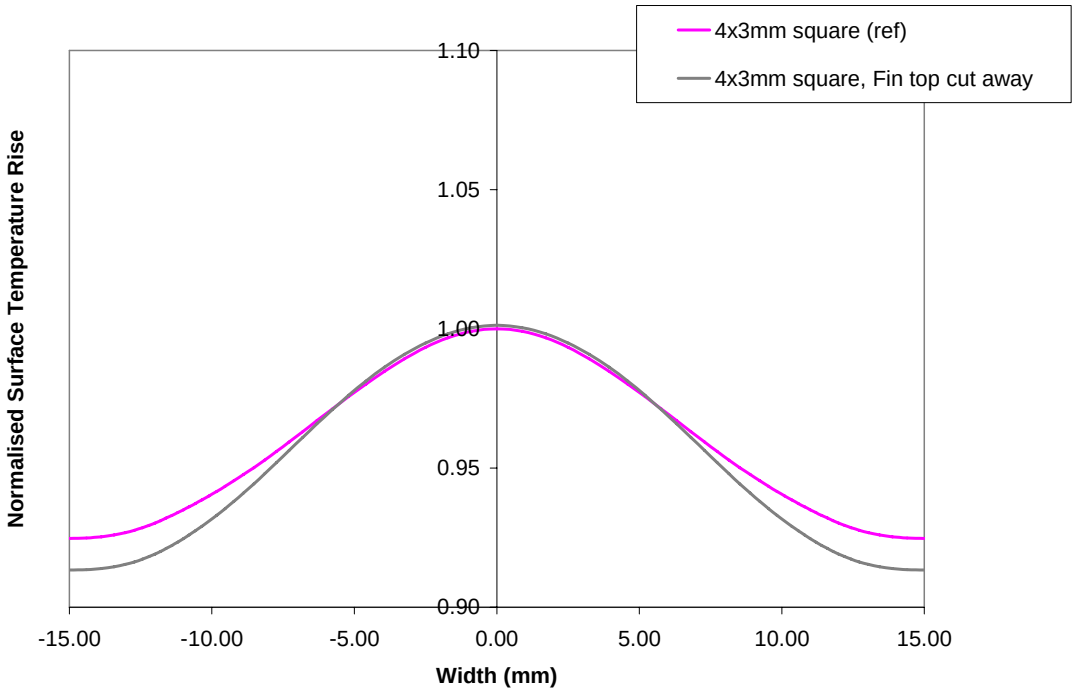


**Figure 115: Impact of angling top of fins**

# 6

# 6 Conclusions and Outlook

An in-depth study into the heat transfer mechanisms present within a HyperVapotron has been undertaken in the context of supporting current and next generation nuclear fusion devices. This chapter summarises the main conclusions drawn from this research as well as proposing future areas of study which may advance both the knowledge and engineering tools critical in developing optimised heat transfer solutions for fusion applications.

## 6.1 Conclusions

HyperVapotrons were first conceived in the 1950's as a method for cooling cylindrical electron tubes. Early studies showed fins combined with boiling heat transfer could sustain heat fluxes in excess of 20MW/m$^2$. It has been proposed that one of the key mechanisms enabling this exceptional performance is the ability to operate with parts of the wetted surface at Critical Heat Flux. Burn out is avoided by conduction of excess heat into other parts of the fins where single phase flow and / or nucleate boiling can safely convect the heat away to the bulk fluid.

As more advanced tokamaks were developed in the latter part of the 20$^{th}$ century, High Heat Flux devices were required for key parts of the tokamak as well the auxiliary heating systems. The JET experiment appears to have been the first tokamak to adapt cylindrical HyperVapotron to a rectangular geometry capable of taking high one-sided heat loads. Following initial feasibility studies, researchers at JET and other fusion associations began a long testing programme beginning in the 1980s and still ongoing today. This programme has produced a wide range of experimental data for a variety of geometries and flow conditions. Whilst this gives useful indications of where improvements can and have been made, the output data is generally restricted to thermocouple measurements in the walls of HyperVapotron and is of limited use when

trying to develop an analytical model of the device (where validation requires more fundamental information within the flow such as velocity distributions, wall superheating, vapour distributions as well as boiling parameters such as nucleation site density, bubble size, detachment frequency etc).

In spite of these challenges, the primary objective of this study was to develop a computational model of the HyperVapotron device of sufficient accuracy to enable it to be used to perform design optimisation and virtual prototyping. This could potentially save significant time and money when searching for improvements in High Heat Flux technologies that are critical to the performance of future fusion reactors.

To achieve sufficient confidence in the results, validation of the modelling techniques is critical. Given the lack of relevant data available from the HyperVapotron tests, the strategy has been based on validation of specific aspects of the problem, using both experimental results and high order ILES results.

The initial part of this study revealed that 2D RANS solutions, with appropriate choice of turbulence model, grid refinement and near wall methods, can demonstrate comparable levels of accuracy when compared to 3D, high order ILES predictions of single phase flow and heat transfer through an idealised HyperVapotron cavity. In addition, if side wall effects are ignored, the need for periodic boundary conditions, 3 dimensional domains and fully developed inlet conditions have all been shown to be negligible in terms of predicting overall performance. One of the benefits of this realisation is that these simplified 2D solutions (with significantly reduced computational requirements) could be used to perform highly efficient design studies (such as determining of the optimum cavity aspect ratio for instance).

Whilst these 2D solutions gave useful guidance on some of the trends, they are of limited use in developing an accurate engineering model of the HyperVapotron device. The finite width and presence of side slots near the wall mean a 3D solution is essential to get an accurate picture of the flow and heat transfer distributions. In addition, at fusion-relevant heat fluxes, boiling heat transfer plays a key role in overall performance. Achieving a converged, multiphase 3D solution for this application, however, is not trivial and strategies have been derived to achieve robust yet efficient convergence for a wide range of cases.

The resultant solutions have confirmed that incorporating the RPI wall boiling approach into a multiphase, CHT model of the HyperVapotron cavity is essential in improving accuracy at elevated heat fluxes. A number of alternative submodels were subsequently examined in an attempt to improve accuracy still further. Of these it was found that a modified version of the Situ correlation for bubble departure frequency was most effective, yielding considerably higher departure frequencies and vapour volume fractions in the hottest regions of the cavity. Using this modified model, it has been confirmed that of all the standard HyperVapotron cavities built thus far, a 4×3mm aspect ratio with square bottom performs best.

In terms of inlet conditions, it has long been known that increased inlet velocity improves thermal performance and this model successfully predicts the magnitude of this

improvement in a number of cases. There have, however, been conflicting theories regarding the effect of some of the other inlet conditions, in particular inlet pressure. The CFD model developed here has been a useful tool in trying to resolve these disparities. For the 4×3mm cavity, it has been shown that reducing pressure at constant inlet subcooling reduces the thermal performance by a small amount (most likely due to small changes in fluid properties at lower pressure) but that this is more than offset by the reduction in absolute temperature due to reduced bulk temperatures. This would tend to suggest that, so long as designers can maintain sufficient margins to burnout, it is desirable to operate HyperVapotrons at reduced inlet pressures and temperatures.

Finally, this research concludes by examining potential design improvements to the standard HyperVapotron geometry. Interestingly, it appears that a square-bottomed, 4×3mm cavity performs exceptionally well and no simple modifications have been found thus far to significantly increase thermal performance and reduce peak temperatures. These are initial indications only, however, and it is highly likely that a full optimisation exercise would reveal improvements that could enhance the power handling capability of the device. A full optimisation exercise, however, was not the subject of this research and it will be up to future researchers to build on this work, using the tools and strategies developed here to develop new HyperVapotron designs that can safely remove significantly more power than the current generation of HHF devices (see section 6.2). Whilst a number of other HHF concepts exist, the intrinsic benefits offered by the HyperVapotron, such as reduced pumping power, predictable transition to CHF and the ability to incorporate this heat transfer enhancement into a wide variety of profiled surfaces, means this tool should be highly relevant in designing HHF devices for future fusion reactors.

## 6.2 Future Work

This study has gone a long way in providing an engineering tool for use in HyperVapotron design. As stated from the outset, however, it was not realistic for the model to cover all ranges of HyperVapotron operation. As a result, the CFD model assumes the nucleate boiling region continues indefinitely and fails to capture the growth of a vapour film around the cavity with associated drop off in heat transfer efficiency and eventual burnout. Until this is incorporated, additional methods are required to calculate the safe operating limit with sufficient margin to burnout. Ultimately, more sophisticated CFD models should be developed to cover all ranges and provide the designer with a complete operating curve and establish a safe operating limit.

Whilst deeper cavities have generally been shown to be less thermally efficient, thorough optimisation studies could well include a much wider range of geometries where large scale flow separation is actually beneficial to performance. In order to successfully model these scenarios, modified boiling models are required that are compatible with standard near wall approaches, ensuring that the model can correctly capture the flow separation and vortex patterns as well as the vapour production within the cavity.

In terms of design improvements, it is clear that some design modifications require much longer or larger models to capture the flow development along the device and establish the correct performance characteristics in middle of the device (such as the swirling flow induced by angled fins for instance). With more time and larger computing facilities dedicated to this problem, these types of modifications could be examined in more detail in a more thorough attempt to optimise the power handling capability of these devices.

# Bibliography


1 http://www.jet.efda.org/pages/jet.html

2 http://www.iter.org

3 Duesing, G., Altmann, H., Falter, H., Goede, A., Haange, R., Hemsworth, R.S., Kupschus, P., Stork, D., Thompson, E. *Neutral Beam Injection System*. Fusion Technology, Vol 11, January 1987

4 Chang, S.H., Baek, W. Understanding, predicting and enhancing Critical Heat Flux. In: *Proceedings of the 10th International Topical Meeting on Nuclear Reactor Thermal Hydraulics (NURETH-10)*, Seoul, Korea, October 5-9, 2003.

5 Beurtheret, C. Transfert de flux superieur a 1kW/cm2 par double changement de phase entre une paroi non isotherme et un liquide en convection forcee, in : *Proceedings of the Fourth International Heat Transfer conference*, Versailles, France, September 1970.

6 Thompson CSF. A breakthrough in anode cooling systems: The Hyper-Vapotron. Internal report. Date unknown.

7 Nukiyama, S. (1934). *The Maximum and Minimum Values of Heat Q Transmitted from Metal to Boiling Water under Atmospheric Pressure*, J. Jap. Soc. Mech. Eng., Vol. 37, pp. 367-364 (in Japanese) (trans. In Int. J. Heat Mass Transfer, Vol. 9, pp.1419-1433 (1966))

8 Cattadori, G., et al. (1993). *HyperVapotron Technique in Subcooled Flow Boiling CHF*. Experimental Thermal and Fluid Science, Vol. 7, p. 230 – 240.

9 Falter, H, Thompson, E. (1996). *Performance of HyperVapotron Beam-Stopping Elements at JET*. Fusion Technology, Vol. 29, p. 584-595

10 Aybay, O., Breuer, M., He, L. *Large–Eddy Simulation of Three–Dimensional Cavity Flow Using a Time–Conservative Finite–Volume Method*, Notes on Numerical Fluid Mechanics and Multidisciplinary Design, 2010, Volume 112/2010, 465-472.

11 Thompson CSF. (1980). Technical Report to JET Contract JC110 VHXX. *Application of HyperVapotron Techniques to source of the JET cooling problems*. (report unavailable).

12 Falter, H. (1983). *Test of Two Hypervaptron Beam Stopping Panels at LBL Berkley*. JET Internal Communication. (unpublished report).

13 Tivey, R., Falter, H., Haange, R., Hemsworth, R., Massmann, P., Stabler, A. Testing of Beam Stopping Elements Using HyperVapotron Cooling. In: *Proceedings for the 12th IEEE/NPSS Symposium on Fusion Engineering*, Monterey, CA, Oct. 1987, p. 1122 – 1125.

14 Blatchford, P. UKAEA Internal Report. *Correlation of ANSYS HyperVapotron modelling with*

*experimental results, and proposal for a new HyperVapotron design*. CD/MU/PP/423/TN/004.

15 Altmann, H., Falter, H., Hemsworth, R., Martin, D., Papastergiou, S., Tivey, R. A comparison between HyperVapotron and Multitube high heat flux beam stopping elements. In: *Proceedings for the 13th IEEE/NPSS Symposium on Fusion Engineering*, Knoxville, TN, October 1989, p. 931 – 936.

16 Falter, H.D., Deschamps, G.H., Hemsworth, R.S., Martin, D., Massmann, P. Test of Divertor Elements, JET Divisional Note, JET-DN-C(91)93

17 Ciric, D., Akiba, M., Falter, H-D., Martin, D., Sato, K., Yokoyama, K. Design Issues and Fatigue Lifetime of HyperVapotron Elements of the JET Neutral Beam Injectors, In: *Proceedings for the 18th IEEE/NPSS Symposium on Fusion Engineering*, Albuquerque, NM, USA. 1999.

18 Massmann, P., Falter, H.D., Deschamps, G.H. Test of a Narrow Channel Vapotron (4mm Fins, 3mm Water Channel), JET Divisional Note, JET-DN-C(91)96.

19 Rohsenow, Hartnett, Ganic. *Handbook of Heat Transfer Fundamentals*.

20 Baxi, B., Falter H. (1992). A Model for Analytical Performance Prediction of HyperVapotron. In: *Proceedings for the 5th International Topical Meeting on Nuclear Reactor Thermal Hydraulics*, Salt Lake City, Utah, 1992.

21 Escourbiac, F., Bobin-Vastra, I., Kuznetsov, V., Missirlian, M., Schedler, B., Schlosser, J. (2005) *A mature industrial solution for ITER divertor plasma facing components: HyperVapotron cooling concept adapted to Tore Supra flat tile technology*. Fusion Engineering and Design, Vol. 75–79, p. 387–390

22 Baxi, C.B. Comparison of Swirl Tube and HyperVapotron for Cooling of ITER Divertor. In: *Proceedings of the 16th IEEE/NPSS Symposium on Fusion Engineering,* 1995, Champaign, IL.

23 Escourbiac, F., et al. (1996). Comparison of various thermal hydraulic tube concepts for the ITER divertor. In: *Proceedings for the 19th Symposium of Fusion Technology*, Lisbon, Portugal, 1996.

24 Boscary, J., Araki, M., Schlosser, J., Akiba, M., Escourbiac, F. (1998). *Dimensional analysis of critical heat flux in subcooled water flow under one-side heating conditions for fusion application*. Fusion Engineering and Design, Vol. 43, p. 147 – 171.

25 Ezato, K., Suzuki, S., Sato, K., Taniguchi, M., Hanada, M., Araki, M., Akiba, M. (2001). *Critical heat flux test on saw-toothed fin duct under one-sided heating conditions*. Fusion Engineering and Design, Vol. 56-57, p. 291-295.

26 Escourbiac, F., Schlosser, J., Merola, M., Bobin Vastra, I. (2003). *Experimental optimisation of a HyperVapotron concept for ITER plasma facing components*. Fusion Engineering and Design, Vol. 66-68, p. 301-304.

27 Ezato, K., Suzuki, S., Dairaku, M., Akiba, M. (2006). *Experimental examination of heat removal limitation of screw cooling tube at high pressure and temperature conditions*. Fusion Engineering and Design, Vol. 81, p. 347-354.

28 Baxi, C.B. Thermal Hydraulics of water cooled divertors. Fusion Engineering and Design 56-57 (2001) 195-198

29 Raffray, A.R., Schlosser, J., Akiba, M., Araki, M., Chiocchio, S., Driemeyer, D., Escourbiac, F., Grigoriev S., Merola M., Tivey R., Vieider G., Youchison D. *Critical heat flux analysis and R&D for the design of the ITER divertor*. Fusion Engineering and Design 45 (1999) 377–407

30 Milnes, J., Ciric, D., Forner, M., Gee, S., Martin, D., Nightingale, M., Sauer, M. HyperVapotron design for the long pulse upgrades on MAST NBI. In: *Proceedings for the 20th IEE/NPSS Symposium on Fusion Engineering*, San Diego, CA., October 2003, p.478-481.

31 Chen, P., Newell, T.A., Jones, B.G., *Heat transfer characteristics in subcooled flow boiling with*

*HyperVapotron*, Annals of Nuclear Energy 35 (2008) 1159–1166

32 Chen, P. *An experimental investigation of critical heat flux performance of hypervapotron in subcooled boiling*, PhD Dissertation, University of Illinois at Urbana-Champaign, 2007

33 Zuber, N., 1955. *The Dynamics of Vapor Bubbles in Nonuniform Temperature Fields*, Int. J. Heat Mass Transfer 2 (1961), pp. 83-98

34 Versteeg, H.K., Malalasekera, W. *An introduction to Computational Fluid Dynamics. The Finite Volume Method*. 1995.

35 ANSYS CFX v11 / v12 Help Manuals

36 Kolev, N.I. *Multiphase Flow Dynamics 2 Thermal and Mechanical Interactions*. 2nd Edition.

37 Stewart, H.B., Wendroff, B. *Review Article. Two-Phase Flow: Models and Methods*. Journal of Computational Physics, Vol. 56, p. 363-409

38 Besnard, D.C., Harlow, F.H. *Turbulence in multiphase flow*. Int. J. Multiphase Flow, Vol. 14, p. 678-699.

39 Enwald, H., Peirano, E., Almstedt, A.E. *Eulerian Two-Phase Flow theory applied to Fluidization*, Int. J. Multiphase Flow, Vol. 22, p. 21-66.

40 Troshko, A.A., Hassan, Y.A. *A two-equation turbulence model of turbulent bubbly flows*. Int. J. Multiphase Flow, Vol. 27, p. 1965-2000.

41 Lahey Jr, R.T. *The simulation of multidimensional multiphase flows.* Nuclear Engineering and Design Vol. 235, p. 1043–1060.

42 Barth, T.J., and Jesperson, D.C. *The Design and Application of Upwind Schemes on Unstructured Meshes*, AIAA Paper 89-0366, 1989.

43 Malick, |Z. *Computational modelling of cavity arrays with heat transfer using Implicit Large Eddy Simulations*. PhD Thesis, Cranfield University, 2010

44 Esch, T., Menter, F., Vieser, W. (2003). Heat transfer predictions based on two equation turbulence models. In: *Proceedings for the 6th ASME/JSME Thermal Engineering Joint Conference*, March 16th – 20th, 2003.

45 Grotjans, H., Menter, F. *Wall Functions for General Application CFD Codes*. AEA Technology, Internal Paper. (unpublished report)

46 Zeitoun, O., Shoukri, M. *Axial void fraction profile in low pressure subcooled flow boiling.* International Journal of Heat Mass Transfer, Vol. 40(4), p. 869 – 879.

47 Steiner, H., Kobor, A., Gebhard, L. *A wall heat transfer model for subcooled boiling flow.* International Journal of Heat and Mass Transfer, Vol. 48, p. 4161–4173.

48 Podowski, M. Z., Alajbegovic, A., Kurul, N., Drew, D. A., Lahey, R. T. Mechanistic Modeling of CHF in forced-convection subcooled boiling. *In: Int. Conference on Convective Flow and Pool Boiling. Irsee, Germany*.

49 Kurul, N., Podowski, M. Z. On the modeling of multidimensional effects in boiling channels, In: *Proceedings for the 27th National Heat Transfer Conference*, Minneapolis, MN, July 28-31, 1991

50 Anglart, H. Modelling of vapour generation at wall in sub-cooled boiling two-phase flow. *In: 1st. CFDS International User Conference*, Eynsham Hall, Oxford, UK, 1993

51 Yeoh, G.H., Tu, J.Y. *A unified model considering force balances for departing vapour bubbles and population balance in subcooled boiling flow*. Nuclear Engineering and Design 235, (2005), pp. 1251–

1265.

52 Krepper, E. CFD modelling of subcooled boiling. In: *Proceedings for NURETH-10*, Seoul, South Korea, 2003.

53 Pascal-Ribot, S., Seiler-Marie, N., Grandotto, M., First step in simulations of HyperVapotron cooling concept for fusion applications. In: *Proceedings for NURETH-11*, Avignon, France, October 2nd – 6th, 2005.

54 Pascal-Ribot, S., Saroli, A.-F., Grandotto, M., Spitz, P., Escourbiac, F. *3D numerical simulations of hypervapotron cooling concept*. Fusion Engineering and Design 82 (2007) 1781–1785

55 Tentner, A., Lo, S. Computational Fluid Dynamics modelling of two-phase flow in a boiling water reactor fuel assembly. *In: Proceedings of the American Nuclear Society Topical Meeting in Mathematics and Computations*, Avignon, France, 2005.

56 Del Valle, V., Kenning, D. *Subcooled flow boiling at high heat flux.* International Journal of Heat and Mass Transfer, Vol. 28(10), pp.1907 – 1920.

57 Tolubinski, V. I., Kostanchuk, D. M. Vapour bubbles growth rate and heat transfer intensity at subcooled water boiling, In: *Proceedings for the 4th International Heat Transfer Conference*, Paris, France, 1970

58 Cole, R, Rohsenow, W.M. *Correlation of Bubble Departure Diameter for Boiling of Saturated Liquid*, Chem. Eng. Progr. Symp. Ser., (1969) 65:92, 211-213.

59 Unal, H.C. *Maximum Bubble Diameter, Maximum Bubble-Growth Time and Bubble-Growth Rate during the subcooled nucleate flow boiling of water up to 17.7MN/m$^2$*, Int. J. Heat Mass Transfer, Vol 19, p643-649.

60 Kolev, N.I. *The Influence of Mutual Bubble Interaction on the Bubble Departure Diameter*, Experimental Thermal and Fluid Science, 1994, Vol 8, p167-174

61 Tu, J.Y., Yeoh, G.H. *On numerical modelling of low-pressure subcooled boiling flows*. International Journal of Heat and Mass Transfer 45 (2002) 1197–1209

62 Cole, R. *A photographic study of pool boiling in the region of the critical heat flux*, AIChE J. 6 (1960) 533–542.

63 Zuber, N. Nucleate boiling. *The region of isolated bubbles and the similarity with natural convection*, International Journal of Heat Mass Transfer 6 (1963) 53–78.

64 Situ, R., Ishii, M., Hibiki, T., Tu, J.Y., Yeoh, G.H., Mori, M. *Bubble departure frequency in forced convective subcooled boiling flow*. International Journal of Heat and Mass Transfer 51 (2008) 6268–6282

65 Lemmert, M., Chawla, J. M. *Influence of flow velocity on surface boiling heat transfer coefficient*, Heat Transfer and Boiling (Eds. E. Hahne and U. Grigull), Academic Press, 1977.

66 Kocamustafaogullari, G., Ishii, M. *Interfacial area and nucleation site density in boiling systems*, Int. J. Heat Mass Transfer, 26 p. 1377, 1983

67 Wang, C.H., Dhir, V.K. *Effect of surface wettability on active nucleation site density during pool boiling of water of a vertical surface*, Trans. ASME, J. Heat Transfer 115 (1993), pp. 659-669

68 Basu, N, Warrier, G.R., Dhir, V.K. *Onset of nucleate boiling and active nucleation site density during subcooled flow boiling*, Trans. ASME, J. Heat Transfer 124 (2002), pp. 717-728

69 Hardenberg, J, Kenning, D.B.R, Xing, H, Smith, L.A. *Identification of nucleation site interactions.* International Journal of Heat and Fluid Flow 25 (2004) pp. 298 – 304.

70 Anglart, H., Nylund, O., 1996. *CFD application to prediction of void distribution in two-phase bubbly*

*flows in rod bundles*. Nucl. Eng. Des. 163, 81–98.

71 Tu, J. Y., Yeoh, G. H., Park G.-C., Kim M.-O. *On Population Balance Approach for Subcooled Boiling Flow Prediction*. ASME Journal of Heat Transfer, March 2005, Vol. 127, p. 253-264

72 Koncar, B., Kljenak, I., Mavko, B. *Modelling of local two-phase flow parameters in upward subcooled flow boiling at low pressure*. International Journal of Heat and Mass Transfer 47 (2004) 1499–1513

73 Ranz, W.E., Marshall, W.R., Chem. Eng. Prog. 48(3), p 141, 1952

74 Krepper, E., Egorov, Y. CFD-modelling of subcooled boiling and application to simulate a hot channel of a fuel assembly. In: *Proceedings for 13th International Conference on Nuclear Engineering*, Beijing, China, May 16-20 2005

75 Bartolemei, C. C., Chanturiya, V. M., *Experimental study of true void fraction when boiling subcooled water in vertical tubes*, Thermal Engineering, Vol. 14, pp. 123-128, 1967

76 Tu, J.Y., Yeoh, G.H. *On numerical modelling of low-pressure subcooled boiling flows.* International Journal of Heat and Mass Transfer 45, (2002), pp. 1197 – 1209.

77 Lai, J.C., Farouk, B. *Numerical simulation of subcooled boiling and heat transfer in vertical ducts*. International Journal of heat and mass transfer, Vol. 36(6), 1993, p. 1541-1551.

78 Milnes, J., Drikakis, D., Malick, Z., Shapiro, E. Advanced CFD Strategies for HyperVapotron flows and heat transfer. In: *Proceedings for the IMechE Seminar, Computational Fluid Dynamics Validation – How much is enough?*. 25 September 2008, London, UK

79 Milnes, J., Drikakis, D. (2009) *Qualitative assessment for RANS models for HyperVapotron flow and heat transfer, Fusion Engineering and Design*, Fusion Engineering and Design, Vol. 84, pp 1305-1312

80 Yamamoto, H., Seki, N., Fukusako, S. *Forced Convection Heat Transfer on Heated Bottom Surface of a Cavity*, Journal Of Heat Transfer, Vol. 101, pp.475-479, 1979

81 Metzger, D.E., Bunker, R.S., Chyu M.K. (1989). *Cavity Heat Transfer on a Transverse Grooved Wall in a Narrow Flow Channel*. Journal of Heat Transfer, Vol. 111, pp. 73-79.

82 Drikakis, D., Govatsos, P.A., Papantonis, D.E. (1994) *A Characteristic-Based Method for Incompressible Flows*. International Journal for Numerical Methods in Fluids, Vol. 19, pp 667-685

83 Drikakis, D., Rider, W. (2005). *High-Resolution Methods for Incompressible and Low-Speed Flows*. Springer.

84 Drikakis, D., Iliev, O.P., Vassileva, D.P. (1998) *Nonlinear Multigrid Method for the Three-Dimensional Incompressible Navier-Stokes Equations*. Journal of Computational Physics. Vol. 146, pp 301-321.

85 Shapiro, E., Drikakis, D. (2006) *Non-Conservative and Conservative Formulations of Characteristics-Based Numerical Reconstructions for Incompressible Flows*. J. Num. Meth. Eng. Vol. 66(9), pp. 1466-1482.

86 Prasad, A. K., Koseff, J. R. *Reynolds number and end-wall effects on a lid-driven cavity flow*, Phys. Fluids A 1 (2), pp.208 – 218, February 1989

87 Lee, T.H., Park, G.-C., Lee, D.J., 2002. *Local flow characteristics of subcooled boiling flow of water in a vertical annulus*. Int. J. Multiphase Flow 28, 1351–1368

88 Anglart, H., Nylund, O., Kurul, N. Podowski, M.Z., 1995, *CFD prediction of flow and phase distribution in fuel assemblies with spacers*; NURETH-7, Saratoga Springs, New York, Nuclear Engineering and Design 177(1997) pp.215-228.

89 Frank,Th., Zwart, P. J., Krepper, E., Prasser, H.-M., and Lucas, D. (2008), *Validation of CFD models for mono- and polydisperse air-water two-phase flows in pipes*, Nucl. Eng. Design 238 pp. 647-649

90 Rossiter, J. Wind Tunnel Experiments on the Flow Over Rectangular Cavities at Subsonic and Transonic Speeds. Reports and Memoranda, 3438, Aeronautical Research Council, 1964.

91 ITER Material Properties Handbook, ref AK02 Cu-Cr-Zr

92 Ranjit, R. *Design of experiments using the Taguchi approach*. John Wiley and Sons.

# Appendix A – Typical modelling choices

| | Category | Model setting | Choices | | | |
|---|---|---|---|---|---|---|
| 1 | Geometry / Mesh | **Domain type** | 3D | 2D | - | - |
| 2 | | **Symmetry used in "Z" direction for 3D model** | Yes | No | - | - |
| 3 | | **Element type** | Hexahedral | Tetrahedral | Hybrid | - |
| 4 | | **Near wall mesh resolution** | y+ < 1 (Low Re method) | y+ > 11 (wall functions) | - | - |
| 5 | Boundary conditions | **Inlet velocity profile** | Uniform | Fully Developed Profile | Experimental Profile | Periodic |
| 6 | | **Inlet temperature profile** | Uniform | Fully Developed Profile | Experimental Profile | - |
| 7 | | **Inlet turbulence profile** | Uniform (default = 5% intensity) | Fully Developed Profile | Experimental Profile | - |
| 8 | | **Outlet type** | Outlet | Opening | Periodic | - |
| 9 | Liquid settings | **Compressibility** | Compressible | Incompressible | - | - |
| 10 | | **RANS turbulence model** | None | k-epsilon | SST k-omega | BSL Re Stress |
| 11 | | **Buoyancy model** | None | Density Difference | Boussinesq | - |
| 12 | Vapour settings | **Morphology** | Continuous Fluid | Dispersed Fluid | Polydispersed Fluid | Droplets |
| 13 | | **Bubble diameter*** | Constant | Fct of subcooling | - | - |
| 14 | | **Heat transfer** | Thermal Energy | Isothermal (T = Tsat) | - | - |
| 15 | | **RANS turbulence model** | None | Dispersed Phase Zero Equation | - | - |

| | Category | Model setting | Choices | | | |
|---|---|---|---|---|---|---|
| 16 | | **Buoyancy model** | None | Density Difference | Boussinesq | - |
| 17 | | **Wall slip condition** | No slip | Free slip | - | - |
| 18 | **Liquid / Vapour pair settings** | **Lift Force** | None | Lift Coefficient defined | Tomiyama method | Saffman Mei method |
| 19 | | **Drag Force** | None | Drag Coefficient defined | Schiller Naumann method | Ishii Zuber method |
| 20 | | **Virtual Mass Force** | None | Virtual Mass Coefficient defined - | - | - |
| 21 | | **Wall lubrication Force** | None | Antal method | Tomiyama method | Frank method |
| 22 | | **Turbulent Dispersion Force** | None | Favre Averaged Drag Force method | Lopez de Bertodano method | - |
| 23 | | **Turbulence transfer model** | None | Sato Enhanced Eddy Viscosity method | - | - |
| 24 | | **Interphase Heat Transfer (liquid)** | Ranz Marshall method | Hughmark method | Nu defined | HTC defined |
| 25 | | **Interphase Heat Transfer (vapour)** | Zero Resistance | Nu defined | HTC defined | - |
| 26 | **Boiling model** | **Bubble Diameter Influence Factor** | 2 | Other | - | - |
| 27 | | **Max. Area Fraction of Bubble Influence** | 0.5 | 0.95 | Other | - |
| 28 | | **Fixed Yplus for Liquid Subcooling** | 250 | Other | - | - |
| 29 | | **Bubble Departure Diameter** | Tolubinski Kostanchuk expression | Cole and Rohsenow expression | Unal expression | Wang and Dhir expression |
| 30 | | **Wall Nucleation Site Density** | Lemmert Chawla expression | Kocamustafaogullari and Ishii expression | Wang and Dhir expression | Basu et al expression |
| 31 | | **Bubble Detachment Frequency** | Cole expression | Zuber expression | Situ expression | - |
| 32 | | **Bubble Waiting Time** | t = (0.8 / freq) | t = 0s | Other | - |
| 33 | | **Liquid Quenching Heat Transfer Coefficient** | Del Valle Kenning method | - | - | - |
| 34 | **Solver control** | **Advection scheme** | Upwind | High Resolution | Specify Blend Factor | - |
| 35 | | **Turbulence numerics** | 1st Order | High Resolution | - | - |
| 36 | | **General - Residual target** | 1e-4 (RMS) | 1e-5 (RMS) | 1e-6 (RMS) | Other |